Faculteit Wetenschappen

Departement Bio-Ingenieurswetenschappen

Ontwerpen van Wervelbedreactoren met Numerieke Stromingsleer voor het Vrijzetten van H_2 uit Vloeibare Organische H_2-dragers

Proefschrift voorgelegd tot het behalen van de graad van doctor in de bio-ingenieurswetenschappen aan de Universiteit Antwerpen door

Laurens Van Hoecke

Promotoren:

Prof. Dr. Ir. Patrice Perreault

Prof. Dr. Ir. Sammy Verbruggen

Antwerpen, 2024

Faculty Of Science

Department of Bioscience Engineering

CFD – Assisted Design of Fluidized Reactors for H_2 Release from LOHC

Thesis submitted to obtain the doctorate degree in
Bioscience Engineering at the University of Antwerp by

Laurens Van Hoecke

Members of the Jury:

Prof. Dr. Verbeeck J.	(chair) University of Antwerp
Prof. Dr. Ir. Pereault P.	(promotor) University of Antwerp
Prof. Dr. Ir. Verbruggen S.	(co-promotor) University of Antwerp
Prof. Dr. Ir. Denys, S.	University of Antwerp
Prof. Dr. Ir. Yi Ouyang	Ghent University
Prof. Dr. Ir. Gonzalez – Quiroga, A.	Universidad del Norte, Colombia

Antwerp, 2024

Samenvatting

In een wereld die zich steeds meer dient aan te passen aan het gebruik van hernieuwbare energie, wordt verwacht dat waterstof (H_2) een sleutelrol zal spelen om het variabele karakter van hernieuwbare bronnen zoals zonne- en windenergie te kunnen opvangen. In dit opzicht zal H_2 een belangrijke rol gaan spelen bij zowel de opslag van overtollige hernieuwbare energie die wordt geproduceerd tijdens uren van piekproductie, als ook door het gebruik ervan als een alternatieve energiebron, tijdens uren met weinig hernieuwbare energieproductie. Een cruciale uitdaging om het gebruik van H_2 als toekomstige energiedrager mogelijk te maken is het ontwikkelen efficiënte opslagmethoden. De lage dichtheid van H_2-gas is nadelig voor de volumetrische opslagcapaciteit. Om het probleem van de lage dichtheid op te lossen, zijn er in het verleden verschillende methoden voorgesteld om de energie-opslagcapaciteit van H_2 te verhogen. Naast de meer bekende oplossingen zoals opslag van H_2 op hoge druk of in vloeibare vorm op lage temperatuur, is er ook de optie om H_2 chemisch te binden aan een dragermolecule en zo een nieuwe chemische verbinding te maken met een hogere energieopslagdichtheid dan zuiver H_2 – gas. Eén zo'n voorbeeld van een dragermolecuul om H_2 chemisch op te slaan is dibenzyltolueen (DBT), dat deel uitmaakt van de klasse van vloeibare organische waterstofdragers of LOHC (Eng.: "Liquid Organic Hydrogen Carriers"). DBT is een aromatische molecule waarin de dubbele koolstof-koolstofverbindingen dienen als bindingsplaats voor H_2. Het opslaan van H_2 in LOHC-moleculen is een cyclisch proces waarbij een aromatische molecule verzadigd wordt en tot een alifatische verbinding wordt omgevormd. De alifatische verbinding, genaamd perhydro-dibenzyltolueen (H_{18}DBT), is een stabiele vloeistof met thermofysische eigenschappen vergelijkbaar met die van dieselbrandstoffen, hierdoor kunnen deze moleculen snel worden geïntegreerd in de huidige brandstofinfrastructuur. H_2 kan worden vrijgemaakt uit de dragermolecule via een katalytische reactie met behulp van een heterogene (edel)metaalkatalysator. Tijdens het vrijkomen van H_2 wordt de dragermolecule teruggebracht naar de aromatische vorm en kan de cyclus worden herhaald. Deze vrijzettingsstap voor H_2 is de meest energieverslindende stap in het proces en vergt tot een derde van de energie die in H_2 is opgeslagen. De vrijgavestap is ook een endotherm proces en koelt zichzelf dus af. Een efficiënte warmteoverdracht tijdens de dehydrogenatiestap is dus cruciaal om het proces zo efficiënt mogelijk te laten verlopen. Eerder is het ook geobserveerd dat de vorming van H_2 bellen op de katalysatordeeltjes tijdens de dehydrogenatiestap het contact tussen de actieve sites van de katalysator en de geladen draagvloeistof blokkeert. Om beide aspecten van verbeterde warmteoverdracht en efficiënte verwijdering van de gasbellen te behandelen, wordt in dit proefschrift het gebruik van wervelbed reactoren voorgesteld voor de dehydrogenatie van H_{18}DBT. In een wervelbed reactor is de wrijvingskracht op de deeltje uitgeoefend door de vloeistof in de reactor gelijk aan het gewicht van de deeltjes, waardoor de deeltjes bewegen in een vloeistofachtige toestand. In dit proefschrift wordt het gebruik van wervelbedden voor de dehydrogenatie van H_{18}DBT bestudeerd via numerieke stromingsleer of CFD (Eng.: "Computational Fluid Dynamics"). De CFD-studies geven een eerste inzicht in de beweging van de deeltjes tijdens de dehydrogenatie. Door de beperkte aard van de CFD code die ontwikkeld was om deze reactie te simuleren, is het nog niet mogelijk om verbeteringen in dehydrogenatie snelheid te voorspellen in wervelbed reactoren, verbeteringen veroorzaakt door verhoogde warmteoverdracht, bijvoorbeeld. Er kon wel gezien worden dat de uniforme verspreiding van de deeltjes in de reactor een grote uitdaging zal zijn.

Dit proefschrift biedt een inleiding in het onderwerp CFD in de vorm van een uitgewerkt voorbeeld, waarin de basisprincipes van CFD-simulaties met behulp van "Finite Volume Method" worden behandeld. Deze tutorial is toegepast op een eenvoudige chemische reactie in eenvoudige reactorgeometrieën, maar laat de benodigde stappen zien om CFD simulaties te starten. Dit voorbeeld diende als basis voor de implementatie van de chemische reacties in CFD-codes, zonder rekening te hoeven houden met eventuele invloeden van faseveranderingsverschijnselen of massa- en warmteoverdrachtsbeperkingen die optreden in complexere heterogene katalytische reacties.

Het gebruik van CFD simulaties wordt verder toegepast in een koude-stroom nabootsingsstudie om het potentieel van fluïdisatie voor de dehydrogenatiereactie van H_{18}DBT te onderzoeken. In deze studie werd een nieuw reactorprototype geïntroduceerd dat gebruikmaakte van kolkende wervelbedreactoren om deeltjes te fluïdiseren in de aanwezigheid van een gelokaliseerde gasstroom. Via CFD-simulatie werd aangetoond dat deze kolkende wervelbedreactor in staat is om een opwaartse spiraalvormige beweging van de vloeistofstroom te genereren, die de deeltjes in een gefluïdiseerde toestand kan brengen en vervolgens de gasfase concentreert in de buurt van de centrale as van de reactor. Een verbeterde verwijdering van de gasfase uit de deeltjes door de wervelende vloeistoffase wordt verwacht op basis van de analyse van de slipsnelheid. Aangezien deze reactor de eerste iteratie van het reactorontwerp is, werden mogelijke wijzigingen in het ontwerp van de reactor voorgesteld op basis van deze koude-stroomstudie. Deze veranderingen werden bestudeerd in het laatste hoofdstuk van dit proefschrift.

De CFD-simulaties voor de dehydrogenatie van $H_{18}DBT$ zijn gebaseerd op het Euleriaanse - Euleriaanse model voor meerfasesystemen. Deze simulatiemethode gaat ervan uit dat elke fase kan worden beschreven door zijn eigen set massa-, momentum- en energievergelijkingen en dat deze vergelijkingen aan elkaar worden gekoppeld door een gedeelde term voor druk en een interactiekracht tussen de fasen. De interactiekracht tussen de fasen berust op een zorgvuldige selectie van modellen om de invloed van de ene fase op de andere nauwkeurig te berekenen. De selectie van deze modellen gebeurt twee-aan-twee, wat betekent dat er een model geselecteerd moet worden voor de vloeistof – gas, voor de vloeistof – vaste stof en voor de gas – vaste stof interacties. Ik heb de invloed op de gesimuleerde deeltjes onderzocht door de selectie van verschillende combinaties van weerstandsmodellen voor elk paar van de aanwezige fasen. De resultaten van de simulaties werden vergeleken met de resultaten van camera-experimenten: in deze studie werd gebruik gemaakt van digitale beeldanalyse, “*Particle Image Velocimetry*” en “*Particle Tracking Velocimetry*”. Er werd een vereenvoudigde geometrie onderzocht in de vorm van een *pseudo* – 2D wervelbedreactor. Uit de analyse van dit eenvoudige *pseudo* – 2D – systeem bleek dat twee van de onderzochte modelcombinaties meer geschikt waren om de driefasensystemen te simuleren dan de andere onderzochte modellen. Dit waren i) het gebruik van het Gidaspow model voor de vloeistof - vaste interacties gecombineerd met het Ishii - Zuber model voor vloeistof – gas interacties en het leveren van geen model voor de gas – vaste stof interacties. Dit model was vooral geschikt om de deeltjeshoogte en het deeltjeshoogteprofiel vast te leggen. ii) Het gebruik van het Gidaspow model voor zowel de vloeistof – vaste stof interacties als de gas – vaste stof interacties, terwijl de vloeistof – gas interacties berekend werden met behulp van het Tomiyama drag model, dit was minder nauwkeurig om de deeltjeshoogte te schatten, maar leverde nauwkeurigere snelheidsmetingen op in vergelijking met de andere modelcombinaties.

In het laatste hoofdstuk van dit proefschrift bestudeerde ik de invloed van de stroomsnelheid op de deeltjeshoogte en de uniformiteit van deeltjes in de reactor tijdens de dehydrogenatie van H_{18}DBT via CFD-simulaties. Aangezien er geen CFD-code beschikbaar was om de dehydrogenatie van H_{18}DBT te simuleren, stel ik voor om een empirische term te gebruiken op basis van een curve- en parameterschatting uit experimentele gegevens in de literatuur. Deze code was in staat om H_2 enkel vrij te zetten op de plaatsen in de reactor waar zowel de vaste katalysator als het vloeibare H_{18}DBT aanwezig is, hierdoor kon het gedrag van een katalytische reactie worden nagebootst. De code voorspelde volumes voor het vrijzetten van H_2 die vergelijkbaar waren met de verwachte waarden op basis van gegevens uit de beschikbare literatuur. De CFD simulaties met de lokale H_2 afgifte van het deeltjesoppervlak toonden aan dat de deeltjes binnen het bed niet uniform verdeeld zijn tijdens de dehydrogenatie, wat waarschijnlijk veroorzaakt wordt door de accumulatie van H_2 gas met toenemende hoogte in het deeltjesbed. Er wordt een hoge mate van dilutie van de katalysator vanuit het deeltjesbed waargenomen, dit is ongewenst omdat deze hoge verdunning van de deeltjes een minder efficiënt gebruik van het reactorvolume maakt. Er wordt een hoog opeengepakt gebied waargenomen aan de onderkant van het bed, wat waarschijnlijk lokaal lage temperaturen veroorzaakt door de endothermiciteit van de reactie. Om de uniformiteit van het deeltjesbed te verbeteren, wordt het prototype van de kolkende wervelbedreactor onderzocht voor de dehydrogenatie van H_{18}DBT. De eerder voorgestelde wijzigingen in de geometrie, d.w.z. de toevoeging van een centrale kegel aan de bodemplaat en het verkleinen van de diameter van de reactor, bleken positieve effecten te hebben op het deeltjesbed. Op basis van de CFD-simulaties werd een uniformer bed aangetoond, zelfs bij lagere stroomsnelheden, door gebruik te maken van de voorgestelde wijzigingen aan de reactorgeometrie. Deze thesis is echter niet het eindpunt maar eerder het begin van het onderzoek naar wervelbed reactoren voor de dehydrogenatie van H_{18}DBT. Door de complexe interacties tussen deeltjesgrootte, hoeveelheid katalysator en stromingssnelheid van H_{18}DBT op het vrijzetten van H_2 uit de dragermolecule is verder geïntegreerd onderzoek op het vlak van katalysatorontwikkeling en reactorgeometrie nodig. Deze thesis stelt een nieuwe reactorgeometrie voor als basis voor dit verdere onderzoek.

Abstract

In a world that is increasingly adapting to the use of renewable energy, Hydrogen (H_2) is expected to play a key role to mitigate the intermittent nature of the renewable sources such as solar and wind power. In this regards H_2 is expected to play a crucial role both in storing the excess renewable energy produced during hours of peak production as by providing an alternative energy source during hours with little renewable energy production. A crucial challenge to enable the use of H_2 as a future energy vector is efficient storage. The low density of H_2 gas is detrimental to the volumetric storage capacity. To solve the problem of the low density, several methods have been proposed in the past to increase the volumetric storage capacity of H_2. Next to the more well – known solutions of compression and liquefaction of H_2, there is also the option to chemically bind the H_2 gas to a carrier molecule and produce a new chemical compound, with a higher energy storage density compared to the pure H_2. One such an example of a carrier molecule to chemically store H_2 is dibenzyltoluene, which is part of class of Liquid Organic Hydrogen Carriers or LOHC. Dibenzyltoluene (DBT) is an aromatic molecule in which the carbon – carbon double bonds serve as a binding site for the H_2 gas. Storing H_2 in LOHC molecules is a cyclic process in which aromatic molecule gets saturated with H_2 gas to form an aliphatic compound. The aliphatic compound, called perhydro-dibenzyltoluene (H_{18}DBT), is a stable liquid with thermophysical properties similar to diesel fuels, which allows for a rapid integration in today's fuel infrastructure. H_2 gas can be released from the carrier molecule via a catalytic reaction using a heterogeneous (noble) metal catalyst. During H_2 release, the carrier molecule is reverted back to the aromatic form, and the cycle can be repeated. The H_2 release step is the most energy demanding step in the process, requiring up to a third of the energy stored in the H_2. The release step is also an endothermic process and as such it cools itself down, so efficient heat transfer during the dehydrogenation step is crucial to keep the process running at maximal efficiency. Furthermore, it has also been seen that formation of H_2 bubbles on the catalyst particles during the dehydrogenation step blocks the contact between the active sites of the catalyst and the charged carrier liquid. To cover both the aspects of improved heat transfer and efficient removal of the gas bubbles, the use of a fluidized particle bed is proposed in this thesis for the dehydrogenation of H_{18}DBT. In a fluidized bed the drag induced by the fluids

present in the reactor equals the weight of the particles, causing the particle to move in a fluid like state. In this thesis, the use of fluidized beds for the dehydrogenation of $H_{18}DBT$ is studied via Computational Fluid Dynamics or CFD. The CFD studies provide a first insight into the movement of the particle bed during the dehydrogenation. However, the code developed and used for this analysis, was not able to provide new insights into possible heat transfer improvements of the fluidization process.

This thesis provides a basic introduction into the topic of CFD in the form of a tutorial case, covering the basics of CFD simulations using the finite volume method. This tutorial is applied to a simple chemical reaction in simple reactor geometries but shows the required steps to properly set up CFD simulations. This served as a basis for the implementation of the chemical reactions in CFD codes, without having to take into account any influence from phase change phenomena or mass and heat transfer limitations that arise in more complex heterogeneous catalytic reactions.

The use of CFD simulations is further applied in a cold flow mock-up study to investigate the potential of fluidization for the dehydrogenation reaction of $H_{18}DBT$. In this study a novel reactor prototype was introduced which made use of swirling liquid flows to fluidize particles in the presence of a localized gas flow. It was shown via CFD simulation that this swirling fluidized reactor is able to generate an upwards helical motion of the liquid flow, which is able to move the particle bed in a fluidized state and subsequently concentrate the gas phase near the central axis of the reactor, this eases the separation of the gas and liquid phase in operational conditions. Increased removal of gas phase from the particles by the swirling liquid phase is expected, based on analysis of the slip velocity. Since this reactor is the first iteration of the reactor design, potential changes in design of the reactor were proposed based on this cold flow study. These changes were studied in the final chapter of the thesis.

The CFD simulations for the dehydrogenation of $H_{18}DBT$ are based on the Eulerian – Eulerian multiphase method. This simulation method assumes that each phase can be described by its own set of mass, momentum and energy equations and that these equations are linked together by a joined pressure term and an interaction force between the phases. The interaction force between the phases relies on careful selection of models to accurately calculate the influence of one phase on the other. The selection of these models is done pairwise, meaning that a model has to be selected for the liquid – gas, for the liquid – solid and for the gas – solid interactions. I have investigated the influence on the simulated particle bed by the selection of different combinations of drag model combinations for each of the phase pairs. The results from the simulations were compared to the results obtained from camera experiments: digital image analysis, particle image velocimetry and particle tracking velocimetry were used in this study. A simplified geometry was investigated in the form of a *pseudo* – 2D fluidized bed reactor. From analysis of this simple *pseudo* – 2D system it showed that two of the studied model combinations were more suited to simulate the three phase systems than the other models investigated. These were i) the use of the Gidaspow model for the liquid – solid interactions combined with the Ishii – Zuber model for liquid – gas interactions and to supply no model for the gas – solid interactions. This model was especially suited to capture the bed height and bed height profile. ii) The use of the Gidaspow model for both the liquid – solid interactions and the gas – solid interactions, while calculating the liquid – gas interactions using the Tomiyama drag model, this was less accurate to estimate the bed height but provided more accurate velocity readings compared to the other model combinations.

In the final chapter of this thesis, I studied the influence of the flowrate on the bed height and disengagement of particles during the dehydrogenation reaction of H_{18}DBT via CFD simulations. Since there was no CFD code available to simulate the dehydrogenation reaction of H_{18}DBT, I propose the use of a source term based on a curve fit and parameter estimation from experimental data in the literature. This code was able to release H_2 gas only in those cells which contain both the solid catalyst as the liquid H_{18}DBT, effectively mimicking the behaviour of a catalytic reaction. The code predicted values for the H_2 release that were similar to the values expected based extraction of data from the available literature. The CFD simulations with the local H_2 release from the particle surface showed that the particles within the bed are not uniformly distributed during the dehydrogenation reaction, which is likely caused by the accumulation of H_2 gas with increasing bed height. A high degree of particle entrainment is observed from the particle bed, which is unwanted since this high dilution of the particles makes less efficient use of the reactor volume. A highly packed region is observed neat the bottom of the bed, which is likely to cause cold spots due to the endothermicity of the reaction. To improve the uniformity of the particle bed, the swirling fluidized reactor prototype is investigated for the dehydrogenation of $H_{18}DBT$. The previously proposed changes in the geometry, i.e., the addition of a central cone to the bottom plate and reducing the diameter of the reactor body showed to have positive effects on the particle bed. A more uniform bed was shown based on the CFD simulations, also at lower flowrates, using the proposed changes to the reactor geometry. This thesis however, is not the endpoint but rather the beginning of the research into the use of fluidized bed reactors for $H_{18}DBT$ dehydrogenation. Due to the complex interactions that affect H_2 release, such as particle size, catalyst loading, velocity of $H_{18}DBT$, there is a need for highly integrated research in catalyst development and reactor geometry to be able to obtain the most ideal process for dehydrogenation of $H_{18}DBT$. This thesis proposes a new reactor design as a starting point for subsequent studies of fluidized bed reactors for H_2 release from $H_{18}DBT$.

Dankwoord – Acknowledgement

Na meer dan vijf jaar aan dit doctoraat te werken, is het eindpunt eindelijk aangebroken. Het was een ongelooflijk boeiend periode in mijn leven waarin ik enorm veel heb bijgeleerd en een periode waar ik altijd met veel plezier en trots op zal terugkijken. Het eindproduct van het werk van de afgelopen jaren, de doctoraatstitel, is een individuele bekroning, maar ééntje die ik enkel gehaald heb dankzij de hulp van een grote groep anderen.

Eerst en vooral wil ik mijn promotor, Patrice, bedanken. Ik was je allereerste doctoraatstudent en hoewel ik maar weinig bekend was met simulatiesoftware, heb je er toch voor gekozen om je vertrouwen in mij te stellen en mij de kans te geven om mijn doctoraatstraject te kunnen vervolledigen. Ik heb enorm veel van jou geleerd, bijvoorbeeld in de cursus *Advanced Reactor Engineering* waar ik blij was dat ik jou lessen mocht bijwonen. Ook voor de vele interessante gesprekken, zowel over wetenschappelijke als niet – wetenschappelijke onderwerpen ben ik heel dankbaar, het was nooit saai met jou aan de lunchtafel in Blue App. Voor de geweldige kans en de mooie tijd, zeg ik daarom diep uit mijn hart en volgens de stijl van onze chat op Teams: “Bednakt, Patrice”. Ik denk dat het maar zelden gebeurt dat een doctoraatstudent al langer aan een universiteit werkt dan de begeleidende promotor, daarom moet ik dus nog twee andere professoren bedanken die mij de kans hebben gegeven om mijn doctoraat te starten: Sammy en Silvia. Jullie gaven me de opporuniteit en het vertrouwen om dit onderzoeksveld in waterstofopslag te starten in onze onderzoeksgroep. Het was zeker geen makkelijke taak om hier als enige student rond te werken, maar mede dankzij jullie steun hebben we een hier een duidelijk overzicht van kunnen geven in een review paper waar ik altijd trots op zal zijn. In dat opzicht wil ik ook Ludovic bedanken die veel nuttige feedback had op de eerste versies en me gemotiveerd heeft het maximale uit de paper te halen. Sammy, ik ben ook blij dat ik steeds op jouw kon rekenen als copromotor om antwoorden te krijgen op administratieve vragen over het doctoraatstraject en voor je feedback op mijn publicaties.

I would also like to express my sincere gratitude to all the members of the jury for the great interest you have shown in reading my work and providing me with additional comments and inputs during the preliminary defence. I believe it has changed the final version of this thesis for the better, which wouldn't be possible without your help.

Eén van de grootste uitdagingen tijdens mijn doctoraat was het autodidactisch aanleren van het gebruik van de software OpenFOAM. Daarom was ik zeer opgelucht dat ik met vragen die ik niet op mezelf kon oplossen altijd te rade kon bij Laurien Vandewalle. In dat opzicht wil ik Tom Lauriks ook bedanken, die me een aantal keer goed geholpen heeft met me op weg te zetten bij het gebruik van OpenFOAM op de supercomputer van de UA. Het CalcUA team, dat de supercomputer van de UA beheert, heeft ook mijn oprechte dankbaarheid voor de samenwerking en communicatie de afgelopen jaren. De rekeninfrastructuur en dienstverlening gebruikt in dit werk werd voorzien door de HPC kernfaciliteit CalcUA van de Universiteit Antwerpen en door het VSC (Vlaams Supercomputer Centrum), gefinancierd door het FWO en de Vlaamse overheid.

I would also like to thank my colleagues who helped make a great atmosphere, which really helped me to keep motivated throughout the five year process. Nithin, you and I have a shared a lot in all the years we worked together, it was inspiring to see you work all those hours and I am very happy that we both reach the end goal of the doctoral degree so close to each other. I really enjoyed all the talks we had together, and that I could always walk into the lab to have a chat. I will really miss being greeted so welcoming with the words "Meneer Van Hoecke" each morning. Secondly, I would also like to thank all the other colleagues at DuEL for all the fun times spend together, especially the Friday evening cards games, I will always remember with great joy. Annelize en Hilde, jullie wil ik ook graag specifiek bedanken voor het alle administratieve hulp en hulp bij bestellingen. Lore, ook jou wil ik ook speciaal bedanken, samen zijn we begonnen aan een doctoraat op 1 oktober 2018 en we hebben elkaar elke dag gesteund. Je was echt een hele grote cheerleader van mijn werk en ik ben echt heel dankbaar dat ik jou zo goed heb mogen leren kennen. Ik hoop dat je reis met Hendrik een fantastische ervaring is, en je je geweldig geamuseerd hebt op de tijd dat ik deze thesis heb geschreven.

Ik zou ook nooit zover zijn gekomen zonder de hulp van mijn vrienden en broers, zussen ouders en grootouders. Mama en papa, dankzij jullie ondersteuning kon ik mij volledig toeleggen op mijn studies als Bio-ingenieur en kon ik zo de kans krijgen om aan dit doctoraat te starten. Thomas, Aster, Losjh, Thomas, Marie, Tom, Eline en Ronald, het is geweldig om jullie allemaal in mijn familie te hebben. Er zijn maar weinig mensen die het geluk hebben van zo’n groot gezin te hebben en om zoveel steun te krijgen als ik van jullie voelde. Ook aan Koen, Anja, Heleen, Nathan, Senne en Salomé, ik had al een geweldige familie, om dan ook nog eens het geluk te hebben zo een geweldige schoonfamilie te hebben is weinigen gegeven. Een speciale vermelding ook aan Simon, Dieter en Jonathan voor de vele leuke momenten samen tijdens de onze studies en op alle talrijke keren dat we samen hebben afgesproken de laatste jaren. Simon, jou wil ik nog eens specifiek bedanken voor je uitstekende MATLAB vaardigheden, waar jij me in hoofdstuk 4 enorm mee vooruit hebt geholpen.

En al laatste: Lize. Het is heel moeilijk om te verwoorden wat jij allemaal voor mij betekent. Jij bent mijn beste vriendin, mijn grootste supporter, mijn sterkste steun, er is niemand anders die me zo goed kent als jij. De laatste maanden heb je me echt enorm geholpen terwijl ik deze thesis aan het schrijven was, je voelde het perfect aan wanneer ik nood had aan ontspanning en wanneer het me beter af zou gaan om nog even door te werken. Dit deed je dan ook nog eens terwijl je zelf bezig was met het afwerken van jouw eigen doctoraat en terwijl je in verwachting was van ons zoontje. Jij bent echt zo’n enorm sterke vrouw en ik heb echt veel geluk dat ik jouw man mag zijn. Ik kijk enorm uit naar ons verdere leven samen en naar alle nieuwe uitdagingen die op ons pad gaan komen. Te beginnen met de kleine baby die we samen verwachten binnenkort.

Table of Contents

Samenvatting V

Abstract IX

Dankwoord – Acknowledgement XIV

Table of Contents XVIII

List of Figures XXI

List of Tables XXVII

Abbreviations and Symbols XXIX

Chapter 1 Introduction into LOHC based H_2 - storage and the potential improvements by fluidization. 1

1.1 Introduction 3

1.2 Hydrogen Storage Methods 4

1.2.1 Compressed Hydrogen 4

1.2.2 Liquid Hydrogen 4

1.2.3 Ammonia 5

1.2.4 Methanol 5

1.2.5 Formic Acid 6

1.2.6 Liquid Organic Hydrogen Carriers 6

1.3 Previous Reactor Design for LOHC 12

1.3.1 Batch or Autoclave Reactors 12

1.3.2 Coated Reactor Structures 14

1.3.3 Microchannel Reactors 15

1.3.4 Catalytic Distillation 16

1.3.5 Tubular Reactors 17

1.4 Fluidized Bed Reactors 21

1.4.1 General Principles of Liquid – Gas – Solid Fluidized Bed Reactors 21

1.4.2 Guiding Principles for Fluidized Bed Reactor Design for H_{18}DBT Dehydrogenation 26

1.5 Scope of The Thesis 28

Chapter 2 Basic Principles of the Finite Volume Method for Computational Fluid Dynamics 31

2.1 Introduction 33

2.2 Theory 34

2.2.1 Mathematics in CFD 34

2.3 The OpenFOAM Case Structure 40

2.4 Proposed Workflow 41
2.4.1 Problem Statement 41
2.4.2 One Dimensional Model 42
2.4.3 Model and Solver Selection 42
2.5 Solved Example 43
2.5.1 Problem Statement 43
2.5.2 Geometry and Meshing 47
2.5.3 Tubular Reactor in OpenFOAM 49
2.5.4 Grid Refinement Study 51
2.5.5 Notched Reactor 55
2.6 Challenges with heterogenous catalytic reactions 57
2.7 Conclusion 58
Chapter 3 Cold Flow Study on a Swirling Fluidized Bed Reactor for H_{18}DBT Dehydrogenation ... 59
3.1 Introduction 61
3.2 Methodology 62
3.2.1 Dehydrogenation Reactor 62
3.2.2 Cold Flow Mock-Up Strategy 63
3.2.3 CFD Simulations Settings 67
3.3 Results and Discussion 70
3.3.1 Computational Domain 70
3.3.2 Fluidization Profile of the Particle Bed 73
3.3.3 Liquid and Slip Velocity 77
3.3.4 Gas Distribution in the Reactor 79
3.3.5 Future Design Changes 81
3.4 Conclusion 82
Chapter 4 Investigation of the model selections for Eulerian – Eulerian simulations of LGSFB ... 85
4.1 Introduction 87
4.2 Methodology 89
4.2.1 Experimental Setup 89
4.2.2 Governing Equations 91
4.2.3 Simulations and Experimental Settings 96
4.2.4 Meshing and Grid Convergence Study 96
4.3 Preliminary Simulations 100
4.3.1 2D Assumption for the three-phase flow 100
4.3.2 Gas phase volume fraction models 101
4.3.3 Gas Phase Turbulence 103

4.3.4 Studied Drag Model Combinations 104
4.4 Results and Discussion 105
4.4.1 Bed Height Analysis 106
4.4.2 Time Averaged PIV 108
4.4.3 Time Averaged Particle Tracking Velocimetry 110
4.4.4 Discussion 112
4.5 Conclusion 114
Chapter 5 Exploring the Influence of Geometry Changes of the Swirling Fluidized Bed Reactor 117
5.1 Introduction 119
5.2 Methodology 123
5.2.1 Catalytic Source Term 123
5.2.2 CFD parameters 127
5.2.3 Case setup conventional fluidized bed 128
5.2.4 Case setup SFB shape exploration 128
5.3 Simulation Results 131
5.3.1 Conventional Fluidized Bed Simulations Using the Catalytic Source Term. 131
5.3.2 Analysis of the number of inlets 134
5.3.3 Influence of the Geometry Changes in the SFB Reactor 135
5.3.4 Analysis of the First Damköhler Number 140
5.4 Conclusion 142
Chapter 6 Conclusions and Future Outlook 145
6.1 General Conclusion 147
6.2 Suggestions for future research 150
Appendix V – Curriculum Vitae 168
Bibliography 173

List of Figures

Figure 1-1 General cycle of H2 storage using LOHC. The hydrogenation reaction is an exothermic reaction requiring elevated pressures. The endothermic dehydrogenation reaction proceeds with increased temperature and low pressures. 7

Figure 1-2 Schematic flow diagram of the hot pressure swing adsorption reactor. [85] 14

Figure 1-3 Screening procedure of flat plate structures coated with catalyst for the dehydrogenation of H_{18}DBT. [88] 15

Figure 1-4 microstructure used in the reactor of Wunsch et al. [91] 16

Figure 1-5 Schematic of the catalytic distillation process proposed by Geißelbrecht et al. [92] 17

Figure 1-6 Dehydrogenation reactor from Kadar et al. [97] near the bottom of the reactor, A) and the top B). With the particle bed I, the heated internal II, and the gas bubbles III. 18

Figure 1-7 Reactor configurations from the work of Heublein et al. [98] showing the reactor orientation in horizontal and vertical operational modes. 1: the liquid feed, 2: liquid product, 3: purified H_2, 4: Recycle of condensate. 19

Figure 1-8 Snapshots of the dehydrogenation experiment by Solymosi et al. [99], showing A) the catalyst during dehydrogenation. B) The inhibited state of the catalyst after a cycle of cooling and reheating. C) the H_2 gas release after mechanical stimulus of the catalyst bead. 20

Figure 1-9 Relative orders of magnitude of heat transfer coefficients for empty tube, fixed and fluidized bed reactors. Data obtained with flow at room temperature and 1 atm. [115] 22

Figure 1-10 A graphical representation of A) a LGSFB in E-I-a-1 mode with a uniformly distributed particle bed and B) a LGSFB operating in E-I-a-2 mode characterized by a denser particle bed near the distributor and a long disengagement section. 23

Figure 1-11 A) Schematic Diagrams of the flow regimes observed in a three phase systems of water, air and 1.5 mm glass beads. The white areas denote the gas phase. [120] B) Flow regime map of the different regimes of a similar fluidized bed in white, shaded section refer to non – fluidized regimes. [121] 24

Figure 2-1 2D representation of spatial discretization schemes, with owner cell centre P and neighbouring cell centre N. F denotes the value on the face, between the two. The value of

F is calculated by: a linear approximation between P and N ((A) linear approximation); extrapolation of the value of the cell centre to the face centre, depending on the sign of the flux, either the value of P or N is selected ((B) upwind scheme); and, the value of the face centre is calculated by the extrapolation of the gradient of the flux within the cell to the face, again this extrapolation depends on the sign of the flux ((C) linear upwind)[144] 38

Figure 2-2 A) Structure for the OpenFOAM case of the PFR model B) Solution algorithm for one time step of the rhoReactionFoam solver. 41

Figure 2-3 A) Mass fraction of n-butane, i-isobutane and i-pentane over the length of the reactor, plotted for the 1D model obtained with MATLAB and via a 1D simulation in OpenFOAM. B) Temperature profile over the length of the reactor plotted for the 1D models obtained via MATLAB and OpenFOAM..44

Figure 2-4 Structured (left) and unstructured (right) meshes. The structured mesh shows a logical ordering of cells where the unstructured mesh does not..48

Figure 2-5 Meshes for example case: A) 1D mesh, B) wedge shape mesh of the conventional tubular reactor, and C) wedge shape of the unconventional notched reactor. 49

Figure 2-6 Plot showing the mass fraction of i-isobutane, comparing the results of the 1D PFR model solved in MATLAB with the result of the OpenFOAM simulation of the conventional tubular reactor shape, extracted from the centre and near the wall of the reactor. 51

Figure 2-7 Mesh geometry for the grid refinement study: coarse grid (left), medium grid (middle), and fine grid (right)...52

Figure 2-8 The temperature on the notched reactor for each of the three meshes used for the grid convergence study. Results are shown for the coarse grid (left)), the medium grid (middle), and the fine grid (right). Liquid flow is introduced from the bottom of the reactor. 52

Figure 2-9 Temperature profile over the length of the reactor shown for the coarse, medium and fine grid. 54

Figure 2-10 Results from the simulation of the notched reactor showing (from left to right) the pressure (in Pa), the velocity (in m s^{-1}), and the mass fraction of i-butane. The direction of the flow goes from bottom to top. 56

Figure 2-11 mass fractions of n-butane and i-butane extracted over the length of the notched reactor at radial distance of 0.006 m...57

Figure 3-1 a) Overview of the reactor setup. I: 200 L tank containing liquid to be sent to the reactor. II: valves: III: pump. IV: pressure relief valve. V: Reactor. VI: 200 L tank containing liquid after passing the reactor. b) Details of the geometry of the reactor. VII: The liquid inlets. VIII: The liquid outlets. IX: the gas outlet. The blue disc represents the position of the fritted disc. 62

Figure 3-2 A) Steady state water volume at 60 s. The translucent part denotes the water level in the full reactor (obtained by VOF). The opaque section is the portion of the geometry used in the Eulerian simulations. B) Steady state water volume obtained by VOF simulations. The dotted grey line denotes the total reactor volume. At 75 L min^{-1} total inlet flow rate a high inlet flow rate was achieved without overflowing the reactor. 72

Figure 3-3 Azimuthal velocity of the solids, extracted in a horizontal plane (10 mm height, 65 mm radius), for meshes with three different refinement levels. Inlet flow rate 75 L min^{-1}, total mass of solids 0.6 kg. Results obtained after 3 s of simulated time. The used azimuthal angle is shown on the insert. 73

Figure 3-4 Comparison between simulations and experiments. a) Reactor operation without gas flow, showing little to no movement of the solid bed. b) Reactor operation with 50 LPM of water and 10 LPM gas flow, showing the fluidization of the glass beads (painted in yellow for better visualization). The cut-off value for the CFD – contour plot of the volume fraction of the solids was set to 0.15. 75

Figure 3-5 The evolution of the bed height near the wall over time. The red line on the graphs corresponds to position A on the front side of the reactor. The line in black corresponds to bed height at position B, at the back side of the reactor. 76

Figure 3-6 The envelopes of the solid fraction shown for a) the view on side and b) the view from the bottom plate (B). The envelopes show the solid volume fraction for 0.1 (blue), 0.25 (cyan), 0.4 (orange) and 0.5 (red). These images was taken from the simulation after 10 seconds. 77

Figure 3-7 Streamlines of the liquid velocity in the reactive zone after 10 seconds. The flow has a helical pattern that swirls upwards and has higher velocity near the walls. 78

Figure 3-8 Velocity profile for the liquid and solid phase, with the resulting slip velocity. Data was extracted at a height of 10 mm and a radius of 65 mm after 10 s of simulation. For the interpretation of the azimuthal angle the reader is referred to Figure 3-3 79

Figure 3-9 Central plane of the reactor showing the distribution of argon gas over the course of the simulation. The lilac arrows denote the magnitude of the gas velocity. 80

Figure 4-1 The fluidized bed reactor studied in this work. A) Real life image. B) 3D representation to show the internal of the system. 1) The liquid inlet. 2) The gas inlet. 3) The gas diffusor. 4) Plexiglass sheet. 5) The closure of the fluidized bed region, the opening has been made smaller than the d_p· 6) The outlets for the liquid – gas mixture. 90

Figure 4-2 GCI study on three different meshes using the time averaged bed height of a liquid – solid simulation.. Three meshes were used: a coarse mesh (7 520 cells), a medium mesh(16 920 cells) and a fine mesh (38 070 cells), the extrapolated value was calculated according to the GCI method reported by Roache.[136] 97

Figure 4-3 Time averaged velocity profiles over the central axis of the 3D simulation cases of the pseudo-2D LGSFB. Comparison of the velocity magnitude and z - component of A) the particle velocity, B) the liquid velocity and C) the gas phase velocity. D) depicts the percentile contribution of each component (x, y, z) to the total velocity magnitude. 101

Figure 4-4 comparing the different settings of the gas phase simulation results to the experimental result A), where a bubble breaking through the particle bed is observed. B) Simulation results of the gas phase (black dots) breaking through the solid bed (yellow, phase volume fractions between 0.2 and 0.48), using a fixed dispersed bubble diameter of 1.2 mm. C) Using a population balance model and D) population balance model simulation with interphase compression between the gas and liquid case turned off ($C\alpha = 0$). 102

Figure 4-5 Time-averaged gas velocity streamlines simulated in the pseudo-2D LGSFB. A) No gas phase turbulence B) gas phase turbulence enabled. Reference video available in Appendix I. 104

Figure 4-6 Procedure to capture the bed height from image analysis. A) the average intensity image from the captured video. B) The average image converted to grey scale. C) An example plot of the grayscale intensity plotted over the red line shown on B. D) Thresholds of the particle beds from the CFD simulations for volume fractions between 0.2 and 0.4, these images served as basis to extract the particle bed height from the CFD simulations. 107

Figure 4-7 Plot of the extracted bed height from CFD (scatter plot), the red line denotes the experimentally determined bed height, with the experimental error interval (±1 mm) as the dotted line. The dashed line marks the 10% deviation from the experimental value (± 16 mm). 108

Figure 4-8 Regions studied for the PIV experiment. A) The full fluidized bed reactor, the blue box denotes the area captured by the camera. B) the area captured by the PIV camera, with the ROI, the area on which the analysis will take place. C) The pre-processed PIV image after subtracting the background and enabling filters. 109

Figure 4-9 Time Averaged Particle Velocity Magnitude. A) Extracted via PIV (experimental values). B) Results from the simulations. The white lines denote the streamlines crossing a line at 38 mm bed reactor height. 109

Figure 4-10 Plot of the time averaged particle velocities obtained from PIV and simulations. The y – velocity component of the velocity was extracted from a horizontal line at 38 mm height in the reactor. The error bars on the experimental values show the 10 % confidence interval calculated on the averaged result. 110

Figure 4-11 Graphical comparison of the extracted velocity profiles 3 mm from the right wall of the pseudo-2D fluidized bed reactor. The error bars on the experimental data represent the standard error calculated on the average velocity. 112

Figure 5-1 Example of a TORBED Reactor showing the central bladed structure and the cone; The blue arrows denote the gas flow from bottom through the bladed structure. 122

Figure 5-2 A) Experimental results of the dehydrogenation experiment of H_{18}DBT from Bulgarin et al. [82], showing the “yield” of H_2 in function of the modified residence time. Data was extracted for 4.9 g of catalyst at flow rates of 0.34 mL min^{-1} to 1.35 mL min^{-1} at 292°C. B) Curve fit of the data of the H_2 yield in function of the modified residence time in SI units. 123

Figure 5-3 Bar plot showing the H_2 yield per flow rate for the dehydrogenation of H_{18}DBT for both the experimental results from Bulgarin et al. [82] and the data obtained via CFD simulations with the catalytic source term. 124

Figure 5-4 Results from the parameter estimation study to improve the accuracy of the catalytic source term. The dark edges show the experimental data from Bulgarin et al., coloured bars show the H_2 yield obtained via CFD simulations with the catalytic source term for 4 different τmod and 16 combinations of parameter 1 and 2. 126

Figure 5-5 Geometries of the reactors investigated in this chapter. A) The geometry of the reactor with similar geometry compared to the reactor in Chapter 3, but with two additional inlets, this is 4inletsNoCone150. B) A reactor with similar outer shape as A, but with a cone added at the central bottom plane, which is called 4inletsWithCone150. C) The reactor with half the diameter of the reactive zone, the height was increased to keep a similar total volume of the reactive zone, this geometry is called 4inletsWithCone75. 131

Figure 5-6 Plot of the $YH2$ in function of τmod, the circles represent the data extracted from Bulgarin et al., the circles represent the $YH2$ extracted from CFD simulations of the reactive pseudo-2D LGSFB. The red curve is the curve fitted from the literature data, see equation 6.3. 132

Figure 5-7 Volume fraction of Al_2O_3 catalyst particles in a pseudo – 2D fluidized bed during dehydrogenation of $H_{18}DBT$ the inlet flowrate varies from 5 % to 100 % of the theoretical minimal fluidization velocity of the particle bed. Snapshots are obtained after 1.5 s of simulation. The grey background shows the mesh. The threshold for the particle bed ranges from 0.1 to 0.5. 133

Figure 5-8 Liquid velocity magnitude profiles observed over a plane at 30 mm height inside the reactor for an increasing number of inlets, A) shows the mesh with two inlets, B) three inlets, C) four inlets. 135

Figure 5-9 Snapshot of the particle bed in rainbow colours and liquid velocity streamlines in black for A) 4InletsNoCone and B) 4InletsWithCone. 136

Figure 5-10 A) glyphs of the time averaged solid velocity extracted over a plane at 20 mm height in the reactor B) glyphs of the time averaged liquid velocity extracated at a plane between two inlets. The rainbow colouring shows the partcle bed in the reactor. 137

Figure 5-11 Snapshots of the particle bed volume fraction thresholds higher than 0.1, obtained after 5 s of simulation time for A) geometry 4InletsNoCone150, B) geometry 4InletsWithCone150, and C) geometry 4inletsWithCone75. D) represents the relative amount of particles present in 6 different intervals of particle volume fraction. 138

Figure 5-12 A) Threshold of the particle bed exceeding a volume fraction of 0.1 in the SFB reactor with halved diameter operated at 15 LPM. B) Bar plot showing the relative distribution of particle bed density on the total bed volume. 140

Figure 5-13 Plot of the first Damköhler number in function of the modified residence time. The kinetics of Bulgarin et al. [82] at 290 °C were used to calculate the Da numbers for a calculated catalyst activity of 0.6 $g_{H2}\ g^{-1}_{cat}\ min^{-1}$...141

Figure 6-1 Proposed reactor geometry for follow up studies. Including a distributor plate with a central cone and a wider section right above the top of the cone. 152

List of Tables

Table 1-1 Comparing H_2 storage and thermophysical properties for several common H_2 carriers. 9
Table 1-2 Summary of the H_2 storage methods based seven different criteria. 12
Table 1-3 Overview of the different simulation approaches and solvers used in this thesis.. 29
Table 2-1 Boundary conditions for the 1D model provided in the context of their implementation in OpenFOAM. 44
Table 2-2 Boundary conditions for the wedge geometry and notched geometry simulations in OpenFOAM 50
Table 2-3 Data for the grid independence study on the temperature probe point 54
Table 3-1 Settings, models and parameters used for the simulations. 71
Table 4-1 Overview and description of models discussed in this work. 87
Table 4-2 Drag Coefficient formulas according to the different models used in this work. ... 93
Table 4-3 Physical properties used for the simulations and experimental setup and CFD boundary conditions. 98
Table 4-4 Models and parameters for the population balance model used. 103
Table 4-5 Overview of the different drag model combinations used for the 12 initial simulations cases., Cases that successfully ran the entire simulation protocol are highlighted in green, failed cases in red. 105
Table 5-1 Description and limitation of chemical reaction approaches in CFD applied to dehydrogenation of H_{18}DBT. 121
Table 5-2 Thermophysical Properties used for the simulations of the dehydrogenation of H_{18}DBT. 127
Table 5-3 Boundary conditions used for the simulations of the SFB reactor geometries. ... 129

Abbreviations and Symbols

Abbreviations

2D	Two Dimensional
3D	Three Dimensional
Ar	Argon
Ar	Archimedes’ Number
BT	Benzyltoluene
CD	Catalytic Distillation
CH_3OH	Methanol
CFD	Computational Fluid Dynamics
Co	Courant, Friederichs, Lewy or CFL number
CO_2	Carbon Dioxide
DIA	Digital Image Analysis
DBT	Dibenzyltoluene
DOD	Degree Of Dehydrogenation
EE	Eulerian - Eulerian
FB	Fluidized Bed
FVM	Finite Volume Method
GCI	Grid Convergence Index
GHG	Green House Gas
H_2	Hydrogen Gas
$H_{18}DBT$	Perhydro Dibenzyltoluene
HCOOH	Formic Acid
He	Helium
IE	Interphase Exchange
KTGF	Kinetic Theory of Granular Flow

LGS	Liquid – Gas - Solid
LGSFB	Liquid Gas Solid Fluidized Bed Reactor
LHSV	Liquid Hour Space Velocity
LHV	Lower Heating Value
LOHC	Liquid Organic Hydrogen Carrier
LPM	Litre Per Minute
NH_3	Ammonia
N_2	Nitrogen Gas
PI	Process Intensification
PIV	Particle Image Velocimetry
PLA	Polylactic Acid
PTV	Particle Tracking Velocimetry
RANS	Reynolds Averaged Navier Stokes
ROI	Region Of Interest
SFB	Swirling Fluidized Bed
SST	Shear Stress Transport
VOF	Volume Of Fluid

Roman

a	Acceleration (m s^{-2})
A	Diagonal Matrix of Implicit Coefficients
c	Concentration of species (mol m^{-3})
C	Force coefficient
Cp	Specific Heat Capacity (J mol^{-1} K^{-1})
d	Diameter (m)
D	Effective Diffusivity
Eö	Eötvös number
f	Number function value
$\mathcal{F}$	Factor in the Ishii – Zuber model

F	Force (N)
$\mathrm{F_l}$	Blending function
$\mathrm{F_s}$	Safety Factor
F	Flux
$\mathbf{F}$	General momentum exchange vector
$\mathbf{g}$	Gravitational acceleration vector (m s^{-2})
H	Specific Enthalpy (J mol^{-1})
$\mathbf{H}$	Matrix of the off-diagonal coefficients
I	Intensity of the turbulent kinetic energy inlet
$\mathbf{I}$	Matrix of Unit Vectors
k	Turbulent kinetic energy
k	First order kinetic constant
K	Equilibrium constant
L	Mixing Length
m	Mass (kg)
$\mathbf{M}$	Matrix of coefficients
$\hat{\boldsymbol{n}}$	Unit Vector Normal to a Surface
$\mathrm{N_{sc}}$	Schmidt Number
p	Pressure (Pa)
p	Apparent Order of Accuracy (for GCI)
Q	General Source Term
r	Reaction Rate (mol m^{-3} s^{-1})
$\mathrm{r_f}$	Refinement Factor
R	Universal Gas Constant (J K^{-1} mol^{-1})
$\mathcal{R}$	Net production rate (mol m^{-3} s^{-1})
Re	Reynolds Number
S	Surface (m^2)
t	Time (s)

T	Temperature (K)
U	Velocity (m s^{-1})
V	Volume (m^2)
x	Cell size (m)
X	Chemical Conversion
Y	Mass fraction
$\boldsymbol{Y_{H_2}}$	Output of H_2
z	Axial coordinate (m)

Greek

α	Phase Volume Fraction
α_t	Turbulent thermal diffusion coefficient (m^2 s^{-1})
Γ	Diffusion coefficient (m^2 s^{-1})
ϵ	Turbulence dissipation rate (m^2 s^{-3})
Θ	Ratio of Flowrates With Respect to the Limiting Reactant
κ	Thermal Conductivity (W m^{-1} K^{-1})
λ	Surface Tension (N m^{-1})
μ	Dynamic Viscosity (Pa s)
ν	Kinematic Viscosity (m^2 s^{-1})
ρ	Density (kg m^{-3})
σ	Surface Tension (N m^{-1})
$\boldsymbol{\tau}$	Stress Tensor
τ_{mod}	Modified Residence Time (kg_{cat} s m^3_{H18DBT})
ω	Specific Turbulent Dissipation Rate (s^{-1})
Ω	Vorticity Magnitude

Subscripts and superscripts

c	Continuous phase
com	Compression
d	Dispersed phase
D	Drag Force
g	gas
i	General Phase
lmf	Minimal liquid fluidization (velocity) with gas phase
Lmf0	Minimal liquid fluidization (velocity) no gas phase
m	Mixture
r	Terminal velocity in the Syamlal O’Brien model
s	Swarm correction
t	terminal
tr	turbulent
TD	Turbulent Dispersion
VM	Virtual Mass Force
α	Interphase compression

Chapter 1

Introduction into LOHC based H_2 - storage and the potential improvements by fluidization.

Based partially on:

Laurens Van Hoecke, Ludovic Laffineur, Roy Campe, Patrice Perreault, Sammy W. Verbruggen, Silvia Lenaerts, *Challenges in the use of hydrogen for maritime applications, Energy and Environmental Science, 2021, 14, 815-843*
DOI: 10.1039/d0ee01545

1.1 Introduction

Hydrogen (H_2) is gaining a lot of attention as a clean fuel, since it can be generated from renewable energy through electrolysis. Although the production of H_2 through electrolysis is an established technology, it is not the current industrial standard. [1] Electrolysis, is a clean technology if excess renewable energy (solar or wind) is used to generate the electricity. [2] Current methods for producing H_2 rely on the use of fossil fuels as a starting material. [3] The potential for solar energy use is huge: on the earth's surface the incident solar power is estimated to be more than 2000 times greater than the worldwide power consumption. [4, 5] With the additional benefit that water and renewable energy are more evenly distributed around the globe than fossil fuels, although cost of electricity can vary widely between regions. [6] The production of renewable energy is highly intermittent, so both grid stabilization during peak renewable production, as an alternative energy source to the renewables are required during low energy production.[7] H_2 can be used in both regards, both as grid stabilization by H_2 production from electrolysis as well as H_2 combustion via fuel cells or combustion engines. [8] The most crucial bottleneck with using H_2 as a fuel is likely not the production or the end-point use but rather the storage, having even been called a show stopper in the past. [9] By weight, H_2 is an excellent energy carrier with a lower heating value (LHV) roughly 3 times that of diesel, 119 MJ kg^{-1} for H_2 compared to 41 MJ kg^{-1} for diesel. However, H_2 is such a light gas that at atmospheric conditions the total energy content is only 0.011 MJ L^{-1} whereas diesel contains 36 MJ L^{-1}, a difference by a factor 3000. To deal with this low volumetric energy content at atmospheric conditions several technologies exists to concentrate H_2 and make storage more efficient. These include: compression, liquefaction and storage in physical or chemical carriers. [10] The storage of H_2 in physical/chemical carriers is an innovative way of handling H_2 storage. The principle is that H_2 is not stored as a pure compound but that it will be bound to a carrier either via adsorption (for physical storage) [11-13] or by chemical bounds. [14-18] In this introductory chapter I will not discuss the use of physical (adsorption) based H_2 storage, but I will specifically discuss chemical carrier molecules for hydrogen, especially the use of Liquid Organic Hydrogen Carriers (LOHC). This is one example of the many carriers for H_2 have been proposed in recent years, which is based on storage in an organic liquid. Other carriers include gasses, such as N_2 or CO_2, [19-22] which form energy dense liquid products. Solid materials have also been proposed as H_2 storage materials, like metals or borane compounds, which can form stable bonds with H_2.

Several methods for H_2 storage have thus been proposed in the past, in this introductory chapter six different methods will be discussed. These include compressed H_2 storage, liquified H_2, storage in ammonia (NH_3), storage in methanol (CH_3OH), storage in formic acid (HCOOH), and storage in LOHC. In the original review paper on which this chapter is based more H_2 storage methods are discussed which include storage of H_2 in synthetic hydrocarbons via the Fischer – Tropsch process, production of synthetic methane via the Sabatier process, and H_2 storage in solid materials, such as metal hydrides and borane compounds. [23]

1.2 Hydrogen Storage Methods

1.2.1 Compressed Hydrogen

Like other gasses, H_2 can be compressed in cylindrical vessels, however the pressure required for this compression is much higher than the pressure used in typical butane gas tanks used for domestic use. Maximal allowed pressure in commercial gas canisters is 1.5 MPa, [24] whereas H_2 storage tanks have pressures ranging from 10 MPa to more than 70 MPa. Based on the materials used to design the storage vessel, a different classification is given in roman numbers ranging from I to V.[25-27] Type I are fully metallic vessels that typically carry only 1.7 wt.% of H_2 when filled completely. Type IV tanks, currently the most advanced tanks used in H_2 powered cars, are made from much lighter composite and polymeric materials and can store up to 5.7 wt.% of H_2 at 70 MPa. [28] Based on the vessel size it was calculated that this amounts to a H_2 storage capacity of 26 g_{H2} L^{-1} or 3.1 MJ L^{-1}. [29]

1.2.2 Liquid Hydrogen

In addition to compression, a second storage method for gasses often considered is to liquefy it. Both N_2 gas and natural gas are well known gasses that are being stored and transported in the liquid form. H_2 however, has a boiling point at 20 K, which is 50 K lower than N_2 and 90 K lower than natural gas. [30] Liquid H_2 is mostly known for its use in aerospace programmes. [31-34] The energy density of liquid H_2 is around 8.5 MJ L^{-1}, which is almost a threefold increase compared to state-of-the-art compressed H_2 tanks at 70 MPa. The process to produce liquid H_2 however, is much more energy intensive than compression, requiring up from 45 to 54 MJ kg_{H2}^{-1}, [35, 36] although the energy could be lowered to 23.5 MJ kg_{H2}^{-1} by using helium (He) refrigerants. [37] Long term storage of liquid H_2 will always be a challenge, as the temperature difference makes it equivalent to trying to keep ice cream cool in a warm oven, which causes boil-off losses over time. [34, 38]

1.2.3 Ammonia

By simply looking at the number of hydrogen atoms in the chemical formula of NH_3, it is clear that ammonia has a clear potential to be used for H_2 storage. NH_3 is globally one of the most industrially produced chemicals, [39] with a yearly production of around 200 million tons. [40] It is produced from N_2 gas and H_2 gas, by the oldest process in the chemical industry, the Haber – Bosch Process. [41]

$$N_2 + 3H_2 \rightleftharpoons 2\,NH_3 \quad \Delta H = -91.8\,kJ\,mol^{-1} \tag{1.1}$$

By weight ammonia contains 17.6 wt.% of hydrogen, it can be easily liquified by either cooling it to -33 °C or by pressurizing above 1 MPa, giving it an energy capacity of 14.7 MJ L^{-1}, should the NH_3 be completely cracked into H_2 and N_2.

Ammonia can serve both as a H_2 carrier molecule, and as a fuel in itself. NH_3 has been used in Belgian busses during WW II, due to fuel shortages. [42] However, NH_3 has severe drawbacks when used in combustion engines, it has a narrow flammability range (15 – 28 vol.%), a high auto-ignition temperature (651 °C) and a low laminar flame velocity (0.015m s^{-1}). [43] These factors complicate engine operations with ammonia. Burning of N_2 rich fuel mixtures is also a known cause of air pollution, so the NO_x compounds have to be mitigated. [44] In the further discussion comparing different H_2 storage carriers, I will consider NH_3 to be a H_2 carrier rather than a combustible. [45] To use NH_3 strictly as a H_2 carrier material, it can be cracked into N_2 gas and H_2. NH_3 can be cracked into these compounds at high temperatures (>450°C) in the presence of metallic catalysts (Fe, or Ru). [46] This is in essence, reversing the Haber – Bosch reaction. NH_3 and H_2 mixtures can serve together as a fuel mixture in combustion engines [43], for use in low temperature fuel cells, NH_3 has to be fully removed since it is a known poison for these devices. [47]

1.2.4 Methanol

Another potential H_2 carrier that is often discussed in literature is methanol, CH_3OH. [48] This chemical contains 12.5 wt.% of H_2, and an energy storage capacity of 11.9 MJ L^{-1}. Like NH_3, that uses N_2 as a carrier for H_2, CH_3OH does the same but with CO_2. CH_3OH can be produced by hydrogenation of CO_2, although this is not the industrial standard to produce CH_3OH. CH_3OH is produced on a megaton per year scale from natural gas. [49] This renewable form of CH_3OH is produced according to reaction 1.2: [50]

$$CO_2 + 3H_2 \rightarrow CH_3OH + H_2O \qquad \Delta H = 50\ kJ\ mol^{-1} \tag{1.2}$$

From this reaction already a major downside in the production process of renewable methanol can be seen, i.e., the byproduct formation of water, which consumes one in every three moles of H_2. Similar also to NH_3, CH_3OH can be used both as a fuel directly, producing CO_2 upon combustion, or the methanol can be reverted back to CO_2 and H_2. This final method has the benefit that the CO_2 waste stream is concentrated, making it easier to close the cycle and not emit any CO_2, by more efficient capture of the CO_2. [51]

1.2.5 Formic Acid

Formic Acid (HCOOH) is an alternative method to CH_3OH to use CO_2 as a storage material for hydrogen. Unlike CH_3OH there are no unwanted byproducts in the formation of HCOOH from CO_2. [52] HCOOH does have a low to moderate H_2 storage capacity of 4.3 wt.%, this is offset by the high density of HCOOH, 1.22 kg $m^{-1,}$ which results in an energy capacity of 6.2 MJ L^{-1}. HCOOHC can be produced from CO_2 according to equation 1.3, however the industrial standard is to use MeOH as a starting product. [53]

$$CO_2 + H_2 \rightarrow HCOOH\ \ \Delta H = 31.2\ kJ\ mol^{-1} \tag{1.3}$$

To use the H_2 stored in formic acid it has to be released from the CO_2 carrier material. However, during this process there is a potential unwanted side reaction possible that produces CO and H_2O. The selection of the catalyst is crucial when converting HCOOH to hydrogen, to avoid this second reaction pathway. [54]

$$HCOOH \rightarrow H_2 + CO_2 \qquad \Delta H = 31.2\ kJ\ mol^{-1} \tag{1.4}$$

$$HCOOH \rightarrow H_2O + CO \qquad \Delta H = 28.7\ kJ\ mol^{-1} \tag{1.5}$$

1.2.6 Liquid Organic Hydrogen Carriers

A final method for H_2 storage that will be discussed, and the main topic of this thesis are the so-called Liquid Organic Hydrogen Carriers (LOHC). This is a class of molecules, consisting of homocyclic or heterocyclic aromatic rings. [55] These compounds have a moderate H_2 storage density between 5 and 7.1 wt.%, resulting in an energy capacity in the order or 6.5 MJ L^{-1}, depending on the exact carrier used. [56] H_2 storage in LOHC is based on the reversible hydrogenation and dehydrogenation of carbon – carbon double bonds. LOHC are thus also hydrocarbon molecules, just like diesel and CH_3OH, but since they are not combusted, they do not emit any CO_2 upon use as long as the stability of the carrier can be guaranteed. [57]

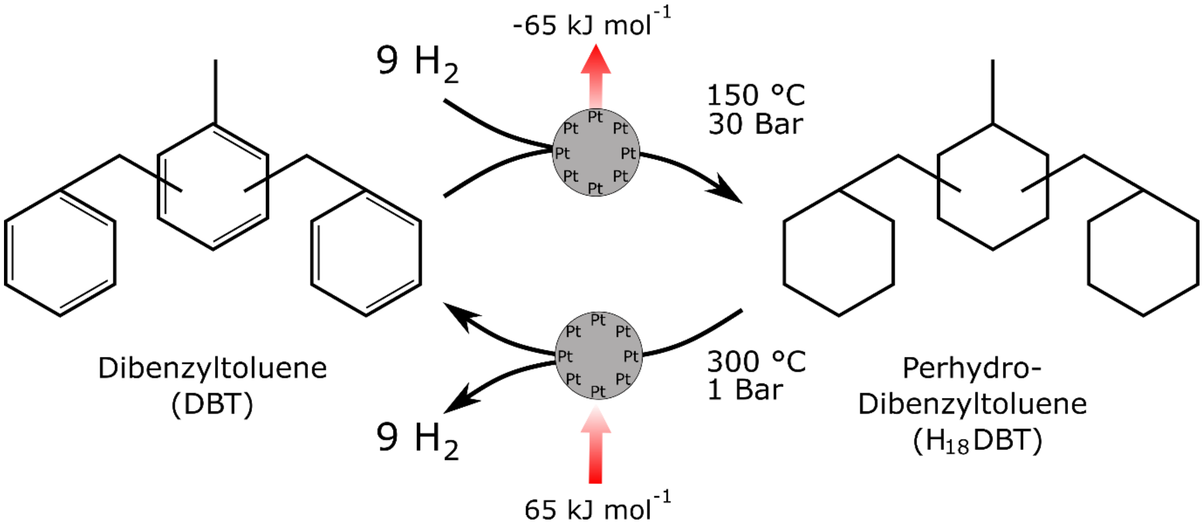

Figure 1-1 General cycle of H2 storage using LOHC. The hydrogenation reaction is an exothermic reaction requiring elevated pressures. The endothermic dehydrogenation reaction proceeds with increased temperature and low pressures.

The cycle of H_2 storage proceeds through two reaction steps, the exothermic hydrogenation reaction to store H_2, and the endothermic dehydrogenation to release H_2 (Figure 1-1) In both catalytic steps of the cycle, proper heat management is crucial for both the extent to which H_2 can be stored, and for the commercial deployment of this technology. [58] For example, in the charging process of dibenzyltoluene (DBT), one of the most studied examples of LOHC, 65 kJ $mol^{-1}{}_{H2}$ of heat is produced and must be removed to avoid thermodynamic equilibrium. The reverse is true for the dehydrogenation process; this process step requires a similar energy input of 65 kJ $mol^{-1}{}_{H2}$ at increased temperature (250 – 300 °C) to release H_2 from the carrier. [59] There are have been many LOHC molecules proposed in the past decade, [60] three of these LOHC molecules are briefly highlighted. The properties of these LOHC molecules are listed in Table 1-1. The physical, safety and practical aspects of using toluene (TOL), N-ethylcarbazole (NEC) and DBT as a H_2 carrier have been reviewed by Preuster *et al.* [61] and benchmarked by reaction enthalpy, boiling point, flash point, melting point, toxicity and gravimetric H_2 content. [61]

1.2.6.1 Toluene

Toluene (C_7H_8, or TOL) is one of the simplest molecules that is considered a viable option for aromatic LOHC technology, having been considered a potential H_2 storage material since 1975. [62] Benzene (C_6H_6) has an even simpler structure than toluene, but due to the high carcinogenicity of this molecule it is not often considered a reliable option.[63] When fully hydrogenated, one mole of TOL can store three moles of hydrogen, resulting in the storage of 6.1 wt.% of hydrogen. [64] If all three carbon – carbon double bonds of TOL have been hydrogenated, the carrier is called methyl-cyclohexane (MCH). Compared to the other LOHC discussed in this work, TOL is a small homocyclic molecule with higher aromaticity, and this increases the energy needed for the hydrogenation and dehydrogenation processes. [65] The temperature range of TOL and MCH shows that both molecules are liquid at room temperature, but at the dehydrogenation reaction conditions (> 250 °C), all reactants are in gas phase, so additional processing of the gas flow is required. The dehydrogenation temperature is also much higher than the flashpoint of either TOL or MCH (±4°C), posing potential fire hazards [61, 63]

Table 1-1 Comparing H_2 storage and thermophysical properties for several common H_2 carriers.

Name	**MCH**	**TOL**	**H_{12} – NEC**	**NEC**	**H_{18} – DBT**	**DBT**	**H_{12} – BT**	**BT**
Structure	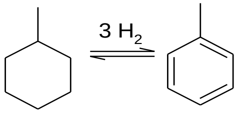		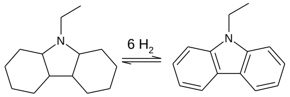		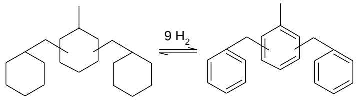		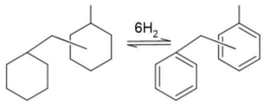	
Density (kg m^{-3})	770	867	937	1158	909	1041	876	996
Gravimetric H_2 Capacity (wt. %)	6.1		5.7		6.2		6.2	
Energy Density (MJ L^{-1})	5.76		6.41		6.76		6.5	
Reaction Enthalpy (kJ mol_{H2}^{-1})	68.3		50.6		62		62	
Melting Point (°C)	-127	-95	84	69	-58	-39	>30	-71
Boiling Point (°C)	101	111	281	378	371	390	270	283
Flash Point (°C)	-4	4		186		212		137

Name	**Nitrogen**	**Ammonia**	**CO_2**	**Methanol**	**CO_2**	**Formic Acid**	**Liquid Hydrogen**
Structure	$N_2 \xrightleftharpoons{3H_2}$	$2NH_3$	$CO_2 \xrightarrow{3H_2} CH_3OH + H_2O$ $CO_2 \xrightarrow{2H_2} CH_3OH$		$CO_2 \xrightleftharpoons{H_2}$	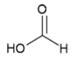	H_2
Density (kg m^{-3})		698		792		1220	70
Gravimetric H_2 Capacity (wt. %)	17.6		12.5		4.3		100
Energy Density (MJ L^{-1})	14.7		11.88		6.3		8.4
Reaction Enthalpy (kJ mol_{H2}^{-1})	91.8		50		31.2		
Melting Point (°C)	-210	-77	-57	-98	-57	8	-259
Boiling Point (°C)	196	-33		65		101	-253
Flash Point (°C)		132		9		69	

1.2.6.2 N – Ethylcarbazole

NEC is the first molecule that drew large attention to heterocyclic aromatic compounds for H_2 storage. [66] The nitrogen atom in the cycle reduces the weight efficiency of H_2 that can be stored but has the advantage that the enthalpy for dehydrogenation is lower compared to non-substituted aromatic cycles, resulting in a lower dehydrogenation temperature. [67] From Table 1-1, it can be seen that the melting point of dehydrogenated NEC is higher than ambient temperatures and therefore it is a solid at normal conditions. [68] This makes processing it slightly more difficult compared to liquid carriers. The thermal stability of NEC is another issue that has to be dealt with, at temperatures above 270 °C the bond between nitrogen and the ethyl chain breaks. [69] This has a twofold negative consequence i) the melting point of unsubstituted carbazole is much higher, around 274 °C ii) the free electron pair on the nitrogen atom is exposed, this free electron pair has a high affinity for the noble metal catalyst and therefore causing deactivation. Another disadvantage of NEC is the low availability of the molecule, the annual production of this chemical is lower than 10 000 tons, all of it is obtained from coal tar by distillation. [14, 61]

1.2.6.3 Dibenzyltoluene

In 2014 Brückner *et al*. [69] published for the first time the use of dibenzyltoluene as a H_2 carrier molecule. The capacity for H_2 storage is similar compared to TOL, see Table 1-1. DBT is made by aromatic substitution of two molecules of TOL on a central TOL molecule. [70] DBT is produced at a capacity of several thousand tons per year, it is mainly used as a heat transfer oil, known as Marlotherm® SH. [71] Based on the availability, the fact that it is a liquid at room temperature and the stability during dehydrogenation, DBT is seen as a superior carrier to NEC. [56, 68] The advantages over toluene are less clear, although the lower fire hazard and lower reaction enthalpy for H_2 release in DBT give it a slight edge over the cheaper toluene.

DBT also has significant advantages over the other H_2 storage methods, it is clear from Table 1-1 that DBT does not have the highest H_2 storage capacity, nor does it have the lowest energy requirements for H_2 release, DBT is still considered a promising H_2 carrier material. It holds the advantage over liquid H_2, since it can be easily stored and transported at ambient conditions, without large changes required to the fossil oil infrastructure that exists today. [72] Clouds that form from liquid H_2 spills, contain a lot of water vapour, this makes the clouds heavier than air, and blocks the dispersion of the gas. This poses potential dangers for asphyxiation and explosions. [73] Spills from DBT – although to be avoided due to the environmental impact [74] – do not pose a significant fire or explosion hazard.[61, 75] DBT and H_{18}DBT are non-flammable liquids, H_2 release from these liquids is only possible when the liquid comes into contact with the catalyst at high temperatures. These specific conditions severely limit explosion hazards of the hydrogen.

Compared to methanol and formic acid, DBT holds the advantage that the empty carrier is a stable liquid intermediate and not CO_2, a greenhouse gas (GHG). [76] Processing of the carrier after H_2 release thus becomes easier. For methanol production especially, it should not be ignored that one in three moles of H_2 is lost during conversion of CO_2 to CH_3OH, the production of H_2 is still the most energy intensive step in the entire production chain. [77] Methanol itself, although biodegradable, is toxic for humans [78] and is also considered a low flash point fuel, [79] which is not the case for DBT.

In the field of chemical H_2 storage, NH_3 is one of the most efficient carriers when looking at energy storage capacity, at least in liquefied form (-33°C or 1 MPa). Globally, it is one of the most produced chemicals, and it is consumed around the world for fertilizer and military purposes. The major downside however is the toxicity. NH_3 reacts with water to form NH_4^+, this ammonium – ion is highly alkaline and causes burns on animal tissue (especially the eyes and lungs). [80] Clouds formed by NH_3 leaks are heavier than air, and they can be moved by the wind, which can extend them over several hundred meters. [81]

Combining all the factors discussed above, DBT stands out due to its improved safety and easy transportability. This is summarized in Table 1-2. The toxicity profile and thermophysical properties are similar to those of diesel fuels, which are safely used by people for over a century. So, it can be a viable alternative energy vector, emitting GHG or other air pollutants emissions, in its overall lifetime. The major downside in the use of LOHC is the energy requirement for the dehydrogenation step. If this step can be covered by waste heat integration, the energy efficiency for H_2 storage in DBT becomes very high, since little purification is required when using this molecule for H_2 storage. [64, 82] In this thesis I will explore the challenges related to using fluidized bed reactors for H_{18}DBT dehydrogenation as a potential improvement for the dehydrogenation efficiency.

Table 1-2 Summary of the H_2 storage methods based seven different criteria.

	H_2 Storage Capacity (MJ L^{-1})	Seasonal Stability	GHG / Air pollutants	Fire Hazard	Environmental Hazard	Human Health Hazard	Infrastructure Availability
Compressed H_2 (700 Bar)	3.1	High	H_2O	High	Low	Low	Low
Liquid H_2	8.4	Low	H_2O	High	Low	Low	Low
NH_3	14.7	High	NO_x	Low	High	High	Medium
CH_3OH	11.88	High	CO_2	High	Medium	High	Medium
HCOOH	6.3	High	CO_2	Medium	Medium	High	Low
TOL/MCH	6.2	High	H_2O + ppm CH_4	High	Medium	High	Medium
DBT/H_{18}DBT	6.2	High	H_2O + ppm CH_4	Low	Medium	Medium	High

In Table 1-1 there is also an entry for benzyl – toluene (BT), the sister molecule of DBT, introduced in the same work of Brückner [69] that first showed the use of DBT for H_2 storage. This work focusses on the development of reactors with highly agitated flows to increase mass and heat transfer of the liquid to the catalyst particle surface. BT has a lower vapour pressure and will thus more easily evaporate than DBT , an unwanted side-effect that will be even more exaggerated by the agitated flows. [83]

1.3 Previous Reactor Design for LOHC

In this PhD Thesis, the use of agitated or fluidized particles inside a LOHC dehydrogenation reactor is discussed. This is a new concept as fluidization has not been previously considered as an operating regime in LOHC dehydrogenation reactors. In this introductory chapter, previously described reactors in literature are discussed.

1.3.1 Batch or Autoclave Reactors

Batch or autoclave reactors have been used for reactions of DBT/H_{18}DBT in many laboratory experiments to test various process conditions for the hydrogenation and dehydrogenation conditions. The first ever hydrogenation and dehydrogenation experiments on DBT were conducted in a autoclave reactor by Brückner et al. [69]. It was tested for the hydrogenation of BT, DBT and NEC, at 150 °C at 5 MPa and with the addition of a 0.25 mol.% Ru/Al_2O_3 catalyst, and showed that in batch operation mode, the hydrogenation of $H_{12}BT$ was more than twice as fast as the hydrogenation reaction of $H_{18}DBT$ expressed in total H_2 loading of the liquid. The dehydrogenation rate of $H_{18}DBT$ was also measured to be consistently lower than that of $H_{12}BT$ at temperatures ranging from 230 – 290 °C and atmospheric pressure. Interestingly, in this first ever publication on the use of DBT as an LOHC, it is also shown that increasing the platinum (Pt) loading on the heterogenous catalyst particles, decreases the H_2 release rate. No further explanation was given for this phenomenon in the paper by Brückner et al., however more recently Ali et al. observed an opposite trend, that with an increase in Pt loading, an increase in conversion of $H_{18}DBT$ could be obtained. [84] A major difference in this work was that Ali et al. used a stirred reactor vessel for the dehydrogenation, whereas the dehydrogenation reactor of Brückner et al. was unstirred. This is a first indication of potential dewetting effects of the catalyst due to the H_2 release from the carrier liquid.

The use of a batch reactor was also examined for its use as a hot pressure swing reactor, seen on Figure 1-2. In this operational mode, the same reactor vessel and catalyst was used for hydrogenation and dehydrogenation of the DBT. By keeping the reactor at sufficiently high temperatures for dehydrogenation (290 – 310 °C), the start-up times for dehydrogenation could be limited and the response time for LOHC based energy generation during dips in available renewable energy can be shortened. Switching between H_2 storage and H_2 release from $H_{18}DBT$ could be achieved by increasing the pressure to 3 MPa (for storage) or by decreasing the pressure to atmospheric pressure (for release). [85]

A batch reactor was also used to assess the ability of H_2 storage in DBT as a joined storage and purification step. Both the addition of water [86] as the addition of CO_2 [87] to the H_2 gas used in a hydrogenation experiment have been investigated. This was done so to mimic H_2 gas streams from electrolysis or steam methane reforming, respectively. H_2 storage in DBT was possible using these polluted H_2 gas streams, but the stability of the DBT molecule varied with the noble metal catalyst used.

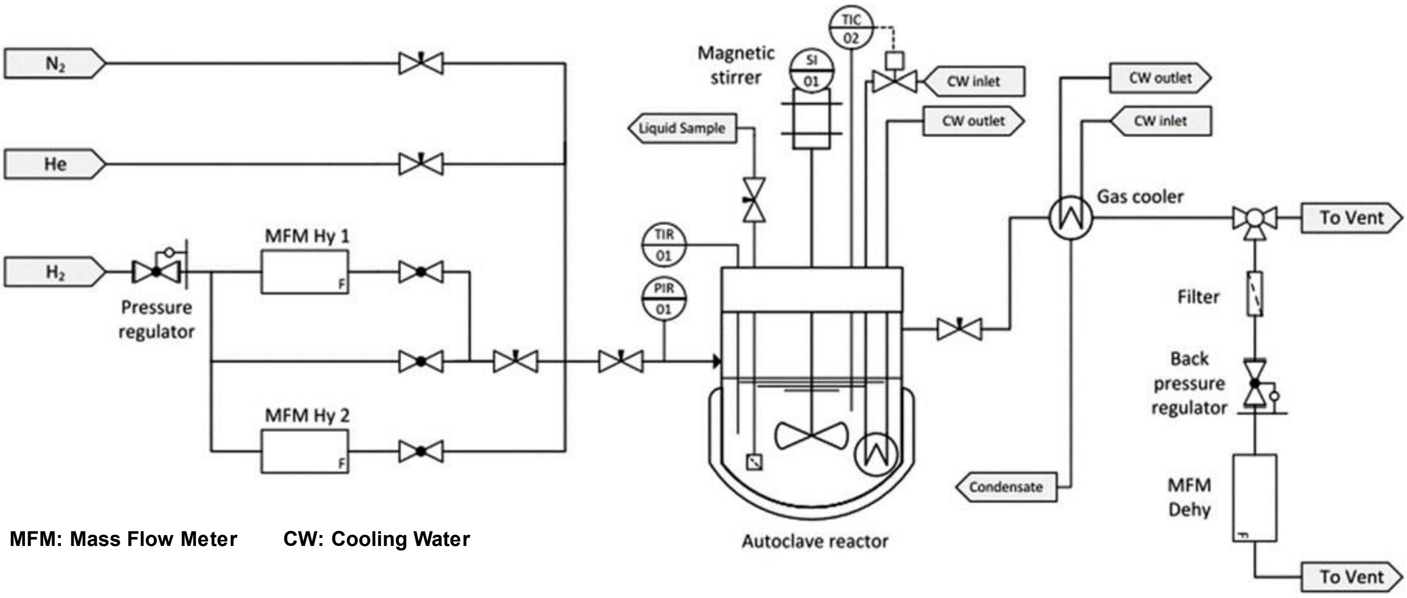
N_2
He
H_2
Pressure regulator
MFM Hy 1
MFM Hy 2
F
Magnetic stirrer
SI 01
TIC 02
CW inlet
CW outlet
Liquid Sample
TIR 01
PIR 01
Autoclave reactor
Gas cooler
CW outlet
CW inlet
To Vent
Filter
Back pressure regulator
Condensate
MFM Dehy
To Vent
MFM: Mass Flow Meter
CW: Cooling Water

Figure 1-2 Schematic flow diagram of the hot pressure swing adsorption reactor. [85]

1.3.2 Coated Reactor Structures

In 2021 Solymosi et al. [88] reported the use of catalytically coated stainless steel plates for the dehydrogenation of $H_{18}DBT$. Figure 1-3 shows the screening procedure for the coating protocols. The goal was to achieve a better heat transfer compared to tubular reactors filled with pellets by coating thin layers of catalyst on flat plates. The narrow contact between the thin layer of catalyst and the heated plates of the reactor rendered lower thermal resistance when compared to a tubular reactor filled with catalyst pellets. The possibility to coat stainless steel plates would allow for the incorporation of dehydrogenation reactors directly into high temperature fuel cell systems, with minimal thermal losses. This paper showed the potential of coating stainless steel structures with different coating techniques, but no benchmarking against a tubular reactor. The main conclusion was that using Pt sulphite acid as a precursor for the coated catalyst was superior to using hexachloroplatinic acid with a $(NH_4)_2SO_4$ post-treatment step.

A patent filed in 2022 by the Xi'an Jiaotong university also discloses the use of coated reactor internals for the dehydrogenation systems. [89] The reactor is cylindrical in shape and contains a separation cylinder coated with the catalyst material. The coated walls are directly heated to enable the dehydrogenation reaction and a centrifugal flow field is used to separate the H_2 gas from the reacting liquid.

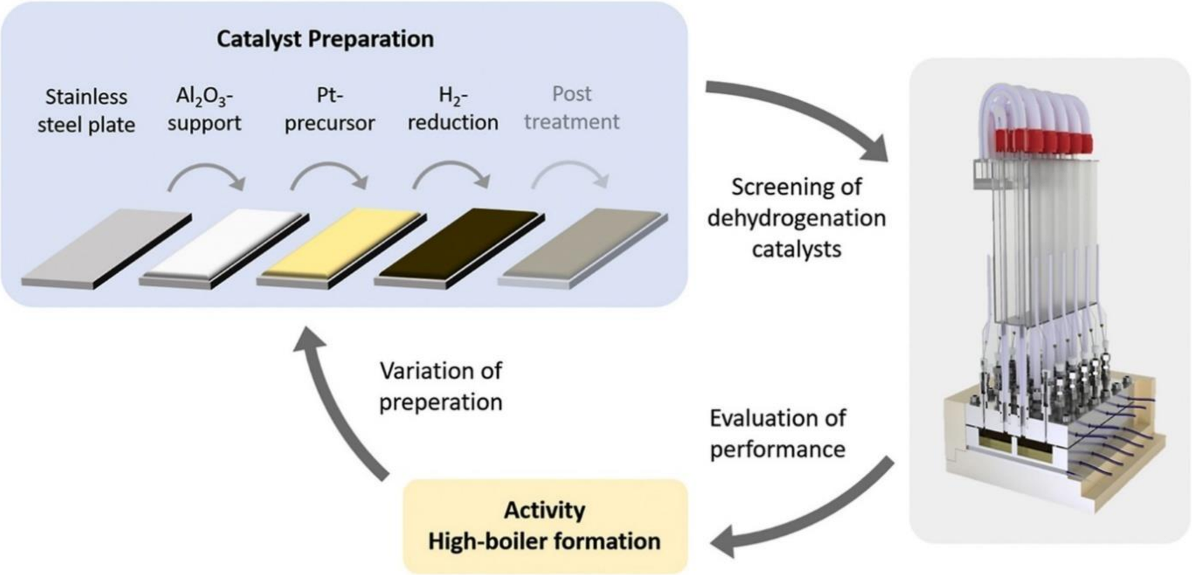
Catalyst Preparation
Stainless steel plate
Al_2O_3-support
Pt-precursor
H_2-reduction
Post treatment
Screening of dehydrogenation catalysts
Evaluation of performance
Activity
High-boiler formation
Variation of preperation

Figure 1-3 Screening procedure of flat plate structures coated with catalyst for the dehydrogenation of H_{18}DBT. [88]

1.3.3 Microchannel Reactors

The use of microreactors is another approach proposed to improve the heat transfer during the dehydrogenation reaction of H_{18}DBT. By keeping the dimensions of the reactor small, i.e., keeping the hydraulic diameter (d_h) below 1 mm, heat transfer from the wall to the reaction medium becomes more efficient. This makes the total reactor volume small, so for real life applications many microchannel reactors are operated in parallel to achieve higher power outputs. For H_{18}DBT, a highly viscous liquid, a large pressure drop is expected from using microreactors. Ali et al. [90] demonstrated that the use of a microchannel reactor had an increased dehydrogenation rate over the use of stirred reactor vessels operating for 20 hours at identical process conditions (290 °C and atmospheric pressure).

Wunsch et al. [91] also investigated the use of a microchannel reactor but added the use of a 5 µm thick AgPd membrane for in situ separation and purification of the released H_2 gas. Using this setup, they managed to obtain a uniform temperature distribution inside the microchannel during the highly endothermic dehydrogenation reaction. By combining the process with a membrane purification step, they managed to achieve a highly pure H_2 mixture (quality 5.0). The downside of the system was that the AgPd membrane required daily regeneration from a H_2 gas stream to retain its purification capacity. The microreactor structure used in this work is shown on Figure 1-4.

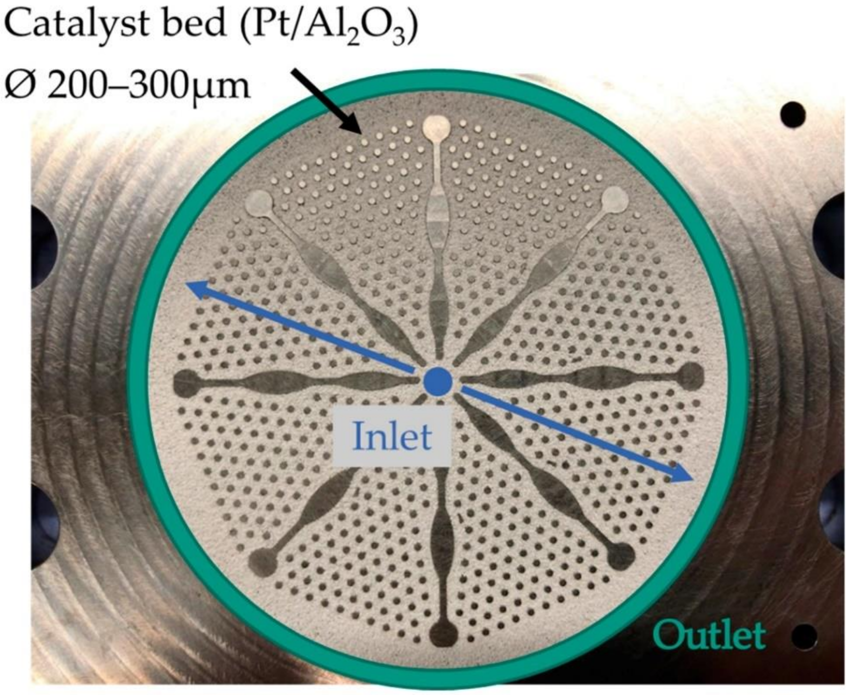

Figure 1-4 microstructure used in the reactor of Wunsch et al. [91]

1.3.4 Catalytic Distillation

Catalytic distillation (CD), which is a form of reactive distillation, is another research avenue to improve the efficiency of the dehydrogenation process. The main goal of the CD process is to avoid the contact between the H_2 lean carrier and the catalyst material, since the high affinity of the aromatic structure for the active metal sites on the catalyst inhibits fast reaction. To achieve this, the H_2 rich carrier material is heated up until it boils and the vapours emerging due to the boiling come into contact with the catalyst bed that is placed in a column above the liquid. Above the column with the catalyst, the vapours are condensed, and the liquid flow is refluxed back over the catalyst bed to ensure adequate wetting of the catalyst. Geißelbrecht et al. [92] were the first to use this system for BT. The choice was made to use BT/H_{12}BT since it has a lower boiling point than DBT/H_{18}DBT, as can be seen in Table 1-1. To increase the thermal efficiency of the CD process, the system was operated at reduced pressures (20 kPa), allowing dehydrogenation of the H_{12}BT fraction at temperatures as low as 200 °C. This showed that the dehydrogenation of LOHC can be performed at lower temperatures, which allows for easier waste heat integration. For their investigation Geißelbrecht et al. used a closed batch operation for the CD system, shown on Figure 1-5.

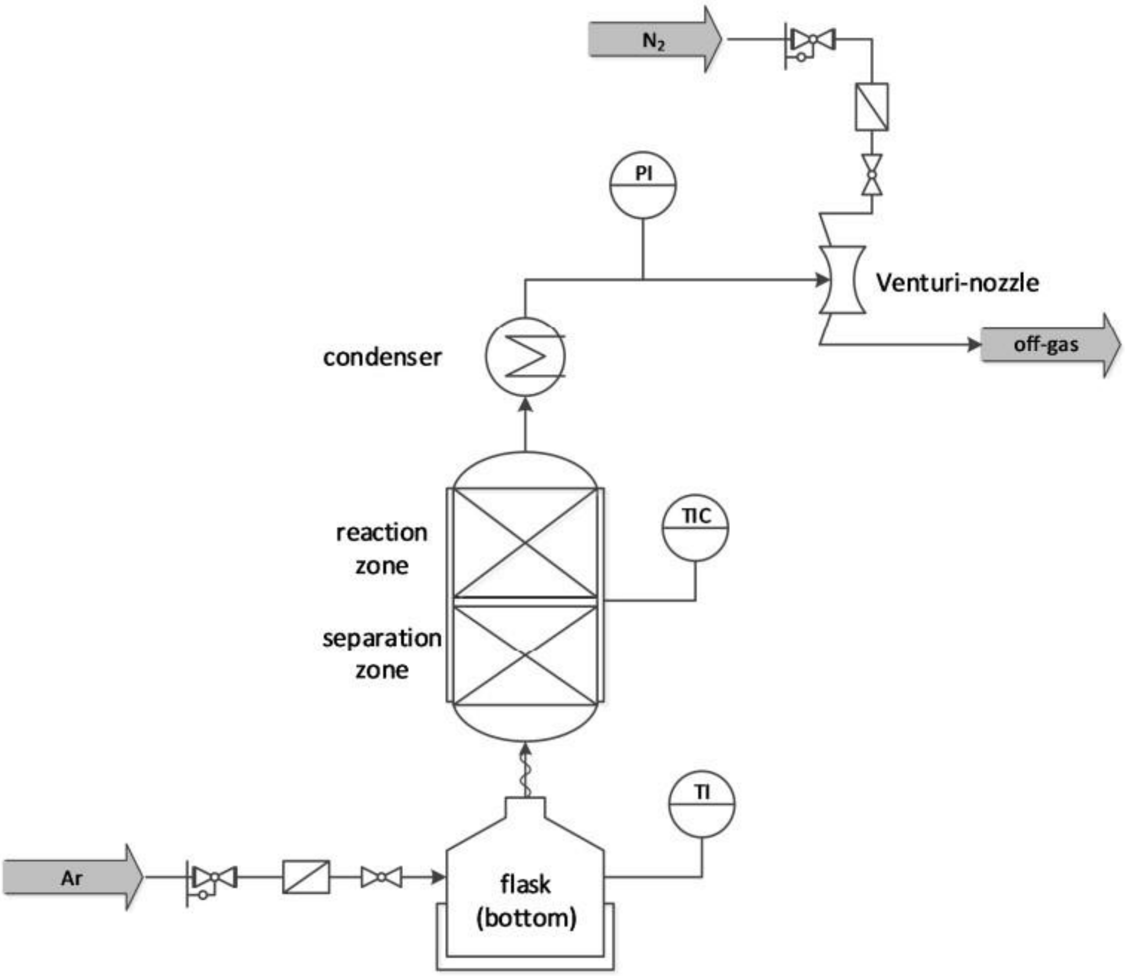

Figure 1-5 Schematic of the catalytic distillation process proposed by Geißelbrecht et al. [92]

Rüde et al. [93] showed the potential of continuously flowing CD dehydrogenation system. They showed an almost fourfold increase dehydrogenation rate compared to a traditional reacting liquid dehydrogenation system operated at the same temperatures. The CD gets its efficiency also from integration with waste heat, this heat is required to boil the LOHC, which is an energy intensive process without waste heat integration. The possibility to operate at temperatures about 50 – 100 °C cooler than liquid based dehydrogenation systems, makes the waste heat integration more straightforward than it would be in a non-CD system, since lower temperature waste heat is more readily available.

1.3.5 Tubular Reactors

On of the earliest commercial LOHC dehydrogenation reactors used, was based on a horizontally placed tubular reactor. [94] This reactor contained a packed bed of particles but was only partly filled with $H_{18}DBT$. The empty space inside the reactor volume was used to allow the H_2 to escape the reaction medium, without altering the residence time of the liquid inside the reactor. This reactor configuration was modelled by Peters et al. [95] using a *pseudo* – 1D approach and the power output of this reactor configuration was linked to the liquid hour space velocity (LHSV) and the obtained conversion of the $H_{18}DBT$ for temperatures ranging from 240 to 310 °C. Another dehydrogenation system developed for dehydrogenation of $H_{12}BT$ and $H_{18}DBT$ for commercial applications consists of a duct shape reactor that is operated in vertical concurrent flow for the liquid and the gas flow. Inside this reactor a bed of pelletized catalysts is kept between two fritted plates to prevent the beads from migrating towards the inlet or outlet tubes of the liquid. The reactor is heated by a collection of heating rods that protrude the reactor body perpendicular to the flow direction. [96] A publication by Kadar et al. [97] of this reactor concept shows it in operation Figure 1-6, this reactor could be operated at the highest achieved power density of 0.76 $kW_{H2\text{-}LHV}L^{-1}_{reactor}$, based on the total reactor volume. In this reactor they made use of a 3 mm 0.3 wt.% Pt/Al_2O_3 catalyst particles and used BT as working liquid. In this publication, the authors highlight the importance of heat transfer from the preheated LOHC and reactor walls and heated internals towards the catalyst particles as the key factor in reactor design. In this regard, they found that operating the reactor at higher flowrates, the reactor operated at higher power density, a six times increase in flowrate resulted in a fivefold increase in H_2 release per minute. This came at the cost of reduced conversion of the DBT. Reaching only 56 % conversion of the LOHC, compared to 80 % at lower flowrates.

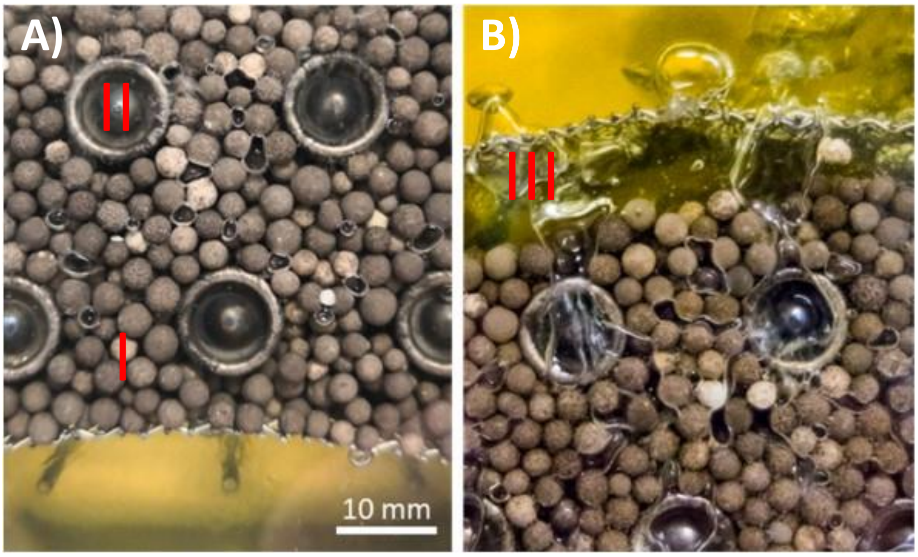

Figure 1-6 Dehydrogenation reactor from Kadar et al. [97] near the bottom of the reactor, A) and the top B). With the particle bed I, the heated internal II, and the gas bubbles III.

Heublein et al. [98] provided a clear overview into the influence of the orientation of the reactor and the influence of using counter or concurrent flow and the use of intermediate gas removal from within the system. For this analysis the researchers used $H_{12}NEC$ as the H_2 – carrier, allowing for operation of the reactor at temperatures between 180 and 280 °C. They showed that the overall power density of the reactor was similar for the horizontal and vertical operational modes. Power density is a critical factor in the design of dehydrogenation reactors as it expresses the amount of energy, in the form of H_2, that can be released per unit of reactor volume per unit of time. The reactor configurations used in this study can be seen in Figure 1-6. It was observed that the heat transfer was greatly increased in vertical operation compared to the horizontal. This is likely due to the increase in turbulence in the liquid medium induced by the movement of the gas phase. A second conclusion from their work stated that the dehydrogenation system showed a lower productivity when the volume fraction of the gas increased in the reactor. This phenomenon was linked to the dewetting of the catalyst.

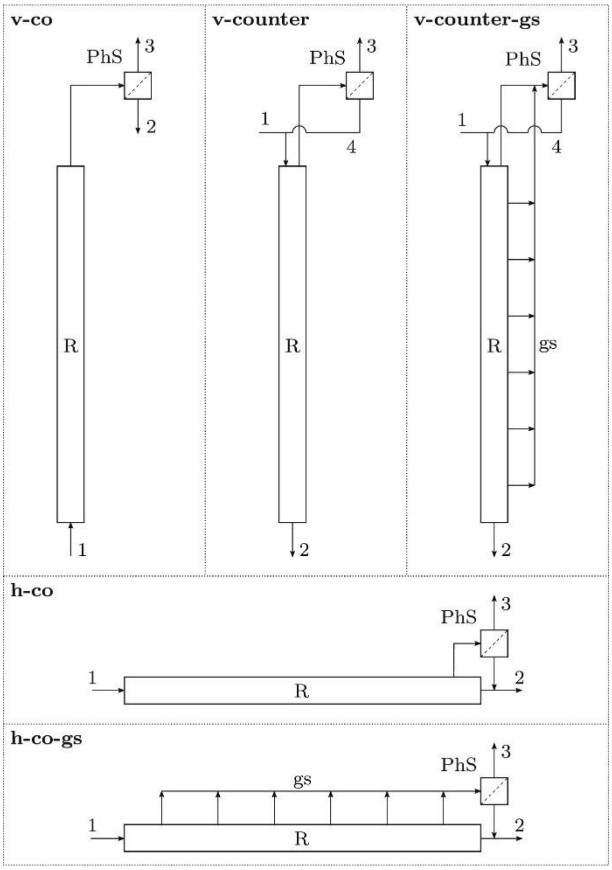

Figure 1-7 Reactor configurations from the work of Heublein et al. [98] showing the reactor orientation in horizontal and vertical operational modes. 1: the liquid feed, 2: liquid product, 3: purified H_2, 4: Recycle of condensate.

The decreased efficiency of H_2 release, induced by the influence of the gas phase near the catalyst was further studied by Solymosi et al. [99] They showed that inhibiting the nucleation of gas bubbles by catalyst pores filled completely with $H_{18}DBT$, was a key mechanism in inhibiting the reaction upon restarting the catalytic reaction after downtime. A mechanism was proposed for gas bubble nucleation inside the catalyst pore and on the outside of the catalyst pellet. According to this mechanism the H_2 gas formed inside the catalyst pore would fill up the pore during the dehydrogenation reaction and once the pore is filled, a bubble would start to form on the outside of the pellet and detach once it reaches a certain bubble size. At the moment of bubble detachment, the pore can be filled again with fresh $H_{18}DBT$ liquid and the H_2 release cycle can start again. The oscillation inside the catalyst pore switching from a gas filled to a liquid filled pore and back again, is expected to have a major influence on the mass and bubble nucleation speed. When the reaction is attempted with prewetted catalyst, so with pores filled with $H_{18}DBT$, the nucleation of H_2 bubbles was not observed, since no H_2 gas bubbles could be formed due the high energy barrier for nucleation caused by the completely wetted particle surface. This effect lasted until the catalyst pellets were mechanically agitated, upon which H_2 gas was seen to be rapidly expulsed from the catalyst beads and the reaction proceeded as normal. It was also reported that the H_2 gas evolution rate increased for the first 30 s after agitation. Figure 1-7 shows the effect of mechanical stimulus to restart the dehydrogenation reaction.

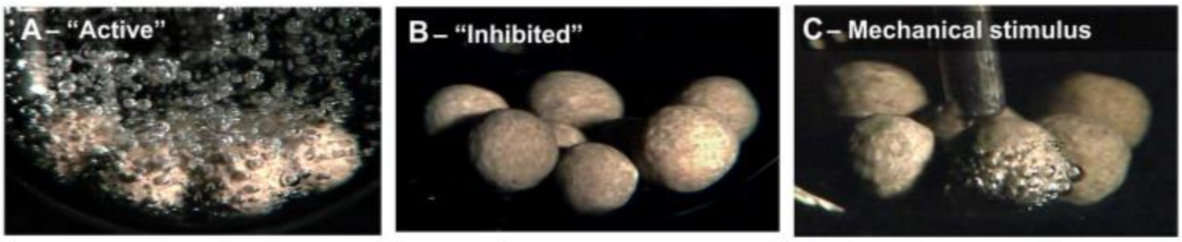

Figure 1-8 Snapshots of the dehydrogenation experiment by Solymosi et al. [99], showing A) the catalyst during dehydrogenation. B) The inhibited state of the catalyst after a cycle of cooling and reheating. C) the H_2 gas release after mechanical stimulus of the catalyst bead.

Two effects from this paper speak in favour of investigation of fluidized bed reactors for the dehydrogenation reaction of $H_{18}DBT$. Firstly, it was observed that the driving force in nucleation of H_2 gas bubbles depended on the oscillation between a liquid filled and a gas filled catalyst pore and that the frequency of the oscillation depends on the rate at which the gas bubble detaches from the catalyst surface. By operating in a fluidized regime, the detachment rate of the particles can be increased, [100] which would enhance the oscillation within the catalyst pores and increase the H_2 release rate. Secondly, the observation that the H_2 release rate was greater immediately after mechanical agitation of the dehydrogenation system can also be explored as in a fluidized regime, there is a constant agitation of the flow. In the following section the basic operating principles of a liquid – gas – solid fluidized bed (LGSFB) are further explained.

1.4 Fluidized Bed Reactors

From past research conducted in the field of LOHC, and specifically in the field of DBT/H_{18}DBT, it has been highlighted that high mass and heat transfer are crucial to operate the system. High mass transfer is needed to remove H_2 gas bubbles from the catalyst surface and to supply H_2 rich H_{18}DBT towards the active sites on the catalyst pellet. Heat transfer towards to catalyst sties is crucial since the high endothermicity of the reaction cools down the system and the reaction would auto-terminate without a proper heat influx. In this light, the use of fluidized bed reactors will be investigated since these systems are well known for improved mass and heat transfer rates compared to fixed particle beds.

1.4.1 General Principles of Liquid – Gas – Solid Fluidized Bed Reactors

In this thesis I will focus on the use of fluidized reactors to with the idea to improve the removal of H_2 bubbles from the catalyst surface to decrease dewetting effects that occur upon dehydrogenation of H_{18}DBT. Fluidization is a phenomenon whereby the drag force that a moving fluid exerts on a particle bed is equal to the effective weight of the particle phase. There are two important parameters to determine if a reactor is operating in fluidized regime, also called the expanded bed regime. The first parameter is the minimal fluidization velocity ($\boldsymbol{U_{lmf}}$): this is the velocity at which the drag force of the fluid equals the particle weight, and the onset of the fluidization regime. At fluid velocities below the $\boldsymbol{U_{lmf}}$, the reactor operates in the fixed bed regime. The second parameter is the terminal velocity, $\boldsymbol{U_t}$, at fluid velocities exceeding $\boldsymbol{U_t}$ the fluid drag on the particles will be so high that the particles start to leave the bed, this operational mode is called the transport regime. The dehydrogenation reaction of H_{18}DBT is inherently a three-phase system containing a liquid (LOHC), a gas (H_2), and catalyst particles (Pt/Al_2O_3). In the systems studied in this thesis, the liquid is the main driver of the fluidization of the particles. However, the presence of a gas phase is known to change (usually decrease) the value of U_{mf} and U_t. For the Liquid – Gas – Solid (LGS) systems, the nomenclature of the $\boldsymbol{U_{lmf}}$and $\boldsymbol{U_t}$ is then altered slightly, the symbol $\boldsymbol{U_{lmf0}}$will denote the minimal fluidization velocity, without gas phase present, $\boldsymbol{U_{lmf}}$ is the minimal fluidization velocity in the presence of a gas phase. For the terminal velocity the symbols $\boldsymbol{U_t}$ and $\boldsymbol{U_t'}$ to denote the terminal velocity without or with the gas phase present, respectively.

Fluidized bed reactors (FB) are over a century old and they have been applied in a plethora of industrial reactions including: fluid catalytic cracking [101], biomass gasification [102], Fisher – Tropsch Synthesis [103] and production of polyethylene [104], polypropylene [105] and acetonitrile [106], these are gas – solid fluidized beds. Liquid – Solid fluidized beds have been used in enzymatic polymerization of phenol [107], for size separation of particles [108] and waste water treatment [109, 110]. The use of thee phasic liquid gas solid fluidized beds (LGSFB) reactors has been seen in the H – oil process and LC -FINING process for the treatment of heavy oil fractions, [111, 112] the H – coal process for coal liquefaction [113] and again in waste water treatment. [114]

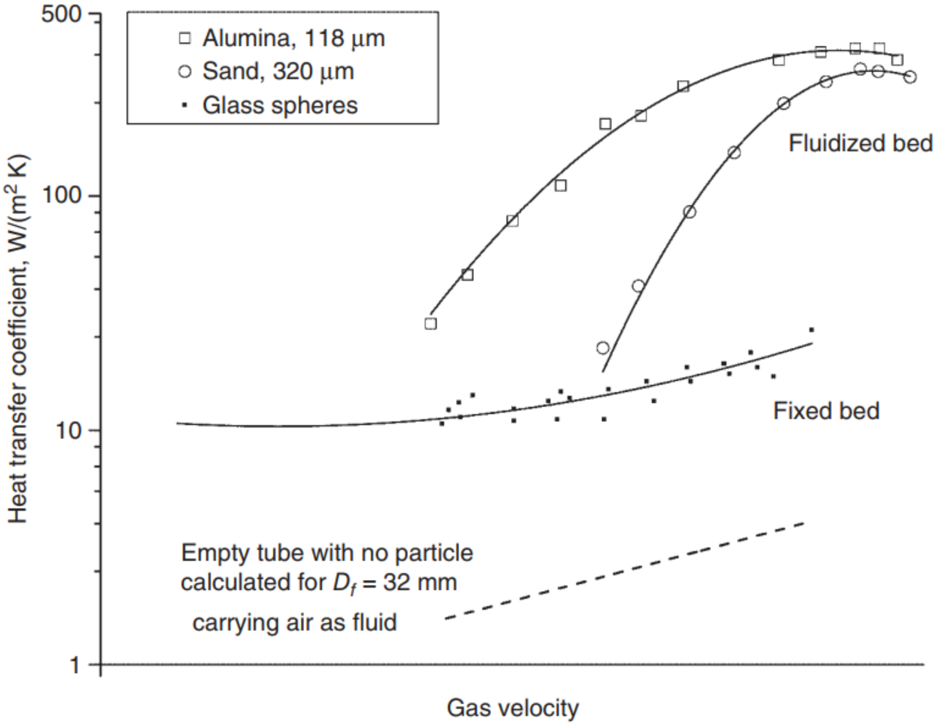

Figure 1-9 Relative orders of magnitude of heat transfer coefficients for empty tube, fixed and fluidized bed reactors. Data obtained with flow at room temperature and 1 atm. [115]

The dehydrogenation reaction of $H_{18}DBT$ is a newly proposed addition in the field of continuous liquid fluidization reactors. Heat transfer from the walls to the catalyst phase has been determined for gas – solid systems to be an order of magnitude higher for fluidized beds compared to fixed beds, as can be seen on Figure 1-9. For dehydrogenation of $H_{18}DBT$ the improved heat transfer is even magnified by the gas – particle interactions. The kinetic energy of the particles will help in bubble breakage leading to smaller bubbles, [116] which further aid in a more uniform bed with improved heat transfer compared to large bubble regimes. [117] Heat transfer is crucial in the process due to the self-cooling effect of the reaction induced by the endothermic nature of the dehydrogenation of $H_{18}DBT$, see Figure 1-1.

The operational mode of a fluidized bed for $H_{18}DBT$ dehydrogenation is new compared to currently described FB reactors. The H_2 gas is not fed at the inlet of the reactor system, but rather it is being produced during the reaction itself. Since the evolved H_2 bubbles are being transported by the liquid flow, the fluidization regime with highest resemblance is that of a co-currently fed LGS fluidization reactor. In the classification system proposed by Fan, this operational mode is called the E-I-a mode, a co-current LGS system, with the liquid phase as the continuous phase. [118] The E refers to the Expanded bed regime, the I denotes the co-current flow in this classification.

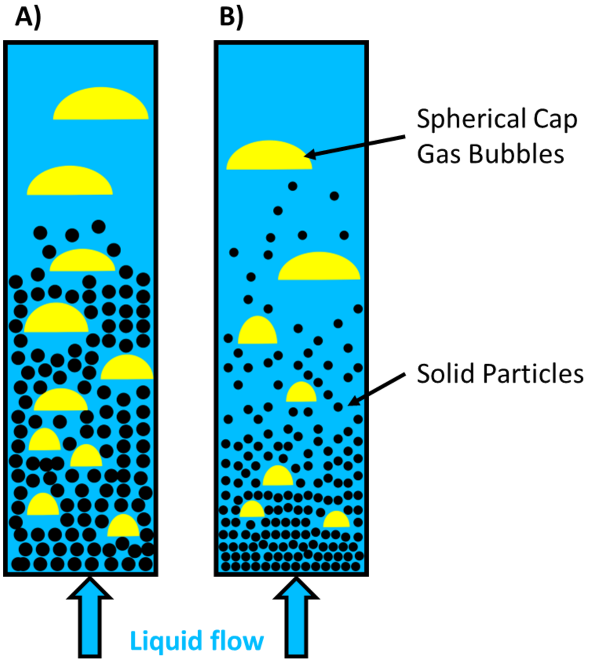

Figure 1-10 A graphical representation of A) a LGSFB in E-I-a-1 mode with a uniformly distributed particle bed and B) a LGSFB operating in E-I-a-2 mode characterized by a denser particle bed near the distributor and a long disengagement section.

Two subclasses exist in this system, mode E-I-a-1, where the U_t exceeds 0.05 m s^{-1}, and mode E-I-a-2, with $U_t < 0.05$ m s^{-1}. The first mode is characterized by a highly uniform particle bed, with a well-defined bed height, in the latter the particle bed is less uniform, and the solids concentration is higher at the bottom of the bed, with more a more diluted bed higher up the reactor. The distinction between E-I-a-1 mode and E-I-a-2 mode is reminiscent of the distinction between bubbling fluidized bed regime and turbulent fluidization regime. [119] Figure 1-9 graphically depicts the difference between these operational modes.

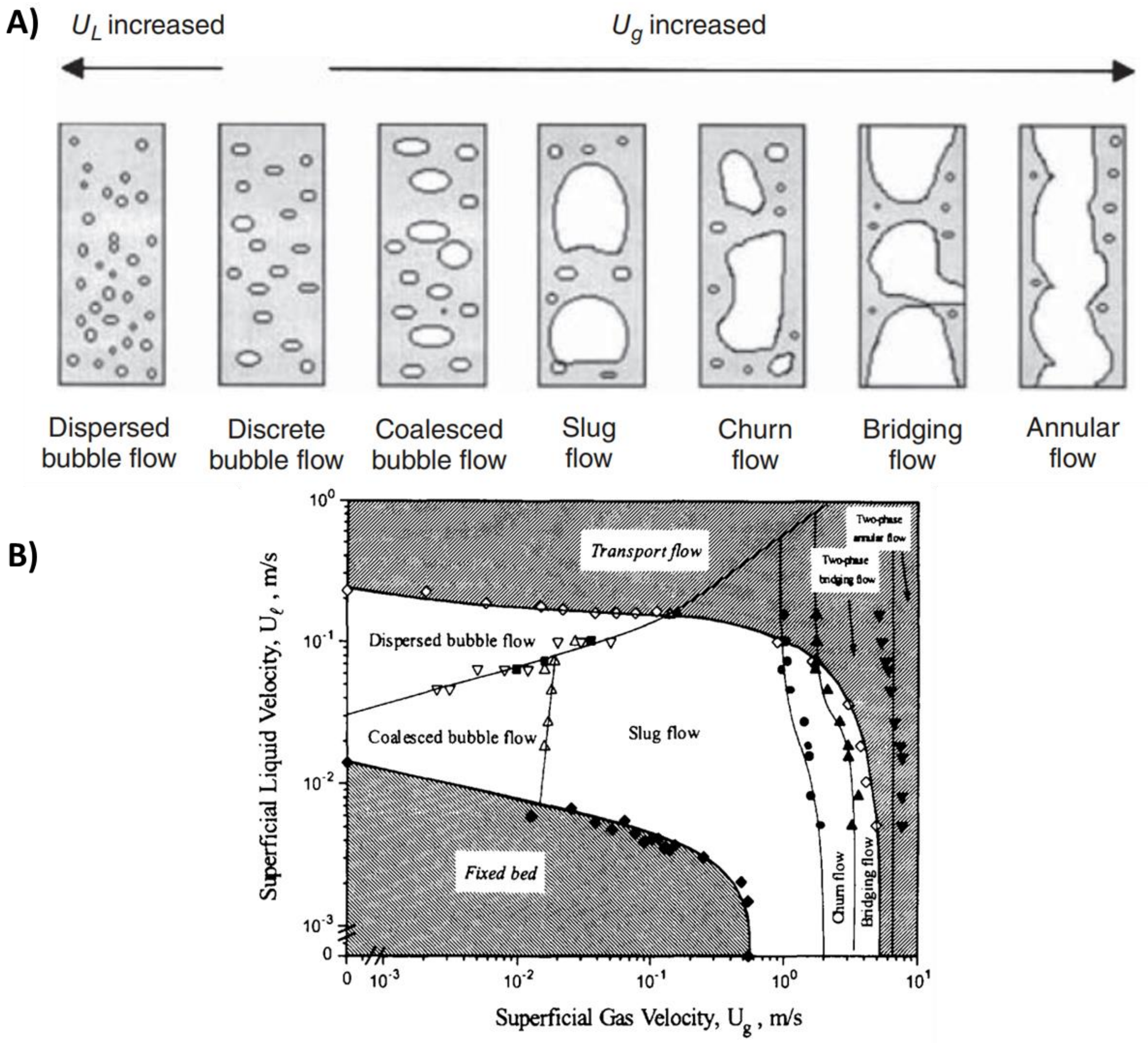

Figure 1-11 A) Schematic Diagrams of the flow regimes observed in a three phase systems of water, air and 1.5 mm glass beads. The white areas denote the gas phase. [120] B) Flow regime map of the different regimes of a similar fluidized bed in white, shaded section refer to non – fluidized regimes. [121]

Fluidized bed reactors consist of three distinct regions: the distributor region, the bulk fluidized bed region and the freeboard region. In regular E-I-a-1 fluidized bed reactors the distributor region is the region near the bottom of the bed where the liquid – gas distribution occurs and the final bubble shape is determined based on the geometry of the distributor plate and on the physical properties of the fluids, however for the dehydrogenation of $H_{18}DBT$ there is no gas injection, since all H_2 evolves from the surface of the catalyst particle. This is expected to have an effect on the bubble shape and size throughout the bed. The bulk region of the LGSFB depends heavily on the operational conditions, several regimes for LGSFB exist, and are shown on Figure 1-10A.

The ratio of the liquid and gas velocities, determines the flow regimes observed in the reactor. These flow regimes can be characterized by small bubbles in the dispersed and discrete bubble regime, at higher liquid velocities. With increasing gas velocity, the relative bubble size increases, from coalesced bubble regime to complete annular flow, where the gas phase completely fills the centre of the FB reactor. [111, 120-122]

The final section in a FB reactor is called the freeboard region and it is the region right above the bed. This region contains particle entrained from the bulk region. [123] In beds with larger dense particles there is a clear distinction between the bulk and freeboard region. This distinction is less pronounced with smaller and lightweight particles. [118]

Characterization of a LGSFB is a complex procedure, due to the multiphase nature of the system and the often-counteracting effects. However, empirical correlations for the design of LGSFB have been developed in the past. The value for the $\boldsymbol{U_{lmf}}$ can be determined from: [124]

$$\frac{\boldsymbol{U_{lmf}}}{\boldsymbol{U_{lmf_0}}} = 1 - 376\boldsymbol{U_g^{0.327}}\mu_l^{0.227} d_{p_e}^{0.213}\left(\rho_p - \rho_l\right)^{-0.423} \tag{1.6}$$

With $\boldsymbol{U_g}$ the gas velocity, μ_l the dynamic viscosity of the liquid, d_{p_e} the effective particle diameter (this is equal to the particle diameter d_p in case of spherical particles) and, ρ_p and ρ_l the particle and liquid phase density. The value for $\boldsymbol{U_{lmf_0}}$ can be determined from the correlations of Wen and Yu for liquid – solid fluidized beds.[125]

$$\boldsymbol{U_{lmf_0}} = \frac{\mu_l}{d_{p_e}\rho_l} \cdot \left(\sqrt{33.7^2 + 0.0408 \cdot Ar} - 33.7\right) \tag{1.7}$$

In this formula Ar equals the Archimedes Number given by for a spherical particle:

$$Ar = \frac{g d_p^3 \rho_l (\rho_p - \rho_l)}{\mu_l^2} \tag{1.8}$$

The correlations based on equation 1.6, 1.7 and 1.8 are valid for $\boldsymbol{U_g}$ between 0 and 0.17 m s^{-1}, and μ_l ranging from 0.0009 Pa s to 0.0114 Pa s. The particle density and effective particle diameter should vary between 1800 kg m^{-3} and 2500 kg m^{-3} and 0.46 to 6.3 mm, respectively. To determine the window of operation for fluidized beds, the particle terminal velocity should be known as well. It has been reported that $\boldsymbol{U_t}$ can be determined from the $\boldsymbol{U_{lmf}}$ by:[118, 126]

$$\boldsymbol{U_{lmf}} = 0.0125 \boldsymbol{U_g^{-0.5}} \cdot \boldsymbol{U_t^{1.64}} \tag{1.9}$$

The correlation in equation 1.9 is valid for $\boldsymbol{U_g}$ ranging from 0.05 m s^{-1} to 0.2 m s^{-1} and U_t between 0.38 and 0.70 m s^{-1}.

1.4.2 Guiding Principles for Fluidized Bed Reactor Design for H_{18}DBT Dehydrogenation

When designing a FB reactor for the dehydrogenation of H_{18}DBT there are several trade-offs in the fluidization regime that should be accounted for due to the nature of the reacting system. As stated above, there are several distinct flow regimes possible in three phase fluidized beds. When operating in the coalesced regime the bubble size is larger and the velocity of the gas phase is greater compared to the bubble breakage regime. This causes a lower gas hold-up in the system, making greater use of the reactor volume, since it is mostly occupied by the reacting liquid and the solid particles and the H_2 gas is expulsed more quickly from the system. By limiting the volume of H_2 present inside the reactor the power density can be increased. [98] However, the interfacial area of a single large bubble is smaller than the interfacial area of the same volume of gas consisting of many small bubbles. A higher interfacial area leads to larger mass and heat transfer rates. [127, 128] There is thus a trade-off in operating regimes in a FB for H_{18}DBT dehydrogenation. Operating in the bubble breakage regime offers increased mass and heat transfer at the expense of power density of the reactor.

A second trade-off in operating regimes can be seen in the onset of fluidization of the particles. This is expressed in equation 1.6, where it can be seen that a higher gas velocity reduces the liquid velocity required to reach a fluidized state. Since larger gas bubbles have a higher velocity in the bed, operating in the bubble coalescence regime will cause fluidization at lower liquid velocities. A lower liquid velocity is linked to a longer residence time in the reactor. A longer residence time increases the chance of $H_{18}DBT$ to come into contact with the active site of the catalyst and thus release H_2 gas, this effect is counteracted by the lower heat transfer rates obtained for larger gas bubbles compared to smaller bubbles, which are observed at higher liquid velocities. [129]

To reduce the minimal fluidization velocity, $\boldsymbol{U_{lmf}}$, the particles properties can also be altered. From equation 1.6 it can be seen that both the diameter of the particle and the particle density are positively related to the $\boldsymbol{U_{lmf}}$. Reducing both, i.e., working with smaller and less dense particles, would decrease the $\boldsymbol{U_{lmf}}$, allowing for fluidization at lower liquid velocities and thus increase the residence time. However, the expansion of the solid bed would then increase, which in turn increases the average bubble diameter in the bed. This effect is not as strong in the bubble breakage regime, but it is prominent in the coalesced bubble regime, where a small increase in the bed expansion ratio leads to a large increase in average bubble size. [130] Furthermore, the use of smaller, lightweight particles tends to produce less uniform particle distribution in the reactor and more pronounced disengagement of particles from the bed. [118] Specifically for the dehydrogenation of $H_{18}DBT$, efficient heat transfer should be the main priority, due the high endothermicity of the dehydrogenation reaction. This was recently highlighted again in the work of Kadar et al. [97], who showed that for high power density of the reactor, the heat transfer should be maximized. Better heat transfer can be obtained by keeping the bubble size small, this is challenging due to the high-volume expansion. Theoretically, 1 mL of $H_{18}DBT$ can produce up to 650 mL of H_2. [55] This will cause large bubbles of hydrogen in the particle bed and a decreased heat transfer. That is why this thesis will also focus on the use of swirling fluidized bed (SFB) reactors, the swirling motion of the liquid is expected to produce a low-pressure zone in the reactor, which will concentrate the H_2 gas in the centre of the reactor, away from the particle bed. By rapidly removing the H_2 gas from the particle region, H_2 release rate is expected to increase.

1.5 Scope of The Thesis

The scope of this thesis is to investigate the potential of fluidization applied to the dehydrogenation reaction of $H_{18}DBT$. This is a completely novel approach to improve the efficiency of the H_2 release step, the most energy intensive step in the DBT based H_2 storage process. By fluidization of the catalytic particles required for the reaction, improved mass and heat transfer are expected to expedite the H_2 release from the $H_{18}DBT$. In this thesis I will focus on improving the uniformity of the particle bed in fluidized systems. A uniform particle bed will allow for improved control of the reaction. However, the current limitation in CFD codes did not allow to assess the extent to which the fluidization of the bed improved mass and heat transfer which is expected from fluidization. The potential for fluidization has been hinted at in the work of Solymosi et al. [99], who showed that recently agitated catalyst particles had a higher activity in the H_2 release rate compared a static particle bed. To investigate the potential of fluidized beds for the dehydrogenation of $H_{18}DBT$, a new reactor prototype was developed which combined the fluidization of the particles with in-situ removal of the gas phase via the use of swirling liquid flows inside the reactor. This new reactor prototype will be studied via CFD simulations. As an introduction to the concept of CFD simulations, **Chapter 2**, covers the basics of setting up a CFD simulation for chemical reactions. This chapter is based on the mini – review article that was published in the Tutorial Series on Experimental Methods in Chemical Engineering. The reaction covered in this article is not the dehydrogenation of $H_{18}DBT$, due to the scope of the review a simpler reaction was studied, i.e., the isomerisation of *n*-butane to *i*-butane. This serves as an starting point in the development of a reactive solver for the dehydrogenation of $H_{18}DBT$, by analysing the implementation of simple homogenous reactions in OpenFOAM. In **Chapter 3**, a cold flow study of the prototype for the swirling fluidized bed reactor is investigated, via multiphase CFD simulations. This prototype reactor was studied by making use of similarity conditions to link the behaviour of $H_{18}DBT$, H_2 and Al_2O_3 catalyst particles to a non-reactive system of water, Argon (Ar), and glass beads. Before moving to reactive $H_{18}DBT$ flows, several different model parameters in Eulerian – Eulerian multiphase simulations were investigated in **Chapter 4**. By analysing the influence of the different model settings, the accuracy of CFD simulations for three phase fluidized beds could be improved. In **Chapter 5**, the CFD implementation to mimic the dehydrogenation of $H_{18}DBT$ via CFD simulation is proposed. This code is used to study the influence of the H_2 release on the particle bed in fluidized regimes. In the final section of this chapter, the improvements to the swirling fluidized bed reactor are proposed based on the newly developed CFD implementation of the $H_{18}DBT$ dehydrogenation reaction.

In this thesis, I use three different CFD solution algorithms to account for the number of phases included in the simulations, Table 1-3 provides a short overview of the different multiphase models used.

Table 1-3 Overview of the different simulation approaches and solvers used in this thesis.

Chapter 2	
Model Used: Single phase simulations Solver: (rho)ReactingFoam	Goal: Analysis of CFD implementation for homogenous chemical reactions
Chapter 3	
Model Used: Volume of Fluid (VOF) Solver: interFoam	Goal: Find the height of the liquid – gas interphase in the reactor at different flowrates
Model Used: Eulerian – Eulerian Multiphase Solver: multiphaseEulerFoam	Goal: Cold flow simulations of three phase system of liquid, gas and solid beads
Chapter 4	
Model Used: Eulerian – Eulerian Multiphase Solver: multiphaseEulerFoam	Goal: Study the influence of the drag model combinations on the simulations of three
Chapter 5	
Model Used: Eulerian – Eulerian Multiphase Solver: multiphaseEulerFoam + custom coded source term	Goal: Investigate the particle bed distribution in fluidized bed systems during the dehydrogenation of $H_{18}DBT$.

Chapter 2

Basic Principles of the Finite Volume Method for Computational Fluid Dynamics

Based on:

Laurens Van Hoecke, Dieter Boeye, Arturo Gonzalez-Quiroga, Gregory S. Patience, Patrice Perreault *Experimental methods in chemical engineering: Computational fluid dynamics/finite volume method – CFD/FVM, Can. J. Chem. Eng.* 2023, 101(2), 545. DOI: https://doi.org/10.1002/cjce.24571

2.1 Introduction

This chapter was originally published as a tutorial review that is part of a series on experimental methods in chemical engineering that highlights key challenges and succinctly reviews recent research areas. [131] Here I showcase Computational Fluid Dynamics (CFD) as a viable alternative to tedious and expensive experiments by means of virtual prototyping. CFD itself, however, is challenging since it relies heavily on numerical schemes and models for the interactions simulated, which all have to be validated. [132, 133] Often,it is possible to reach a solution, but to achieve the correct solution, it requires an understanding of the workflow of a CFD project. [134] With this chapter I aim to provide an entry-level assessment of the theory behind finite volume method (FVM)-CFD simulations, and how to correctly set up a CFD study to achieve reliable and accurate results. An example case performed with the open-source software package OpenFOAM illustrates how to set up the problem. [135]

The first section of this chapter, discusses the theoretical background of CFD simulations, delving into the basic mathematical equations required to describe fluid flow problems. It is briefly discussed how these algebraic formulas are discretized to linearized equations, a step required for the equations to be solved by computers. Two computational algorithms, PISO and SIMPLE are also discussed, by showing the order in which they solve the set of equations. The main emphasis on this chapter, however, is the example case provided on the isomerization of *n*-butane, to *i*-butane. The different verification steps required, prior to solving a reactive case, are shown. This simplified single phase chemical reaction serves as a basis to investigate the nature of simulations of more complex reactive cases for future development of CFD packages for liquid phase catalytic reactions, such as the dehydrogenation reaction of H_{18}DBT. This chapter also covers a hands-on approach to use the grid convergence index (GCI) method, initially described by Roache. [136] This is required to assess the accuracy of the computational grid. After all these initial steps, the results of CFD simulations are shown of an unconventional tubular reactor, containing a notch locally restricting the flow of the reactants.

2.2 Theory

2.2.1 Mathematics in CFD

2.2.1.1 Governing Principles

CFD codes are used to describe fluid flow, including granular phases,which are then treated as *pseudo*-fluids. The four main constitutive relations (conservation laws) to fully describe reacting flow of Newtonian fluids are:

- The continuity equation (law of mass conservation)

$$\frac{\partial \rho}{\partial t} + \nabla \cdot (\rho \mathbf{U}) = 0 \tag{2.1}$$

- The momentum or Navier–Stokes equations, which is an extension of Newton's second law for fluid motion (F = $m \cdot a$), is given as equation 2.2, and used to calculate pressure and velocity fields for an incompressible flow. The source term, $\boldsymbol{Q_U}$, represents external forces including gravity acting on the fluid per unit volume (i.e., $\rho\mathbf{g}$). The uppercase symbol ^{T} denotes the transpose of a matrix.

$$\frac{\partial \rho \boldsymbol{U}}{\partial t} + \nabla \cdot (\rho \boldsymbol{U}\boldsymbol{U}) = -\nabla p + \nabla \cdot \{\mu[\nabla \boldsymbol{U} + (\nabla \boldsymbol{U})^T]\} + \boldsymbol{Q_U} \tag{2.2}$$

- The species balance equation is required for flows involving multicomponent mixing and/or reactions, equation 2.3. This generalized expression of the convection-dispersion equation includes source terms for chemical reactions, $\mathcal{R}_k$.

$$\frac{\partial}{\partial t}[\rho Y_k] + \nabla \cdot (\rho Y_k \boldsymbol{U}) = \nabla \cdot \left(\rho D_{eff,k} \nabla Y_k\right) + \mathcal{R}_k \tag{2.3}$$

- The conservation of energy, equation 2.4. is used to calculate the temperature over the simulation domain at every time step, based on the enthalpy and reaction rates. The addition of the term Q_T in OpenFoam allows the use of a (heat) source term.

$$\frac{\partial \rho C_p T}{\partial t} + \nabla \cdot \left(\rho C_p \boldsymbol{U} T\right) = \nabla \cdot (\kappa \nabla T) + Q_T \tag{2.4}$$

The physicochemical properties expressed in the above relationships include pressure (p), velocity ($\boldsymbol{U}$), density (ρ), mass or mole fraction (Y), effective diffusion coefficient (D_{eff}), temperature (T), heat capacity (C_p) and thermal conductivity (κ), which are linked by an equation of state when at thermodynamic equilibrium. The ideal gas law is one example of an equation of state (p = ρRT). The challenge in resolving this set of equations resides in the fact that both pressure and velocity fields must be calculated via the momentum equation. For turbulent reacting flows, additional computational challenges arise in modelling turbulence and simulating the chemistry- turbulence interactions,[137] which are covered further in this chapter.

2.2.1.2 The Finite Volume Method

In the FVM, the entire design space is divided into many small, non-overlapping control volumes, which are called cells. The collection of these cells is a called a mesh. To evaluate the primary variables of the Navier–Stokes equations in each cell, which determines how each phase is transported through the mesh, equation 2.5 is used:

$$\int_V \left[\frac{\partial \phi}{\partial t}\rho\phi\right] dV + \int_V [\nabla \cdot (\rho \boldsymbol{U} \phi)] dV = \int_V \left[\nabla \cdot \left(\boldsymbol{\Gamma}^{\phi} \nabla \phi\right)\right] dV + \int_V Q_{\phi} dV \qquad (2.5)$$

where, ϕ is a fluid property, e.g., T, $\boldsymbol{U}$, or turbulent kinetic energy and $\boldsymbol{\Gamma}^{\phi}$ is the diffusion coefficient of the ϕ. Equation 2.5 is solved for each transport variable ϕ in the system and the transport equation represents the conservation of a variable in a FVM cell. This equation thus allows to solve all the conservativion equations. In that sense, CFD-FVM can be truly understood as a computational transport phenomenon.[138] The following fluid properties are to be resolved in equation 2.5:[139, 140]

- The first term is the *unsteady term* or *accumulation term* and represents the accumulation of a certain variable within a control volume over time.
- The second term represents the *convection term* as it includes the velocity vector.
- The third term is the *diffusive term* and accounts for changes in fluid properties due to gradients in the flow.
- The *source term* (final term) comprises phenomena related to the local production and destruction of a fluidproperty within the control volume (e.g., external forces in the momentum balance equation).

The FVM model assumes that the value of a variable in a cell is stored at the cell centre, and that all variables vary linearly across the cell, both in time and space. The overall solution involves computing the transport equation for each cell independently. In order to reach a solution, boundary conditions are imposed for each transport variable. The requirements for these cells are that they are non-overlapping, their faces are planar, and they do not protrude into each other. Theoretically, they can be of any shape. In practice, regular shapes are best. Although the solution is obtained by solving the transport equation for each cell, the value in each cell also depends on the values of the neighbouring cells, which are transmitted through the diffusion and convection terms. The divergence operator, associated with the diffusion and convection terms, highlights the dependency on the vector field surrounding the cell. Assessing this vector field would be impractical with volume integrals. For this reason they are converted to surface integrals using the Divergence or Gauss–Ostrogradsky theorem, which states that the volume integral can be replaced by a surface integral of the flux over the surface faces:[141]

$$\int_V \nabla \cdot \boldsymbol{F}\, dV = \int_S \boldsymbol{F} \cdot \hat{\boldsymbol{n}}\, dS \tag{2.6}$$

An additional benefit of the Gauss–Ostrogradsky theorem is that the equations are now conservative since they are based on the flux at the surface. This means that when a flux enters a cell, the same flux leaves the cell in the opposite direction. However, there is still a surface integral to be solved, which—being a mathematical operation—requires a numerical approximation.To estimate this integral, it is assumed that i) the surface integral over the entire cell is equal to the sum of the integrals for everyface and ii) the value of a surface integral of a face can be approximated by the value at the centre of the face. Smaller cells increase the accuracy. These two assumptions transform the integral to a sum of the values at the face centre, which is an essential step to discretize the integrals to be solved numerically. This shifts the problem to finding the value at the *face* centres while only the values of the *cell* centres are known. Therefore, interpolation is required to determine the value from the cell centre to the face centre. The three main linearization or discretization schemes are shown on Figure 2-1 and are:

- Linear differencing
- Upwind differencing

- Linear upwind differencing

In the linear differencing scheme, the value at the face centre, ϕ_F, is computed as the sum of the cell centre, ϕ_P, and its neighbour cell centre, ϕ_N, multiplied by a factor f_x to account for the distance between the cell centre and the face. This scheme depends on two points and thus is second-order accurate.

$$\phi_F = f_x \phi_P + (1 - f_x)\phi_N \tag{2.7}$$

Upwind differencing is simpler and more stable, but it is only first-order accurate, which is convenient to initialize simulations due to the increased stability. Higher order methods are required in the final stage of the simulation as they minimize numerical diffusion issues observed with first-order schemes like smearing sharp interfaces. Numerical diffusion comes from truncation errors of the second- and higher order terms, leading to an additional component associated with the diffusion term, proportional to grid size, density, and velocity in the upwind scheme.[138, 142] It states that the value at the face is extrapolated directly from the value at the cell centre. When the flux is positive, that is, pointing towards the outside of the cell, the value at the face equals the value at the owner cell ϕ_P; when the flux is negative, it takes the value of the neighbouring cell ϕ_N.

$$\phi_f = \begin{cases} \phi_f = \phi_P for\ F \geq 0 \\ \phi_f = \phi_N for\ F \leq 0 \end{cases} \tag{2.8}$$

Linear upwind differencing lies between the linear differencing and the upwind differencing scheme. It uses a gradient to compute the cell values at the face, but this gradient is not computed between the owner cell and the neighbour at that face. In this case, the gradient is computed between the owner cell and the neighbour of the opposite cell of the target face. This gradient is then extrapolated to the target face. This scheme is also second-order accurate, and, more importantly, it can be limited for flows with rapid changes, making it more stable than the linear scheme with a slight decrease in accuracy.[138, 143]

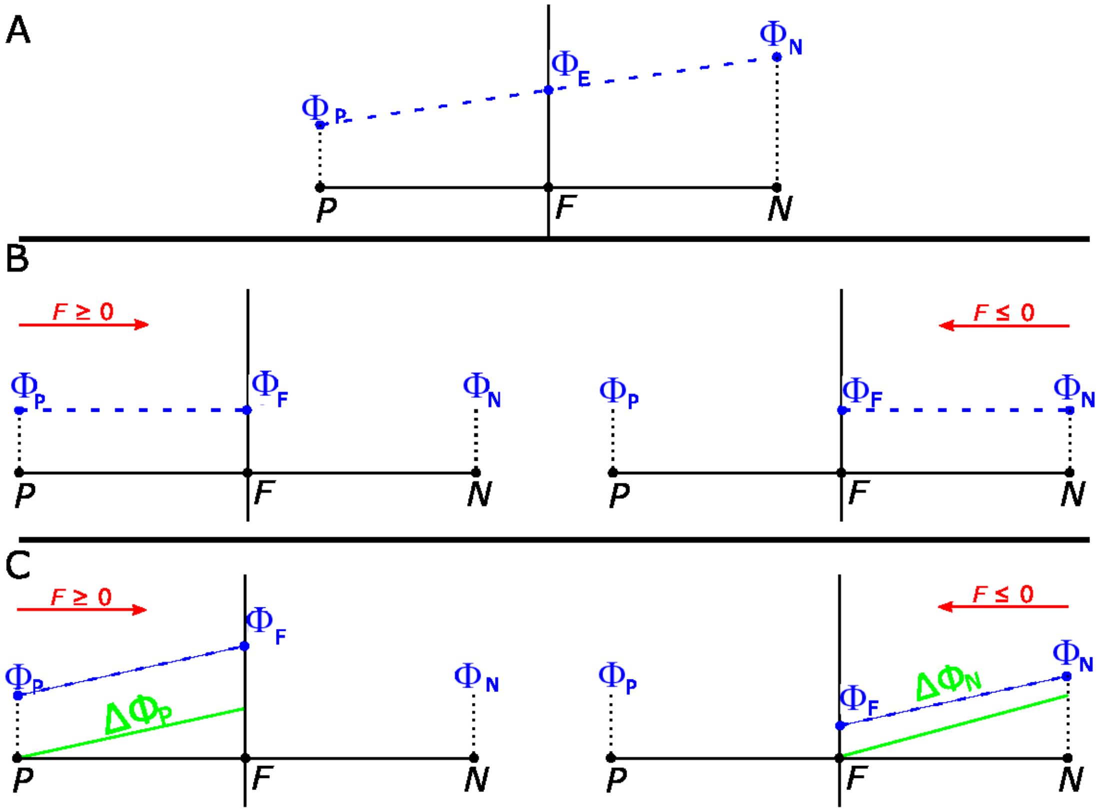

Figure 2-1 2D representation of spatial discretization schemes, with owner cell centre P and neighbouring cell centre N. F denotes the value on the face, between the two. The value of F is calculated by: a linear approximation between P and N ((A) linear approximation); extrapolation of the value of the cell centre to the face centre, depending on the sign of the flux, either the value of P or N is selected ((B) upwind scheme); and, the value of the face centre is calculated by the extrapolation of the gradient of the flux within the cell to the face, again this extrapolation depends on the sign of the flux ((C) linear upwind)[144]

The numerical schemes thus provide a solution to solve the convection term. The diffusion term requires additional corrector terms [145] and other approaches deal with the source and unsteady terms.[134] Each term of the transport equations is discretized and placed in a matrix of coefficients, either in the matrix $\boldsymbol{M}$, for implicit terms (i.e., their value depends on other variables in the current time step) or they are added to the matrix $\boldsymbol{B}$ for explicit terms (those that are independent of other variables in the current time step). The entire process comprises solving Equation 2.9 with the matrix $\boldsymbol{U}$, the matrix for the velocity terms:[143, 146]

$$\boldsymbol{M} \cdot \boldsymbol{U} = \boldsymbol{B} \tag{2.9}$$

This equation is solved iteratively starting from an initial condition input. The solver evaluates the equation, calculates the errors on the estimate, makes a new estimate, and repeats until the errors fall below a used – defined threshold, which is further explained below.

Examples of FVM-CFD software packages are OpenFOAM, [135] Ansys Fluent, [147] and Star CCM; [148] the latter two are commercial FVM-CFD software packages.

An example of an iterative process is the pressure-velocity coupling, a solution method used mostly for incompressible flows. In this method a system of four equations is iteratively solved until the pressure and velocity both satisfy a "user-defined threshold":

- $\boldsymbol{M} \cdot \boldsymbol{U} = -\nabla \mathcal{P}$
- $\boldsymbol{H} = \boldsymbol{AU} - \boldsymbol{MU}$
- $\nabla(\boldsymbol{A}^{-1} \nabla \mathcal{P}) = \nabla(\boldsymbol{A}^{-1} \boldsymbol{H})$
- $\boldsymbol{U} = \boldsymbol{A}^{-1} \boldsymbol{H} - \boldsymbol{A}^{-1} \nabla \mathcal{P}$

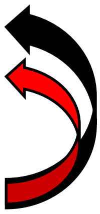

This system can be solved in two methods, either via the black arrow, which denotes the Semi-Implicit Method for Pressure-Linked equations algorithm (SIMPLE). [149] This system is mostly used for steady-state simulations. The red arrow shows the Pressure Implicit Splitting of Operators (PISO) loop; [150] this algorithm is mostly used for transient cases. The momentum predictor step is only solved once, which speeds up the simulation but for accurate solutions, a limiter is needed on the size of the time step. This limiter is known as the Courant, Friederichs, and Lewy condition or the CFL-number, Co.[151]

$$Co = \frac{\Delta t \cdot U}{\Delta x} \tag{2.10}$$

This condition ensures that the fluid travels less than the distance of one cell during each time step (leak-forward diffusion). [152]

In the field of CFD, the term "user-defined threshold", mentioned above, is often referred to as the residual and it is one of the key parameters to monitor in order to confirm that the simulation is running smoothly. Residual values are calculated for each of the transport variables in the simulation, and they are based on the principle of conservation from Equation 2.6, which makes the residual a scalar field within the simulation domain. Ideally, the deviation between the flux into a cell equals the flux outwards, so the residual equals zero. Most CFD codes use a representative residual to assess convergence and provide plots of residual versus the number of iterations. The residuals in the plot should decrease until they reach a steady level. When the value of the residual drops below the threshold set by the user this indicates the program has converged on a solution. It should be stressed that converged residuals are only one metric to assess the coherency of the solution. Another criterion to consider is the conservation of the transport properties over the mesh, referred to as the global imbalance. If the global imbalance is small, this means that the quantity is preserved within the complete computational domain. Other qualitative approaches to assess the simulation convergence include the minimum and maximum values of transport properties and point or line monitors within the mesh. [146] These qualitative approaches require a certain knowledge of the system beforehand, to check whether or not the maximum value is realistic.

2.3 The OpenFOAM Case Structure

To set up a simulation case in OpenFOAM requires various folders, shown on Figure 2A,here the blue text represents files, green text the folders. The three main folders are *0*, *constant*, and *system*. The *0* folder contains all the information regarding the initial and boundary conditions for temperature, velocity, pressure, turbulence parameters, and chemical species. [153] It is advised to always modify an existing (tutorial) simulation case to s rather than preparing this file from scratch. As a simulation runs, new time folders are written with the same structure as the *0* folder, i.e., containing files for every variable calculated but named with the selected *write time* in the simulation settings, e.g., folder 10 for the result after 10 seconds in the case of transient simulations. The *constant* folder contains i) the chemical species thermophysical properties, ii) chemical reactions along with their reaction rates (as well as how to model the interaction between chemistry and the fluid flow), iii) the fluid properties such as the turbulence model if required, located in the *momentumTransport* file, and iv) the mesh either imported or defined by the user, which is stored in the *polyMesh* folder. In the *system* folder, the user specifies the parameters needed for the solution, including simulation settings, discretization schemes, and solvers. The *controlDict* file has the time step, the write step, start and end times, and run-time post-processing requirements, using custom-built or built-in functions, e.g., for residuals, forces, or streamlines. In addition, the *system* folder contains the *blockMeshDict* in which the parameters required for the mesh generation are specified. The meshing tool provided with OpenFOAM is *blockMesh*, which generates the *polyMesh* file in the *constant* folder.

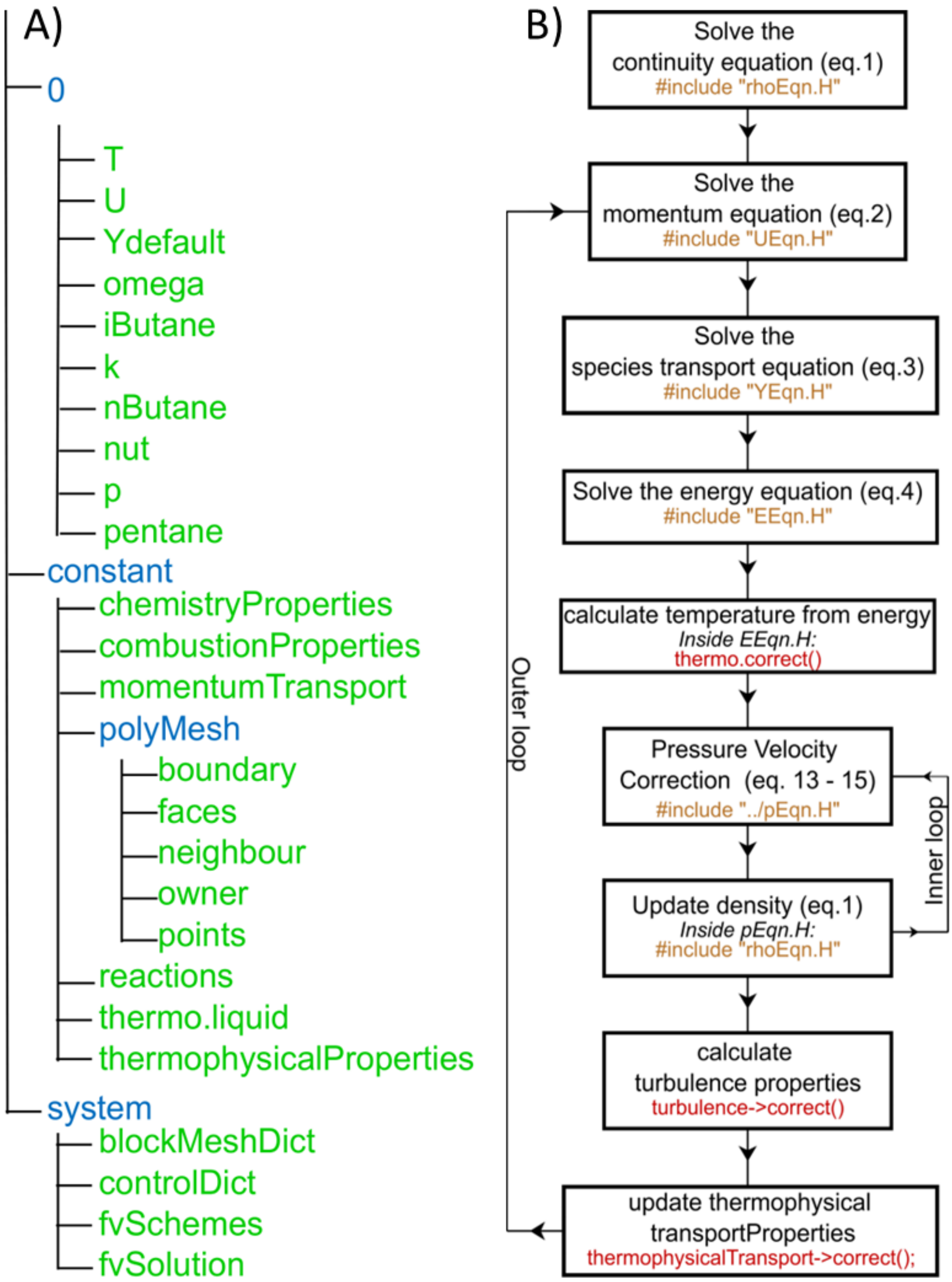
A)
0
T
U
Ydefault
omega
iButane
k
nButane
nut
p
pentane
constant
chemistryProperties
combustionProperties
momentumTransport
polyMesh
boundary
faces
neighbour
owner
points
reactions
thermo.liquid
thermophysicalProperties
system
blockMeshDict
controlDict
fvSchemes
fvSolution
B)
Solve the continuity equation (eq.1)
#include "rhoEqn.H"
Solve the momentum equation (eq.2)
#include "UEqn.H"
Solve the species transport equation (eq.3)
#include "YEqn.H"
Solve the energy equation (eq.4)
#include "EEqn.H"
calculate temperature from energy
Inside EEqn.H:
thermo.correct()
Pressure Velocity Correction (eq. 13 - 15)
#include "../pEqn.H"
Update density (eq.1)
Inside pEqn.H:
#include "rhoEqn.H"
calculate turbulence properties
turbulence->correct()
update thermophysical transportProperties
thermophysicalTransport->correct();
Outer loop
Inner loop

Figure 2-2 A) Structure for the OpenFOAM case of the PFR model B) Solution algorithm for one time step of the rhoReactionFoam solver.

2.4 Proposed Workflow

2.4.1 Problem Statement

The first step in a CFD study is to establish the goal and select the required information to be extracted, to keep the runtime of the simulation and the required storage as low as possible. I demonstrate the workflow of a CFD problem by the liquid phase adiabatic isomerization of n-butane in 90 % n-pentane at 2 MPa. [154] Since the reaction only requires a trace amount of catalyst, it is assumed the liquid phase is homogeneous. The reaction is first-order, and the rate constant is 31.1 h^{-1} at 360 K with an activation energy of 65.7 kJ · mol^{-1}. The equilibrium constant, K_c, equals 3.03 at 373 K.

$$r = k\left(c_{n_{C_4}} - \frac{c_{i_{C_4}}}{K_c}\right) \tag{2.11}$$

The conventional 1D plug flow model was first solved with MATLAB R2019a with the Runge-Kutta method and a variable time step ($ode45$), which provided a baseline to compare results from the CFD simulations, seen on Figure 2-3. I also tested an irregular-shaped tube to test the simulation. Indeed, the ideal plug flow design equation is independent of the reactor shape (c.f. Fogler's "Picasso" reactor). [154] The irregular reactor, tested in this work, consists of a tube with a sudden expansion, immediately followed by a contraction, this is a notched reactor, which is shown on Figure 2-5C. This geometry represents an exaggerated case of coupling between two tubes with a tight joint to illustrate the expansion–contraction effect on n-butane conversion.

2.4.2 One Dimensional Model

In the case of the conventional 1D model, the resolution boils down to the coupled mass Equation 2.12 and energy balances Equation 2.13. The momentum balance is excluded since the reaction rate is independent of pressure for a constant density liquid-phase reaction.

$$\frac{\partial c_i}{\partial t} = -\frac{\partial (u_z c_i)}{\partial z} + \mathcal{R}_i \tag{2.12}$$

The energy balance reduces to a linear relationship between the conversion of n-butane, and the reactor temperature, neglecting the temperature dependency on the heat capacity, as well as the temperature correction for the enthalpy of reaction.

$$T = T_0 - \frac{X\Delta H}{C_{p_{nC_4}} + \Theta_{nC_4} Cp_{iC_4} + \Theta_{C_5} C_p C_5} \tag{2.13}$$

2.4.3 Model and Solver Selection

CFD packages, and OpenFOAM especially, come with various codes to solve different types of problems. A package of CFD codes that solves a specific task is called a solver: simple solvers treat single-phase, isothermal, and incompressible flows while advanced solvers handle problems related to heat transfer, multi-phase flow, and chemical reactions. [155] Since a constant density chemical reaction in the liquid phase was assumed, the $rhoReactingFoam$ solver was selected, which solves the equations of continuity, momentum, species conservation, and energy sequentially, see equations 2.1 - 2.4. The solution algorithm for these equations is shown on Figure 2-2B. The solution algorithm starts with the continuity equation, solved prior to entering in the outer loop. The outer loop then starts with the momentum equation 2.2, followed by the species transport equation, 2.3 and the energy equation, 2.4. The energy equation is solved considering enthalpy or internal energy (the former here), and the temperature is derived from:

$$C_p = \left[\frac{dH}{dT}\right]_p \tag{2.14}$$

The solution algorithm then enters in the inner loop, which consists of solving the pressure–velocity coupling and the continuity equation. After the solver has completed a user-defined number of inner iterations, the turbulence parameters are calculated and the numerical values of D_{eff} and α_{eff} are updated to account for the turbulence: The effective diffusivity of each species is the sum of the molecular and turbulence diffusivity (ratio of the molecular viscosity and density and that of the turbulent kinematic viscosity and the Schmidt number, N_{Sc}, respectively). As a final step, ρ, C_p and κ are updated. The solution algorithm finally returns to the momentum equation and iterates over this outer loop a user-defined number of times. Once the number of programmed iterations is reached (or the accuracy is reached), the time step is updated, and the solution algorithm repeats until the final time step.

2.5 Solved Example

2.5.1 Problem Statement

A good practice for chemical reactions is to first check the kinetic expressions in a simplified simulation case. This minimizes the risks of dimensional errors. OpenFOAM requires mass – based reaction rates and thermo-physical properties, where conventional chemical engineering approaches favour mole – based values. Table 2-1 lists the boundary conditions for the OpenFOAM model. The physical interpretation of the boundary conditions are here self-explanatory (e.g., “fixedValue”, or “zeroGradient”), except for the pressure, where I used a “fixedFluxPressure” boundary conditions, allowing to calculate the pressure gradient based on velocity. The results from both simulations agree well with only a $0.14\ \%$ difference in i-

butane mass fraction at the outlet and $0.007\ \mathrm{K}$ difference for temperature, which can be seen on Figure 2-3.

Table 2-1 Boundary conditions for the 1D model provided in the context of their implementation in OpenFOAM.

	U (m s^{-1})	p (Pa)	T (K)	Species (g g^{-1})
Inlet	Fixed-Value	Fixed-Flux-Pressure	Fixed-Value	Fixed-Value
Outlet	Zero-Gradient	Fixed-Value	Zero-Gradient	Fixed-Value
defaultFaces	Empty	Empty	Empty	Empty

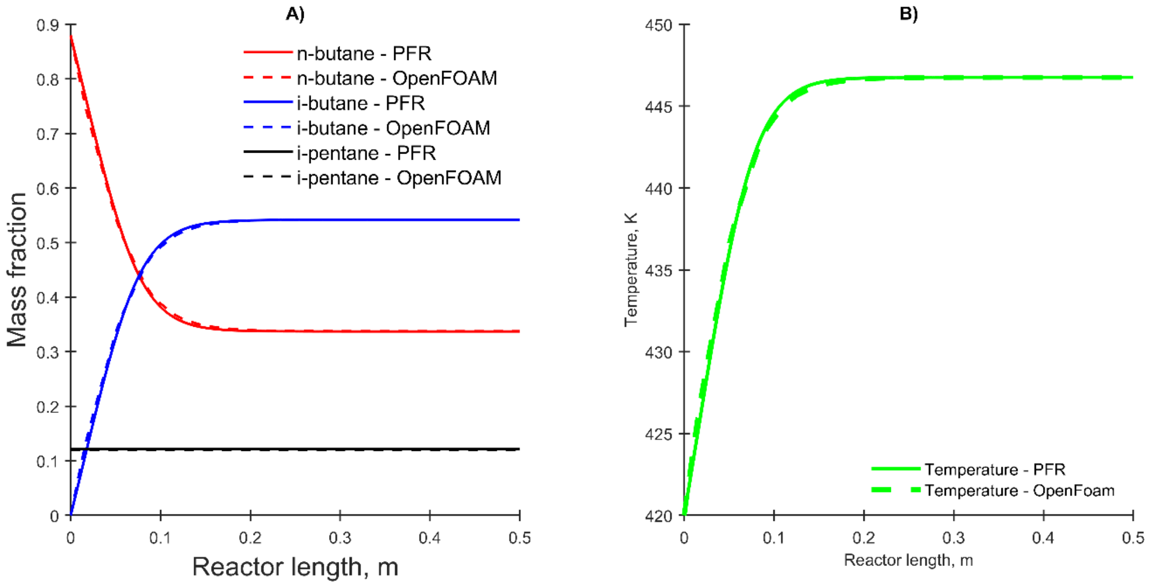

*Figure 2-3 A) Mass fraction of n-*butane, *i-*isobutane and *i-*pentane over the length of the reactor, plotted for the 1D model obtained with MATLAB and via a 1D simulation in OpenFOAM. B) Temperature profile over the length of the reactor plotted for the 1D models obtained via MATLAB and OpenFOAM.

With this confirmation, I demonstrated that the kinetic model was correctly implemented which is a first step in verification of the CFD code. Then I built the conventional and irregular-shaped geometries in the form of 5° wedges along the length of the reactor. This wedge shape is a simplification of the tubular shape of the reactors that accelerates the simulation by making use of azimuthal symmetry about the longitudinal axis of the tube. When setting up the CFD simulation, one must select between laminar and turbulent flow regimes. Erroneously selecting a laminar regime for high Reynolds number flows or clearly non-laminar flows produces artefacts and oscillations in the residuals. Turbulence modelling is a field on its own [156] and a plethora of models exist, each with its strengths and weaknesses. For the example case, I used the Reynolds averaged Navier–Stokes (RANS) approach. [157] The Reynolds Averaging approach is based on splitting the calculation of any variable ϕ into a mean component $\bar{\phi}$ and a fluctuating component ϕ'. For a given time, t and position x. This yields:

$$\phi(\boldsymbol{x},t) = \bar{\phi}(\boldsymbol{x},t) + \phi'(\boldsymbol{x},t) \tag{2.15}$$

Most commonly, a time averaging operation is used to calculate $\bar{\phi}$. Using Reynolds Averaging, the governing equations for mass, momentum and energy change to equations 2.16, 2.17 and 2.18, respectively:

$$\nabla \cdot [\rho \bar{\boldsymbol{U}}] = 0 \tag{2.16}$$

$$\frac{\partial(\rho\bar{\boldsymbol{U}})}{\partial t} + \nabla \cdot (\rho\bar{\boldsymbol{U}}\bar{\boldsymbol{U}}) = -\nabla\bar{p} + [\nabla \cdot (\bar{\boldsymbol{\tau}} - \rho\overline{\boldsymbol{U}\boldsymbol{U}}] + \bar{\boldsymbol{Q}}_{\boldsymbol{U}} \tag{2.17}$$

$$\frac{\partial\left[\rho C_p \bar{T}\right]}{\partial t} + \nabla \cdot \left(\rho C_p \bar{\boldsymbol{U}}\bar{T}\right) = \nabla \cdot \left[\kappa\nabla\bar{T} - \rho C_p \overline{\boldsymbol{U}'T'}\right] + \bar{Q}_{\boldsymbol{R}} \tag{2.18}$$

The Reynolds Averaging approach introduces a new term $-\rho\overline{\boldsymbol{U}\boldsymbol{U}}$ in the continuity equation (2.17) and a term $-\rho C_p \overline{\boldsymbol{U}'T'}$ in the energy equation (2.18). This first term is called the *Reynolds Stress Tensor* and it is symbolized by $\boldsymbol{\tau}^{\boldsymbol{R}}$**.** This tensor introduces six new unknowns in equation 2.17. The turbulent heat flux term, newly introduced from the Reynolds Averaging procedure, is symbolized by $\boldsymbol{q}^{\boldsymbol{R}}$ and introduces three new unknowns in equation 2.18. Both $\boldsymbol{\tau}^{\boldsymbol{R}}$ and $\boldsymbol{Q}^{\boldsymbol{R}}$ are shown in equation 2.19.

$$\boldsymbol{\tau}^{\boldsymbol{r}} = -\rho \begin{pmatrix} \overline{u'u'} & \overline{u'v'} & \overline{u'w'} \\ \overline{u'v'} & \overline{v'v'} & \overline{v'w'} \\ \overline{u'w'} & \overline{v'w'} & \overline{w'w'} \end{pmatrix} \quad \boldsymbol{q}^{\boldsymbol{R}} = -\rho C_p \begin{bmatrix} \overline{u'T} \\ \overline{v'T} \\ \overline{w'T} \end{bmatrix} \tag{2.19}$$

To solve these equations the Boussinesq hypothesis is introduced, which assumes that the Reynolds stress is a linear function of the mean velocity gradient. The Reynolds Stress Tensor can then be rewritten as:

$$\boldsymbol{\tau}^{\boldsymbol{R}} = -\rho\overline{\boldsymbol{U}\boldsymbol{U}} = \mu_t[\,\nabla\bar{\boldsymbol{U}} + \nabla(\bar{\boldsymbol{U}})^T] - \frac{2}{3}[\rho k + \mu_t(\nabla \cdot \bar{\boldsymbol{U}})]\boldsymbol{I} \tag{2.20}$$

This equation introduces two key variables to model the turbulent behaviour of the flow. The turbulent kinetic energy, k and the turbulent viscosity, μ_t which is a measure for the turbulence induced resistance of the fluid against the flow. In contrast to the molecular viscosity, this is not a property of the fluid but a property of the flow, which has to be modelled. The turbulent kinetic energy, k, is expressed as equation 2.21. In equation 2.20, k will be multiplied with ρ which expresses the overall term in energy per unit of volume:

$$k = \frac{1}{2}\,\overline{\boldsymbol{U'} \cdot \boldsymbol{U'}} \tag{2.21}$$

RANS based turbulence models are based on expressing the turbulent viscosity in relation to the turbulent kinetic energy. A similar derivation is made for the turbulent heat fluxes where the turbulent thermal diffusivity (α_t) is introduced:

$$\boldsymbol{q^R} = -\rho C_p \overline{\boldsymbol{U'}}\overline{T'} = \alpha_t \nabla \overline{T} \tag{2.22}$$

In general RANS models provide a relation between the turbulent viscosity and the turbulent kinetic energy, for the case studied in this chapter, I focused on the use of the k – ω SST model, which is an example of a two – equation model. These two – equation models require an equation for the turbulence kinetic energy, k and one for either the specific dissipation rate (ϵ), or the dissipation frequency (ω). These later terms can be used interchangeably in different models since they can be expressed by the following relation:

$$\omega = \rho \frac{\epsilon}{C_\mu k} \tag{2.23}$$

With C_μ a model constant, typically set at 0.09. The interchangeability of the variables ϵ and ω is used in the $k - \omega$ shear stress transport (SST) model, which is a blended turbulence model with higher accuracy than either the k - ϵ model or the k - ω model from which it is derived. [158] It is especially suited for flows that detach from walls, which is the case in the notched reactor. The $k - \omega$ SST model adds two additional transport equations to be solved by the CFD software, one for k, and one for ω.

$$\frac{\partial \rho k}{\partial t} + \nabla \cdot (\rho \boldsymbol{U} k) = \nabla\left(\mu_{eff_k} \nabla k\right) + G_k - \beta^* \rho k \omega \tag{2.24}$$

$$\frac{\partial \rho \omega}{\partial t} + \nabla \cdot (\rho \boldsymbol{U} \omega) = \nabla\left(\mu_{eff_\omega} \nabla \omega\right) + C_{\alpha_{SST}} \frac{\omega}{k} G_k - C_{\beta_{SST}} \rho \omega^2 + 2(1 - F_1)\sigma_{\omega 2} \frac{\rho}{\omega} \nabla k \cdot \nabla \omega \tag{2.25}$$

With G_k representing the generation of turbulent energy which is represented by:

$$G_k = \boldsymbol{\tau}^{\boldsymbol{R}} \overline{\frac{\partial u_j}{\partial x_i}} \tag{2.26}$$

The terms μ_{eff_k} and μ_{eff_ω} are respectively calculated by:

$$\mu_{eff_k} = \mu + \frac{\mu_t}{\sigma_k} \tag{2.27}$$

$$\mu_{eff_\omega} = \mu + \frac{\mu_t}{\sigma_\omega} \tag{2.28}$$

The model coefficients, $C_{\alpha_{SST}}, C_{\beta_{SST}}, \sigma_k, \sigma_\omega$ are blended version of the model coefficients used in the k – ϵ and k – ω models. The blending of these models is evaluated using the blending factor F_1. The values used for the model coefficients of the unblended functions can be found in [159], the blending procedure in [158]. For $\sigma_{\omega 2}$, in equation 2.25, OpenFOAM uses a value of 0.856 by default. From the results of equations 2.24 and 2.25, the turbulent viscosity can be calculated, by using equation 2.29. This equation includes another blending function, using F_2, the distance to the wall and the vorticity, Ω, where its value is given by $k \,/\, \omega$, except in an adverse pressure gradient where the dissipation of turbulent kinetic energy is greater than its dissipation rate. The coefficient a_1 is set as 0.31 in OpenFOAM.

$$\mu_{tr} = \frac{\rho a_1 k}{\max(a_1 \omega, \Omega F_2)} \tag{2.29}$$

2.5.2 Geometry and Meshing

Once the problem of interest has been clearly defined, the geometry has to be established and the mesh has to be created. Meshing is often one of the most time-consuming steps in a project. A high-quality mesh improves stability and accuracy. Meshing discretizes the design space into cells connected via their cell faces to the neighbouring cells. The FVM is constructed in such a way that each cell should have 1 neighbouring cell per cell face (except for the cells near the boundaries). [134] Structured meshes have a logical indexing structure and each cell has an index (i, j, and z) and its next neighbour will have (i+1, y+1, and z+1). This makes numerical interpretation of the cell indices easy. For unstructured meshes, two adjacent cells do not necessarily have the same index, and this numerical interpretation has to be taken into account in the solver. In practice, the structured meshes tend to consist of the same cell type (in most cases hexahedral cells), unstructured meshes can consist of a wide collection of cell types with different polyhedral shapes. OpenFOAM has integrated automated meshing codes for both structured (blockMesh) [160] and unstructured meshes (snappyHexMesh). [161] SALOME, [162] Pointwise, and ANSYS - Fluent have open-source and commercial software packages to generate meshes.

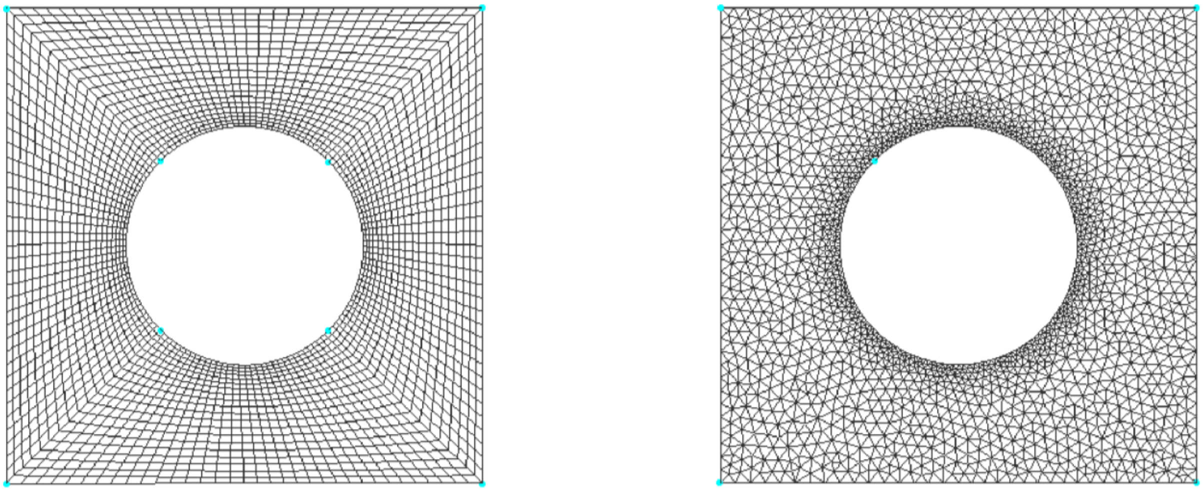

Figure 2-4 Structured (left) and unstructured (right) meshes. The structured mesh shows a logical ordering of cells where the unstructured mesh does not.

2.5.2.1 Mesh Quality

The mesh is a collection of the cells in the design space. However, not all meshes are equally suited for CFD, and before the start of the simulation, the quality of the mesh, which depends on the quality of the individual cells, should be checked. Much like the strength of a chain depends on the weakest link, the quality of a mesh is defined by the cell with the lowest quality. The four metrics for mesh quality are: aspect ratio, skewness, orthogonality, and smoothness. [163]

2.5.2.2 Example Meshes

Three distinct meshes were created for the example cases (Figure 2-5):

A. A coarse 1D structured mesh with an inlet and outlet boundary condition to confirm the chemical rate equations was correctly implemented. All other faces are defined using the OpenFOAM-specific type boundary *empty*, representing dimensions of the flow where no solution is required.

B. The tubular reactor mesh is constructed as a 5° wedge of a tubular reactor with a 0.1 m height and a 0.5 m diameter. The simplification is due to the azimuthal symmetry of the reactor.[164]

C. The mesh represents the notched reactor and is designed to ensure that the total volume of the reactor was the same as the conventional tubular reactor (Figure 2-5B). This shape illustrates that CFD simulations apply to variable geometries for which a PFR model is inapplicable. [165]

All of these meshes are structured meshes created with the blockMesh utility in OpenFOAM.

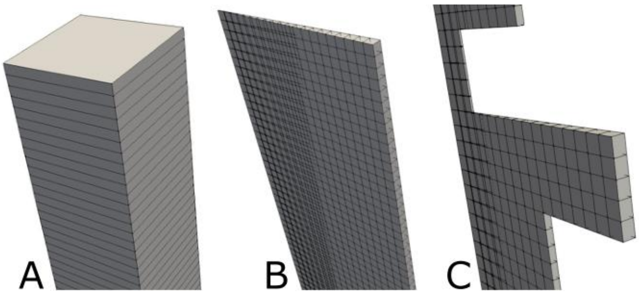

Figure 2-5 Meshes for example case: A) 1D mesh, B) wedge shape mesh of the conventional tubular reactor, and C) wedge shape of the unconventional notched reactor.

2.5.3 Tubular Reactor in OpenFOAM

The boundary conditions to simulate the tubular reactor with FVM-CFD can be found in Table 2-2. The turbulent boundary conditions, *TurbulentIntensityKineticEnergyInlet* and *TurbulentMixingLenghtFrequencyInlet* relate to turbulence model-specific boundary conditions and only require as entries the intensity of turbulence for the former and the mixing length, for the latter. The value for the intensity (I) is usually between 2 and 5 % and the mixing length, (L) is calculated as the hydraulic diameter multiplied with 0.007. The turbulence intensity at the inlet is estimated as:

$$k = 1.5(IU_0)^2 \tag{2.30}$$

The numerical value of the turbulent specific dissipation is calculated from the turbulent kinetic energy using:

$$\omega = \frac{k^{1/2}}{L} \tag{2.31}$$

- *zeroGradient*: The normal gradient of the selected variables is fixed at zero so the values at the boundaries are calculated.
- *InletOutlet*: A mixed boundary condition to prevent fluid re-entering through the face by using the $zeroGradient$ when fluid flows out of the domain and a $fixedValue$ (here, set to 0), when the fluid flows into the domain. This approach is used to disable any backflow into the computational domain.
- Wall functions (applied here to both k and ω): Empirically derived functions to simulate the flow near the wall. No input from the user is required.

Table 2-2 Boundary conditions for the wedge geometry and notched geometry simulations in OpenFOAM

	U (m s^{-1})	p (Pa)	T (K)	Species (g g^{-1})	k (m^2 s^{-2})	ω (s^{-1})
Inlet	Fixed-Value (0 0 26)	Fixed-Flux-Pressure	Fixed-Value 420	Fixed-Value *n*-butane (0.88)	Turbulent-intensity-kinetic-energy-inlet	Turbulent-Mixing-Length-Frequency-Inlet
Outlet	Zero-Gradient	Fixed-Value	Zero-Gradient	Fixed-Value	Inlet-outlet	Inlet-outlet
Walls	NoSlip	Fixed-Flux-p	Zero-Gradient	Empty	kqrWallFunction	OmegaWallFunction

I ran the simulations with second-order accuracy in space from the beginning since the meshes required for the example problem were simple. The PISO algorithm was used to reach the solution of the simulation seen on Figure 2-6. I used three inner correctors for the pressure correction and zero non-orthogonal correctors, since a highly orthogonal mesh was used. The simulation results agree with the PFR model obtained from MATLAB, which was expected due to the tubular geometry and high Reynolds number. For increasing Reynolds number, turbulent flow velocity profiles approach a plug flow profile. The main differences can be attributed to the no-slip conditions at the wall. This example shows that the CFD simulation accurately predicts n-butane conversion to i-butane in a conventional reactor case, and so I assume that the physicochemical and reaction properties of the simulation case are correctly implemented. With this assumption, the cases for the notched reactor could be solved with a reasonable certainty.

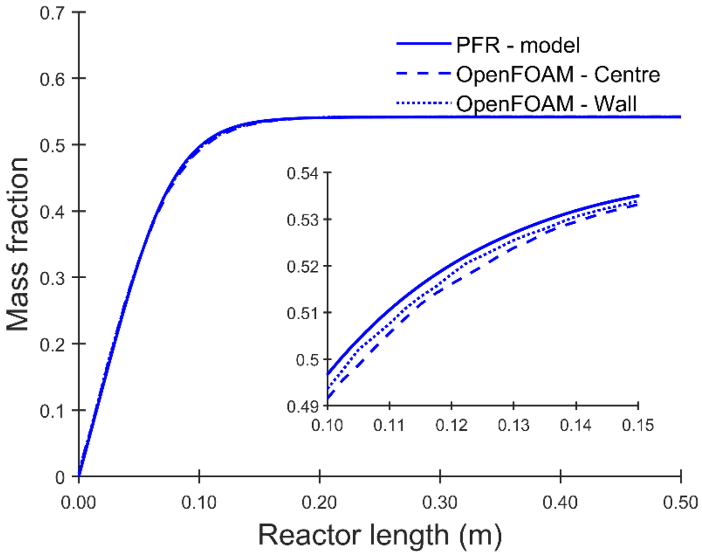

*Figure 2-6 Plot showing the mass fraction of i-*isobutane, comparing the results of the 1D PFR model solved in MATLAB with the result of the OpenFOAM simulation of the conventional tubular reactor shape, extracted from the centre and near the wall of the reactor.

2.5.4 Grid Refinement Study

CFD simulations heavily depend on the grid on which they are computed, to demonstrate this, I will first show the basic principles of a grid refinement study applied to the notched wedge reactor that I aimed to simulate in this example study. The grid refinement study applies a grid convergence index (GCI) to quantify the grid independence of the solution. The GCI applies the Richardson extrapolation to estimate the refinement error when comparing simulation solutions with distinct grid spacing. It was originally designed to estimate the results from any mesh refinement when a grid is doubled (r_f = 2). To quantify the GCI, one must simulate at least two but preferably three meshes, with an increasing number of cells. Then, a given quantity of interest is extracted from those simulations, i.e., temperature, pressure or concentration. Using this quantity of interest the GCI is then computed. [136] To illustrate the procedure, I extracted the temperature in the region after the expansion–contraction, where the flow is developed. The overall grid convergence process is as follows:

- Create three meshes with a set refinement ratio, that is, the number of points in a direction in the mesh. In the example, the refinement ratio was 2, which means that for the 2D mesh, there was a coarse mesh with 1000 cells, an intermediate mesh with 4000 cells, and a finer mesh with 16 000 cells, seen on Figure 2-7.

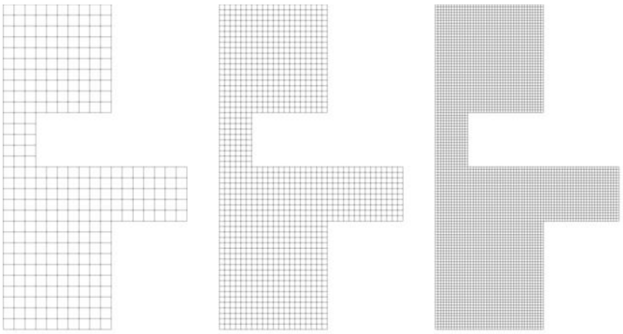

Figure 2-7 Mesh geometry for the grid refinement study: coarse grid (left), medium grid (middle), and fine grid (right)

- Simulate the system with the three meshes. To reduce simulation time for the finer meshes, I apply the results of a coarser mesh as initial conditions, since these inputs are closer to the expected value than best initial guesses. In OpenFOAM, the mapFields function completes this operation. [166]

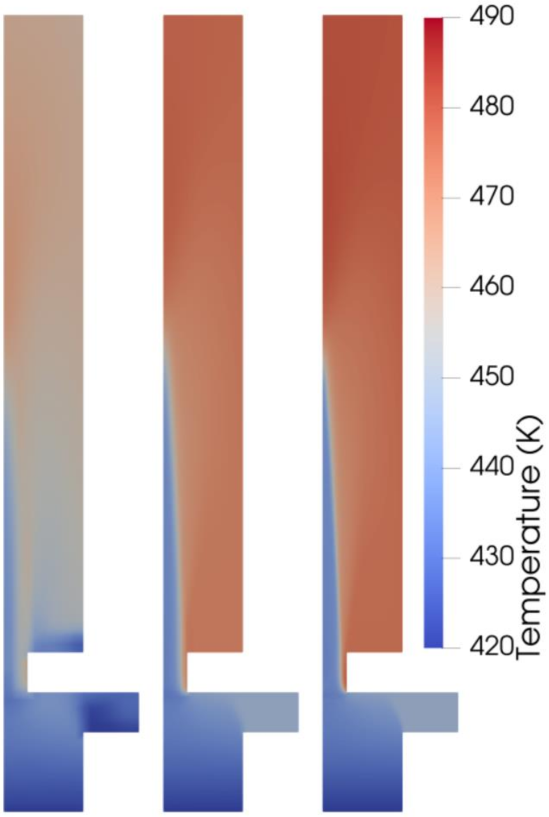

Figure 2-8 The temperature on the notched reactor for each of the three meshes used for the grid convergence study. Results are shown for the coarse grid (left)), the medium grid (middle), and the fine grid (right). Liquid flow is introduced from the bottom of the reactor.

- The temperature from the same location from each of the three meshes was extracted to compute the GCI: the probe point was placed 0.35 m in the axial direction and 0.0075 m in the radial direction (Table 2-3). From these data, the real order of convergence can be computed, which is different from the theoretical order of convergence ($r_f = 2$ in this case) due to stretching and non-linearity in the solution. The calculated order of convergence is obtained by using Equation 2.32. The simulated temperature profiles along the axis of the notched reactor for the three resulting meshes are presented in Figure 2-9.

$$p = \frac{\ln\left(\frac{\Delta T_{coarse} - \Delta \mathrm{T}_{med}}{\Delta T_{med} - \Delta T_{fine}}\right)}{\ln r_f} = \frac{\ln\left(\frac{45.9 - 55.4}{55.4 - 59.5}\right)}{\ln 2} = 1.19 \tag{2.32}$$

- The next step is to calculate the temperature at a grid with zero spacing, that is, a theoretically infinitely fine grid, based on a Richardson extrapolation.

$$T_\infty = \Delta T_{fine} + \frac{\Delta T_{fine} - \Delta T_{med}}{r_f^p - 1} = 59.5 + \frac{59.5 - 55.4}{2^{1.19} - 1} = 62.7 \tag{2.33}$$

- After the extrapolation step, the GCI is calculated between two grids: GCI_{12} considers the change from grid 1 to 2 and GCI_{23} from grid 2 to 3. A safety factor, F_s = 1.25 was applied, for a grid independence study using three meshes and a higher value if only two are used grid study. [167]

$$GCI_{12} = F_s \cdot \frac{|\delta_{12}|}{r_f^p - 1} = 1.25 \cdot \frac{\left|\frac{59.5 - 55.4}{59.5}\right|}{2^{1.19} - 1} = 0.07 \tag{2.34}$$

$$GCI_{23} = F_s \cdot \frac{|\delta_{23}|}{r_f^p - 1} = 1.25 \cdot \frac{\left|\frac{55.4 - 45.9}{55.4}\right|}{2^{1.19} - 1} = 0.16 \tag{2.35}$$

- To check if the GCI study was successful the two values obtain for GCI_{12} and GCI_{23} are compared to each other via equation 2.36. The result should approximate 1.

$$r_f^p \frac{GCI_{12}}{GCI_{23}} = \frac{2^{1.19} 0.07}{0.16} = 1.07 \cong 1 \tag{2.36}$$

- Finally, it can be stated that the temperature at the probe point in the mesh equals 420.0 K + 62.7 K = 482.7 K and the error with respect to the temperature rise (63 °C) (ΔT_∞ -ΔT_{in}) is 7 %. The fine mesh and intermediate mesh temperature profiles are similar while the coarse mesh is noticeably cooler, see Figure 2-9. I conclude that the fine mesh is sufficient to extract quantitative data from the simulation, as the simulated temperature is within the 7 % error of the Richardson extrapolation. I also want to highlight that even though the simulation on the coarse mesh converged nicely, the errors induced from the mesh were quite high.

Table 2-3 Data for the grid independence study on the temperature probe point

Grid	N_{cells}	Normalized Grid Spacing	ΔT (K)
Coarse	1 000	4	45.9
Medium	4 000	2	55.4
Fine	16 000	1	59.5

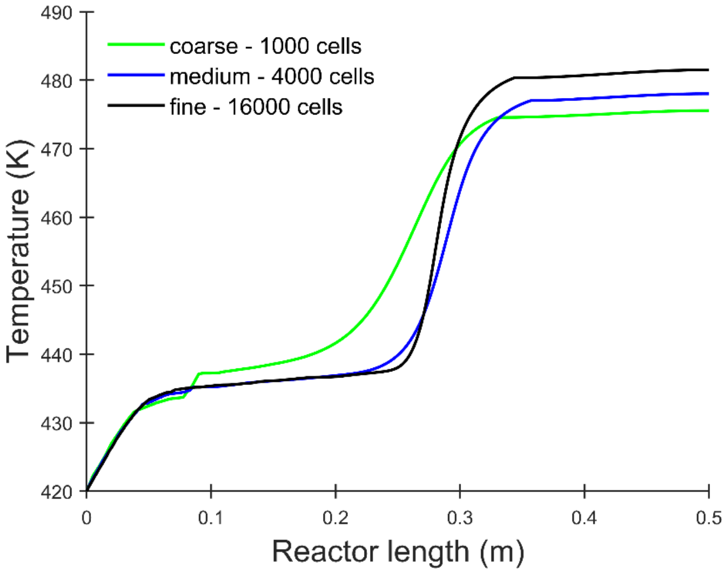

Figure 2-9 Temperature profile over the length of the reactor shown for the coarse, medium and fine grid.

As a final note, the GCI method for grid convergence identifies numerical errors on a grid. I only illustrated the procedure using a simple example at one temperature at a singular point in the mesh. However, complete datasets can be used to check the GCI, for instance, using the data extracted over a line in the mesh. [168] After performing a grid refinement study, the CFD engineer should make a choice on accuracy versus time. The finer the grid, the more accurate the solution tends to be, but, on the other hand, the computational time for the simulation will increase. In this example, I used a single Intel Core i7 (8th gen) processor, and the wall time to obtain the results with the coarse mesh took 392 s, 1296 s for the intermediate mesh, and 6772 s for the fine mesh, for only 0.2 s of simulated time. Using maximal Co – numbers of 1 for each of the cases, see equation 2.10.

The reported clock times are very short (simple homogeneous reaction) and highlights the effect of simulation using 5° wedge geometries. For more complex cases (e.g., multiphase turbulent reacting flows), the clock time can exceed weeks, even considering parallel computing. It is also worth checking which areas of the mesh need additional refinement to reach grid convergence, as not all areas of a geometry tend towards convergence at the same pace. [169] Sometimes, the GCI is not reported, and authors use a less rigorous approach. For example, grids with increasing refinement are used until there is no longer a change in the value of interest. [170, 171] This is a valid, qualitative approach to reduce grid-related numerical errors, and offers an alternative to the quantitative GCI procedure.

2.5.5 Notched Reactor

The simulation results for the notched reactor can be seen on Figure 2-10, which shows the results after 0.2 s, for the pressure, the velocity magnitude and the mass fraction of *i*-butane. It can be clearly seen that the presence of the notch influences the flow within the reactor. The narrow passage through which the reactive mixture has to pass, increases the pressure before the notch. Naturally, this affects the velocity of the flow which increases more than tenfold compared to the inlet velocity of 26 m s^{-1}. In the wider region before the notch, there is a high conversion to *i*-butane, the products formed in this region seem to be trapped there, due to the geometry. It is clear that the notch induces a radial gradient, the flow direction, which makes the standard 1D models unfit for to describe this reactor. This highlights the importance of CFD simulations for unconventional reactor types.

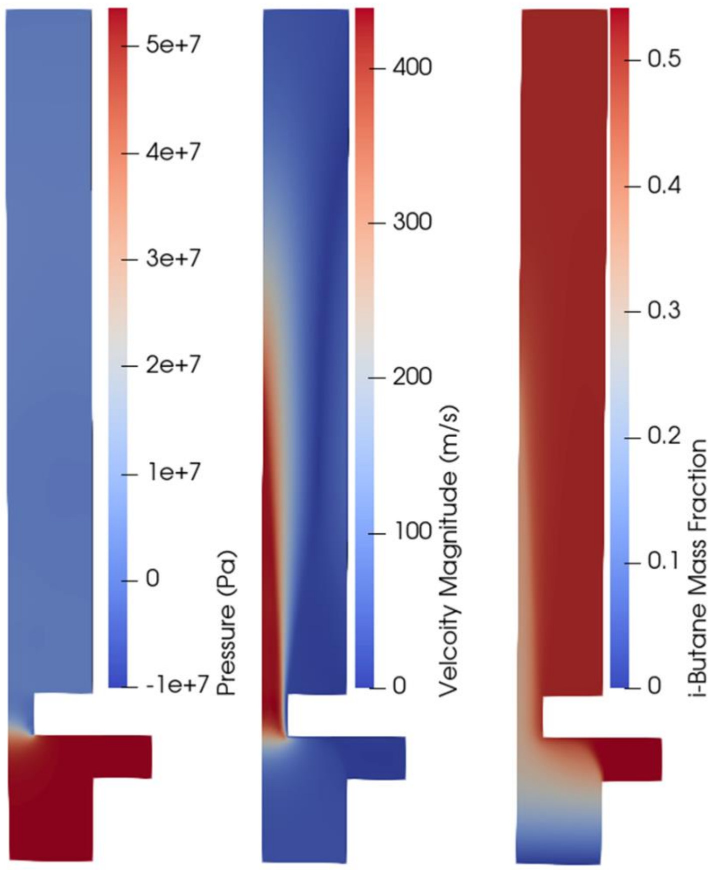

Figure 2-10 Results from the simulation of the notched reactor showing (from left to right) the pressure (in Pa), the velocity (in m s^{-1}), and the mass fraction of i-butane. The direction of the flow goes from bottom to top.

The difference between the 1D – PFR model and the simulation is further highlighted by Figure 2-11, which shows the difference in mass fraction obtained from the notched reactor compared to what would be expected via the PFR model. In the notched reactor, the steady state is achieved further in the reactor and conversion of *n*-butane to *i*-butane is lower than in the ideal case. To achieve these results for this non-conventional reactor, a two-step verification approach was used. Both the implementation of the kinetic model via a 1D approach and the implementation of the flow properties via a 2D simulation, including turbulence were verified. The error on the grid was reduced by relying on the GCI – approach. Nevertheless, this does not guarantee that the simulation results will completely correspond to experimentally obtained values. CFD results in general should preferably be corroborated by experimental validation. CFD is a highly useful tool in the early design stages of new reactors, to show expected trends in the flow behaviour, but it is not yet sufficiently accurate to be 100 % correct.

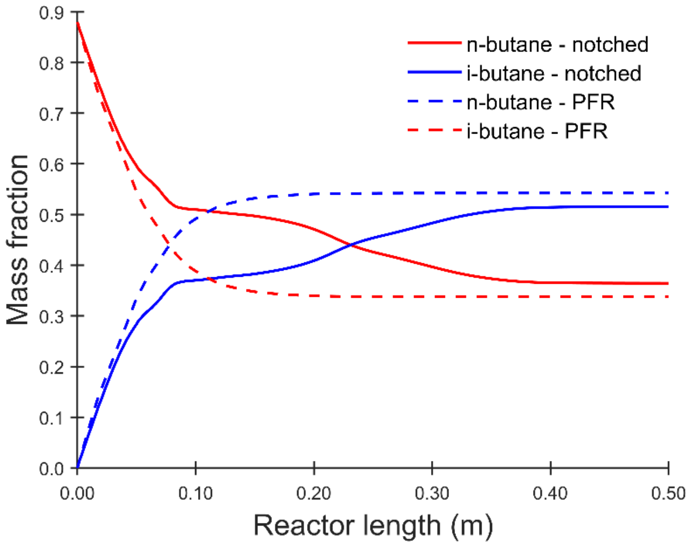

Figure 2-11 mass fractions of n-butane and i-butane extracted over the length of the notched reactor at radial distance of 0.006 m.

2.6 Challenges with heterogenous catalytic reactions

In this example, a simple reaction was shown where the presence of the catalyst is ignored and the liquid phase is treated as homogenous. This served as an intermediate step in the development of a reactive CFD implementation for $H_{18}DBT$ dehydrogenation, by analysing the basic implementation of the CFD code for chemical reactions. For the dehydrogenation of $H_{18}DBT$, more complex CFD code is required. The dehydrogenation reaction is a heterogeneously catalysed reaction, so the reaction only takes place when the liquid phase comes into contact with the catalyst. The catalyst phase has to be simulated in the context of the dehydrogenation reaction of $H_{18}DBT$ and the H_2 release in each cell of the mesh should be based on the local volume fraction of $H_{18}DBT$ and the catalyst. This is a different approach than used in this tutorial chapter. In the next two chapters, the use of multiphase simulations for three phase systems is introduced, in chapter 5, the first attempt for a novel CFD implementation for the dehydrogenation reaction is introduced. Due to the unavailability of intrinsic kinetics in literature, it was not possible to develop a CFD solver based on a kinetic approach. The CFD solver in chapter 5 is based on a curve fitting approach of available literature data from dehydrogenation experiments.

2.7 Conclusion

The aim of this chapter was to provide an overview into the basic principles of CFD. The mathematical basis of CFD was briefly highlighted. With this chapter I aimed to provide insights into the steps required to set-up a CFD study of a reactive system and provide a hands-on approach to setting up a simulation case in OpenFOAM. I showed the different verification steps required, prior to starting a CFD simulation for a new reactor type. Firstly, the implementation of the kinetic model was demonstrated by comparing it with the PFR model for the same reaction in an identical 1D system. This showed that the results obtained via the 1D CFD simulation closely matched those obtained from the PFR model. A next verification step was required to check the implementation of the flow characteristics, most importantly, the turbulence model. This was achieved by comparing the results of a 2D wedge shape of a tubular reactor with a 1D case, the influence of the wall effects were shown to be minimal, which was to be expected since the PFR model was designed for tubular reactors, with little radial variation. Thirdly, the influence of the computational grid was evaluated for three different grid sizes. This evaluation was simplified to illustrate the procedure and was thus only evaluated for a single point in the mesh. In reality, it is better to use the GCI approach on a larger dataset, extracted from the computational domain. After completion of the preliminary steps, a reactor could be simulated, whose geometry did not allow for the use of the PFR model. This was demonstrated by the change in mass fraction over the reactor length, comparing the conventional tubular reactor and the unconventional notched reactor. As a final remark, I would like to highlight that CFD simulations, especially for turbulent, multiphasic and/or reactive systems are not yet of such quality that they can be relied upon without additional experimental validation. With this introductory chapter, I have provided a procedure to develop new CFD codes and compare the implementation to simplified models. Future development of a CFD solver for H_{18}DBT dehydrogenation should best proceed via a similar procedure.

Chapter 3

Cold Flow Study on a Swirling Fluidized Bed Reactor for H_{18}DBT Dehydrogenation

Based on:

Laurens Van Hoecke, Nithin B. Kummamuru, Hesam Pourfallah, Sammy W. Verbruggen, Patrice Perreault, *Intensified swirling reactor for the dehydrogenation of LOHC, International Journal of Hydrogen Energy, 2024, 51, D, 611-623,*

DOI: https://doi.org/10.1016/j.ijhydene.2023.08.150

3.1 Introduction

In this chapter, the swirling fluidized bed (SFB) reactor will be introduced as a novel dehydrogenation reactor for H_{18}DBT. The SFB reactor was designed to use the principles of Process Intensification (PI) on the dehydrogenation of H_{18}DBT. PI is the strategy to reduce the size of chemical processing equipment while still maintaining high reactor output. For dehydrogenation systems, this is related to increasing the power density of the reactor, which is a measure for the power of the reactor related to the volume occupied by the entire system. Both the equipment and methods subdomains of PI proposed by Stankiewicz and Moulijn [172] are addressed by this system. The equipment subdomain is covered by the use this reactor, which was designed specifically with the dehydrogenation of H_{18}DBT in mind. The use of a Fluidized Bed (FB) reactor is a novel concept for the dehydrogenation of H_{18}DBT, and the main study of this thesis is based on the hypothesis that the H_2 release rate could be improved in fluidized bed systems. The concept of the SFB goes even further, by injecting the liquid in a swirling flow pattern into the reactor, the gas and particle phase will experience a centrifugal drag force which should aid in separation of the gas from the particle surface. [100] It was also hypothesised that the centrifugal flow field will also provide a low-pressure zone within the centre of the reactor, which would cause the H_2 gas to be concentrated in the centre, from which it would travel upwards, away from the catalytic particles. These particles, being the heaviest fraction in the flow system would tend to stick near the walls and near the bottom of the reactor. I expect that two bubble size regimes will be present within the reactor: In the particle bed proper, smaller bubbles are expected than near the centre where the bubbles would tend to agglomerate. The smaller bubbles in the particle bed, would locally increase the mass and heat transfer, as mentioned in Chapter 1. The large bubbles in the centre will have a higher upwards velocity compared to smaller bubbles, and thus be removed from the reactor system more rapidly. By using this singular system, it was aimed to increase the mass and heat transfer by fluidization and increase the separation between the gas phase and the particle phase. This is a completely different approach than currently used continuous flow systems for LOHC H_{18}DBT, which often rely on low flowrates to achieve more complete dehydrogenation of H_{18}DBT. [82]

In this chapter I will study via cold flow CFD simulations the potential of an SFB for the dehydrogenation reaction of H_{18}DBT. The cold flow simulations will be conducted with water, argon gas and glass beads, to serve as a thermophysically similar system as H_{18}DBT, H_2 and Al_2O_3 – catalyst beads. The simulations will be compared to experiments to study the fluidization behaviour within the SFB unit.

3.2 Methodology

3.2.1 Dehydrogenation Reactor

The setup for the reactor is depicted on Figure 3-1. On Figure 3-1a) the piping system is shown, with the required storage tanks, valves, the pump, and the position of the reactor. Two 200 L vessels were used, the left one to store fresh liquid, the right one hold the liquid after it passes the reactor. However, in the cold flow setup used, all liquid was recirculated back to the left tank. This left tank was connected to an Iwaki magnet drive pump capable of 250 LPM flow rate, the flow was measured using a Prosonic 91 W flow sensor. Valves were put in place to control the flow rate towards the reactor. The piping setup was a combination of stainless steel tubing with flexible plastic tubing, which covered the final 1.5 m from towards the reactor.

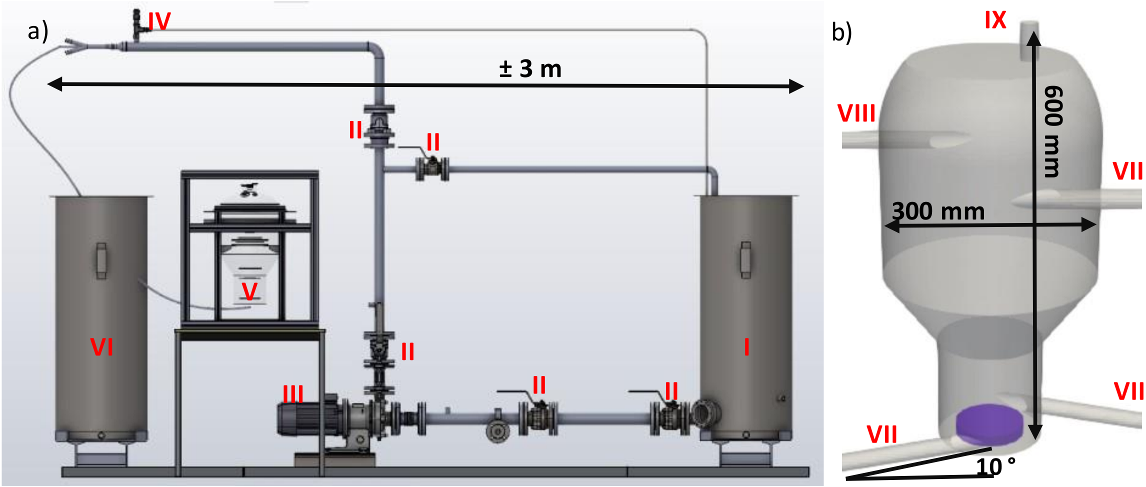

Figure 3-1 a) Overview of the reactor setup. I: 200 L tank containing liquid to be sent to the reactor. II: valves: III: pump. IV: pressure relief valve. V: Reactor. VI: 200 L tank containing liquid after passing the reactor. b) Details of the geometry of the reactor. VII: The liquid inlets. VIII: The liquid outlets. IX: the gas outlet. The blue disc represents the position of the fritted disc.

Figure 3-1b shows the quartz prototype of the reactor, which had a total height of 600 mm and a maximal diameter of 300 mm. The reactor is based on a concept with three distinct zones. The first zone is the reaction zone (the lowest section of the reactor), with a diameter of 150 mm and a height of 150 mm, the inlets are placed tangentially on the walls the reactor. These inlets are 25.4 mm ID pipes that form an angle of 10 degrees with the horizontal plane. In this reactive zone, the catalyst bed is present, and this is the area where the H_2 release will happen from the LOHC liquid.

Since this setup is currently build as a cold flow prototype, gas will be introduced via a fritted disc placed at the bottom of the reactor. The main goal of this reactor is to generate swirling flow patterns within the reactive zone, which will intensify local heat and mass transfer. [173] This is highly beneficial in the case of LOHC dehydrogenation: the reaction requires a high thermal input. Due to the endothermicity, the catalyst particles tend to decrease in temperature during the reaction. Increased mass transfer is also beneficial to remove the produced H_2 from the pores and surface of the catalyst particles. An expansion zone was designed after the reactive zone, where the diameter increased from 150 mm to 300 mm. The height of this zone is 100 mm. In the expansion zone the velocity will decrease, causing solids to fall down back into the reactive zone. Finally, the top section of the reactor which functions as a disengagement section is 300 mm in height with the upper 100 mm section rounded. At a height of 380 mm from the bottom, two more 25 mm ID outlets for the liquid are situated tangentially from the wall parallel to the horizontal plane. I would like to stress that the design of this reactor is an initial prototype, used to show the fluidization of glass beads in presence of gas in swirling flows. The different sections of the reactor are overdimensioned to ensure that the beads will remain in the reactor and to study the separation behaviour of the gas in the swirling flows.

3.2.2 Cold Flow Mock-Up Strategy

The pre-pilot LOHC test rig was designed allowing to a liquid flow up to 250 LPM. The process was designed for the dehydrogenation of either BT or DBT, dehydrogenated using the commercial eggshell 0.3 wt.% Pt catalyst supported on 2 mm alumina beads (Clariant). The choice of BT and DBT is based on their relatively high H_2 storage capacity, 6.2 wt.% and 56 g L^{-1}, excellent thermal properties, a good (eco)toxicological profile and technical availabilities, it beaing a commercial heat transfer fluid. [69, 174, 175] BT has a lower viscosity, but a lower boiling point and increased vapour pressure compared to DBT, thus less suited for the operational conditions inside the proposed reactor, where a large liquid free surface is expected. This would cause more evaporation of the BT LOHC compared to the DBT counterpart. [83, 176]

In this cold flow mock-up study no heating was applied to the system. The pre-pilot setup is able to heat the liquid in the storage tanks to 300 °C. H_2 release would the occur once in contact with the catalyst the preheated liquid would start to release the H_2 gas. Secondly, an induction heating is also included to heat the metal of the catalyst particles directly, providing local heat to the catalyst. However, in the cold flow setup no external heating was used and it was decided to mimic this reacting system using a simplified system with water; Ar and glass beads. The relationship between this system and one of the dehydrogenation of H_{18}DBT was based on dimensionless groups, a method commonly used for fluidized beds, especially for catalytic applications. [177] The philosophy of Knowlton et al. [178] was kept in mind during operations, as they showed that such scaling relations are most relevant for cold flow models used to improve the operation of an existing plant, versus using them for scale-up purposes. As the design and scale-up of swirling fluidized bed is still at its infancy, especially for liquid-gas-solid (LGS) applications, where to the best of the authors knowledge, no such procedure has been proposed, it was decided to minimize the risk related to the reactor design by relying on such similarities.

The Reynolds and Stokes similarities were retained, and maintained the centrifugal acceleration imposed on the solid phase by the liquid. Water at 20 °C was used as the working fluid. The set of scaling relations used is thus composed of the Reynolds & Stokes dimensionless groups, imposing the fluid velocity and water as the working fluid. To compare the Reynolds numbers of the cold flow and reactive systems, an identical fluid velocity was used to evaluate the particle size. This gave the expression for the particle size based on the Reynolds numbers:

$$Re = \frac{\rho_l U_l d_p}{\mu_l} \tag{3.1}$$

$$d_{p_{H_2O}} = \frac{\mu_{H_20}}{\mu_{H_{18}DBT}} \cdot \frac{\rho_{H_{18}DBT}}{\rho_{H_2O}} \cdot \frac{U_{H_{18}DBT}}{U_{H_2O}} \cdot d_{H_{18}DBT} = \frac{0.001 Pa\ s}{0.0016\ Pa\ s} \cdot \frac{766 \frac{kg}{m^3}}{1000 \frac{kg}{m^3}} \cdot d_{H_{18}DBT} \tag{3.2}$$

Using an average particle diameter of the commercial catalyst,2.78 mm for the reactive system, this resulted in an average particle diameter of 1.33 mm for the glass spheres in the cold flow systems.

The density of the cold flow particles could be calculated from the Stokes number:

$$Stk = \frac{\rho_p \cdot U_l \cdot d_p}{18\mu_l} \tag{3.3}$$

$$\rho_{p_{H_2O}} = \rho_{p_{H_{18}DBT}} \cdot \frac{d_{H_{18}DBT}}{d_{p_{H_2O}}} \cdot \frac{\mu_{H_20}}{\mu_{H_{18}DBT}} \cdot \frac{U_{H_{18}DBT}}{U_{H_2O}} = \rho_{p_{H_{18}DBT}} \cdot \frac{2.78\,mm}{1.33\,mm} \cdot \frac{0.001 Pa\ s}{0.0016\ Pa\ s} \tag{3.4}$$

The density of the commercial catalyst, $\rho_{p_{H_{18}DBT}}$ was 2300 kg m^{-3} which results in a density of 3000 kg m^{-3}. To mimic the catalyst phase, I used glass spheres with a diameter in the range of 1.5 – 2 mm. Using these particles, I used an overestimation of the particle size, to counter the underestimation of the particle density, since the density of the glass beads was 2500 kg m^{-3}. To further strengthen this correlation I looked at the onset of fluidization as described by Wen and Yu in the book by Fan for spherical particles in liquid – solid fluidized beds. [118, 125]

$$\boldsymbol{U_{lmf0}} = \frac{\mu_l \cdot \sqrt{33.7^2 + 0.0408 \cdot Ar} - 33.7}{\rho_l \cdot d_p} \tag{3.5}$$

With Ar the Archimedes number defined as: [179]

$$Ar = \frac{d_p^3 \cdot \rho_l \cdot (\rho_s - \rho_l) \cdot g}{\mu_l^2} \tag{3.6}$$

I used this relation where I assumed the particle phase fraction at minimal fluidization velocity α_p as 0.5 and spherical particles, i.e., the sphericity (s) as 1, to calculate the minimal fluidization velocities for both the real case of H_{18}DBT fluidizing porous Al_2O_3 beads and water being used to fluidize glass beads. I found that $\boldsymbol{U_{lmf0}}$ for H_{18}DBT was 0.018 m s^{-1} and for water this value resulted in 0.015 to 0.021 m s^{-1} depending on the particle diameter (1.5 – 2 mm). This fluidization calculation is valid for bottom fed fluidized beds and does not consider the influence of gas phase. The close similarity in $\boldsymbol{U_{lmf0}}$ between the cases does provide some confidence that the results of the cold flow mock-up will give general trends that can be applied to a reactive system. In the work by Fan it is shown that the addition of gas to a liquid based fluidized bed will reduce the $\boldsymbol{U_{lmf}}$, [118] the influence of the thermophysical parameters of the gas is however not further studied in this work.

The mass of catalyst beads was estimated from the molar catalyst to LOHC ratio (Jorschick et al. [85]). I assumed the catalyst mass to be the same as the amount of catalyst used in their batch reactor experiments, by using the same ratio of 6667 mol $H_{18}DBT$ per mol Pt. In the 25 L system with $H_{18}DBT$ heated to 573 K, this would result in a total mass of around 600 g. Due to the Reynolds and Stokes similarities, I assumed the mass of Al_2O_3 based catalyst particles to be the same as the mass of glass beads required.

To further mimic the dehydrogenation of LOHC, I generated the stream of diffused argon using a porous fritted disc, with a diameter of 100 mm and thickness of 18 mm (Hailea, model-ASC-100) from the lower part of the reactive section of the dehydrogenation unit. To simulate the H_2 produced during dehydrogenation, I extracted the maximum H_2 production rate from the same published data of Jorschick et al. [85] that was used to estimate the amount of beads. From the published data it was calculated that around 10 LPM of argon should be continuously fed to the fritted disk.

This figure was estimated from the maximal slope of the work by Jorschick on the second dehydrogenation cycle of the fifth figure in his work. [85] I extracted a slope and then converted it to a productivity of $2.34 \cdot 10^{-4}\ Nm^3_{H2}\ g^{-1}_{LOHC}\ h^{-1}$. The maximal value of this curve was used since the experiments performed by Jorschick were done in a batch reactor and in the system, there is a constant influx of new $H_{18}DBT$. I assumed further that only 2/3 of the reactive zone would contain catalyst beads at a given time, so using this volume I calculated the mass of $H_{18}DBT$ to 1.3 kg, using density correlations extracted from the work of Aslam extracted for 573 K [180]. Using these relations, I calculated the volume of H_2 released and corrected this for a dehydrogenation temperature of 573 K, this corresponded to a value of $1.77 \cdot 10^{-4}\ m^3\ s^{-1}$ or 10.6 LPM. For practical purposes of available mass flow controllers, I rounded this value down to 10 LPM.

3.2.3 CFD Simulations Settings

3.2.3.1 Governing Equations

The CFD simulations are performed using OpenFOAM's multiphaseEulerFOAM solver (OpenFOAM version 8). The solver is based on the Euler-Euler (EE) approach for modelling multiphase systems. This approach is based on the idea of interpenetrating continuums, with each continuum described by its own continuity and momentum equation. The continuity equation is:

$$\frac{\partial}{\partial t}(\alpha_i \rho_i) + \nabla \cdot (\alpha_i \rho_i \boldsymbol{U}_i) = 0 \tag{3.7}$$

Where α_i is the volume fraction of phase i, ρ_i is the density and $\boldsymbol{U_i}$ is its velocity. The momentum equation of each phase is defined as:

$$\frac{\partial}{\partial t}(\alpha_i \rho_i \boldsymbol{U}_i) + \nabla \cdot (\alpha_i \rho_i \boldsymbol{U}_i \boldsymbol{U}_i) = -\alpha_i \nabla p + \nabla \cdot (\alpha_i \boldsymbol{\tau_i}) + \alpha_i \rho_i \boldsymbol{g} + \boldsymbol{F_{ji}} \tag{3.8}$$

With p is the pressure shared between the phases, $\boldsymbol{\tau_i}$ denoting the stress tensor,$\boldsymbol{g}$ represents the gravitational acceleration and $\boldsymbol{F_{ij}}$ denoting the momentum exchange from phase *j* on phase *i*. This momentum exchange can include drag, lift, wall lubrication, virtual mass, and turbulent dispersion. In line with the work from Hu et al. [181] for three phase simulations, only the contributions from drag, virtual mass and turbulent dispersion are included. For this cold flow mock-up study the energy equation was not considered in the simulation.

3.2.3.2 Drag Correlation

Due to the low abundance of gas and solid phases when compared to liquid phase, it is assumed that both the gas and the solid phases are treated as dispersed phases, with the liquid phase as the continuous phase. The drag force exerted between the gas – liquid and solid – liquid phases is expressed in the momentum equation as:

$$\boldsymbol{F_{dl}^{D}} = C_{dl}(\boldsymbol{U_d} - \boldsymbol{U_l}) \tag{3.9}$$

With d representing the dispersed phase (gas or solids) and l the liquid phase. C_{dl} represents the specific drag correlation for each of these cases. In OpenFOAM $C_{dl}$is calculated via the term $C_D Re$ which depends on the drag model used. The drag correlation for the gas – liquid system is calculated according to the model of Ishii and Zuber. [182] This drag correlation considers three different flow regimes: a dense spherical particle regime, a dense distorted particle regime and a dense spherical cap regime. [183, 184] These are accounted for by the following formulas:

$$C_D Re = \begin{cases} 24 \cdot (1 + 0.1 Re_m^{0.75}) \mid Re_m \leq 1000 \\ 0.44 Re_m \mid Re_m > 1000 \end{cases} \tag{3.10}$$

In this formula the expression for Re_m is given by [185]:

$$Re_m = \frac{|\boldsymbol{U_g} - \boldsymbol{U_l}| \cdot d_g}{\mu_{mix}} \tag{3.11}$$

With d_g the diameter of the gas bubble and μ_{mix} the dynamic mixture viscosity that is calculated by:

$$\mu_{mix} = \mu_l \cdot \left(1 - \alpha_g\right)^{-2.5 \cdot \frac{\mu_g + 0.4\,\mu_l}{\mu_g + \mu_l}} \; with \max\,\left(1 - \alpha_g\right) < 0.001 \tag{3.12}$$

The second case for distorted particles (or bubbles) is defined as

$$C_D Re = \frac{2}{3} \cdot \frac{1 + 17.67\,\mathcal{F}^{6/7}}{18.67\,\mathcal{F}} \cdot \sqrt{E\ddot{o}} \cdot Re_d \tag{3.13}$$

With $\mathcal{F}$ defined as:

$$\mathcal{F} = \min\left(\frac{\mu_l}{\mu_{mix}} \cdot \sqrt{1 - \alpha_g}, 1e^{-03}\right) \tag{3.14}$$

And with Eötvös number (Eö) is the ratio of the gravitational forces and the surface tension (σ):

$$E\ddot{o} = \frac{g\left(\rho_l - \rho_g\right) d_g^2}{\sigma} \tag{3.15}$$

The term Re_d expresses the phase pair Reynolds number in the OpenFOAM code, which is calculated according to

$$Re_d = \frac{|\boldsymbol{U_g} - \boldsymbol{U_l}| \cdot d_g}{\mu_l} \tag{3.16}$$

The drag coefficient for the dense spherical cap bubble regime is defined as:

$$C_D Re = \frac{8}{3} \cdot \left(1 - \alpha_g\right)^2 \tag{3.17}$$

The solid – liquid drag interaction was calculated by the Gidaspow drag correlation model. This model is a combination of the Ergun and Wen & Yu drag models. The Ergun drag model is used if the volume fraction, $\alpha_l < 0.8$, and the Wen & Yu correlation is used when the volume fraction of the continuous phase equals or exceeds 0.8. [168]

The Ergun term is given by: [186]

$$C_d Re = 150 \cdot \frac{\alpha_s (1 - \alpha_l) \mu_l}{\alpha_l d_s^2} + \frac{1.75 \rho_l \alpha_s |\boldsymbol{U_s} - \boldsymbol{U_l}|}{d_s} \tag{3.18}$$

The Wen & Yu drag correlation uses an intermediary calculation $C_D Res$: [125]

$$C_D Res = \begin{cases} 24 \cdot [1 + 0.15 \cdot (Re_d - \alpha_d)^{0.687}] \mid Re_d \cdot (1 - \alpha_d) < 1000 \\ 0.44 \cdot Re_d \cdot (1 - \alpha_d) \mid Re_d \cdot (1 - \alpha_d) \leq 1000 \end{cases} \tag{3.19}$$

The value $C_D Re$ can then be calculated via:

$$C_D Re = C_D Res * (1 - \alpha_d)^{-3.65} \cdot \alpha_c \tag{3.20}$$

3.2.3.3 Virtual Mass

The virtual mass is the term that accounts for the inertia induced in the system by the deflection of mass caused by an accelerating (or decelerating) object in the fluid. The model for a constant coefficient of virtual mass was selected based on the work by *Hu* et al.: [181]

$$\boldsymbol{F_{gl}^{VM}} = C^{VM} \alpha_g \rho_l \left(\frac{D\boldsymbol{U_g}}{Dt} - \frac{D\boldsymbol{U_l}}{D_t} \right) \tag{3.21}$$

For the gas – liquid interaction the constant coefficient used was $C^{VM} = 0.5$. The virtual mass interaction was not accounted for in the solid – liquid phase pair, C^{VM} used was set to 0 in the latter case.

3.2.3.4 Turbulent Dispersion

The turbulent dispersion forces represents the diffusion of the turbulent kinetic energy of the dispersed phase caused by the presence of the continuous phase eddies. [187] This interaction like the virtual mass is only accounted for in the gas – liquid phase pair. The specific momentum exchange term is given by:

$$\boldsymbol{F}_{\boldsymbol{gl}}^{\boldsymbol{TD}} = C^{TD}\alpha_g\rho_l k_l \nabla\alpha_\mathrm{g} \tag{3.22}$$

The turbulent dispersion coefficient C^{TD} was kept constant at 1.0, the symbol k_l represents the turbulent kinetic energy of the liquid. [181]

3.2.3.5 Turbulence Model

In this study the RANS type k-Omega SST (Shear Stress Transport) turbulence model of Menter [158] was used for the liquid phase, since it has shown good results with swirling flows. [188] The dominant flow inside the reactor will be the liquid phase, therefore it was opted to reduce the computational complexity by turning the turbulent contributions of the gas flow off. To account for the solid particles in the EE modelling approach, the kinetic theory of granular flow was used, see Table 3-1.

3.3 Results and Discussion

3.3.1 Computational Domain

The computational domain for the comparison with the experimental work is a simplified geometry of the real reactor: the studied area of the reactor was limited to a height of 450 mm of the original 600 mm height. This limited height corresponded to a total volume of the reactor of 21.3 L. This approach was selected so that there was less computational effort required to resolve the gas – liquid interphase, a known computationally expensive phenomenon. [189] The interphase does not contribute in this case to the overall results of the simulation, since I was mostly interested in the interactions of the liquid, gas and solids near the bottom of the reactor. The height of 450 mm was chosen to be below the gas – liquid interphase near the top of the reactor, as can be seen in Figure 3-2A. The height of this gas-liquid interphase is dependent on the flow rate and was found to follow the trends observed for the liquid level in the reactor as a function of time for various inlet flow rates, seen on Figure 3-2B. These results were obtained from a Volume of Fluid (VOF) simulation for simplicity on a mesh created for the full reactor. Numerical implementation of VOF in OpenFOAM is well explained in a work from Larsen et al. [190] From this I can conclude that with an inlet flow rate of 75 LPM the water volume caps at 25.9 L, when the water inflow reaches steady state. This justifies the use of the mesh with a capped upper section, with the entire computational domain filled up with water.

Table 3-1 Settings, models and parameters used for the simulations.

	Operational Parameters
Particle Density	2500 kg m^{-3}
Particle Diameter	1.5 mm – 2 mm
Total Particle mass	0.600 kg
Water Density	1000 kg m^{-3}
Water dynamic viscosity	$1.05 \cdot 10^{-3}$ Pa·s
Water surface Tension	0.07 N m^{-1}
Gas Density	Calculated by ideal gas law
Gas dynamic viscosity	$2.1 \cdot 10^{-5}$ Pa·s
Gas influx rate	$3.14 \cdot 10^{-4}$ kg s^{-1}
	Boundary Conditions
Water inlet flow rate	$4.165 \cdot 10^{-4}$ m^3 s^{-1}
Water inlet temperature	300 K
Outlet Pressure	$1 \cdot 10^{5}$ Pa
Fluid – Wall Interaction	No – Slip Condition
Solid – Wall Interaction	Johnson Jackson Particle Velocity
	Restitution Coefficient 0.2
	Specularity Coefficient 0.1
	Turbulence Models
Water turbulence model	K – omega SST
Gas turbulence model	none
	Kinetic Theory Conditions
Max packing limit	0.65
Max frictional limit	0.5
Viscosity Model	Syamlal model
Conductivity Model	Syamlal model
Granular pressure model	Syamlal, Rogers & O’Brien model
Frictional stress model	Schaeffer model
	$\phi = 36$
Radial model	Carnahan & Starling Model
	Interfacial Exchange Models
Solid – liquid drag model	Gidaspow
Gas – liquid drag model	Ishii & Zuber
Gas – liquid Virtual Mass model	Constant Coefficient model
Gas – liquid Turbulent Dispersion model	Constant Coefficient model

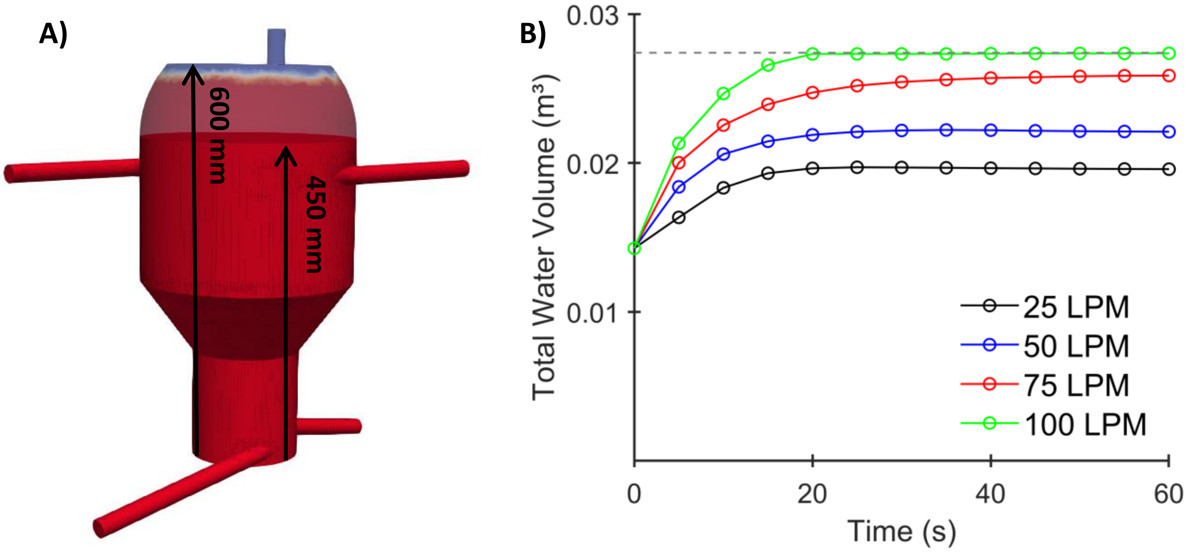

Figure 3-2 A) Steady state water volume at 60 s. The translucent part denotes the water level in the full reactor (obtained by VOF). The opaque section is the portion of the geometry used in the Eulerian simulations. B) Steady state water volume obtained by VOF simulations. The dotted grey line denotes the total reactor volume. At 75 L min^{-1} total inlet flow rate a high inlet flow rate was achieved without overflowing the reactor.

For the three phase Eulerian simulations I introduced the water in the system from the inlets at flow rates of 50 LPM for comparison with the experimental work, or 75 LPM for other simulations. As this was close to the maximal achievable flow rate within the reactor. A mass of 0.6 kg of glass beads was initialized near the reactor inlet. The argon gas was introduced with a flow rate of 3.95 kg s^{-1} via a source term. The active volume in the mesh for this source term was chosen to correspond to the same volume of the fritted disc that was used in the experiment, see also Figure 3-1. The parameters used to describe the different phases can be found in Table 3-1.

On this capped geometry a mesh independent study was performed. This mesh independence study used the Grid Independence Index (GCI) approach from Roache (1994) [136] and is explained in Chapter 2. The results of this grid independence study can be seen in Figure 3-3. For this study, three meshes with different refinement levels were used, coarse: 464 780 cells, medium: 1 478 514 cells and fine: 4 689 241 cells. The results are obtained after 3 seconds of simulated time, with 0.6 kg of solids present. The initial particle bed height amounts to 32 mm. Boundary conditions for this case can be found in Table 3-1. Solids were introduced into the computational domain in a cylinder with a 32 mm height and 148 mm diameter and a volume fraction of 0.45. Gas was being generated by a semi-implicit source term in a cylinder of 100 mm diameter and 18 mm height, i.e., with the same dimensions as the fritted disc used in the cold flow experiments. The results show a converging behaviour between the three meshes, as demonstrated by the *extrapolated* line, calculated from the approach by Roache. [136] The profile of the azimuthal velocity of the medium mesh, fits that of the extrapolated curve, and with an underprediction of 4 % of the maximal azimuthal solid velocity. This was deemed to be sufficient accuracy for the simulations since computational time required for the medium mesh was about five times shorter when compared to the fine mesh. Simulations were run using a maximal Co – number of 0.1 for the first second of simulated time, afterwards this value was increased to 0.5 for the remainder of the simulations.

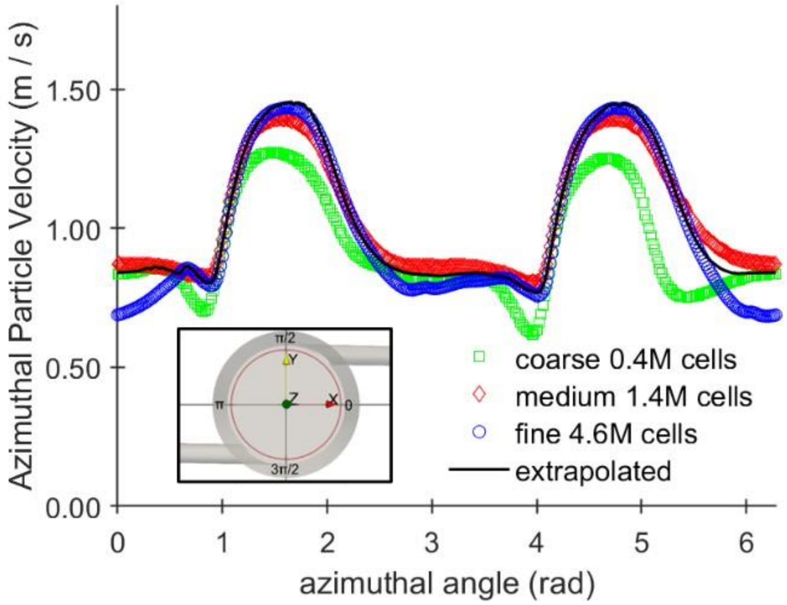

Figure 3-3 Azimuthal velocity of the solids, extracted in a horizontal plane (10 mm height, 65 mm radius), for meshes with three different refinement levels. Inlet flow rate 75 L min^{-1}, total mass of solids 0.6 kg. Results obtained after 3 s of simulated time. The used azimuthal angle is shown on the insert.

3.3.2 Fluidization Profile of the Particle Bed

The reactor was designed with the idea in mind to have fluidization of the beads in order to improve the mass and heat transfer rate and subsequently having a more efficient dehydrogenation of $H_{18}DBT$ by removing the gas bubbles from the catalyst surface and by supplying fresh and heated H_2-rich LOHC continuously. In order to achieve this, the particles have to be dragged along by the inflowing liquid, but this behaviour should be studied in a three-phase LGS system since in the reactive application H_2 is generated at the catalyst surface during reactor. The proof that this concept is able to fluidize beads in a three-phase flow is shown in Figure 3-4 by the cold flow mock-up. In this figure, it is observed that when the liquid drag is imposed on the particles without any gas, the bed expansion is minimal, as is the particle movement (Figure 3-4A). The CFD results confirm this trend. To do so, I plotted a contour plot of the volumetric solid fraction with a cut-off value of 0.1. I also see that the bed height is clearly visible (and comparable to the original bed height at rest at the beginning of the simulations), and only affected by the high velocity jets of the entering liquid slightly upstream of the liquid inlets. This tendency is clearly confirmed by the experiments. The effect of the simulated production of H_2 gas on the fluidization is striking (Figure 3-4B). The injection of 10 LPM of argon results in a solid bed with an increased volume. I can expect that the considerable volume increase of the solid bed will be highly beneficial to ensure an adequate H_2-rich LOHC-catalyst contact to allow for the dehydrogenation reaction to happen. The fluidization of the solid bed also ensures a sufficient bed agitation, thus in line with the recent findings of Solymosi et al. [99] highlighting the importance of mechanical agitation for mass transfer as well as to initiate nucleation on the catalyst. This comparison between the experimental and computation particle bed orientation shows that the CFD results can be relied upon to perform a qualitative analysis of the general trends seen from the simulation. In the remainder of this work the results will be discussed from the CFD study.

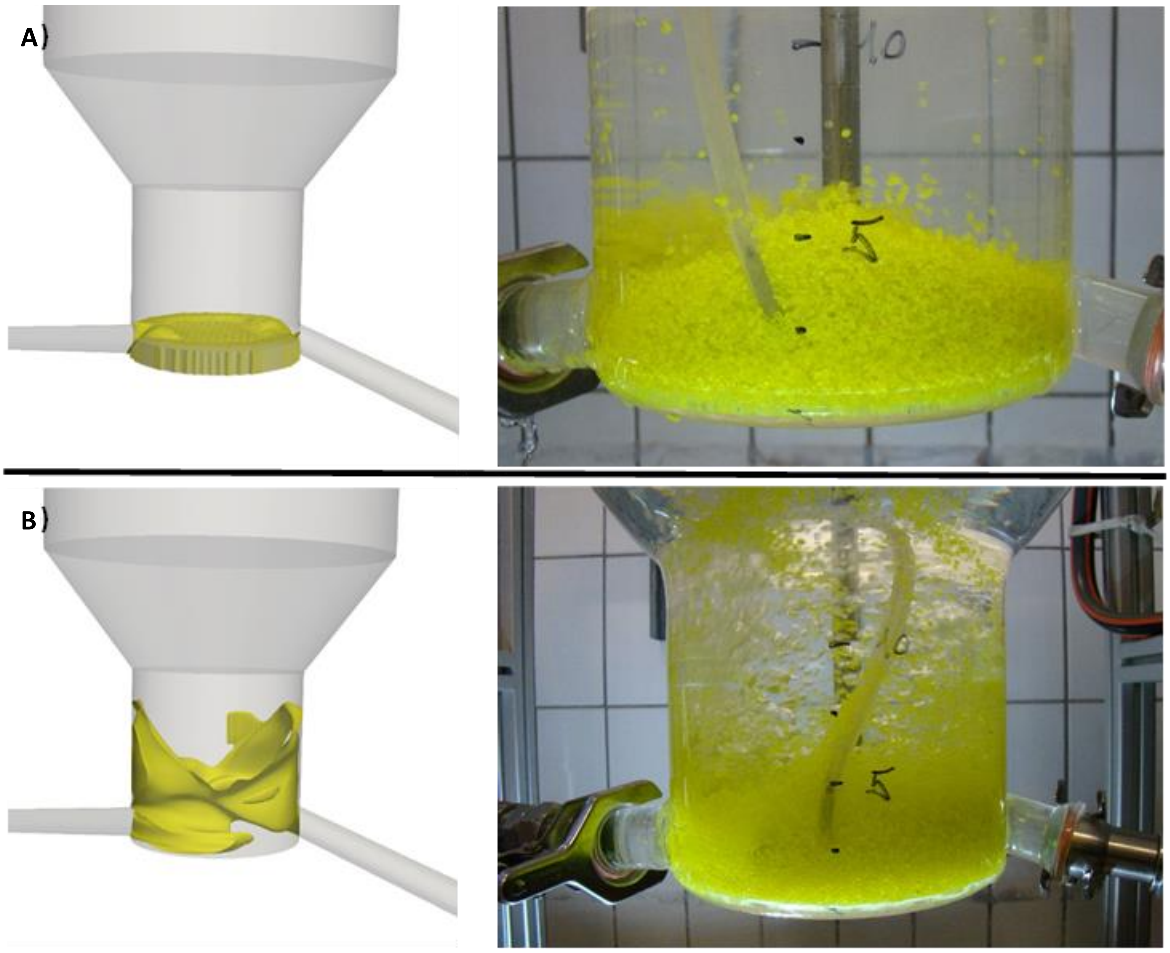

Figure 3-4 Comparison between simulations and experiments. a) Reactor operation without gas flow, showing little to no movement of the solid bed. b) Reactor operation with 50 LPM of water and 10 LPM gas flow, showing the fluidization of the glass beads (painted in yellow for better visualization). The cut-off value for the CFD – contour plot of the volume fraction of the solids was set to 0.15.

Figure 3-5 shows the height the particles can reach within the first ten seconds of operating the reactor, as seen near the wall, and analysed from the transient simulation every 2 seconds. Two interesting behaviours of the solids can be noted. First, it can be seen that the particles are dragged by the flow to heights exceeding 100 mm in the reactive zone, while still maintaining a packing density of more than 40 %. In the experimental image in Figure 3-4b it can be seen that particles also exceed 100 mm height, even at the lower flow rate of 50 LPM used in the experimental setup. Second, it can be seen that in the initial transient behaviour of this flow there is a certain periodicity between the black and red lines, especially in the case of 4 and 6 seconds and in the case after 8 and 10 seconds However the results after 4 and 6 seconds differ widely from those at 8 and 10 showing that this periodicity is temporary and the chaos within the flow is increasing as one would expect in a fluidized bed. This periodicity is likely caused by the symmetry of the reactor and identical inlet conditions.

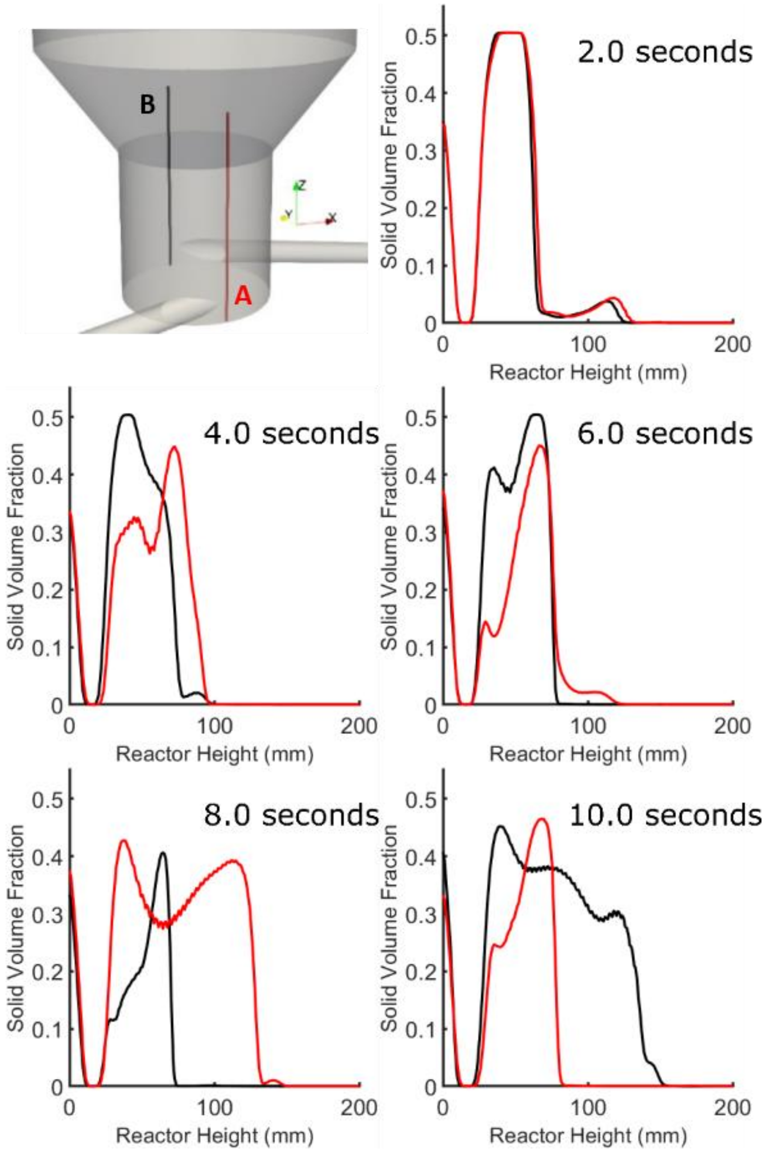

Figure 3-5 The evolution of the bed height near the wall over time. The red line on the graphs corresponds to position A on the front side of the reactor. The line in black corresponds to bed height at position B, at the back side of the reactor.

The position of the black and red lines are shown in the reactor (upper left). The particles achieve a height exceeding 100 mm. In Figure 3-6A, it can also be seen that the catalyst particles move upwards on the side of the walls. This figure also shows the periodicity of the flow since the movement on the walls is only visible on one side of the reactor. Notably, comparing Figure 3-6A with Figure 3-4B shows that the solids in the simulation also move up until the expansion zone in small quantities. Figure 3-6B shows the reactor from the bottom and here the presence of accumulated solids is noticeable. The presence of this accumulated area near the bottom of the reactor means that H_2-rich LOHC liquid comes into contact with a high concentration of catalyst beads when it is newly injected into the reactor. This is beneficial for both the reaction and for heat transfer purposes: i) the high concentration of

$H_{18}DBT$ in the feed favours a maximum reaction rate, and ii) this newly injected/recirculated hot LOHC act as a heat source to counteract catalyst particles cooling due to the endothermicity of the reaction. Future designs should take this into account to avoid this dead space of beads in the reactor and static beads, whilst still keeping these beads near the inlets. In Figure 3-6, the absence of solid beads or low volume fraction near the inlets of the liquid is also noticeable. This is due to the high inlet velocities and will allow for easy injection of the liquid since the solid beads do not obstruct the inlets.

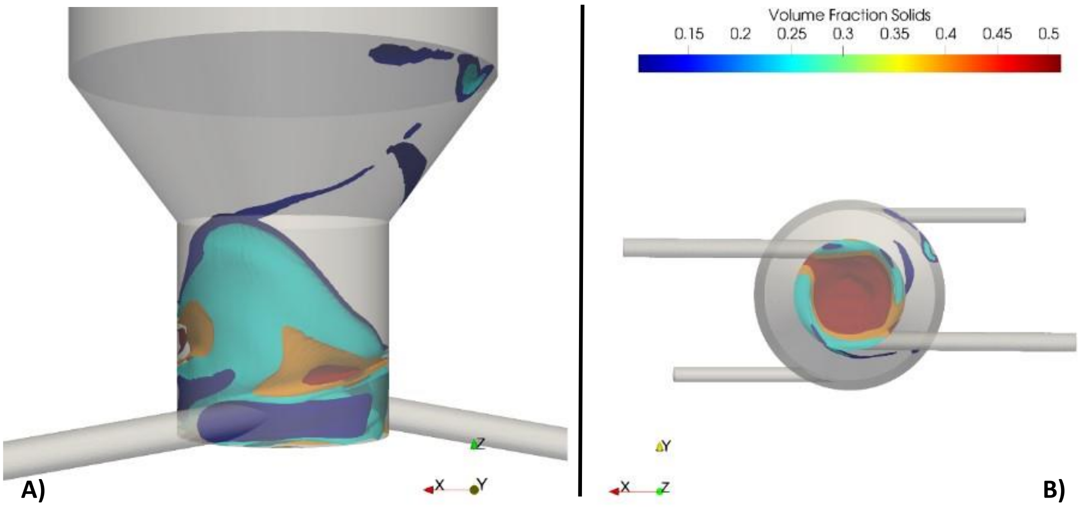

Figure 3-6 The envelopes of the solid fraction shown for a) the view on side and b) the view from the bottom plate (B). The envelopes show the solid volume fraction for 0.1 (blue), 0.25 (cyan), 0.4 (orange) and 0.5 (red). These images was taken from the simulation after 10 seconds.

3.3.3 Liquid and Slip Velocity

Next to the distribution of the solid, the behaviour of the liquid flow is critical. The streamlines of the liquid after 10 seconds of simulation can be seen in Figure 3-7. They show that the liquid flow in the reactor is swirling in a helical upwards pattern, which is caused by the orientation of the inlets. In this figure it is observed that the fluid velocity is higher near the walls and the inlets, reaching a velocity of 1.4 m s^{-1} in these areas.

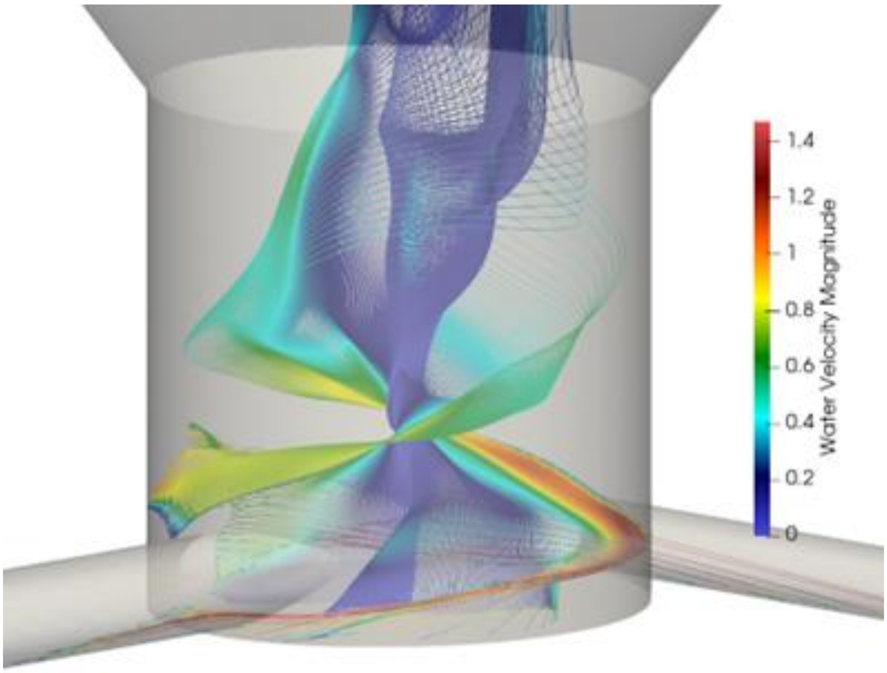

Figure 3-7 Streamlines of the liquid velocity in the reactive zone after 10 seconds. The flow has a helical pattern that swirls upwards and has higher velocity near the walls.

A second parameter to study the interaction between the liquid and the solid particles is the slip velocity (the difference in velocity magnitude between the solid and liquid phase). An increase in solid-liquid slip velocity is beneficial for both heat and mass transfer, both phenomena are highly advantageous for the endothermic dehydrogenation reaction where the catalyst is deactivated by the liquid product, and where the H_2 gas bubbles tend to stay in the packed bed. Figure 3-8 shows the slip velocity extracted at a height of 10 mm and in a circle with a radius of 65 mm after 10 seconds of simulation. During the reactor operation the slip velocity reaches a maximal value of 0.4 m s^{-1}, and it shows nonzero values almost completely over the full extent of the azimuthal profile of the reactor. These data points were extracted from the simulation results, the agreement of the GCI – study in section 3.1 proves that I can rely upon these results with an estimated relative error of about 4 %.

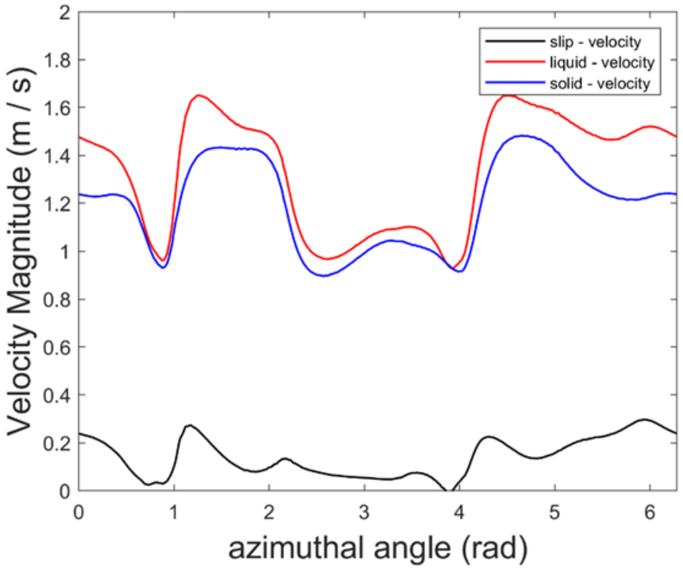

Figure 3-8 Velocity profile for the liquid and solid phase, with the resulting slip velocity. Data was extracted at a height of 10 mm and a radius of 65 mm after 10 s of simulation. For the interpretation of the azimuthal angle the reader is referred to Figure 3-3

3.3.4 Gas Distribution in the Reactor

In order to improve the reaction, a fast removal of the gas phase is required. The gas phase present around the particles can inhibit the reaction of the liquid H_{18}DBT by covering the surface of the catalyst particles with H_2 bubbles, thus leading to catalyst dewetting. When investigating the distribution of the gas phase it was seen that most of the gas that is generated at the bottom plate tends to remain in the centre of the reactor. This is caused by the rotational movement of the liquid, which forces the light density gas towards the centre. The reactor design proposed here shows to have a separation effect to remove the gas from the liquid flow, seen on Figure 3-9. In this figure the lilac arrows show the magnitude of the gas velocity extracted from CFD simulation, with its point of origin on the central plane. These arrows show that the gas phase within the reactive zone of the reactor is also influenced by the swirling flow of the liquid. It is this effect that helps to concentrate the gas phase in the centre of the reactor. While this figure does not show the distribution of the gas bubble size, it can be seen that there is an accumulation of the gas in the centre, which aids in rapid removal of gas phase from the particle bed.

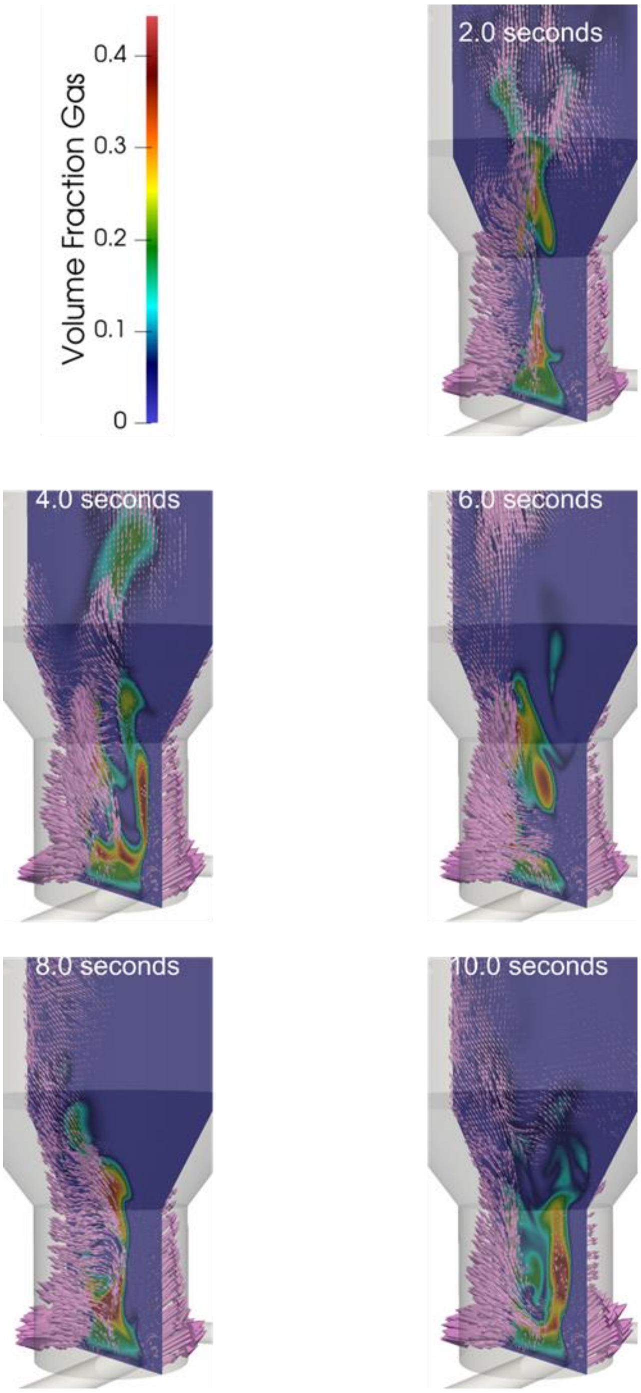
Volume Fraction Gas
0.4
0.3
0.2
0.1
0
2.0 seconds
4.0 seconds
6.0 seconds
8.0 seconds
10.0 seconds

Figure 3-9 Central plane of the reactor showing the distribution of argon gas over the course of the simulation. The lilac arrows denote the magnitude of the gas velocity.

3.3.5 Future Design Changes

With this reactor I have shown the first concept that the use of a swirling fluidized bed can be applied to a system with water, glass beads and Ar gas. The parameters for this three-phase system were calculated to have high similarities with $H_{18}DBT$, Al_2O_3 catalyst particles and H_2 gas. This initial design is far from the optimal design, a simple calculation of the liquid hour space velocity (LHSV) shows that with current operating parameters: 75 LPM inlet flow rate and only 0.6 kg of catalyst, the LHSV exceeds 9000 h^{-1}. This is an order of magnitude of 100 times higher than what the chart of Peters et al. [95] on the relation between LHSV and temperature is designed for, and thus gives a very low Degree of Dehydrogenation (DoD) of $H_{18}DBT$. [191] For this reason, I suggest using a higher catalyst mass as much more catalyst can fit in the reactor, than was used in this study. Secondly, the minimal inlet flow rate should be found where the catalyst will remain in fluidized state. Thirdly, using recirculation of the liquid is also highly recommended, as this is often used in liquid based fluidized beds. [114] Recirculation of the liquid is not advised in the current geometry and with current operating conditions. To estimate the number of recirculation passes in the system, I calculated the 1st Damköhler number for this system according to Otalvaro – Marin and Machuca – Martinez, [192] with the kinetic parameters obtained from Bulgarin's work. [82] The residence time inside the reactor was estimated from the average liquid holdup in the particle bed. Since a high flowrate and low mass of solids was used, the obtained residence time was as low as 0.11 s. Calculating the Damköhler number reached a value as in the order of 10^{-6}, which is an order of magnitude of 5 lower, than the required criterium of Da = 0.1, which was set by Otalvaro – Marin and Machuca – Martinez to reach conversions of 60 % with 10 recirculation steps. The definition of DoD is closely related to conversion, in the current setup more than 1000 recirculation passes would be required to reach functional DoD of 50 – 80 %. [95] Operating the reactor in its current form is thus far from optimal, an changes to both the design as the operating conditions, such as decreased inlet flowrate and increased catalyst mass. Some design changes that can be made to improve this reactor further towards a higher DoD are proposed in the following. For example, elongating the reactive zone to allow more catalyst to fit. Doing so will decrease the LHSV, yielding a higher DoD. This however, will come with the drawback of additional pressure drop due to the longer bed. [179] Due to the higher flowrates required in this swirling fluidized bed reactor, the residence time in this reactor will not be long enough to achieve sufficiently high DoD in a single pass. Recirculation will probably be required, which will introduce back-mixing of unloaded DBT in the catalyst bed. This will lower the efficiency of the process; this is a trade-off with the increased mass and heat transfer than can be achieved by the swirling catalyst bed. Additional research is required in this field to find the optimum between a high flowrate which would increase swirling behaviour and increase mass and heat transfer, but these higher flowrates would require more recirculation passes, lowering the catalyst efficiency.

By decreasing the radius of the reactive zone there will be a stronger rotational acceleration on the particles, causing stronger swirling behaviour even at lower flow rate, which should increase residence time of the liquid in the fluidized regime. This increase in rotational force will likely also help with faster removal of the gas phase, leading towards a more efficient reaction. [193]

A third design change I would propose to future systems is a way to eliminate the accumulation of the catalyst near the bottom plate of the reactor, for this I could use a conical shaped bottom plate. This would remove the dead zone inside the reactor and ensure that more of the catalyst is freely flowing, similar to the effect of a cone in a TORBED reactor. [194]

In addition to the design changes for the reactive zone, the upper sections of the reactor should also be optimized to allow for quick degassing of the liquid, while keeping the total volume of the reactor low. [195] This would increase the power density of the total reactor system. Another factor that can help with the increased fluidization in the size of the catalyst beads. From Eq. 3.1, it can be seen that the diameter of the particle is inversely proportional to the $\boldsymbol{U_{lmf}}$, decreasing the size of the particle will therefor decrease the minimal flow rates required for the fluidization. This would also lead to longer residence time and improved DoD, while still having the added benefit of the increased mass and heat transfer that arises from fluidizing the beads. [179]

3.4 Conclusion

In this chapter a prototype of a swirling fluidized bed reactors was introduced for the dehydrogenation of H_{18}DBT. A cold flow mock-up study using both CFD simulations and experiments allowed to study the behaviour of the liquid, gas and solid phases in the system. Firstly, I showed that the onset of the particle bed fluidization drops when the gas phase is introduced in the system, as is the case in conventional three phase fluidized bed systems.

The bed height exceeded 100 mm, an increase from the initial height by more than 70 mm. This increase only occurred in the three-phase system, as for liquid – solid operation only, the bed height remained static. The use of an expansion zone within the reactor allowed for the beads to remain within the bottom section of the reactor. There was, however, an accumulation of the solids near the centre of the bottom plate of the system. Secondly, the CFD simulations of the liquid phase showed that the liquid swirls in an upwards helical pattern with little backflow. The liquid exerts a drag force on the solid phases, which can be seen by the slip velocity between the liquid – solid phase. This slip velocity aids in the removal of gas from the catalyst surface and will also be beneficial in heat transfer during the endothermic dehydrogenation reaction. Due to the swirling flow, the gas phase is being concentrated in the centre of the reactor, which allows for efficient removal of the released gas. The reactor discussed in this chapter is only a prototype and will require additional optimization steps for the geometry to increase its potential as a dehydrogenation reactor for H_{18}DBT. The potential improvements to this system will be further discussed in chapter 5.

Chapter 4

Investigation of the model selections for Eulerian – Eulerian simulations of LGSFB

Based on:

Laurens Van Hoecke, Nithin B. Kummamuru, Arturo Gonzalez – Quiroga, Sammy W. Verbruggen, Patrice Perreault, *A Comparison of Multiphase Eulerian – Eulerian Drag model Combinations to Simulate Liquid – Gas – Solid Fluidized Beds,*

Planned submission in *Powder Technology*

4.1 Introduction

In Chapter 3, the first simulations in this thesis using the Eulerian – Eulerian (EE) multiphase framework were introduced, combined with qualitative visual experiments to assess the capacity for fluidization of the SFB reactor. In this chapter I aim to further explore the differences in possible simulation settings of three phase simulations while using EE simulations. This will be combined with validation experiments in a *pseudo* – 2D fluidized bed reactor, operated in liquid – gas – solid (LGS) regimes. The nomenclature of LGS is chosen over gas – liquid – solid, to highlight that the liquid phase is the dominant phase in the liquid gas solid fluidized bed (LGSFB). Throughout this chapter, several different models are discussed, Table 4-1 provides a single sentence description of these models for clarity.

Table 4-1 Overview and description of models discussed in this work.

Model Name	One Sentence Description
Ishii - Zuber	Drag model for bubbly, droplet or particulate flows.[182]
Schiller Naumann	Drag model for dispersed bubbly flows. [196]
Tomiyama (Kataoka Zun Sakaguchi)	Model for drag coefficients of single bubbles under normal and micro gravity conditions. [197]
Lain	Drag model for turbulent bubble columns for the Euler – Lagrangian systems.[198]
Syamlal O'Brien	Fluid – solid particle drag model. [199]
Gidaspow	Fluid – solid particle drag model.[200]
Zhang Vanderheyden	Fluid – solid drag model that takes into account the mesoscale structures in particle dense regions fluidized beds. [201]
k-omegaSST	Turbulence model for free flows and boundary layer flows. [158]
Prince – Blanch	Bubble coalescence model for air – sparged bubble columns
Lehr – Millies – Mewes	Binary breakup model for bubble columns, binary breakup means each bubble is split into two daughter bubbles.

In the EE simulation framework, interactions between the different phases are selected pairwise. This means that different models can be enabled for the liquid – gas, liquid – solid, or gas – solid interactions. These different interphase exchange (IE) terms are described by the drag, the lift, the virtual mass, the turbulent dispersion, and the wall lubrication. [202, 203] In liquid dominated flows, the drag force is the most dominant of the IE terms, and this will be the main focus of this chapter. The drag force is always opposite to the direction of the movement of the object. In three phase systems, the object can be a solid particle, a gas bubble, or a liquid droplet. Simulations of LGS systems have been conducted using several different combinations of the drag models for each of the phase pairs. Yu et al. [204] investigated single bubble LGSFB reactors and devised theoretical continuous element models to describe the drag interactions. With respect to the effect of drag models used for simulations in three phase systems, Li and Zhong [205] found that for bubble columns the combination of the Zhang – Vanderheyden model for gas – liquid drag, the Schiller – Naumann model for solid – liquid drag and using no model for the solid – gas drag force, the best results were obtained. A different set of models was used by Hamidipour et al., [206] for the liquid – solid drag force they used the Gidaspow model (a combination of the Wen and Yu fluidization correlation model and the Ergun equation). The gas – liquid and gas – solid interactions were evaluated via the Schiller – Naumann model, this assumption was made since the gas bubbles and solid particles often follow the same trajectory in the system. An older work from Panneerselvam et al. [207] uses the Tomiyama model for the gas – liquid drag and the Gidaspow model for solid – liquid drag. Solid – gas drag was evaluated using a user-defined function defined in the CFD software, in line with the work from Wang et al. [208] Recent work by Liu et al. [209] used the Tomiyama model for gas – liquid drag, the Schiller – Naumann model for liquid – solid and the Gidaspow model for the gas – solid model, as solids they studied 3 mm plastic beads, with a density of 1050 kg m^3. Hu et al. [181] studied three-phase systems not as fluidized beds but in stirred tanks, using the Tomiyama model for the liquid – gas drag and the Gidaspow model for liquid – solid drag, the use of a gas – solid model was omitted in this study using 150 µm beads, with a density of 1190 kg m^3 as the solid phase.

In this chapter, the simulations will be compared to data obtained from camera experiments of a *pseudo* – 2D LGSFB. The data was obtained from Digital Image Analysis (DIA), Particle Image Velocimetry (PIV) and particle tracking velocimetry (PTV) from laboratory experiments with the Computational Fluid Dynamics (CFD) results of a LGSFB. The goal of this work is to test different combinations of drag models and compare the results obtained from these simulations to results obtained from image analysis of a similar experimental system. The system investigated consists of water, He gas and 2 mm diameter glass beads. This was chosen so due to the similarity calculations between these phases those present in the dehydrogenation of $H_{18}DBT$.

I investigated the system by simulations of a *pseudo*-2D LGSFBs using an EE multiphase approach, data and results from the simulations were compared to experimental values obtained via DIA, PIV and PTV. As highlighted in a recent review by Neogi et al. [210] PIV on three phase fluidized beds is a scarcely discussed topic in literature, and this is even more true for liquid dominated LGSFBs. The validation and selection of the drag models for the EE multiphase simulations will be based on the PIV approach for other types of fluidized bed reactors, where the time averaged solid velocity profile is investigated. [211-214]. The experimental bed height will be determined via DIA, based on the analysis of a time averaged grayscale image analysis. [215] Furthermore, based on a statement of Ghatage et al. [216] I also propose the use of a time averaged PTV method for fluidized beds containing large particles. In these systems, the local vertical velocity profile of a settling particle is known to differ from the average settling velocity, due to the random movement of the particle. Averaging the local settling velocities of tracked particles over time is thus necessary for comparison with EE CFD simulations.

4.2 Methodology

4.2.1 Experimental Setup

4.2.1.1 2D Fluidized Bed Reactor Design

The *pseudo* – 2D fluidized bed reactor was 3D printed using polylactic acid (PLA) at 210 °C in an extrusion printer, with a heated print bed at 60 °C and fan cooling enabled. An image and a 3D sketch of the reactor are given in Figure 4-1. Special focus was laid on making the reactor water- and airtight, by using a layer-to-layer distance of only 0.07 mm and by printing 2.0 mm thick walls. The width of the bed is 40 mm, the distance between the gas diffusor and the top of the bed region is 188 mm, however, due to the design of the structure the first 5 mm above the diffusor are not visible and only the upper 183 mm of the fluidized bed region is available for visualisation. A plexiglass sheet (188 x 65 x 4 mm) was placed on the front and back side of the reactor. The back of the reactor was covered with a white sticker to reduce background noise during image capturing. The depth of the reactor was chosen to be less than 9 times the particle diameter, to ensure 2D flow in line with literature on *pseudo* – 2D liquid – solid fluidized beds. [212] A commercial silicon based transparent sealant (TEC-7) was used to fuse the plexiglass sheet to the PLA reactor body.

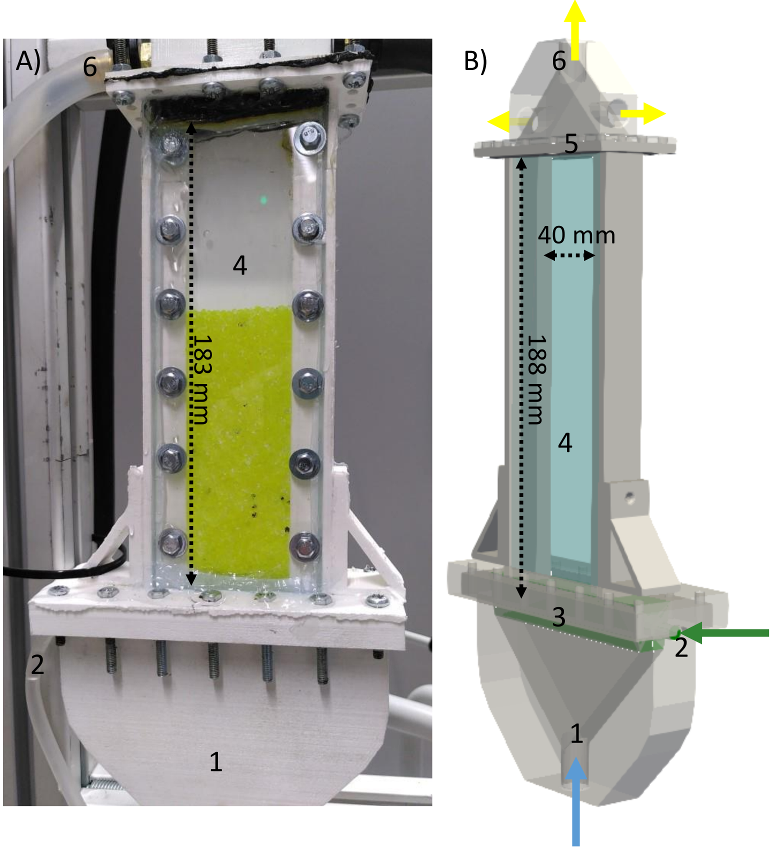

Figure 4-1 The fluidized bed reactor studied in this work. A) Real life image. B) 3D representation to show the internal of the system. 1) The liquid inlet. 2) The gas inlet. 3) The gas diffusor. 4) Plexiglass sheet. 5) The closure of the fluidized bed region, the opening has been made smaller than the d_p. 6) The outlets for the liquid – gas mixture.

To ensure uniform gas distribution in the system, I used a JBL ProSilent Aeras Micro S as a gas diffusor, with a 20 mm thickness. Gas flow was enabled via a 4 mm inner diameter flexible tube, connecting the gas diffusor with a thermal Bronkhorst mass flow controller. Liquid flow was measured using a Keyence FDH-10 Clamp-on Flow Sensor attached on a stainless-steel pipe of 300 mm with an outer diameter 16 mm. The reactor was filled with 0.050 kg of glass beads with a diameter of 2 mm. For visualisation these beads were spraypainted yellow, while 20 of these glass beads were painted black to allow for particle tracking, with PTV. The size of the glass beads was chosen to show similar fluidization characteristics in water to a system of DBT with Al_2O_3 catalyst beads, according to Reynolds and Stokes number similarities, shown in chapter 3. [217]

4.2.1.2 Image Analysis

Image analysis for determination of the expanded bed height and particle tracking experiments were taken using a Sony Cyber-shot 9.1-megapixel Camera. The opensource image analysis software ImageJ was used to examine the obtained results. [218] For particle tracking, the TrackMate add-on was used. [219] The PIV images were recorded with a high speed PCO Panda 26 M-USB, 5120 x 5120 camera using a Rodagon 35 lens, with a focal length of 35.1 mm and a 50 mm object width. A LED-PS pulsed laser LED module from Optolution was placed slightly above the camera and operated at 100 % intensity. The PIVlab software package available in MATLAB was used to analyse the PIV images. [220]

4.2.2 Governing Equations

4.2.2.1 Mass & Momentum Equations

CFD simulations were performed making use of the multiphaseEuler solver module in OpenFOAM version 11. [135] This solver uses the EE multifluid approach for modelling multiphase flows. This approach evaluates the equations for mass, and momentum for each phase separately. The phases are linked to each other by a shared pressure term and by the interface exchange term which is the main subject of interest in this work.

Continuity equation:

$$\frac{\partial}{\partial t}(\alpha_i \rho_i) + \nabla \cdot (\alpha_i \rho_i \boldsymbol{U}_i) = 0 \tag{4.1}$$

In this equation α_i is the volume fraction of phase i, ρ_i denotes the density and $\boldsymbol{U}_i$ is the velocity vector.

Momentum equation:

$$\frac{\partial}{\partial t}(\alpha_i \rho_i \boldsymbol{U}_i) + \nabla \cdot (\alpha_i \rho_i \boldsymbol{U}_i \boldsymbol{U}_i) = -\alpha_i \nabla p + \nabla \cdot (\alpha_i \boldsymbol{\tau_i}) + \alpha_i \rho_i \boldsymbol{g} + \boldsymbol{F}_{ji} \tag{4.2}$$

Compared to the continuity equation, the following terms are added: p for the pressure, $\boldsymbol{\tau}_i$ the stress tensor, $\boldsymbol{g}$ the gravitational acceleration, which also accounts for the buoyancy vector and $\boldsymbol{F}_{ji}$ the momentum exchange from phase *j* on phase *i*. This interfacial momentum exchange is calculated by the sum of all interphase exchange terms for each selected interaction. Included IE interactions in this work are drag force, the virtual mass force, and the turbulent dissipation.

4.2.2.2 Drag Models

The drag models account for the drag interaction in the different phases caused by the friction that occurs by the relative movement of one phase to another. In this system, this would be drag caused by relative movement of the solid in the liquid phase, of gas bubbles in the liquid phase, solid particles in the gas phase and liquid droplets in the gas phase. Since the system was completely filled with water with little of the volume being taken up by the gas phase, the drag interaction of the gas phase on liquid droplets was therefore omitted. The drag force, $\boldsymbol{F_D}$ per unit volume in OpenFOAM is calculated:

$$\boldsymbol{F}_{\boldsymbol{D}_{\boldsymbol{dc}}} = C_D(\boldsymbol{U}_d - \boldsymbol{U}_c) \tag{4.3}$$

The small letter *d* denotes the dispersed phase, the *c* denotes the continuous phase. C_D represents the drag coefficient for a dispersed and continuous phase pair. In fluid dynamics a drag coefficient is a dimensionless coefficient, which depends on the geometry of the object. In OpenFOAM the drag coefficient is calculated based on the model selected, via the term $C_D Re$. Calculating the drag coefficient in OpenFOAM looks as following:

$$C_D = \frac{3}{4} \cdot C_D Re \cdot C_s \cdot \ \rho_c \cdot \frac{\mu_c}{d_d^2} \cdot \alpha_d \tag{4.4}$$

The formulas for the drag coefficient $C_D Re$ used in this work are listed in Table 4-2. The symbol C_s denotes the coefficient for the swarm correction which has not been studied in this work. The value of $C_D Re$ depends on the, the phase pair Reynolds number Re_d, which is calculated according to equation 4.17. This is however not a true Reynolds number since it does not include the density of the continuous phase. For this reason the term ρ_c is included in equation 4.4.

Table 4-2 Drag Coefficient formulas according to the different models used in this work.

Schiller Naumann	$C_D Re = \begin{cases} 24 \cdot (1 + 0.15 Re_d^{0.687}) \mid Re \leq 1000 \\ 0.44 Re_d \mid Re > 1000 \end{cases} \qquad (4.5)$	[196]
Ishii Zuber	Dense spherical particle regime: $C_D Re = \begin{cases} 24 \cdot (1 + 0.1 Re_m^{0.75}) \mid Re_m \leq 1000 \\ 0.44 Re_m \mid Re_m > 1000 \end{cases} \qquad (4.6)$ Distorted particle regime $C_D Re = \frac{2}{3} \cdot \frac{1 + 17.67\, \mathcal{F}^{6/7}}{18.67\, \mathcal{F}} \cdot \sqrt{E\ddot{o}} \cdot Re_d \qquad (4.7)$ Dense spherical cap regime $C_D Re = \frac{8}{3} (1 - \alpha_d)^2 \cdot Re_d \qquad (4.8)$ With Re_m $Re_m = \frac{\lvert U_d - U_c \rvert \cdot d_g}{\mu_m} \qquad (4.9)$ With μ_{mix} $\mu_{mix} = \mu_c \cdot (1 - \alpha_d)^{-2.5 \cdot \frac{\mu_d + 0.4 \cdot \mu_c}{\mu_d + \mu_c}} \text{ for } \max(1 - \alpha_d) < 0.001 \qquad (4.10)$ With $\mathcal{F}$ $\mathcal{F} = \min\left(\frac{\mu_l}{\mu_{mix}} \cdot \sqrt{1 - \alpha_c}, 1e^{-3}\right) \qquad (4.11)$	[182]
Tomiyama Kataoka Zun Sakaguchi	$C_D Re = max\left(\frac{24}{Re_d}(1 + 0.15 Re_d^{0.687}), \frac{8}{3} \frac{E\ddot{o}}{E\ddot{o} + 4}\right) \cdot Re_d \qquad (4.12)$	[181]

Lain	$C_D Re = \begin{cases} 16 \quad \| Re_d > 1.5 \\ 14.9 \cdot Re_d^{0.22} \mid 1.5 < Re_d < 80 \\ 48 \cdot \left(1 - 2.21 \cdot \sqrt{Re_d}\right) \mid 80 < Re_d < 1500 \\ 2.61 \cdot Re_d \mid 1500 < Re_d \end{cases}$ (4.13)	[198]
Gidaspow **Ergun** **Wen** **Yu**	Ergun term for $\alpha_c < 0.8$ $C_D Re = \frac{4}{3} \cdot \left(150 \cdot \frac{(1 - \alpha_c)}{\alpha_c} + 1.75 \cdot Re_d\right)$ (4.14) Wen and Yu term for $\alpha_c \geq 0.8$ $C_D Res = \begin{cases} 24 \cdot [1 + 0.15 \cdot (Re_d - \alpha_d)^{0.687}] \| Re_d \cdot (1 - \alpha_d) < 1000 \\ 0.44 \cdot Re_d \cdot (1 - \alpha_d) \mid Re_d \cdot (1 - \alpha_d) \leq 1000 \end{cases}$ (4.1) $C_D Re = C_D Res * (1 - \alpha_d)^{-3.65} \cdot \alpha_c$ (4.16)	[200]
Phase Pair **Reynolds** **Number**	$Re_d = \frac{d_d \|U_d - U_c\|}{\mu_c}$ (4.17)	[181]
Eötvös **Number**	$E\ddot{o} = \frac{\|g\|(\rho_c - \rho_d) d_d^2}{\sigma}$ (4.18)	[181]

4.2.2.3 Virtual Mass

The virtual mass force, also called the added mass, is the inertia required to move the continuous fluid away to make space for the accelerating discrete phase. It is a force that – in general – slows down the movement of the discrete phase. In OpenFOAM virtual mass force is calculated by:

$$\boldsymbol{F_{VM}} = C_{VM} \cdot \alpha_d \cdot \rho_c \left(\frac{D\boldsymbol{U_d}}{Dt} - \frac{D\boldsymbol{U_c}}{Dt}\right) \tag{4.19}$$

The term $\frac{D}{Dt}$ represents the material derivative for the velocity for each phase. Different models are available to account for the virtual mass force, but to limit the scope it was opted to only use a constant C_{VM} value of 0.5. This was done in accordance with the work of Hu et al. [181] Attempting to run three – phase fluidized bed simulations without the addition of the virtual mass rendered the simulations highly unstable. It was opted to always keep the virtual mass model enabled in any simulation.

4.2.2.4 Turbulent Dispersion

The turbulent dispersion force is a force that increases the dispersion of the discrete phase in the direction perpendicular to the continuous flow. This force is due to the turbulent eddies in the continuous flow that drag the discrete phase along in their path. The turbulent dispersion force in OpenFOAM is evaluated by: [181]

$$\boldsymbol{F_{TD}} = C_{TD} \cdot \alpha_d \cdot \rho_c \cdot k_c \cdot \nabla \alpha_c \tag{4.20}$$

In this equation C_{TD} represents the turbulent dispersion coefficient, which equals 1 for the gas – liquid terms and 0 for other phase pair interactions. The value of k_c is the turbulent kinetic energy for the continuous phase. Like the virtual mass, attempting to simulate the three-phase fluidized bed was unstable and thus it was opted to always turn this model on for the gas and liquid interactions.

4.2.2.5 Interphase Compression

This term in the multiphaseEulerFoam solver allows to switch between EE multiphase model and the Volume Of Fluid (VOF) approach based on the volume fraction of the phases, which can be set dynamically by the user. The VOF approach is a method to solve multiphase flows with continuous – continuous flow systems only, and makes use of an artificial compression term in the transport equation of the volume fraction to keep the interphase between the phase sharp. [221]

$$\frac{\partial \alpha_i}{\partial t} + \boldsymbol{U}_i \cdot \nabla \mathrm{\alpha_i} + \nabla \cdot \left(\boldsymbol{U}_{com} \alpha_i (1 - \alpha_i)\right) = 0 \tag{4.21}$$

With $\boldsymbol{U}_{com}$ the compression velocity and *i* a general symbol for either phase.

$$\boldsymbol{U}_{com} = C_\alpha |\boldsymbol{U}_i| \cdot \frac{\nabla \alpha_i}{|\nabla \alpha_i|} \tag{4.22}$$

The term C_α can be either 0 when the compression factor is not used or 1 when it is turned on, or any intermediate value. [222]

4.2.2.6 Turbulence

The chaotic nature of the LGSFB requires the need for a turbulence model in the simulation framework. I opted to use the Reynolds Averaged Navier Stokes (RANS) method for turbulent modelling, as it provides a decent accuracy for turbulent flows at reasonable computational cost to other turbulence modelling approaches. For the liquid phase simulations, the k-omega Shear Stress Transport (SST) model developed by Menter was always enabled. [158] The use of a turbulence model for the gas phase was one of the criteria investigated in the preliminary analysis of the simulation system. In these sections the gas phase turbulence model was not enabled, from section 4.3.3 onwards the k-omega SST model was always enabled after a 1 second initialization period to increase stability of the simulation. Simulating the particle phase in this Eulerian framework was done by making use of the Kinetic Theory of Granular Flow (KTGF). [223]

4.2.3 Simulations and Experimental Settings

The physical properties and operation settings of the CFD simulations and the experimental work are shown in Table 4-3. The use of the KTGF requires specific values to account for particle wall – and particle – particle collisions, these are the specularity and restitution coefficients, respectively. These values are also listed in Table 4-3. Generally, in CFD simulations using the KTGF, an estimation of the specularity and restitution coefficient is required, however, for liquid driven systems the errors induced by these coefficients are only a few percent. [224, 225]

The fluidized bed is operated by flowing water at $1.5\cdot 10^{-5}$ m³ s^{-1} or 0.9 LPM, with a He gas flow of $1.1\cdot 10^{-6}$ Nm³ s^{-1} which was measured by a Bronkhorst thermal mass flow controller.

4.2.4 Meshing and Grid Convergence Study

The mesh used for the CFD simulations is a 2D mesh prepared using the native OpenFOAM meshing utilities “blockMesh”. The mesh has dimensions of 40 mm by 188 mm, the z – direction for which no solutions are solved has a thickness of 8 mm. This was done to keep the total volume of the mesh identical to the real-life situation, which allows for easier calculations and comparison between the CFD case and the real 2D fluidized bed. Since the 2D mesh was used, the inlet of the gas and liquid selected was the entire lower section of the mesh. Firstly, to study the influence of the grid size of the mesh a Grid Convergence Index

(GCI) was conducted according to method of Roache. [136] Three meshes were created with a refinement level of 1.5 in the x and y directions, yielding a coarse mesh with 7 520 cells, a medium mesh containing 16 920 cells, and a fine mesh of 38 070 cells. The GCI was evaluated based on the time averaged particle bed height, one of the properties on which the simulations is evaluated also experimentally. The models used were the same as the models used in Case 1, see Table 4-5. I used similar simulations settings as in Chapter 3, but I also added a switch between the dispersed, segregated and continuous regimes for the liquid and gas. The solid – liquid drag model used was the Gidaspow model, and the Ishii – Zuber model was used without swarm correction for the gas phase, the Schiller-Naumann model was used for gas – solid interactions. The GCI study showed an asymptotic convergence of 0.999, which is close to 1, i.e., the criterion for convergence. This is graphically represented by Figure 4-2. Relative errors between the meshes are minor compared to the extrapolated value. The finest mesh was selected, to keep the errors as low as possible and since the simulations could be completed within 30 hours on a single compute node consisting of a dual 32-core AMD Epyc 7452 Rome generation CPU.

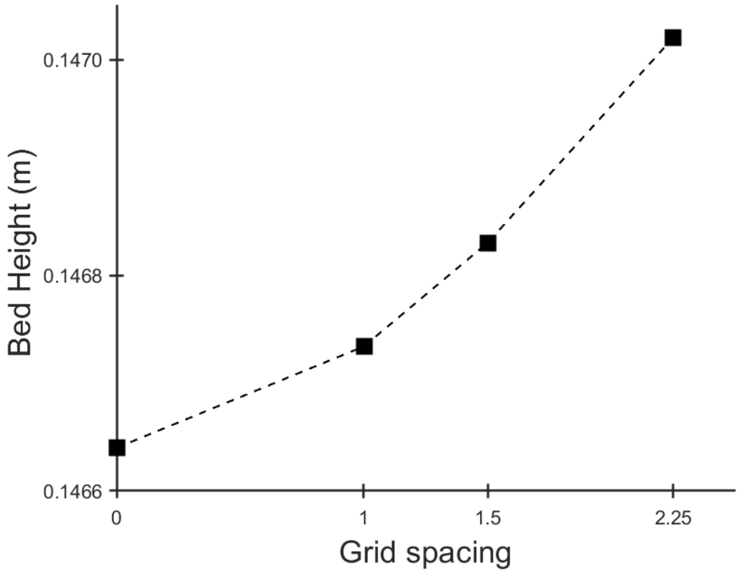

Figure 4-2 GCI study on three different meshes using the time averaged bed height of a liquid – solid simulation.. Three meshes were used: a coarse mesh (7 520 cells), a medium mesh(16 920 cells) and a fine mesh (38 070 cells), the extrapolated value was calculated according to the GCI method reported by Roache.[136]

Table 4-3 Physical properties used for the simulations and experimental setup and CFD boundary conditions.

	Physical Properties
Liquid phase	**Water**
Liquid phase state	Continuous / Dispersed
Liquid density	1000 kg m^{-3}
Liquid dynamic viscosity	$1.0 \cdot 10^{-3}$ Pa s
Liquid surface tension	0.07 N m^{-1}
Gas phase	**Helium**
Gas phase state	Dispersed / Continuous
Gas density	Calculated by ideal gas law
Gas dynamic viscosity	$1.96 \cdot 10^{-5}$ Pa s
Particle phase	**Glass**
Particle phase state	Dispersed
Particle density	2500 kg m^{-3}
Particle diameter	0.002 m
Particle Mass	0.050 kg
Particle Restitution Coefficient	0.8
Particle Specularity Coefficient	0.01

Boundary Conditions CFD

	Inlet	**Outlet**	**Walls**
Hydrostatic Pressure	FixedfluxPressure	PrghPressure p = 1e5 Pa	FixedfluxPressure
Liquid Velocity*	FlowRateInletVelocity $\dot{V}$ = 3.0e-5 m³ s-1	ZeroGradient	NoSlip
Gas Velocity*	FlowRateInletVelocity $\dot{V}$ = 2.3e-6 m³ s-1	ZeroGradient	NoSlip
Particle Velocity	Fixed Value U = (0 0 0) m s-1	Fixed Value U = (0 0 0) m s-1	JohnsonJacksonParticleSlip Specularity Coeff = 0.01
Liquid Volume* Fraction	FixedValue α = 0.5	InletOutlet α = 1	ZeroGradient

Gas Volume* Fraction	FixedValue α = 0.5	InletOutlet α = 1	ZeroGradient
Particle Volume Fraction	FixedValue α = 0	FixedValue α = 0	ZeroGradient
Liquid k	turbulentIntensityKineticEnergyInlet I = 0.05	zeroGradient	kqrWallFunction
Liquid omega	turbulentMixingLengthFrequencyInlet L = 0.00174	zeroGradient	omegaWallFunction
Gas k	turbulentIntensityKineticEnergyInlet I = 0.05	zeroGradient	kqrWallFunction
Gas omega	turbulentMixingLengthFrequencyInlet L = 0.00174	zeroGradient	omegaWallFunction
Particle Granular Temp.	fixedValue Θ = 0.0001	zeroGradient	JohnsonJacksonParticleTheta Specularity = 0.01 Restitution = 0.8
Number function gas	fixedValue f = 1	zeroGradient	zeroGradient

---

* The flowrate is calculated from $\alpha \cdot \dot{V}_{in}$

4.3 Preliminary Simulations

In the field of Eulerian – Eulerian (EE) multiphase simulations, there is a large number of parameters that can be selected that influence the outcome of the simulation. Before diving into the main body of the CFD study, i.e., the selection of appropriate drag models for LGSFBs, four of these parameter settings are selected for initial comparison. These are the applicability of a 2D case, the use of a population balance model for the dispersed gas phase diameter, the use of interphase compression to switch between a full Eulerian and a VOF computational approach for the gas – liquid interphase and finally, the effect of gas phase turbulence on the results. These initial cases will be compared qualitatively to select the settings for the best simulations settings. The drag model combinations for the simulations used during the preliminary simulations were the same as those used for the GCI analysis.

4.3.1 2D Assumption for the three-phase flow

The assumption of 2D *pseudo*-homogenous flow for granular flows dispersed in liquid phases holds when the width of the reactor vessel does not exceed 9 times the particle diameter. [212] To be able to extrapolate these findings for LGSFBs, a 3D simulation was run with an identical grid in the z – direction as was used for the GCI study, i.e., the aspect ratio obtained in the mesh for the 3D case was exactly 1.

Using this mesh of 685 260 cells for a simulation of the fluidized bed reactor investigated in this work, I conclude that for the liquid and particle velocities, the z – component of the velocity is negligible compared to the total velocity magnitude. However, for the gas velocity, the z-component is larger compared to the particle and liquid fractions, see Figure 4-3A, B and C. When evaluating the z-component contribution to the total magnitude of the gas velocity, it can be seen that this z – component contribution is still negligible, so the 2D assumption can also hold in the studied LGS system. This corresponds also to earlier observations of EE – simulations of *pseudo*-2D fluidized beds for larger particles, which seem to be much less influenced by wall effects compared to simulations of small particles. [226]

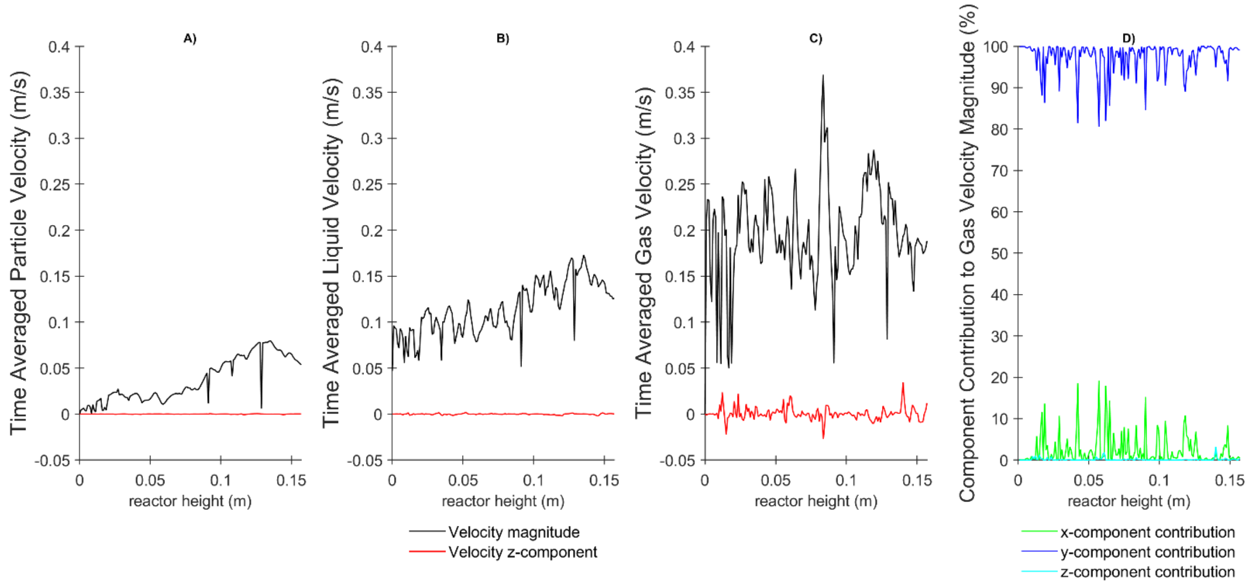

Figure 4-3 Time averaged velocity profiles over the central axis of the 3D simulation cases of the pseudo-2D LGSFB. Comparison of the velocity magnitude and z - component of A) the particle velocity, B) the liquid velocity and C) the gas phase velocity. D) depicts the percentile contribution of each component (x, y, z) to the total velocity magnitude.

4.3.2 Gas phase volume fraction models

The second aspect of the three-phase simulations that were checked, was the model for the gas phase. Figure 4-4A shows a snapshot of a bubble breaking through the particle bed in the pseudo-2D fluidized bed. A link to the video of the experiment can be found in Appendix I. When the gas bubbles are bursting at the surface of the solid bed, it tends to happen via a singular large bubble, which is an indication of more coalesced bubble flow regimes. This regime seems to be most adequately captured using simulations with population balance models and interface compression, seen in Figure 4-4C. This observation was made from comparing the gas bubbles bursting at the solid bed interface during the experiment, seen on Figure 4A, with the simulated results, i.e., considering Figure 4B a fixed dispersed bubble diameter, Figure 4C a population balance with interface compression, and Figure 4D a population balance model without interface compression. The models for coalescence and breakup and maximal and minimal bubble size used for the population balance model can be found in Table 4-4.

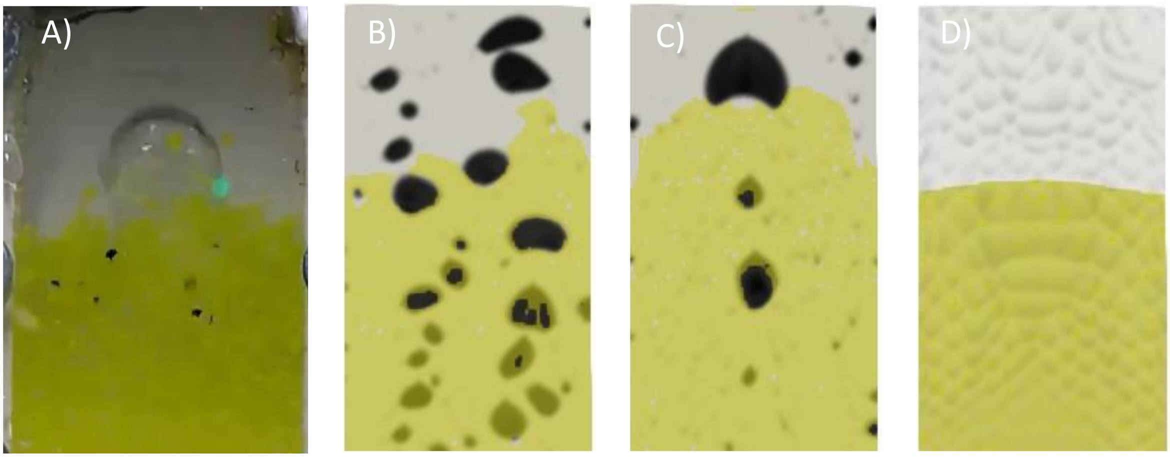

Figure 4-4 comparing the different settings of the gas phase simulation results to the experimental result A), where a bubble breaking through the particle bed is observed. B) Simulation results of the gas phase (black dots) breaking through the solid bed (yellow, phase volume fractions between 0.2 and 0.48), using a fixed dispersed bubble diameter of 1.2 mm. C) Using a population balance model and D) population balance model simulation with interphase compression between the gas and liquid case turned off ($C_\alpha = 0$).

The best results were obtained by using a population balance model for the diameter of the dispersed gas phase, i.e. when the volume fraction of the gas falls below 0.4. This value is the recommended cut-off value according to Černe et al. [227] for interphase sharpening. The modelled bubble diameter of the dispersed gas phase is thus allowed to increase, resulting in larger simulated bubbles of gas with volume fractions above 0.4. The use of the interphase compressions scheme, see Eq. 4.21 and 4.22, has an obvious influence on the behaviour of the gas bubbles in the LGSFB simulations. When the interphase compression is turned off ($C_\alpha = 0$), it means there is no term to increase the sharpness between the liquid and the gas interphase, and no large gas bubbles appear in the simulation. This is why it was opted to keep the interphase compression on ($C_\alpha = 1$) in all subsequent simulations, i.e. using the setup from Figure 4-4C.

Table 4-4 Models and parameters for the population balance model used.

Coalescence Model	Prince – Blanch
Binary Breakup Model	Lehr – Millies – Mewes
Min. Bubble Size	1 mm
Max. Bubble Size	30 mm

4.3.3 Gas Phase Turbulence

The final aspect checked for the preliminary screening, was the addition of a turbulent flow in the gas phase. In all previous results in this work, phase turbulence was not enablded. In OpenFOAM 11 the multiphaseEuler solver module allows to enable turbulence models for each phase individually. The simulation, however, will not compute past the first timestep if a turbulence model is turned on without the phase being present inside the computational domain. For this reason, I decided to simulate the first second of the simulation without adding the gas phase turbulence. After this second of initialization, the gas turbulence model was activated, and the simulation was run for an additional 5 seconds to extract the time-averaged velocity field. Time averaging of the case with laminar gas flow was obtained over the same absolute timesteps. Figure 4-5 compares the time-averaged gas velocities upon simulation in the LGSFB. By enabling the turbulence model, in Figure 4-5B, the gas velocity starts to take on a wavelike pattern at the bottom of the reactor, rather than moving straight up as is the case of the laminar system. Comparing this to the actual experiment, as can be seen in the video of the experiment in Appendix I, the gas bubbles indeed tend to move sideways initially before moving upwards, which is why it was selected in the subsequent simulations to always enable the gas phase turbulence model after a 1 s initialization period following the gas injection in the simulation.

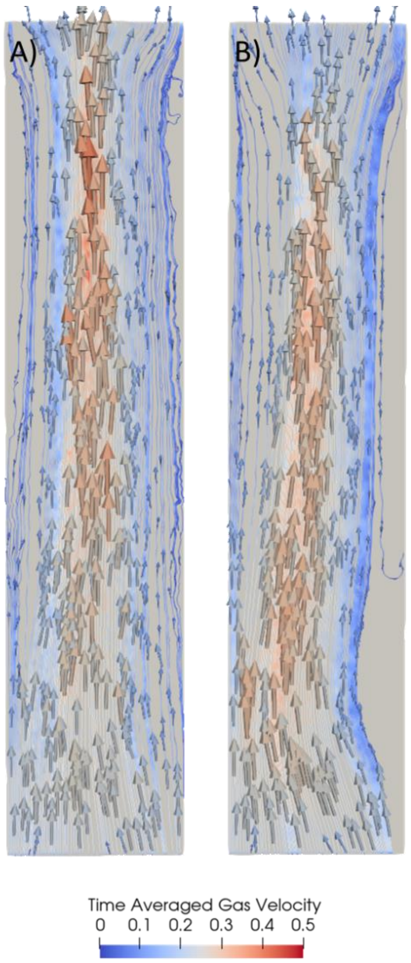

Figure 4-5 Time-averaged gas velocity streamlines simulated in the pseudo-2D LGSFB. A) No gas phase turbulence B) gas phase turbulence enabled. Reference video available in Appendix I.

4.3.4 Studied Drag Model Combinations

A total of 12 simulation cases were constructed combining drag models for the gas – liquid and solid -gas interactions. In each of these simulated cases, the liquid – solid drag was selected to be the Gidaspow – Ergun – Wen – Yu model, as this model combines both the fixed bed regime by the Ergun model for the initialization of the simulation cases and it can automatically switch to the Wen and Yu model for the fluidized state. The alternative to the Gidaspow model, the Syamlal O'Brien model fell outside of the scope for this thesis, since no large difference between the two was expected in this particular setup. The Syamlal O'Brien model and Gidaspow model show a high similarity in predicted drag coefficients in the range of α_p 0.4 – 0.5, the expected range for fluidized beds of the studied 2 mm glass spheres in liquid – solid operation. [228] The cases are constructed to evaluate four different drag models for the gas – liquid interactions. For each of these drag models, there are three options. The solid – gas interactions are modelled by the Schiller – Naumann approach, by using the assumption that the drag models can be described by gas phase models since the particles tend to follow the gas phase trajectories. [206] The second option for the solid – gas interactions is the use of the Gidaspow – Ergun – Wen and Yu models, which is the same model as used for the liquid – solid interactions. Thirdly, the option was chosen to ignore the solid – gas drag model, meaning that drag on the particles was only evaluated by the drag force of the liquid on the solid phase.

Table 4-5 Overview of the different drag model combinations used for the 12 initial simulations cases., Cases that successfully ran the entire simulation protocol are highlighted in green, failed cases in red.

	Case1	**Case2**	**Case3**
Gas - Liquid	Ishii – Zuber	Ishii – Zuber	Ishii – Zuber
Solid - Gas	Schiller - Naumann	Gidaspow – Ergun – Wen - Yu	X
	Case4	**Case5**	**Case6**
Gas - Liquid	Schiller - Naumann	Schiller - Naumann	Schiller - Naumann
Solid - Gas	Schiller - Naumann	Gidaspow – Ergun – Wen - Yu	X
	Case7	**Case8**	**Case9**
Gas - Liquid	Tomiyama – Kataoka - Zun – Sakaguchi	Tomiyama – Kataoka - Zun – Sakaguchi	Tomiyama – Kataoka - Zun – Sakaguchi
Solid - Gas	Schiller Naumann	Gidaspow – Ergun – Wen - Yu	X
	Case10	**Case11**	**Case12**
Gas - Liquid	Lain	Lain	Lain
Solid - Gas	Schiller Naumann	Gidaspow – Ergun – Wen - Yu	X

4.4 Results and Discussion

All of the cases were simulated for 11 seconds in total. From 0 – 1 s, solid beads were introduced in the system and allowed to settle. From 1 – 4 s the liquid flow was enabled, rendering liquid – solid only simulations. From 5-6 seconds the gas phase was introduced with the turbulence model disabled. Starting from 6 seconds the gas turbulence model was enabled. All temporal averages calculated based on the simulation data were obtained from 7 to 11 seconds. This timeframe was selected to make sure little influence from the simulation without gas phase turbulence model was included in the temporal average. Of the total twelve simulations presented in Table 4-5 only ten cases successfully completed all these intermediate steps, these ten simulation cases will be further evaluated. The successful and failed state of the simulations cases is shown by the green or red colour respectively in Table 4-5. The five cases that resulted in failed simulations, failed because the sum of the phase fractions inside the domain was not conserved. This occurred when the particle phase reached the outlet of the mesh, where the boundary condition did not allow for particles to pass. This was in correspondence with the experimental setup where the outlet was also closed for the particulate phase. In these transient simulations, the Co – number from equation 2.10 was kept at 0.05, which resulted in time steps around $2 \cdot 10^{-5}$ s.

4.4.1 Bed Height Analysis

The bed height was determined experimentally from DIA. The frames were extracted from a video recording of 5 min and 18 seconds long. Using the Grouped Z project tool from ImageJ, the average intensity of these images was calculated, as seen in Figure 4-6A. This average image was then converted to an 8-bit grayscale image, as can be seen in Figure 4-6B. By plotting the grayscale value over a line, the final peak value in the grayscale plot was used as a criterion for the time averaged bed height. The bed height was determined from averaging this peak position by plotting the intensity over the bed height at 10 different positions along the x-direction of the reactor. An additional length of 11.9 mm was added to the average height determined from DIA. This was done to account for the added height at which the image was taken relative to the bottom of the actual bed. From the analysis it showed that the bed height totaled 160 ± 1 mm. The bed height from the CFD simulations was extracted in a similar method using images of the time averaged particle volume fraction, a threshold between 0.2 and 0.4, as shown in Figure 4-6D. This value was selected to determine the bed height since the highest volume fraction obtained did not exceed 0.4.

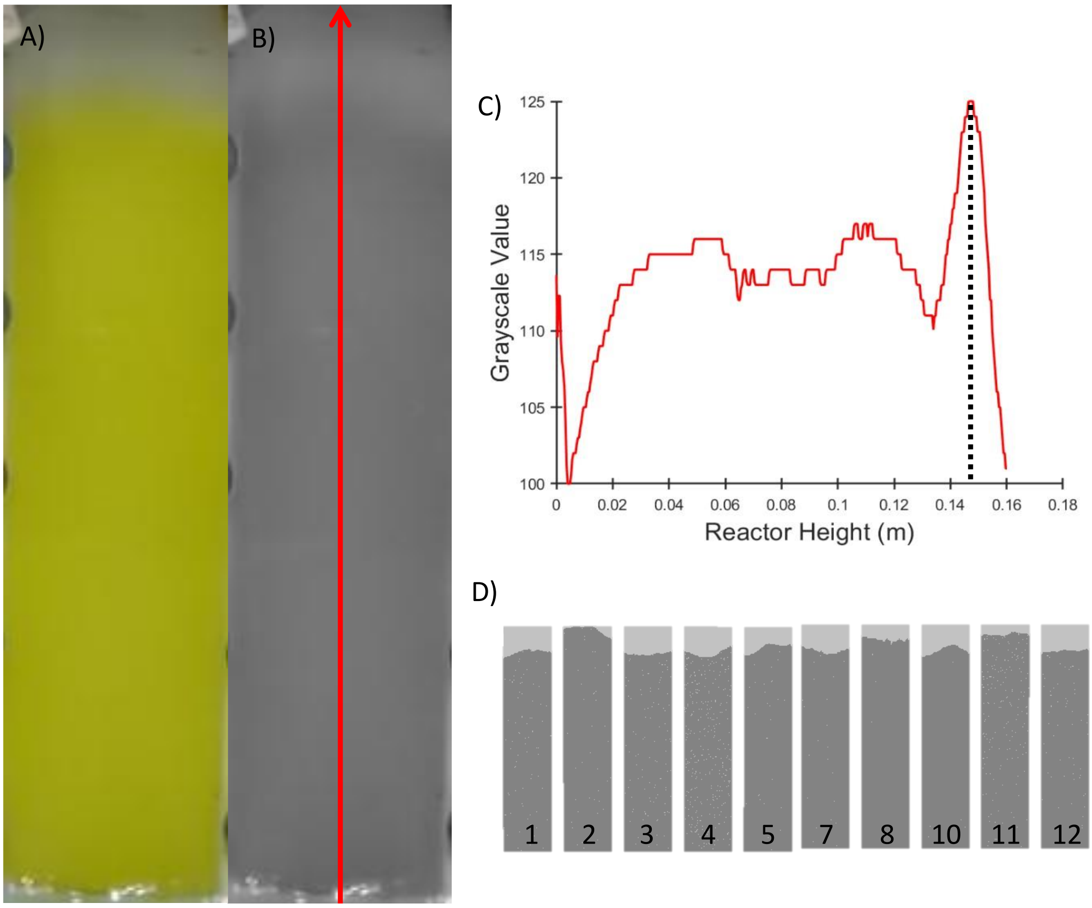

Figure 4-6 Procedure to capture the bed height from image analysis. A) the average intensity image from the captured video. B) The average image converted to grey scale. C) An example plot of the grayscale intensity plotted over the red line shown on B. D) Thresholds of the particle beds from the CFD simulations for volume fractions between 0.2 and 0.4, these images served as basis to extract the particle bed height from the CFD simulations.

The results of the extraction of the bed height are visualised in Figure 4-7 and it is clear that the CFD simulations tend to overestimate the bed height compared to the experimental value. Secondly, it can be seen that in the cases where the Gidaspow model has been selected for the solid – gas interactions (Case2, Case8 and Case11), the bed height is highest and deviates most from the experimental values. Case 8 narrowly falls within a 10% deviation from the experimental results, as opposed to cases 2 and 11. The other model combinations are able to predict the time averaged bed height quite accurately. Combining the results from Figure 4-7 with the observations from Figure 4-7A and Figure 4-7D, it can be seen that cases 3 and 12 show a relatively flat bed, in line with the experimental observation. The particle bed height determined from these models differs by less than 10% from the experimentally derived value, making these combinations suitable to predict the particle bed in a *pseudo*-2D fluidized bed.

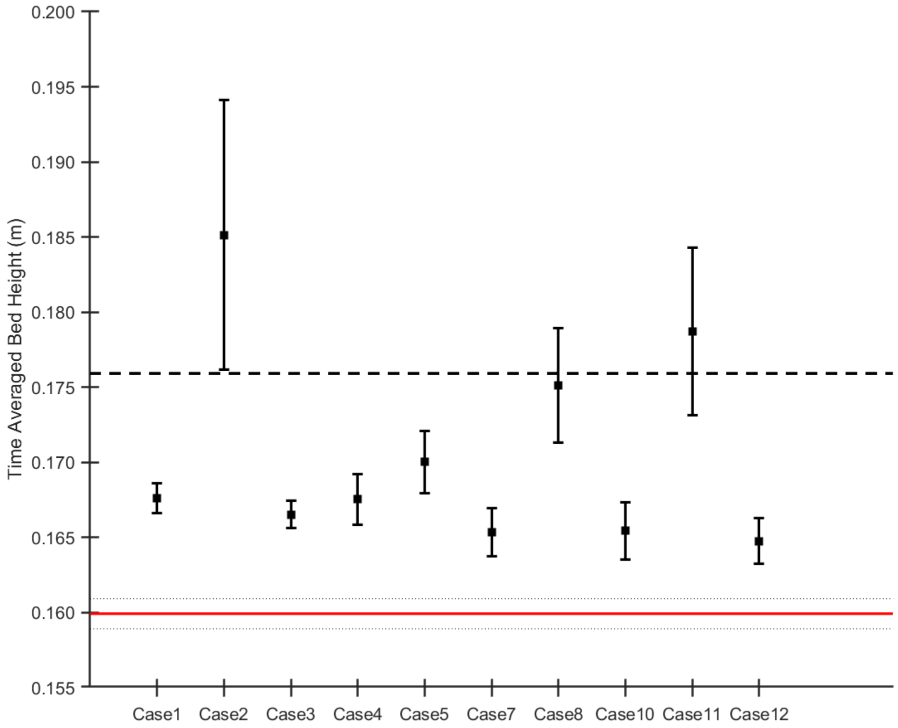

Figure 4-7 Plot of the extracted bed height from CFD (scatter plot), the red line denotes the experimentally determined bed height, with the experimental error interval (±1 mm) as the dotted line. The dashed line marks the 10% deviation from the experimental value (± 16 mm).

4.4.2 Time Averaged PIV

PIV analyses of LGSFB, especially liquid-dominant systems are limited in literature as pointed out by a recent review from Neogi et al. [210] This is partly because LGSFB are inherently chaotic systems, which makes them difficult to study and analyse. To limit this complexity, the *pseudo*-2D fluidized bed was studied by PIV only in the bottom region of the bed, since in this region the gas bubbles are not yet fully coalesced compared to the top of the bed, rendering more accurate time averaged results of the PIV analysis. Figure 4-8A depicts via the blue dashed box, the studied region in the LGSFB, Figure 4-8B shows one of the images obtained from the PIV experiment, with the selected region of interest (ROI) as the red box. Figure 4-8C shows the pre-processed image to start the PIV analysis, with the background data subtracted and by using a contrast limited adaptive histogram equalization filter at 512 pixels and with the intensity capping filter enabled. For the PIV experiments, 100 image pairs were generated, with a frame rate for the laser pulses at 5 Hz. The time required to generate the 100 image pairs was 79 s.

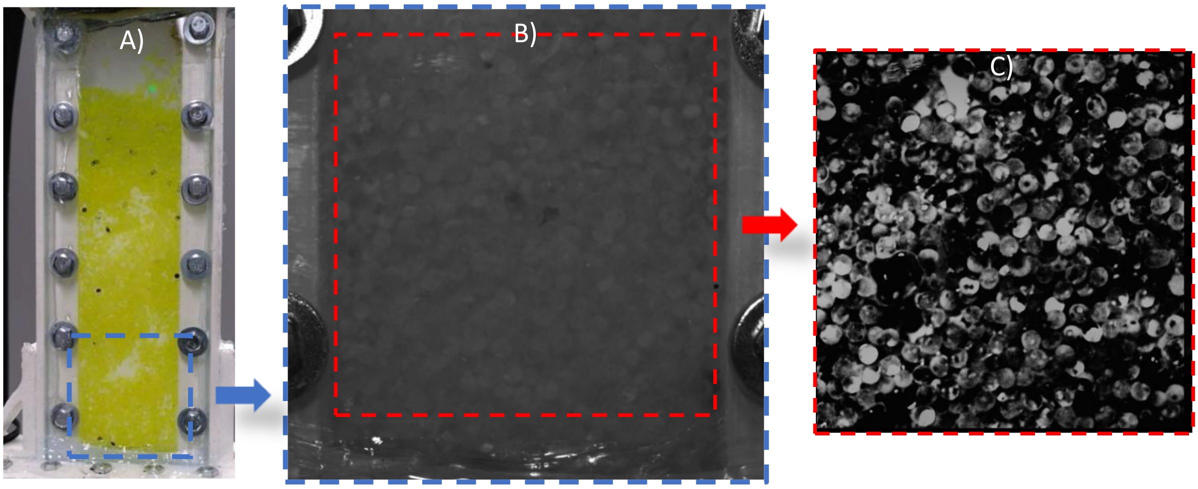

Figure 4-8 Regions studied for the PIV experiment. A) The full fluidized bed reactor, the blue box denotes the area captured by the camera. B) the area captured by the PIV camera, with the ROI, the area on which the analysis will take place. C) The pre-processed PIV image after subtracting the background and enabling filters.

A visual representation of the extracted particle velocity magnitude from the PIV experiment and from the simulations can be seen in Figure 4-9A. A simple visual observation allows to discriminate qualitatively between the resulting velocity profile from the different drag model combinations: Only a few model combinations show a profile in velocity streamlines matching that obtained from PIV. These cases are cases 3, 7 and 8 and to a certain degree cases 4 and 11.

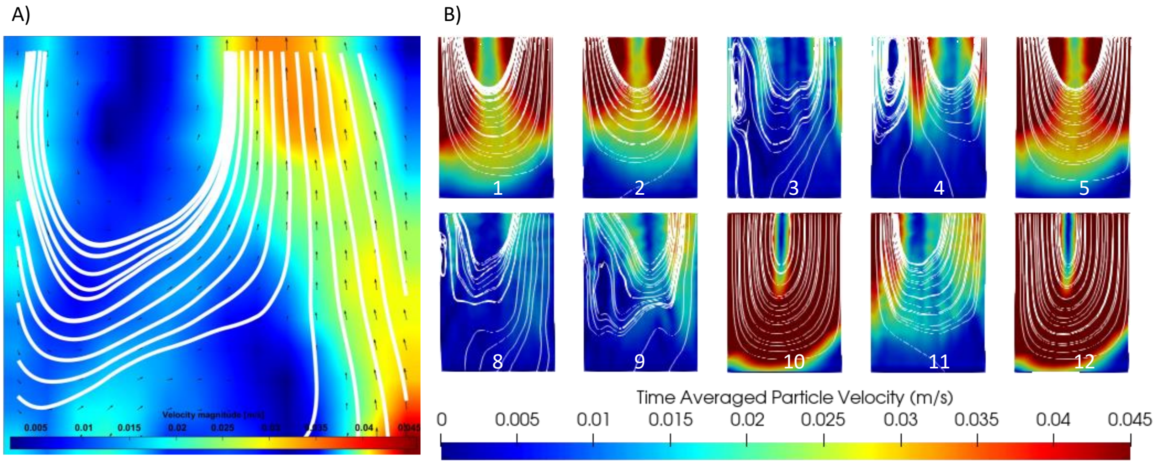

Figure 4-9 Time Averaged Particle Velocity Magnitude. A) Extracted via PIV (experimental values). B) Results from the simulations. The white lines denote the streamlines crossing a line at 38 mm bed reactor height.

This visual observation is also further corroborated by plotting the y-component of the time averaged particle velocity as is depicted in Figure 4-10. This plot shows that the particle velocity is captured closest by case 7, especially for the middle of the reactor. The model combination of case 7 is less accurate closer to the walls. The data near the wall is more accurately captured by case 8, but it deviates more from the centre. Case 8 also captures the switching between upwards and downwards particle flow over the full reactor width, which is depicted by the sign change of the y component of the velocity.

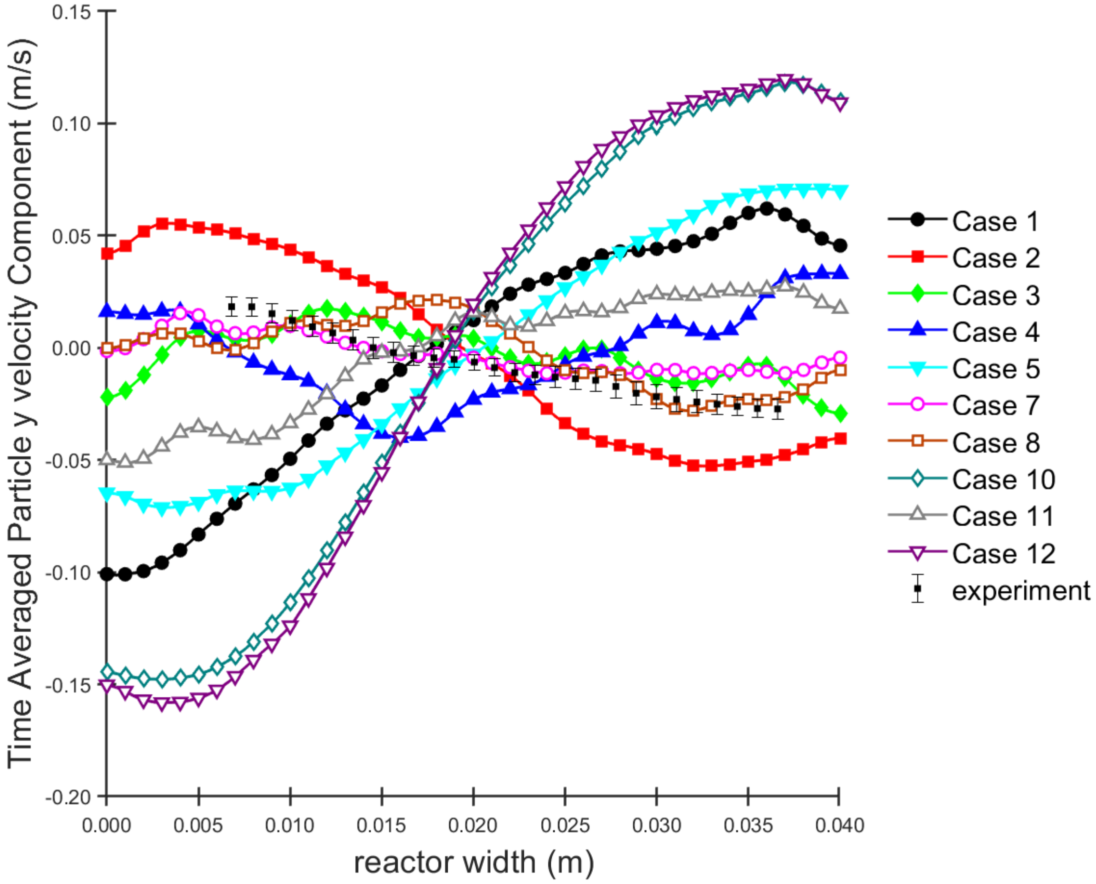

Figure 4-10 Plot of the time averaged particle velocities obtained from PIV and simulations. The y – velocity component of the velocity was extracted from a horizontal line at 38 mm height in the reactor. The error bars on the experimental values show the 10 % confidence interval calculated on the averaged result.

4.4.3 Time Averaged Particle Tracking Velocimetry

By averaging the Lagrangian Particle Data over time on a specific location, the results from the obtained time averaged velocity profile can be compared to Eulerian time-averaged results. [229] In this regard, I used PTV to determine the fluid velocities of the particles when they are moving downwards next to the wall. To analyse this, a 5 min 18 s long video was recorded of the complete fluidized bed region, with 20 black beads serving as tracers. The video was then firstly converted to individual frames, which were then converted to a grayscale before being binarized. The resulting images were analysed with the ImageJ extension TrackMate. The datapoints could be captured by TrackMate using a thresholding filter, and the simple LAP tracking method was used to generate the tracks. After filtering the tracks that travelled at least 20 mm downwards in the region of interest, a total of 164 tracks was detected by the TrackMate. To calculate the average velocity magnitude, the x and y – positions on the tracks were rounded towards the closest 2 mm interval and on each of these positions the average of the velocity observed on these datapoints was extracted. The x – positions after rounding corresponded to 9,7,5,3,1 mm distance from the right wall, the y – positions varied from 71 to 161 mm reactor height.

Figure 4-11 compares the data extracted at 3 mm from the wall for both the simulations and the experiment. None of the simulations show a velocity profile that fully corresponds with the measured results. In the middle section of the reactor, from 70 mm to 120 mm height, cases 3 and 8 show the closest correspondence to the experimental data. Between 120 mm and 140 mm in height, case 8 and 11 closely match the measured particle velocity. However, between 140 mm and the top of the bed, the measured particle velocity is not accurately captured by the simulations. This region is a highly chaotic region due to the local spouting of the bed which complicates the measurements of the particle velocity. Since case 8 follows the trend of the measured particle velocities the most closely, I would recommend using this set of models when investigating the downwards particle movement.

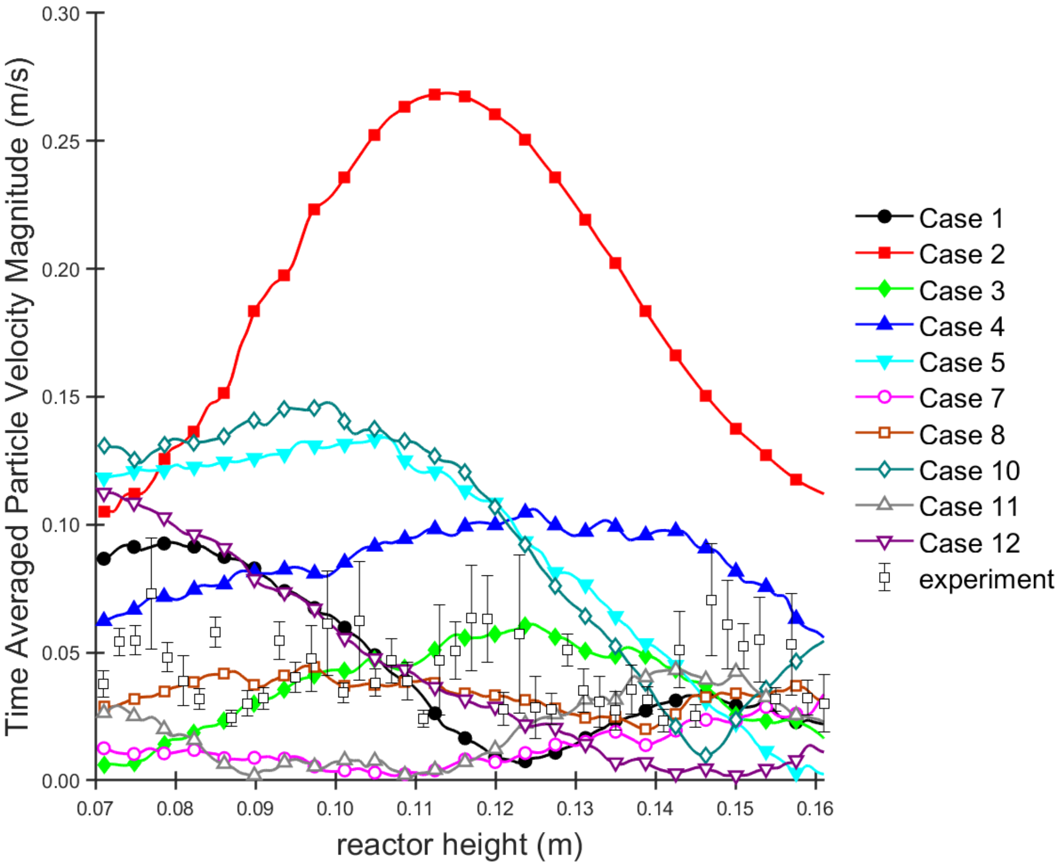

Figure 4-11 Graphical comparison of the extracted velocity profiles 3 mm from the right wall of the pseudo-2D fluidized bed reactor. The error bars on the experimental data represent the standard error calculated on the average velocity.

4.4.4 Discussion

By comparing several simulation settings in this chapter, I aimed to highlight that these settings can have a considerable influence on the results of the simulation. In certain cases, it can even be the difference between obtaining any simulation results or not, as only 2 of the attempted model combinations did not prove to provide stable simulations. By comparing the simulated cases with experimental results on three distinct aspects, no ideal simulation case setting was determined to simulate this system of water, He, and glass, but some of the simulation settings clearly outperformed others to predict the behaviour of the LGSFB. From the analysis of the bed height, it was shown that by using the Gidaspow model to account for solid – gas drag interactions, the simulated bed height was overpredicted, compared to similar cases where it is not used. However, case 8 which did feature this model showed to predict the particle velocity profile adequately for both the bottom region of the bed and near the wall. Case 3 on the other hand, showed to have a more accurate prediction of the bed height, and also a flatter profile of the time averaged bed. The results of the velocity measurements using case 3 tended to deviate more from the experimentally obtained values compared to case 8, but still showed similar trends in velocity profiles. From this research alone, I could not highlight a model combination to simulate LGSFB that clearly outperformed the others. Based on this system, I would recommend using case 3 since it showed a similar bed height profile compared to the experiment and showed a high similarity in particle velocity profiles in the two regions investigated. The model combinations of cases 3,7 and 8 showed to be often closest to the experimental values. Some model combinations, on the other hand, deviated noticeably from the experimentally obtained data. By using case 2, the bed height is greatly overpredicted, it also greatly overpredicted the rate of the downwards velocity profile. The streamlines and velocity profiles of cases 1, 2, 5, 10 and 12 also deviated greatly from the experimentally obtained values, this warrants always special attention when simulating LGSFB as faulty results can be obtained simply by the selection of models to account for the interphase exchange forces (and especially drag forces) between the phases.

The analysis of the different drag models presented here offers yet another set of model combinations that can be used for LGS simulations using EE multiphase models. The proposed model combination of either, case 3, the Ishii – Zuber model for the liquid – gas interactions, without any models for the gas – solid interactions or the use of case 8, the Tomiyama model for the liquid – gas with the Gidaspow model for the gas – solid interactions proved to be two model combinations that showed highest similarity for use of LGSFB. This is a different result than what has been previously published on other three-phase EE simulations. For bubble columns the use of completely different drag models was proposed based on a similar comparison of different drag models. [205] The use of the Tomiyama model for the liquid – gas interactions, with a Gidaspow model for the liquid – solid and gas – solid drag model, was deemed best in a recirculated fluidized bed with 0.4 mm particles, a different system the one under investigation in this chapter. [230] This hints that there is no one – fit solution to simulate LGSFB, and the appropriate models will depend on the studied system.

For this LGSFB system, I see that two distinct model combinations proved superior over the others. Firstly, the model combination uses the Ishii – Zuber model without any models for the gas – solid drag interaction. The Ishii – Zuber model is originally designed to predict the drag coefficient in bubbly, droplet, and particulate flows, which already hints at is collective nature for different flow types. This is also seen in the mathematical expressions of equations 4.6 – 4.11, which show that this model changes based on the prevalent bubble regime. This model is able to accurately predict the particle bed, which is a culmination of the many effects present in a *pseudo* – 2D fluidized bed reactor. Interestingly, by adding the Gidaspow model for the gas – solid interactions, the bed height was overpredicted, which is not the case when the Schiller – Naumann model is included. It was observed in the simulations that the gas phase volume fraction in the mesh rose above 0.8. At this point, the Gidaspow is similar to the Schiller – Naumann interpretation but with an added multiplication factor based on the phase fraction. This factor is likely what causes additional drag on the particulate phase which causes the increased bed height predicted by the combination of the Ishii – Zuber model with the Gidaspow model for gas – solid drag. Increased bed height is observed for all the cases where the Gidaspow model for gas – solid drag was included, compared to the cases with a similar liquid – gas drag model.

Looking at equations 4.5 and 4.10 for the Schiller – Naumann and Tomiyama drag model respectively, it can be seen that these equations are very similar, but with a different limiter function, either based on the Reynolds number or on the Eötvös number. Comparing the cases which used the Schiller – Naumann or the Tomiyama model, it shows that the Tomiyama has a more accurate prediction of the velocity profiles obtained from PIV and PTV data. The use of the Lain model, which was originally developed for bubble columns using an Eulerian – Lagrangian [198] approach does not seem to warrant itself for use in a LGSFB. This model predicts the drag coefficient based on empirical correlations of the Reynolds number, as can be seen in equation 4.13.

4.5 Conclusion

In this chapter, I compared the results of several simulations using the multiphase Eulerian – Eulerian approach to simulate a *pseudo* – 2D fluidized bed containing water, He gas and glass beads with a particle diameter of 2 mm. I initially compared four simulation settings to simulate LGSFB, these were the assumption of a 2D geometry, the use of a gas phase population balance model, the use of interphase compression to capture the gas phase more accurately, and finally the addition of a turbulence model for the gas phase. It was concluded that the simulations could be run using 2D assumptions, that using a population balance model increased the bubble size captured by CFD simulation, as did the addition of interphase compression between the gas – liquid interphase. Finally, it was shown that the addition of a gas phase turbulence model tends to predict the trajectory of the bubbles in the bed more accurately than cases without gas phase turbulence. In the next step, I compared different drag model combinations to simulate the interactions between the liquid, gas, and solid phases in a pairwise manner. From this analysis it showed that using the Gidaspow model for the solid – liquid interactions and the Ishii – Zuber model for the gas – liquid interactions, while using no model to account for the solid – gas interactions proved to be a good choice to analyse the bed height by CFD simulation while showing similar trends in velocity profile compared to the experimental results. This model combination is the one I would recommend when simulating LGSFB with glass particles of 2 mm diameter.

Chapter 5

Exploring the Influence of Geometry Changes of the Swirling Fluidized Bed Reactor

5.1 Introduction

In this chapter I will study the influence of the H_2 gas release from H_{18}DBT on the uniformity of the particle bed in fluidization regimes. I will study the fluidization state of the particle bed both in a conventional fluidized bed reactor and in the SFB reactor of introduced in Chapter 3. By using the simulation settings of the EE multiphase framework that were explored in Chapter 4, the interactions between the liquid, gas and solid phases are captured based on a validated CFD settings for cold flow simulations of a LGSFB. This chapter will also include an exploratory study of the influence of design changes to the SFB on the flow distribution within the reactor.

To simulate the dehydrogenation of H_{18}DBT in Chapter 3, I made use of a source term which relates the amount of H_2 gas release per second to a theoretical H_2 release rate extracted from a reaction in a batch reactor. [85] In this Chapter, I will firstly introduce a custom programmed source term to mimic the H_2 release rate depending on the local volume fraction of particles in the cell and the volumetric flowrate of H_{18}DBT. This is a new approach to mimic the catalytic dehydrogenation reactions via CFD simulations. In the currently existing CFD codes there is no method available yet for heterogeneously catalysed reactions of liquid phases with a gas phase end product, with a moving catalyst bed. CFD codes have currently been developed mostly for non-catalytic or homogenously catalysed reactions as was shown in Chapter 2. The interpretation of the chemical reactions that was used as a tutorial example in Chapter 2, has previously been extrapolated to heterogeneously catalysed reactions of gas – solid systems for fixed bed systems. In this approach only the gas phase is simulated, the effect of the particle phase is modelled by a porosity source term, to account for momentum change in the gas phase. [231-235] This approach is only valid for fixed particle beds, since the porosity source which accounts for the particle bed is predefined prior to the start of the simulation. In the EE multiphase framework, reactions have been included in OpenFOAM since 2014, [236] however it only allowed for reactions of either the gas phase or the solid phase. A tutorial example is the formation of TiO_2 from the reaction of $TiCl_4$ and O_2. Upon reaction of the gas phase $TiCl_4$ and O_2 gasses, TiO_2 particles are formed. A step-up from this approach to simulate fluidized beds has been proposed by Qiu et al. [237] They proposed the use of an efficiency factor to alter the reaction rate of the catalytic tar cracking process. The reaction rate within each cell depended on the maximal reaction rate multiplied with an effectiveness factor, the mass transfer of the gas towards the particle surface and the local volume fraction of catalyst. The effectiveness factor was defined as a function of the Thiele modulus, which itself is a function of the particle diameter, the apparent reaction kinetic constant and the diffusivity of the tar molecules in the pores of the catalyst. The dependency of the reaction rate on the local volume fraction of the particle phase is what allowed the simulation to handle fluidized bed reactors.

Currently, the most accurate methods that have been developed to simulate catalytic reactions for moving particle beds, are the catchyFoam solver developed by Vandewalle et al. [155] and the expansion of catalyticFoam for EE multiphase simulations by Micale et al. [238, 239]. These were solvers developed for catalytic gas – solid reactions and were specifically developed to include the microkinetic models to describe the chemical reactions. A microkinetic model is a detailed description of the elementary steps of a chemical reaction near the catalyst surface, often obtained from calculations based on the electronic structure of the reaction components. [240] Unfortunately, for the dehydrogenation reaction of $H_{18}DBT$ these microkinetic models are not available. Additionally, the catchyFoam and catalyticFoam solvers were not developed for liquid – solid catalytic reactions and models for the evolution of a gas phase were not included.

In Table 5-1 the limitations for the chemical reaction approaches previously developed are listed together with the limitation why it cannot be used for the dehydrogenation reaction of $H_{18}DBT$. In this Chapter, I will briefly introduce the custom catalytic source term that was developed to mimic the dehydrogenation reaction of $H_{18}DBT$ and allow for H_2 to be released in each cell based on the available catalyst mass and volumetric flowrate. This source term will be used to further study the uniformity of the distribution of the particles in the bed during the dehydrogenation reaction. The development of this catalytic source term is the first step-up towards a CFD solver that will be fully capable to simulate the dehydrogenation of $H_{18}DBT$. The source term approach used in this chapter shows its usefulness by allowing to study the effect of the localized H_2 release on the particle bed. Firstly, the fluidization is studied in a conventional fluidized bed reactor and subsequently, the potential improvements for to the reactor design of the SFB reactor are discussed, which were highlighted at the end of Chapter 3.

Table 5-1 Description and limitation of chemical reaction approaches in CFD applied to dehydrogenation of $H_{18}DBT$.

Method	Limitation
Porosity Source Term	Not applicable to fluidized beds, since it does not allow for movement of the solid bed
EE reaction models	Does not include chemical reactions between the separate phases
Effectiveness factor approach	No available data on diffusion of $H_{18}DBT$ in particle, diffusion highly dependent on local H_2 release rate [241]
Microkinetic solvers	No available microkinetic models for $H_{18}DBT$ dehydrogenation No Phase changes in reactive system

After a conventional fluidized bed reactors was investigated using the novel source term, I started with the study on the geometry changes for the SFB by varying the number of inlets of the reactor, followed by analysing the influence of these changes on the uniformity of the liquid flow. A uniform liquid flow in the reactor is more likely to produce uniformly distributed particle beds and uniform velocity profiles. In a non-uniform bed, which occurs for particle beds with a low terminal velocity, [118] the mass and heat transfer in the dense section of the bed is expected to differ from the particles in the diluted section. In a second phase of the geometry explorations, the particle bed during the dehydrogenation reaction is studied in the SFB. This SFB is similar in geometry to the reactor studied in Chapter 3. Subsequently, the influence of two design changes are investigated, which were proposed in section 3.3.5. These are i) the influence of a conical structure at the bottom of the reactor to remove the region of static beads at the bottom plate and ii) using a reactive zone with only half the diameter, elongated to retain the same total volume of reactive zone.

The original prototype of the SFB reactor was designed with only two inlets since it allowed for easier experimental operation of the system. Fewer inlets decrease the chances for leaks and maldistribution of the flow from a single pump. However, from the cold flow study in Chapter 3, it was seen that the reactor shows a periodicity in maximal measured bed height. The periodicity implies a non – uniformity in the particle bed. By increasing the number of inlets, a more uniform flow distribution of the liquid was expected, which would in turn provide a more uniform particle bed. This potentially increases the chances for leaks, but this can be covered by adding a distributor prior to the main reactor body, which spreads the flow evenly over the all the inlets of the main reactor body. [242, 243] The exact design of such a distributor is not covered in the scope of the thesis.

To reduce the section of the particle bed that was stagnant on the bottom plate of the reactor, the idea is proposed to insert a structure within the reactor body to eliminate any this accumulations. This is similar in idea to the use of the central cone in the TORBED reactor. A TORBED reactor is an example of a swirling reactor, used for gas – solid processing and is characterized by high mass and heat transfer. This is caused by the high velocities obtained within the reactor due to the narrow slits between the blades. The TORBED reactor is used for combustion, separation, drying and thermal processing of both fine particles (< 50µm) to mm size particles, i.e., particles classified as the Geldart B or D type particles. [244-246] This bed of particles is situated above the right above the blades and moves in a swirling pattern within the reactor. From the TORBED geometry, only the conical structure will be used for the SFB studied in this chapter. The cone in the centre of the TORBED has two purposes, i) it serves the remove the dead space in the reactor, where particles do not move, ii) the shape of the cone gradually increases the cross section of the reactor with increasing height in the reactor. An increase in cross section results in a gradual decrease in superficial gas velocity, which is used in the TORBED reactor to operate deeper beds at high velocities with less risk of particle elutriation.[247]

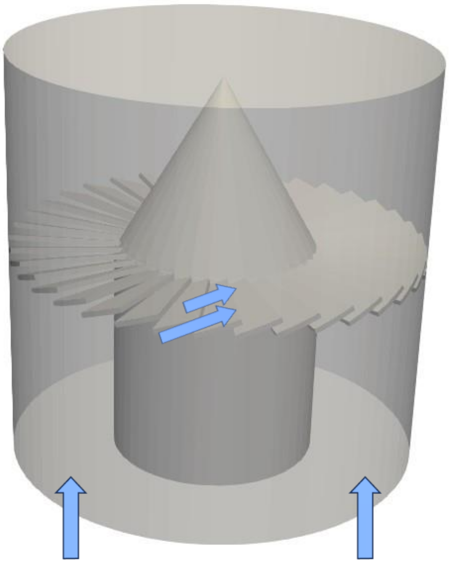

Figure 5-1 Example of a TORBED Reactor showing the central bladed structure and the cone; The blue arrows denote the gas flow from bottom through the bladed structure.

The final change proposed to the geometry is to reduce the diameter of the reactor. This limits the cross section of the reactor and therefor a higher liquid velocity should be obtained for similar flowrates in a wider SFB. To keep the volume of the narrow reactor similar to the volume of the wider reactor, the total reactor height is increased.

5.2 Methodology

5.2.1 Catalytic Source Term

To release H_2 only in the cells of the mesh that contain particles and liquid, a newly made source term was implemented to take these factors into account. The development of the source term is based on a curve fit from the work of Bulgarin et al. [82] Using this approach a simple relation between the H_2 release rate, the available catalyst mass and the volumetric flowrate should become apparent which can then be implemented into the *massSource* source term available in OpenFOAM, which applies a mass source to the continuity equation. [248] The experimental data on which the catalyst source term is based is shown on Figure 5-2A.

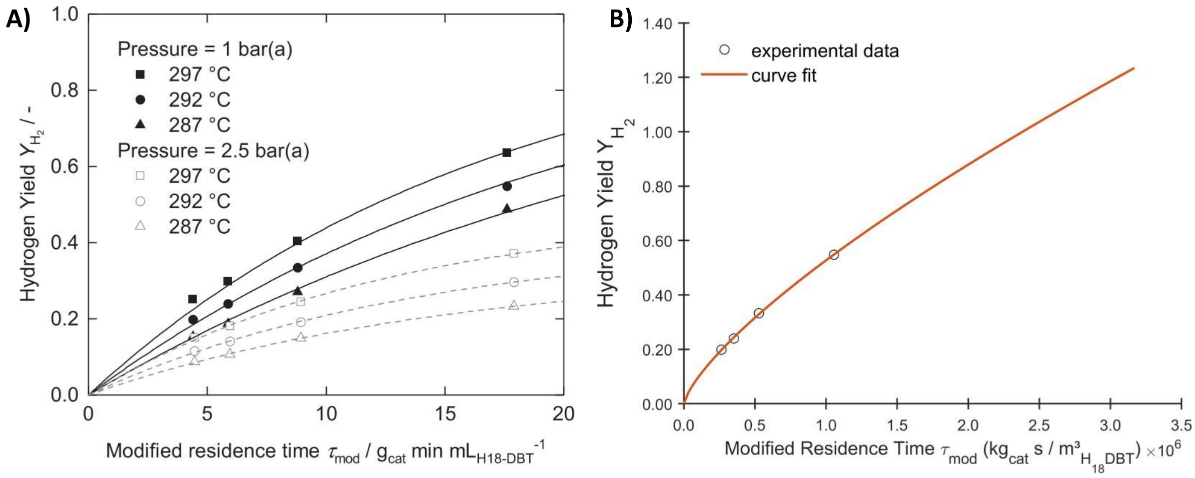

Figure 5-2 A) Experimental results of the dehydrogenation experiment of H_{18}DBT from Bulgarin et al. [82], showing the "yield" of H_2 in function of the modified residence time. Data was extracted for 4.9 g of catalyst at flow rates of 0.34 mL min^{-1} to 1.35 mL min^{-1} at 292°C. B) Curve fit of the data of the H_2 yield in function of the modified residence time in SI units.

The term "Yield", Y_{H_2} seen in Figure 5-2 is defined from: [249]

$$Y_{H_2} = \frac{\dot{n}_{H_{2}out}}{\dot{n}_{H_{2}in}} = \frac{\dot{n}_{H_2}}{9 \cdot \frac{\dot{n}_{H_{18}DBT}}{MW_{H_{18}DBT}}} \tag{6.1}$$

In this expression for Y_{H_2} in equation 6.1, the term $\dot{n}_{H_{2_{in}}}$ refers to the theoretical total molar flowrate of H_2 that is bound to the LOHC carrier, since the H_2 gas is chemically bonded to the to the LOHC carrier. Looking at Figure 5-2A an n-root trend can be observed between the values for Y_{H_2} in function of the modified residence time τ_{mod}, which is the ratio of the catalyst mass and the flowrate of the liquid. Using the *lsqcurvefit* tool from MATLAB, followed by simple mathematical relations a mass flowrate of H_2 could be extracted in relation to the catalyst mass and volumetric flowrate in each cell of the mesh. The detailed derivation of the source term is shown in Appendix II.

To test the implementation of the source term, I ran simulations using the 2D mesh used in Chapter 4 with a fixed bed of particles, and identical τ_{mod} of the experimental datapoints of Bulgarin et al. The results of this simulations can be seen on Figure 5-3, which show to underpredict the Y_{H_2} values compared to the experimental values. This is likely due to the dependence of the H_2 release rate on the volume fraction of the liquid phase, in the cell. This was introduced to relate the total flowrate in the system to the local flowrate in the cell.

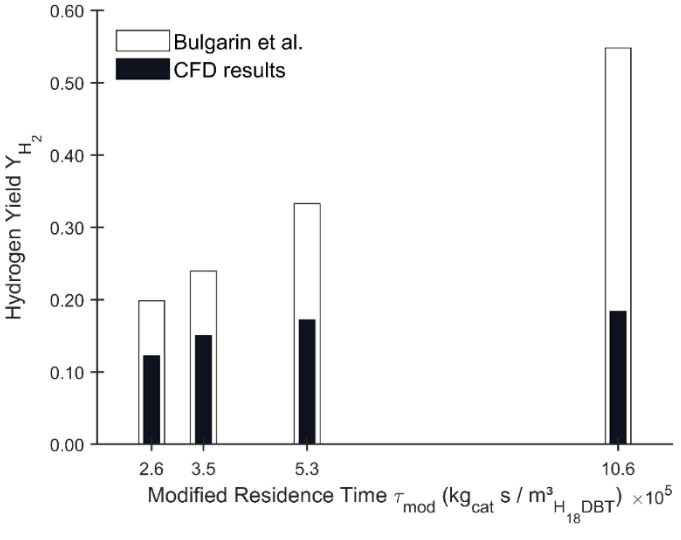

Figure 5-3 Bar plot showing the H_2 yield per flow rate for the dehydrogenation of $H_{18}DBT$ for both the experimental results from Bulgarin et al. [82] and the data obtained via CFD simulations with the catalytic source term.

The code of the catalytic source term relates the mass flux of H_2 for each cell based on the volume fraction of liquid and catalyst mass. Due to the low density of the H_2 gas, the reactor is rapidly filled with H_2 gas which lower the H_2 release rate in the total system. This effect has not been accounted for in the code and is the likely reason for the underprediction of the H_2

release compared to the literature data. To account for this effect, I used a parameter fitting approach to fit the values of Y_{H_2} closer to the data reported in the work of Bulgarin. I used two parameters, one for the equation in the high flowrate regimes, one for data in the lower flowrate regimes, which yield a higher Y_{H_2}. This changes the equations used in the source term to:

$$\dot{m}_{H_2} = Parameter1 \cdot \frac{1.9734e^{-5} \cdot 9 \cdot MW_{H_2}}{MW_{DBT_{H_{18}}}} \cdot \rho_{H_{18}DBT} \cdot m_{cat}^{0.7378} \cdot \dot{V}_{H_{18}DBT}^{0.2622} \tag{6.2}$$

And for the limiting function in case of high τ_{mod}, see Appendix II for the derivation, equation 6.3 is used. This limiter was used to account for the values of the τ_{mod}, where the Y_{H_2} would be higher than 1, since his would be a unphysical result.

$$if\ \tau_{mod} \geq 2.5e^{6} \rightarrow \dot{m}_{H_2} = Parameter2 \cdot 9 \cdot \frac{MW_{H_2}}{MW_{H_{18}DBT}} \cdot \rho_{H_{18}DBT} \cdot \dot{V}_{H_{18}DBT} \tag{6.3}$$

To fit the parameters to the experimental data of Bulgarin et al. a total of 64 CFD simulations were run on a fixed bed reactor to test the effect of both parameters 1 and 2 on the results. Figure 5-4 graphically depicts the results of the CFD simulations with respect to the experimental data extracted from the literature. Comparing these 64 different cases it is clear that the addition of the parameter to the catalytic source term increases the accuracy of the CFD simulations. The use of the two-parameter implementation is also warranted by the trends seen on Figure 5-4. For the simulations with a high τ_{mod}, i.e., the simulations at low flowrates, the second parameter influences the results much more than the cases with low τ_{mod}. Cells in the low flowrate regimes are thus much more likely to end up in the limiting flow rate regime of equation 6.3, than in the case of higher flowrates. At τ_{mod} of $1.06 \cdot 10^6$, the H_2 release rate is always underpredicted, no matter which parameter combination is selected. At higher flowrates or lower τ_{mod} the accuracy of the simulations increases with an increase in parameter 1, which justifies the use of the highest value of parameter 1, that was studied, i.e., 1.65. For parameter 2, the effect on the intermediate flowrates also has to be discussed, at τ_{mod} of $5.28 \cdot 10^5$ the H_2 release rate is always overpredicted by the catalytic source term, an effect which increases with increase in parameter 2. To keep this overprediction at a minimum for intermediate flowrates, while still keeping the accuracy for the higher flowrates as high as possible, I selected parameter 2 to be 2.8. This is justified since the fluidized bed system that I aim to study with this implementation will operate in regimes at higher flowrates.

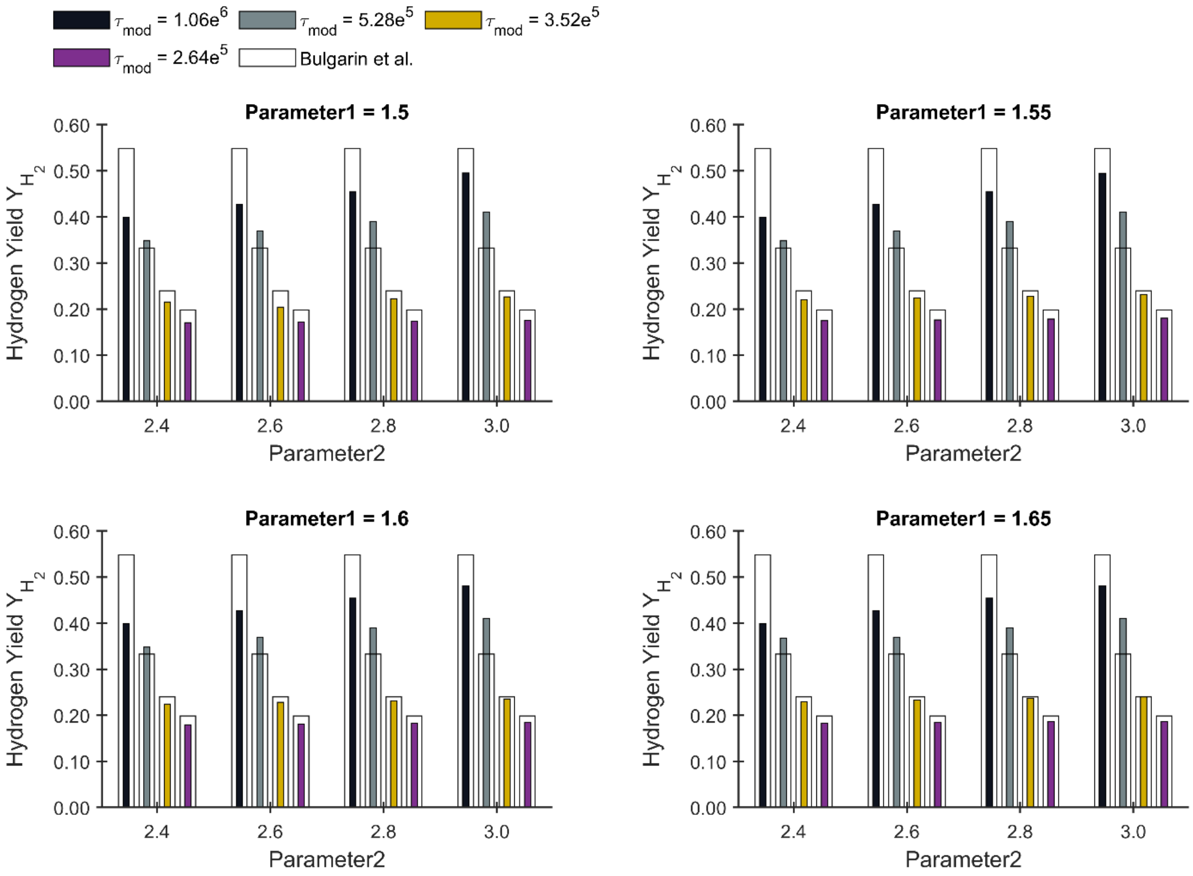

Figure 5-4 Results from the parameter estimation study to improve the accuracy of the catalytic source term. The dark edges show the experimental data from Bulgarin et al., coloured bars show the H_2 yield obtained via CFD simulations with the catalytic source term for 4 different τ_{mod} and 16 combinations of parameter 1 and 2.

The catalytic source term for the dehydrogenation of $H_{18}DBT$ is implemented via equations 6.2 and 6.3. Since it mimics a catalytic reaction, it will only happen when there is catalyst mass present inside the cell. That is why a conditional loop was added in the code, to only allow equations 6.2 and 6.3 to be activated in cells which contain a volume fraction of at least 0.1. This cut-off value of the volume fraction, is a third factor in the implementation of the catalyst source term but the influence of this factor was not further evaluated on the accuracy of the source term. A value of 0.1 was chosen as the lower value, as cells which contain less than 10 % of particle phase, will likely contain a high amount of gas phase, which puts the particles in a mass transfer limited regime. The second function of this cut-off value was to reduce the influence of the numerical drift of the particle phase on the in situ gas release. The C++ source code for this newly implemented source term can be found in Appendix III.

Finally, I would like to stress that that this catalytic source term is implemented to study to effect of localized H_2 generation on a particle bed during the dehydrogenation of $H_{18}DBT$. This code was designed to be dependent on the total flowrate of $H_{18}DBT$ and showed reasonable accuracy when simulating fixed bed regimes. However, no thermal effects are included in the implementation of the catalytic source term, so it will not be possible to state if a fluidized regime will release more H_2 compared to a fixed bed regime due to the superior heat transfer in a fluidized bed. [250] It will be possible to study the onset of the fluidization during the $H_{18}DBT$, which will differ from theoretical LGS fluidization described in chapter 1, since the gas will be generated throughout the height of the bed, rather than be injected at the bottom.

5.2.2 CFD parameters

CFD simulations using the EE multiphase solver module multiphaseEuler were conducted in OpenFOAM version 11, the catalytic source term was developed specifically to work with this version of OpenFOAM. In this chapter firstly, the fluidization of the particles in a conventional fluidized bed is studied, to check the influence of the in situ H_2 release rate on the particle distribution within the bed. In the second part of this chapter design changes to the SFB reactor are investigated.

In both these simulation studies $H_{18}DBT$ is used as the liquid phase, at a temperature of 565K, similar to the temperature of the H_2 release experiments from Bulgarin et al. H_2 gas is the gas phase, and the 0.3 wt.% Pt/Al_2O_3 catalyst [251] was used as the particle phase in the form of 2 mm diameter spheres. The thermophysical properties for the simulations can be seen in Table 5-2. The thermodynamic properties for $H_{18}DBT$ were calculated based on extrapolations of the work of Müller et al. [176], Aslam et al. [180], and Berger - Bioucas et al. [252] Curve fitting for these values can be found in Appendix IV.

Table 5-2 Thermophysical Properties used for the simulations of the dehydrogenation of $H_{18}DBT$.

	$H_{18}DBT$	H_2	Al_2O_3
ρ(kg m^{-3})	739	Perfect Gas	2300
µ (Pa s)	$1.8 \cdot 10^{-3}$	$1.37 \cdot 10^{-5}$	
λ (N m^{-1})	0.0097		

5.2.3 Case setup conventional fluidized bed

CFD simulations of the dehydrogenation reaction in conventional fluidized bed reactors were performed using the same 2D mesh as was used for the simulations of the *pseudo* – 2D fluidized bed reactor used in Chapter 4. This mesh of 38 070 cells has been subject prior to a GCI analysis, so this step is skipped in this chapter. The goal of the simulations in this fluidized bed reactor setup was to study the influence of the flowrate of the liquid on the particle bed. To do this I calculated the expected minimal fluidization velocity without gas phase, the $\boldsymbol{U_{lmf0}}$ from equation 1.7 using the values in Table 5-2. This resulted in $\boldsymbol{U_{lmf0}}$of 0.017 m s^{-1}. Simulations were run with initial liquid velocities of 5, 10, 25, 50, 75, and 100 % of this calculated velocity. The mass of particles in the system was 0.046 kg. The simulations in this conventional fluidized bed reactor allowed to analyse the influence of the H_2 gas generation on the particle entrainment and bed uniformity.

5.2.4 Case setup SFB shape exploration

The first investigation of possible design changes to the SFB prototype is based on the number of inlets. To study the influence of the number of inlets on the liquid flow profile a liquid – solid simulation was run. This approach was selected to limit the influence of the gas phase on the liquid flow profile. Allowing for an easier analysis of the uniformity of the flow within the reactor.

The additional inlet tubes for were placed similarly to the original inlets described in Chapter 3. The angles of the inlet tubes with respect to the horizontal plane were unchanged at 10°, the number of inlets varied from to either have 2,3 or 4 inlets, placed at regular intervals for each reactor geometry. Inlet tubes were placed on the reactor in intervals of 180°, 120° and 90° from each other for the case of two, three and four inlets, respectively.

The meshes used for this analysis, had a similar grid size to those used in Chapter 3. So, the GCI investigation is skipped for these meshes. The boundary conditions used for the simulations are listed in Table 5-3.

Table 5-3 Boundary conditions used for the simulations of the SFB reactor geometries.

	Inlet	**Outlet**	**Walls**
U. liquid	flowRateInletVelocity	pressureInletOutlet Velocity	NoSlip
U.gas	fixedValue U = (0 0 0)	pressureInletOutlet Velocity	NoSlip
U.particles	fixedValue U = (0 0 0)	fixedValue U = (0 0 0)	JohnsonJacksonParticleSlip Specularity = 0.8 Restitution = 0.01
p_rgh	fixedFluxPressure	PrghPressure p = 10 000	fixedFluxPressure
alpha.liquid	FixedValue α = 1	inletOutlet α_{in} = 1	zeroGradient
alpha.gas	FixedValue α = 0	inletOutlet α_{in} = 0	zeroGradient
alpha.particles	FixedValue α = 0	FixedValue α = 0	zeroGradient
Theta.particles	FixedValue $\Theta = 1 \cdot 10^{-4}$	zeroGradient	JohnsonJacksonParticleTheta Specularity = 0.8 Restitution = 0.01
k.liquid	turbulentIntensity KineticEnergyInlet I = 0.05	zeroGradient	kqRWallFunction
omega.liquid	turbulentMixingLength FrequencyInlet L = 0.001745	zeroGradient	omegaWallFunction

To study the influence of the central cone and the narrow reactor geometry, two new meshes were created, again with similar grid size to the mesh used in Chapter 3, the geometries of these reactors can be seen on Figure 5-5. Firstly, the base geometry of the SFB, which was discussed in Chapter 3 of this thesis, will be further analysed. In this chapter the catalytic source term will be used for simulations of the SFB geometries, this allows for the H_2 gas to be released only in those cells which contain particles. This is an improvement in the simulation setup compared to the fritted disc approach used for the cold flow study of the SFB. One design change compared to the cold flow SFB has already been implemented, which is the addition of two more liquid inlets, to improve the uniformity of the liquid flow. This reactor geometry will be called *4inletsNoCone150* in the remainder of this chapter. The number 150 refers to the diameter, in mm of the reactive zone of the reactor. The first potential improvement to the SFB system is the addition of a central cone in the middle of the reactor. This cone had a lower diameter set at 2/3 of the total diameter of the reactive zone of the SFB. This is based on the design of the Torbed reactor by Naz et al. [253] The height of the cone extended to half of the height of the reactive zone. The aim of the cone in the centre of the reactor was to remove the dead zone of non-moving particles that was observed in the middle of the bottom plate of the reactor and to achieve a higher liquid flow velocity at the bottom of the reactor to achieve more uniform fluidization of the particle bed. The geometry of the mesh with the central cone will be called *4InletsWithCone150*. The third and final geometry discussed in this chapter it the reactor with half the diameter of the reactive zone. The height of this reactor was increased to keep the total volume of the reactive zone close to the volume of the reactive zone of the other SFB reactors. Inside the small diameter reactor, a central cone was placed with a half the diameter of the cone in the wide reactor and with twice the height of the original cone, this is *4InletsWithCone75*. On Figure 5-5 the geometries are shown without the sidewards outlets that are normally present on the reactor body. This was a simplification to further reduce the computational time required for the simulations since the outlet tubes are unlikely to influence the flow near the bottom of the reactor.

The reactors were filled with around 600 g of catalyst beads each to allow for a comparison in particle bed behaviour, this mass is similar to the mass used during the cold flow mock-up study. In Chapter 3, high flowrates were used to analyse the behaviour of the particle beads and obtain high fluidization. In this Chapter, I want to focus more on lower liquid flowrates, since a lower flowrate will reduce the residence time in the reactor and will allow for a more complete dehydrogenation of $H_{18}DBT$. In the study of the SFB only 1 flowrate is used for the comparison of the three different reactors, 30 LPM. This value corresponds to a modified residence time, τ_{mod} of 1200. Theoretically this corresponds to a Y_{H_2}around 2 %, based on the obtained H_2 release rates from the swirling fluidized bed reactor, See Figure 5-2.

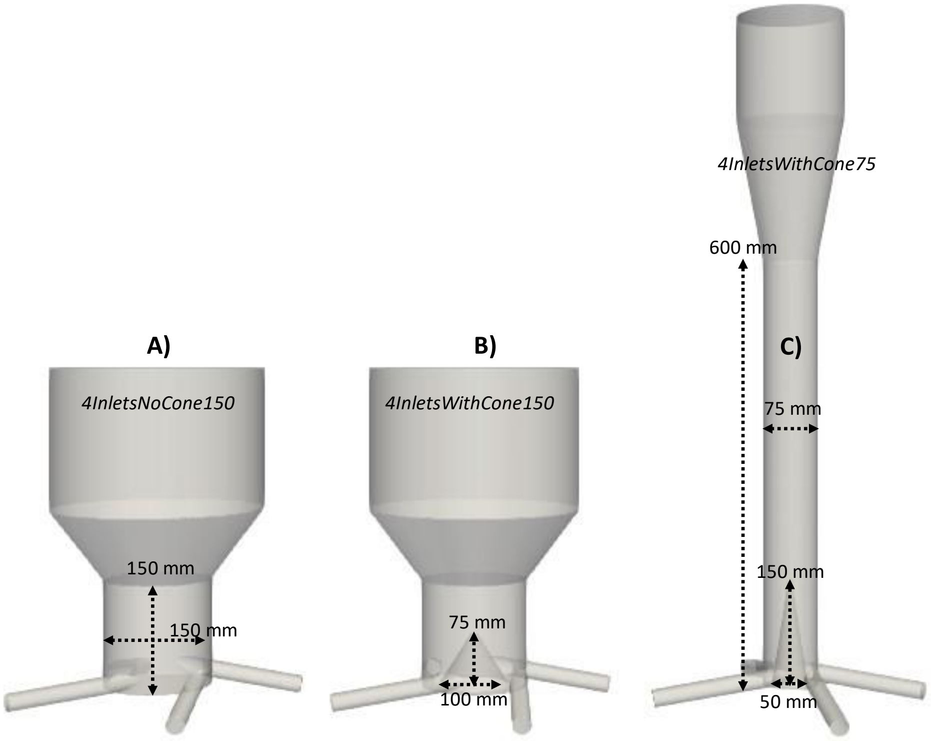

Figure 5-5 Geometries of the reactors investigated in this chapter. A) The geometry of the reactor with similar geometry compared to the reactor in Chapter 3, but with two additional inlets, this is 4inletsNoCone150. B) A reactor with similar outer shape as A, but with a cone added at the central bottom plane, which is called 4inletsWithCone150. C) The reactor with half the diameter of the reactive zone, the height was increased to keep a similar total volume of the reactive zone, this geometry is called 4inletsWithCone75.

5.3 Simulation Results

5.3.1 Conventional Fluidized Bed Simulations Using the Catalytic Source Term.

The first simulations to study the fluidization of the catalyst beads during dehydrogenation of $H_{18}DBT$ were conducted making use of the catalytic source term approach in a conventional fluidized bed reactor. Five simulations were run with an increasing liquid flowrate, ranging from 5 to 100 % of the theoreticalU_{lmf0}. Based on the total mass of catalyst in the system, 0.046 kg, the modified residence times, τ_{mod}, ranged from $8.5 \cdot 10^3$ to $1.7 \cdot 10^5$. The H_2 release simulated by the catalytic source term was determined for this new set of simulations and plotted on Figure 5-6. This shows that the total amount of H_2 release is close to the values which would be expected from H_2 release experiments at higher flowrates. This is only an estimate of the total H_2 release in the system. The simulations using the catalytic source term do not take into account any additional mass and heat transfer which would be expected from the fluidization.

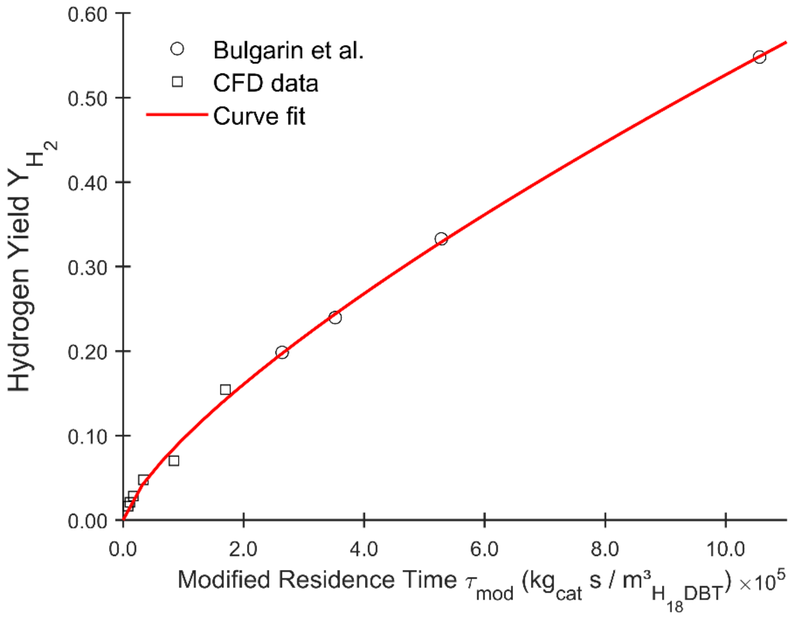

Figure 5-6 Plot of the Y_{H_2} in function of τ_{mod}, the circles represent the data extracted from Bulgarin et al., the circles represent the Y_{H_2} extracted from CFD simulations of the reactive pseudo-2D LGSFB. The red curve is the curve fitted from the literature data, see equation 6.3.

Nevertheless, the simulations which use the catalytic source term release a realistic amount of H_2 gas in function of the τ_{mod} and can thus serve as a first tool to study the fluidization of the catalyst particle bed during the dehydrogenation reaction. Figure 5-7 shows the particle bed behaviour with increasing liquid flowrate. The simulations of this particle bed shows a much stronger particle entrainment than seen on simulations of the cold flow LGSFB studied in Chapter 4. Increased entrainment of the particles is often seen in beds of small and lightweight particles. [118] Higher axial solid dispersion is also seen in particle beds with large bubbles with a high bubble frequency. Fluidized beds operating in the bubble coalescence regime are thus more likely to have larger disengagement zones than fluidized beds operating in bubble breakage regimes. [254]

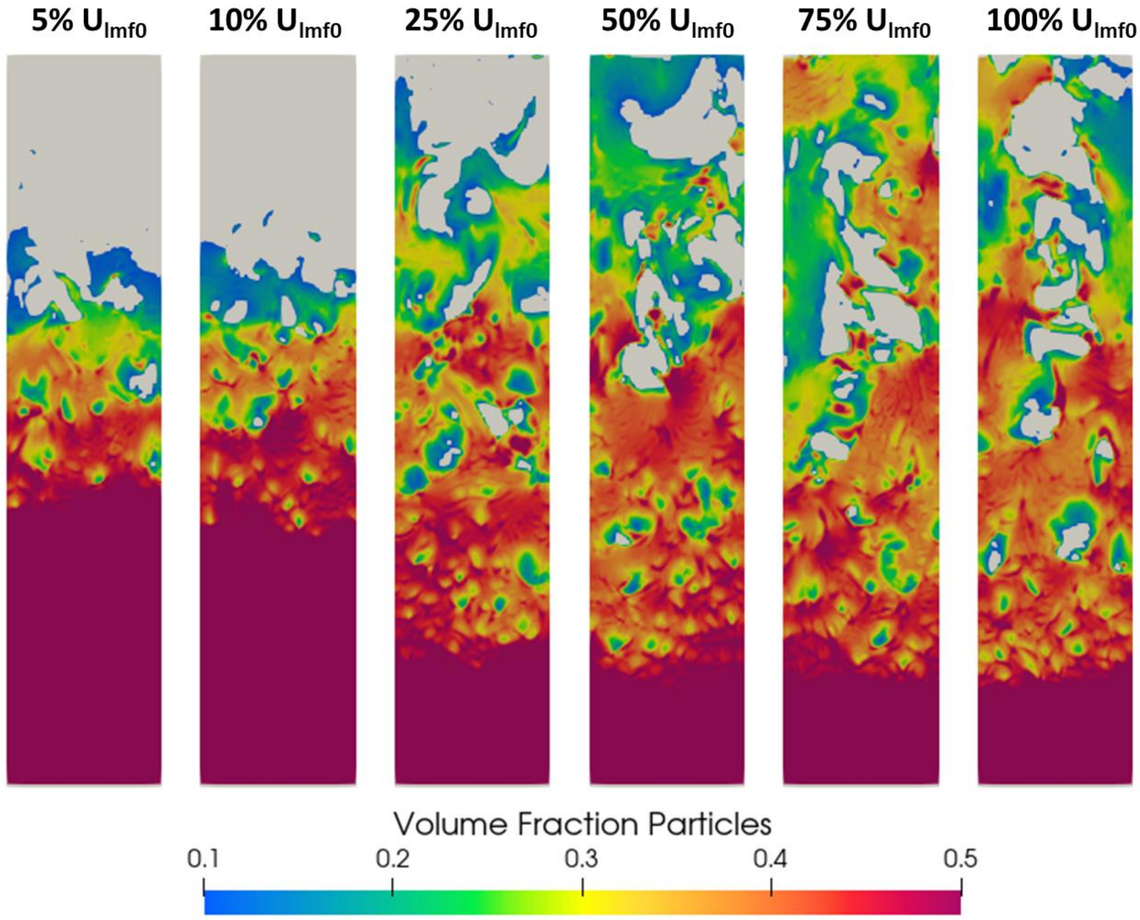

Figure 5-7 Volume fraction of Al_2O_3 catalyst particles in a pseudo – 2D fluidized bed during dehydrogenation of $H_{18}DBT$ the inlet flowrate varies from 5 % to 100 % of the theoretical minimal fluidization velocity of the particle bed. Snapshots are obtained after 1.5 s of simulation. The grey background shows the mesh. The threshold for the particle bed ranges from 0.1 to 0.5.

On Figure 5-7 it also shows that the region of high particle volume fraction decreases with increasing liquid flowrates. This is a joint effect of the increased liquid drag by the higher liquid flowrates and in the higher mass of H_2 released in the system at higher flowrates, expressed in absolute values. The particle entrainment is further amplified by these high flowrates, as particles only tend to fall back when the local liquid velocity around a bubble drops below the terminal velocity of the particle. [254] From this initial analysis it can be observed that generating a uniform particle bed for this system will be challenging, due to the increasing mass of H_2 over the length of the bed. The liquid flowrate can be kept constant at the inlet, but the effect of the gas bubbles during the dehydrogenation increases the fluidization of the particle bed which causes the particles to ultimately become disengaged from the bed. When the gas bubbles rise in the bed, the bubble size tends to increase, increasing the bubble velocity which lowers the minimal fluidization velocity for LGS systems, see equation 1.6. To counteract the increase in bubble velocity, which means lowering the $\boldsymbol{U_{lmf}}$, either the particle phase density or diameter can be increased, or the liquid velocity should be decreased. Since the gas velocity is not constant in the bed the changes to particle properties or liquid velocity profile should be gradual. A possible approach to counter the locally increasing $\boldsymbol{U_{lmf}}$ is to use mixture of particles with different particle diameters. With heavier particles on top, the $\boldsymbol{U_{lmf}}$ would increase, which counterbalances the effect of the increase gas velocity. This would require having a bed of particles with a greater diameter on top of the bed and a smaller diameter at the bottom. This is somewhat counterintuitive, but studies of solid – liquid fluidized bed using binary mixtures of particles with different densities and sizes have shown that such a regime is possible at low liquid velocities. An inversion of this equilibrium will occur at increasing liquid velocities, where the denser smaller particles will move towards the top of the bed and the larger particles will stick to the bottom. [255-257] This is an extra factor which should be taken into account and which renders the exact prediction of the ideal particle size distribution difficult. The addition of the released gas phase during the dehydrogenation of H_{18}DBT, would add even more complexity to keep this bed profile with the larger particles towards the top of the bed. One approach could be to add wire meshes between zones of particles with different diameters, this would stop the particle phase from mixing, while keeping the larger particles towards the top of the bed and the smaller closer to the bottom.

However, for the remainder of this chapter, I will focus on another approach to counter the effect of the increased velocity of H_2 gas on the particle bed, by gradually increasing the cross section of the reactor which decreases the local liquid velocity. This can be achieved for example by the addition of a central cone in the reactor. In the next section of this thesis, the swirling fluidized bed is being investigated and especially the influence of the cross section of the reactor on the particle bed.

5.3.2 Analysis of the number of inlets

As was shown from the simulations of the conventional fluidized bed reactors, simulations of the dehydrogenation of H_{18}DBT render a non-uniform distribution of the particle bed. This particle bed was characterized by a high entrainment of the particles with increased axial distance but with a dense particle bed near the inlet. To improve the uniformity of the bed in the SFB, I firstly investigated the influence that the number of inlets had on the liquid velocity profile within the reactor. The geometry of the reactor studied was similar to the SFB reactor studied in Chapter 3. The angles of the inlet tubes with respect to the horizontal plane were unchanged at 10°, the number of inlets varied from two to four inlets, placed at regular intervals for each reactor geometry. Figure 5-8 shows the liquid velocity magnitude profile obtained from the reactors with two, three and four inlets. The total flowrate flowing inside the reactors, i.e., the flowrates summed over each of the inlets remained constant. It can be seen that by increasing the number of inlets, the velocity profile inside the reactor becomes more uniform and the maximal obtained velocity drops inside the main reactor body. The number of inlets also influence the periodicity of the flow in the reactor. The periodic spots of higher local velocity magnitudes are similar in number to the number of inlets used. By using four inlets, the flow profiles becomes more uniform, however there are still areas of low velocity present inside the mesh, visible by the areas in darkest blue on Figure 5-8. These low-velocity zones were located right before each of the liquid inlets and in the centre of the reactor. The size of the central low-velocity zone increases with the number of inlets.

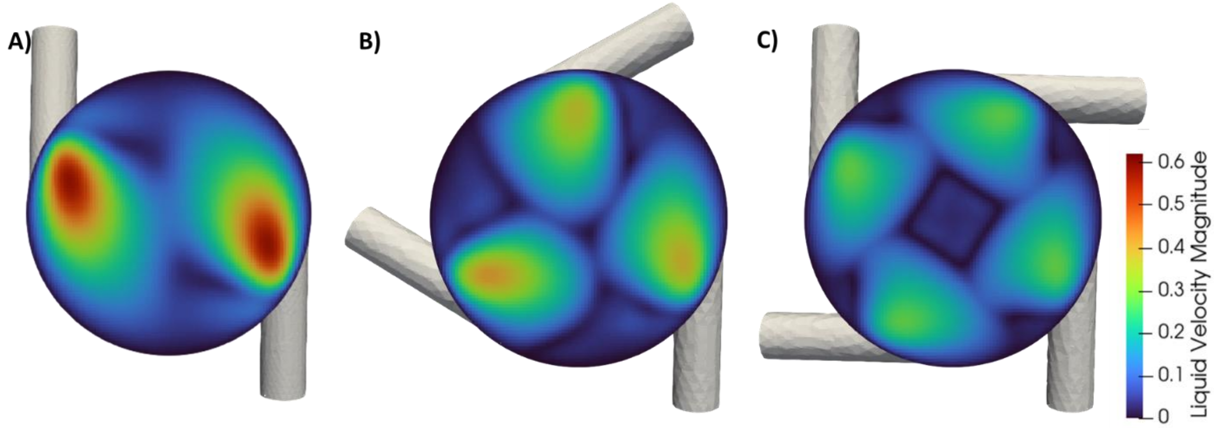

Figure 5-8 Liquid velocity magnitude profiles observed over a plane at 30 mm height inside the reactor for an increasing number of inlets, A) shows the mesh with two inlets, B) three inlets, C) four inlets.

5.3.3 Influence of the Geometry Changes in the SFB Reactor

The first alteration that was investigated for the SFB reactor was the addition of a conical structure in the centre of the bottom plate. Figure 5-9 shows the effect that the central cone has on the particle bed. From the snapshots shown it can be seen that the particle bed in the *4InletsNoCone150* geometry is being moved around near the bottom plate of the reactor, see Figure 5-9A. However, the particle bed is not uniform in this case and forms an upwards slope. This means that the distribution of the particle bed is not uniform within the reactor.

Especially near the inlets, the non-uniform particle distribution is detrimental for the dehydrogenation of $H_{18}DBT$. On Figure 5-9A especially, it can be seen that there are no particles near two of the four inlets of the reactor. Any $H_{18}DBT$ that would be injected via these inlets is flows over the bed rather than through it, which is shown by the liquid velocity streamlines. Newly injected liquid, in operational conditions, will have a higher concentration of $H_{18}DBT$ and higher temperature than liquid that has previously reacted. The newly injected liquid should make contact with the particle bed upon entering the reactor. The *4InletsNoCone150* geometry based on the original first iteration prototype of the SFB is thus not an optimal dehydrogenation reactor for $H_{18}DBT$.

Figure 5-9B shows that by adding a cone, the particle bed distribution becomes much more uniform in the reactor. The streamlines of the liquid velocity pass through the bed uniformly and show swirling behaviour right above the particle bed and around the conical structure. The particle bed observed from geometry *4InletsWithCone150*, however, still shows a region with high volume fraction of particles indicating poor uniformity in the fluidization of the particle bed.

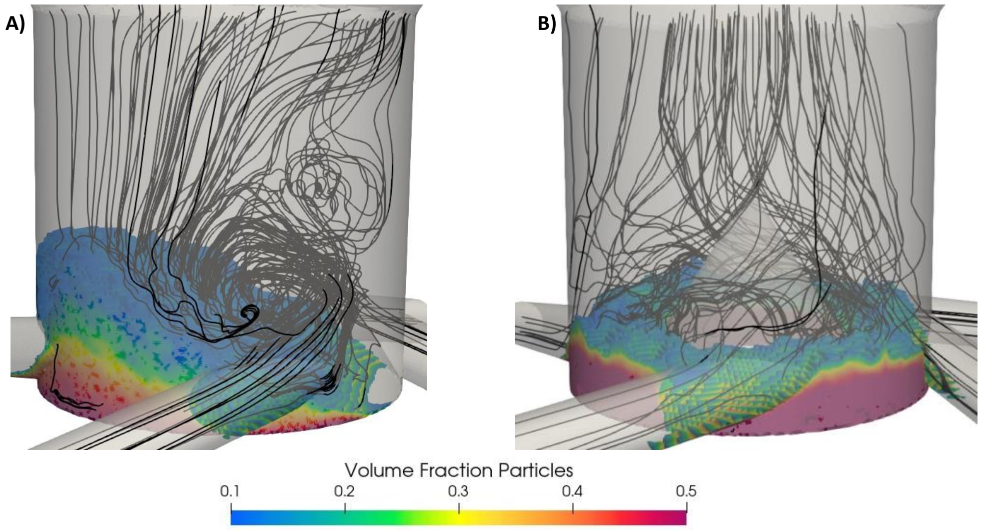

Figure 5-9 Snapshot of the particle bed in rainbow colours and liquid velocity streamlines in black for A) 4InletsNoCone and B) 4InletsWithCone.

The velocity profile of the particles and the liquid within the SFB system can be seen on Figure 5-10, in the form of glyphs oriented according to the time averaged particle velocity in a plane extracted at 20 mm height in the reactor, Figure 5-10A and the time averaged liquid velocity extracted at a plane in the middle between two inlets, Figure 5-10B. From the orientation of the glyphs of the particle velocity, it can be seen that the particles move downwards near the walls, both near the cone and the outer wall. The red colour of the arrows near the inlet jets indicate a high velocity of particles that are present in this region. Upwards arrows are also shown in the centre of the bed, indicating an upwards movement of the particles in this direction, although at much lower velocities than those near the jet. This behaviour is reminiscent of conventional fluidized bed reactors, where the particles tend to move upwards via the centre region and downwards via the walls, which is seen for Geldart A & B type particles in gas – solid fluidized bed reactors with a height to diameter ratio of 1. [258] Based on the orientation of the arrow there is however limited radial mixing of the particles in the bed, and the mixing seems to be dominated by axial and tangential movement of the particles. For the liquid velocity profile, the liquid moves upwards in a swirling pattern above the particle bed and moves down via the cone. Within the particle bed, the liquid moves upwards via the centre of the bed, lifting the particles higher in this region.

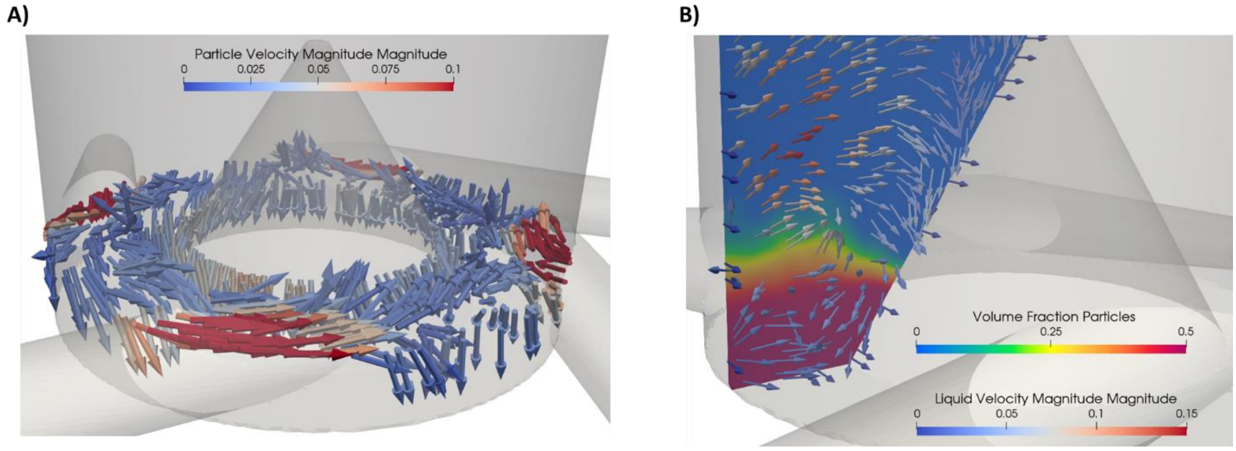
A)
Particle Velocity Magnitude Magnitude
0
0.025
0.05
0.075
0.1
B)
Volume Fraction Particles
0
0.25
0.5
Liquid Velocity Magnitude Magnitude
0
0.05
0.1
0.15

Figure 5-10 A) glyphs of the time averaged solid velocity extracted over a plane at 20 mm height in the reactor B) glyphs of the time averaged liquid velocity extracated at a plane between two inlets. The rainbow colouring shows the partcle bed in the reactor.

To produce a less dense particle bed in the reactor, the local velocity of the liquid has to be increased. By reducing the cross section of the reactor, while keeping the flowrate constant, higher velocities and more fluidization of the particle bed is expected. The effect of the particle fluidization in reactor geometry *4InletsWithCone75* is shown on Figure 5-11C. On this figure, the particle bed height from simulations of the three geometries are compared and it clearly shows that by decreasing the cross section of the reactor the particle bed moves up much higher in the reactor compared to the cases with the wider reactive zone. From the snapshots in Figure 5-11 A, B, and C it also shows that the particles seem to move upwards until reaching the disengagement zone. By plotting the volumetrically integrated particle volume fractions relative to the total volume of particles, it clearly shows that the relative amount of particles situated in dense areas of the bed decreases sharply for geometry *4InletsWithCone75*, compared to geometry *4InletsNoCone*150 and *4InletsWithCone*150. However, for geometry *4InletsNoCone75* there is a large increase in the relative amount of particles that are highly diluted in the reactor, i.e., the volume fraction below 0.1. This indicates that the particles do not form a well-defined particle bed, but likely they are entrained by the high flow velocities obtained within the reactor. Although, this is not the fluidization regime that was aimed for with the design of this reactor this is still a promising result. The simulations of each of the studied geometry where run with an inlet flowrate of 30 LPM. While this was not sufficient to achieve fluidization in the wider geometries, this flowrate was too high for the narrow case, seemingly moving the particles into transport regime. This means that for geometry *4InletsWithCone75*, a fluidized state of the beads is expected at much lower flowrates. Operating the reactor at lower flowrates, will improve the efficiency of the dehydrogenation process by achieving higher conversion of the $H_{18}DBT$, increasing the relative amount of H_2 gas that can be released.

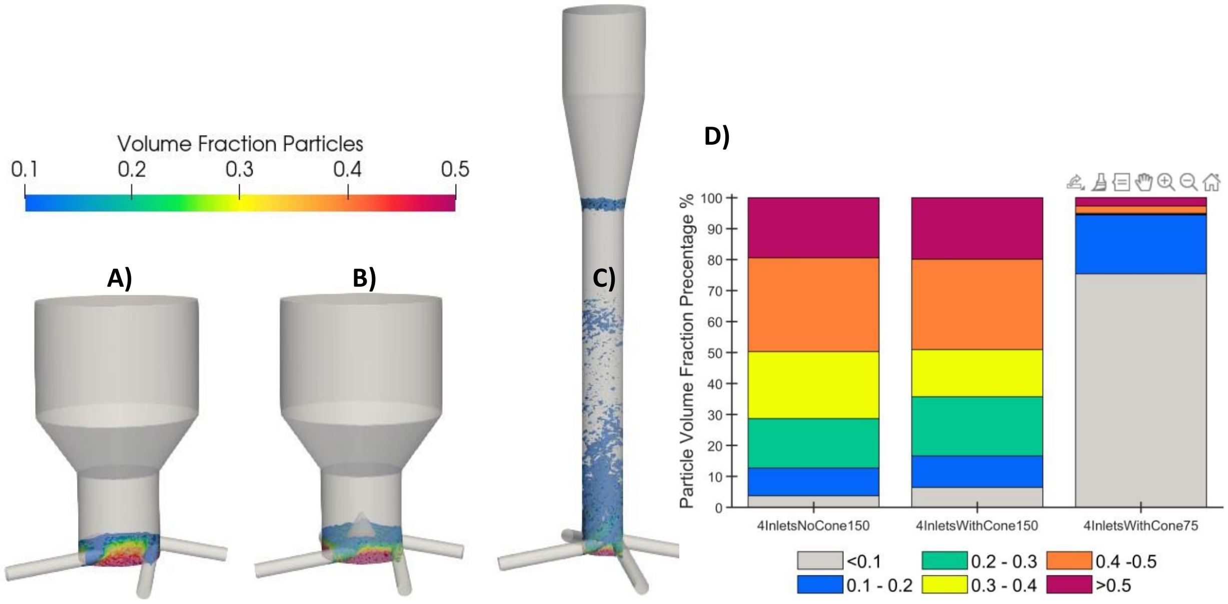

Figure 5-11 Snapshots of the particle bed volume fraction thresholds higher than 0.1, obtained after 5 s of simulation time for A) geometry 4InletsNoCone150, B) geometry 4InletsWithCone150, and C) geometry 4inletsWithCone75. D) represents the relative amount of particles present in 6 different intervals of particle volume fraction.

The design of the SFB borrows some aspects from high – G fluidization equipment for gas – solid processing, i.e., the use of a conical structure is borrowed from the TORBED, and tangential inlets are also seen in gas solid vortex reactors. The operational concept of this reactor differs from these gas – solid processing reactors. In vortex chambers high G forces are induced on the particle phase by extremely high gas velocities, ranging from 50 to 110 m s^{-1}, [259] ejected tangentially on the particulate phase. Due to the high gas velocities and the tangential orientation, the particulate phase starts to rotate in the reactor chamber at high rotational velocities which cause high G – fields. The high G – field keeps the particulate phase from leaving the particle bed, i.e., it effectively increases the terminal velocity of the particles in the bed, which leads to fluidization of particles at much higher velocities than in conventional fluidized bed reactors, which are limited by the gravitational field of the Earth.[168, 243] This high G approach would not be recommended for the dehydrogenation of H_{18}DBT, due to the extremely high velocities that would have to be obtained by pumping the liquid. To reach a high conversion of H_{18}DBT, this would also require a large number of passes in the reactor, which would be unpractical.

Lowering the liquid flowrate in the system, which lowers the drag force on the particles has been simulated by decreasing the flowrate to 15 LPM from the previously used 30 LPM on the *4inletsWithCone75* geometry. The results are shown on Figure 5-12. On Figure 5-12A, a threshold of the particle bed of volume fractions exceeding 0.1 is shown, which shows a much more compact particle bed compared to Figure 5-11C. The bar plot shown on Figure 5-12B, shows the comparison numerically. Where operating the reactor at 30 LPM yielded a very dilute bed with about 75 % of the particle bed in the diluted section of the bed, reducing the flowrate to 15 LPM increased the contribution of the particle volume fraction between 0.1 and 0.3 indicating a more compact fluidized bed. For liquid – solid fluidized beds, volume fractions between 0.18 and 0.38 have been experimentally determined to have the highest heat transfer for the reactor wall to the catalyst bed. [257]

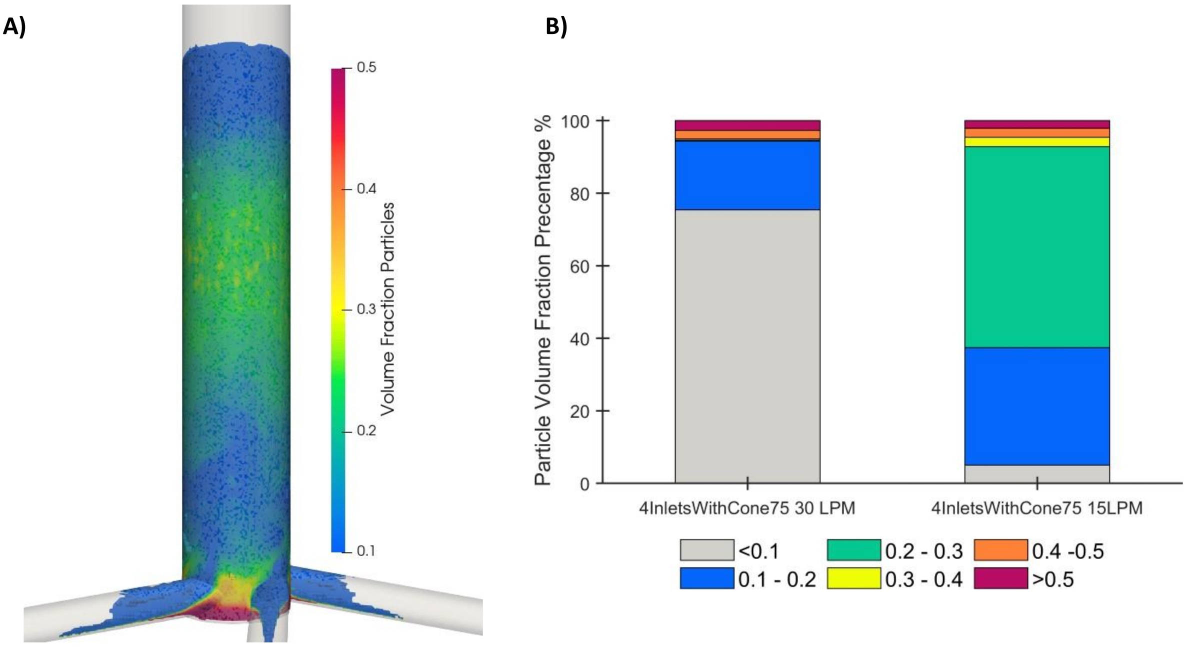

Figure 5-12 A) Threshold of the particle bed exceeding a volume fraction of 0.1 in the SFB reactor with halved diameter operated at 15 LPM. B) Bar plot showing the relative distribution of particle bed density on the total bed volume.

By lowering the liquid flowrate, there is less particle entrainment by the liquid compared to a higher flowrate. This leads to a more compact particle bed, which still shows only a little fraction of beads in the densely packed region. This hints at a high dependency of the flowrate on the operational window of the reactor operation. This is similar to other swirling flow reactors or vortex reactors, in which the size of the reactor determines the relationship between the flowrate and the particle properties that can be used for efficient fluidization and proper operation of the reactor. [260] SFBs for dehydrogenation of $H_{18}DBT$ will thus likely only be operated for specific power outputs, which are determined by the reactor geometry and particle properties.

5.3.4 Analysis of the First Damköhler Number

By altering the reactor geometry, I was able to observe a fluidized particle bed at reduced flowrates compared to the flowrates used in chapter 3. A reduction in flowrate tends to increase the residence time of the liquid inside the particle bed, thus increasing the Damköhler (Da) number. The Da number relates the reaction time to the residence time in the reactor, as a rule of thumb a Da number of 0.1 results in conversion of 10 %, a Da higher than 10 results in 90 % conversion of the reaction product. [154] Looking at the black line in Figure 5-13, which is calculated for a calculated for a catalyst activity of 0.6 $g_{H2}\ g^{-1}_{cat}min^{-1}$, in line with the data extracted at low flowrates from Bulgarin et al. [82] It can be seen than Da values above 0.1 can only be obtained at higher residence times. However increasing the activity of the catalyst material, will increase the Da number. The catalyst used in this study had a low Pt loading at 0.3 wt. %, the activity of the material can be improved by increasing the Pt loading, as was observed by Ali et al. [84], under stirred conditions. Increasing the catalyst activity fivefold, a target set for future LOHC catalysts [261], will yield much higher Da numbers, even with higher flowrates, i.e. lower τ_{mod}, which required for fluidized bed reactors. Except for increase Pt loadings, reduced particle density and reduced particle size will allow for fluidization at reduced local fluid velocities, shifting the curve towards higher Da numbers and thus increased Degree of Dehydrogenation (DoD) of the system per pass of the reactor.

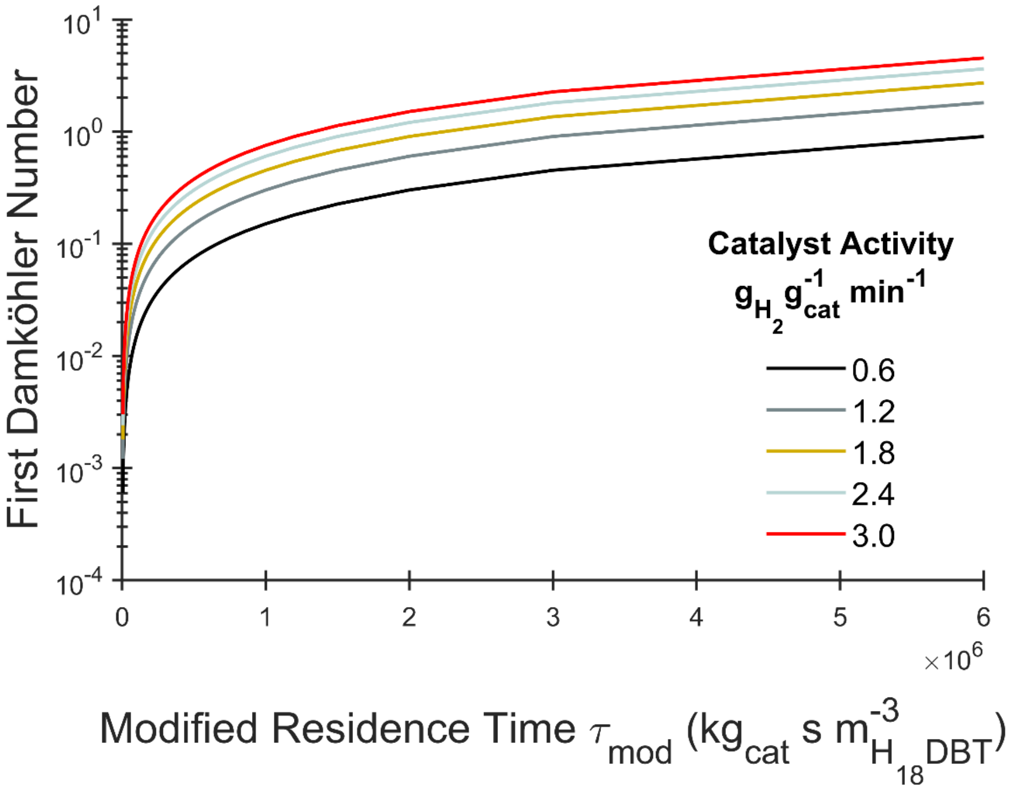

Figure 5-13 Plot of the first Damköhler number in function of the modified residence time. The kinetics of Bulgarin et al. [82] at 290 °C were used to calculate the Da numbers for a calculated catalyst activity of 0.6 $g_{H2}\,g^{-1}_{cat}$ min^{-1}.

Lower DoD at increased flowrate is a phenomenon also observed in the recent work of Kadar et al. [97] However, the decreased DoD is a trade-off with higher power densities which were observed at higher liquid flowrates in literature. The increase in power density observed by Kadar et al. occurred at flowrates which are still 200 times lower than the U_{lmf0} for the large, 3 mm particles used in their reactor setup. Lowering the particle size, to 0.5 mm, and reducing the size of the reactor from 128 mm x 80 mm to 42.6 mm x 40 mm, should be enough to operate the dehydrogenation reactor at fluidized bed conditions while using flowrates similar to the reported 6 L h^{-1} reported by Kadar et al. An alternative to a simple reduction in reactor cross section, could be the addition of the central cone in a conventional tubular shaped reactor unit. The exact height and slope of the cone should be designed to decrease the local liquid velocity to counter the increased gas phase induced agitation of the particle bed over the axial length of the reactor body.

5.4 Conclusion

In this chapter the fluidization of the particle bed during dehydrogenation of H_{18}DBT has been investigated in different reactor configurations, via CFD simulations. The CFD simulations were run with a custom developed code that mimics the H_2 release rate in those cells of the mesh which contain both particles and H_{18}DBT liquid. The total mass of H_2 released during the simulations of the dehydrogenation reaction, approached the extrapolated flowrate of experimental data from literature. The CFD simulations showed that by operating the dehydrogenation reaction in fluidized regimes, entrainment of the particles is expected, due to the accumulation of H_2 over the length of the bed which causes the particles to leave, and which renders a highly diluted particle phase. To counter the entrainment caused by the increasing amounts of H_2 gas in the bed, it is proposed to gradually decrease the flowrate over the bed. One such method to do this, is by adding a central cone in a swirling reactor geometry, which causes a gradual increase in cross section of the reactor and thus gradually lowering the local liquid velocity which reduces the entrainment of the particle phase. The addition of a central cone in the reactor has also shown via CFD simulation, to generate a bed that is more uniformly distributed in the reactor. Reduction of the diameter of the reactor has shown to drastically alter the fluidization behaviour of the particle bed. Reducing the diameter by 50 %, almost complete entrainment of the particle bed was observed at identical flowrates in a larger diameter reactor. By reducing the flowrate in the narrow reactor, a more compact particle bed could be obtained compared to the simulations at higher flowrates. This hinted a high dependency of the fluidization behaviour of the particles on the geometry of the reactor and the flowrate used, which is common in swirling fluidized bed reactors. This chapter provides a first insight into the potential improvements of the SFB prototype introduced in this work and can serve as a basis for a future fully parameterized shape optimization study.

Chapter 6

Conclusions and Future Outlook

6.1 General Conclusion

In the global search of a new, clean energy vector, H_2 has been identified as a likely candidate to fulfil this role. H_2 can be produced from renewable sources and has no inherent polluting properties, not as molecule on its own nor as the combusted product, which is water. Furthermore, it has a high gravimetric energy storage capacity, triple that of diesel fuel. The main downside of this molecule is its incredibly low density, which reduces the volumetric storage capacity of the gas. In recent years, several different strategies have been proposed to increase the volumetric energy density of H_2. These strategies include compression, liquefaction, adsorption and chemical reactions to higher density carriers. This thesis focusses on the last H_2 storage strategy, i.e., the chemical conversion to a high – density carrier. In **Chapter 1**, different chemical reactions are discussed that can be used to store H_2 at increased densities and it introduces the H_2 carrier of interest and main topic of research in this thesis. This is the molecule dibenzyltoluene, DBT and its hydrogenated counterpart perhydro-dibenzyltoluene, H_{18}DBT. DBT is an example of a Liquid Organic Hydrogen Carrier, LOHC. This molecule was identified as a highly promising H_2 carrier due to the inherent safety of the molecule, since it is a non-flammable, low-toxic organic liquid. It also has similar physicochemical properties compared to diesel fuel and can easily be fitted in existing fuel infrastructure, allowing for a fast integration of this carrier molecule into our society. The main downside in the use of this molecule is the energy requirement to release the H_2 from the carrier. The H_2 release process is an endothermic process requiring up to a third of the energy of the H_2 gas for the release reaction. Due to the endothermic nature of the release reaction, efficient mass and heat transfer during this process are crucial, to keep the process running at maximal efficiency. The H_2 release step is a catalytic process, meaning that the H_2 gas is only released when H_2 – rich carrier liquid comes into contact with a solid (noble) metal catalyst. In this thesis, the use of fluidized bed reactors is proposed, since they are known for increased mass and heat transfer compared to fixed bed reactors, which are the commercially available reactors for H_{18}DBT dehydrogenation. To study the potential of using fluidized bed reactors for the dehydrogenation of H_{18}DBT, I made use of computational fluid dynamics, CFD. The basic principles of the CFD simulations, applied to a simplified homogenous reacting systems have been explained in **Chapter 2**, by analysing CFD simulations of a reaction of *n*-butane to *i*-butane, which was part of a tutorial series of experimental methods in chemical engineering. CFD simulations were then used as a tool to evaluate the fluidization of a particle bed in **Chapter 3**. This study consisted of a cold flow mock-up of the dehydrogenation of $H_{18}DBT$ in a new reactor prototype. This reactor is considered a swirling fluidized bed reactor, SFB. This is a distinction from regular fluidized bed reactors since the flow is injected tangentially in the reactor causing a swirling motion of the liquid, rather than upwards flow which is used in conventional fluidized bed reactors. Since the dehydrogenation reaction of $H_{18}DBT$ is always three phasic, containing a liquid phase, a solid phase and a gas phase, the specific models to describe these interactions in CFD simulations were further analysed. This was the topic of **Chapter 4**, where I studied a *pseudo* – 2D fluidized bed reactor containing a liquid, gas, and solid phase. The CFD simulations of this simplified setup were analysed with camera techniques to assess the accuracy of different combinations of models required for the multiphase CFD simulations. This allowed for better model selection for the CFD simulations, to further increase the accuracy of the simulations. Finally in **Chapter 5**, the fluidization behaviour during dehydrogenation reaction of $H_{18}DBT$ was investigated. Due to the unavailability of both existing CFD solvers to simulate liquid – gas – solid catalytic reactions and the unavailability of intrinsic kinetics of the $H_{18}DBT$ dehydrogenation reaction, a new piece of software was coded to mimic the H_2 gas release during the reaction. This piece of code was based on a curve fitting and parametric estimation approach and showed to predict the H_2 release rates similarly compared to literature values. This allowed for simulations of the dehydrogenation reaction of $H_{18}DBT$ and study the behaviour of the particle bed in fluidized bed regimes. The fluidization of the particle bed was studied both in conventional fluidized bed reactors and in the prototype reactor that was proposed in **Chapter 3**. The potential improvements to the prototype reactor were evaluated in **Chapter 5**, this was the addition of a central cone and a reduction in cross section of the reactor body to improve the uniformity of the particle bed. The conclusions for each of the chapters of this thesis are listed in the following paragraphs.

In **Chapter 3** a new reactor prototype is introduced for the dehydrogenation of $H_{18}DBT$, to operate in swirling fluidization regimes. Key in this reactor design was the tangential position of the inlets on the main reactor body which caused a swirling behaviour of the liquid flow. From similarity correlations, a cold flow mock-up system was developed to study the behaviour of each of the three phases in the system. Both experiments and CFD simulations showed that the fluidization of the particle phase was possible in the prototype reactor.

However, at the operating conditions of the reactor, the fluidization of the particle bed was only possible when the liquid flow was combined with gas injection within the particle bed. This corresponded with literature on three phase fluidizations, where the addition of a gas phase lowers the required liquid velocity for fluidization. The azimuthal slip velocity between the particle and the liquid phase, was shown to be beneficial for H_2 gas removal, which would be produced during the H_2 release reaction. Inside the main reactor body, the liquid flow showed an upwards helical pattern, caused by the orientation of the inlets. The helical pattern caused the released gas to be concentrated in the centre of the reactor, which allows for easy separation of the gas phase and the liquid phase. The reactor itself is still a prototype designed to showcase the potential for fluidization of the dehydrogenation reaction of H_{18}DBT, and further design changes are required which are discussed in **Chapter 5**.

Before delving deeper into the design changes to the SFB, I explored the influence of different model combinations on the results of CFD simulations, which was the topic of **Chapter 4**. To investigate the effect of the models on the outcome of the simulations, I studied a very simple reactor configuration, a *pseudo* – 2D fluidized bed reactor, using water, He gas and glass beads as the three phases. This reactor had transparent walls, to allow for visualisation of the behaviour of the three phases. Using three different camera techniques, direct image analysis, particle image velocimetry and particle tracking velocimetry, the movement of the particle phase was tracked, and the experimental data was compared to the data obtained from simulations. This analysis showed that a three-phase *pseudo* – 2D fluidized bed can be simulated using a 2D simulation, with interface compression, a population balance model and gas phase turbulence enabled. The model combinations to simulate the interphase drag between the different phases that performed the best, based on this study were identified to be the following. For liquid – solid drag, the Gidaspow model was used, for liquid – gas drag the Ishii – Zuber model and no model for the gas – solid interaction. The other option that performed well was to use the Gidaspow model for liquid – solid drag and for gas – solid drag while using the Tomiyama model to account for the liquid – gas drag force.

Ultimately in **Chapter 5**, the findings from **Chapter 4** were used to simulate the prototype reactor from **Chapter 3** and explore further design changes to this system. The simulation procedure used in this chapter, made use of a novel approach to mimic the H_2 gas release in the presence of catalyst beads. This source term approach was based on curve fitting approach of literature data on $H_{18}DBT$ dehydrogenation, combined with a parameter estimation to achieve H_2 release values from the overall system comparable to those obtained from experimental data in literature. This custom-made piece of CFD code was firstly used to simulate a conventional fluidized bed reactor at different inlet flowrates. The simulations indicated that the particle distribution in the bed obtained from fluidization of the $H_{18}DBT$ dehydrogenation process is not uniform. This is due to the increasing amount of gas that is being generated in the system, the particle bed shows a significant particle entrainment which is detrimental to the efficiency of the dehydrogenation reaction, since the non-uniformity of the bed is likely to cause cold spots inside the densely packed region in the reactor, situated near the bottom of the system. Due to the dilution of the bed near the top of the reactor, the reactor volume is not used efficiently. The particle entrainment is likely caused by the rapid increase in gas hold-up in the system upon dehydrogenation of the $H_{18}DBT$ liquid. To counter this increase in gas – induced fluidization, the liquid velocity should locally decrease. An increase in cross section of the reactor body is a potential approach to achieve this. This is investigated in the final section of the thesis, where a central cone is added to the bottom of the SFB geometry from **Chapter 3**. The effect of the cone shows that the distribution of the particles in the bed becomes more uniform compared to the case without a cone, however the particle bed still shows dense regions near the bottom of the reactor body. To increase the fluidization of the particles, and reduce the dense particle bed near the bottom, the diameter of the cross section of the reactor was halved. This showed to have a huge effect on the fluidization of the beads as most of the beads moved from a dense section near the bottom of the bed towards a diluted transport regime, with both reactors operating at similar flowrate. Lowering the flowrate improved the uniformity of the particle bed, which indicates that there will be a close relationship between the design size of the reactor cross section and the flowrate at which it should operate for optimal H_2 release.

6.2 Suggestions for future research

This thesis served as the first study into the potential of fluidization for the dehydrogenation of $H_{18}DBT$ and provided insights into future research avenues. Insights in future work based on this thesis are twofold, both further improvements into the accuracy of three phase CFD simulations and new reactor geometries for the dehydrogenation of $H_{18}DBT$ are fields of research that should be further evaluated in the future.

In this thesis, I investigated the use of different model combinations and tested the accuracy on the prediction the particle bed height, bed profile and the local particle velocity. Additional testing is required to study the influence of these model combinations on the gas phase. This can be done by studying the bubble size distribution within the particle bed and comparing this to CFD simulations. The distribution of the gas phase has been shown to have large influence on the particle bed. So, an increased accuracy of the bubble size distribution via CFD simulations will increase the accuracy of the simulations of the three phase system. This can be achieved by further evaluation of the population balance models and included specific models for bubble breakage under the influence of bubble – particle collisions.

On the CFD side, there is currently a lack of a proper CFD solver to simulate liquid phase catalytic reactions. Development of such a solver, based on the intrinsic kinetics of the $H_{18}DBT$ dehydrogenation reaction will be crucial for CFD analysis of the system and will allow to include the effect of increased mass and heat transfer from fluidization. Development of this solver will firstly require further experimental work to extract the intrinsic kinetic parameters. Furthermore, due to the high endothermicity of the dehydrogenation reaction, different heat transfer models should be evaluated to further increase the accuracy of the CFD simulations. For this purpose I would propose a study of the different heat transfer models and assess the accuracy, similar to how drag models were evaluated to study the particle bed height and particle velocity in this thesis.

The emphasis of this thesis was placed mostly on CFD simulations, and even though I have tried to obtain simulations with a reasonable degree of accuracy via careful analysis of the grid size and the numerical models, these simulations will still require additional experimental work for validation. Based on the 2D simulations of the fluidized bed reactor, I would propose to investigate the dehydrogenation of $H_{18}DBT$ in a transparent reactor to monitor the particle entrainment visually in the fluidized bed regime and compare this to the simulations.

In the final section of this thesis, I explored the influence of design changes to the geometry of the SFB. This served as a first basis to build a full parametric study on. I have shown that there is a noticeable effect on the uniformity of the liquid velocity by the total number of inlets. The distribution of the particles within the reactor varies with the width of the reactive zone and the addition of a central cone. In the proposed parametric study further, these effects from an increased number of inlets should be further evaluated. The ratio of the cone width and height to the reactor diameter should be included in this study, as well as the optimal flowrate and the particle size. In this thesis, the use a swirling flow has been investigated, this is an extra complication to work with for parametric studies. As a first iteration of the reactor design based on the work of this thesis, I would propose the use of a conical shape reactor that is bottom fed. Via a plate distributor with a cone mounted directly on in the centre of it. The function of the cone is to decrease the cross section of reactor near the bottom, to have a higher liquid velocity in this region. A higher liquid velocity in the bottom of the reactor is required for fluidization since no gas phase is present initially, which will aid in fluidizing the particles. Once the reaction occurs and H_2 is being released from the carrier material, the liquid velocity will decrease due to the shape of the cone, this should be done to account for the gas phase induced fluidization, in order to keep the particle bed uniform. To elongate the effect of a gradually increasing cross section to reduce local liquid velocity, the outer edges of the reactor can we widened which is commonly seen as a disengagement section in fluidized bed reactors. The slope of both the inner and outer cones should be varied as a function of the H_2 release rate to account for the gas induced fluidization. Additionally, the H_2 can also be removed in situ to control the maximal H_2 gas present inside the reactor, which will control the fluidization of the particles in this three phase system. The proposed starting reactor for future studies is shown on Figure 6-1.

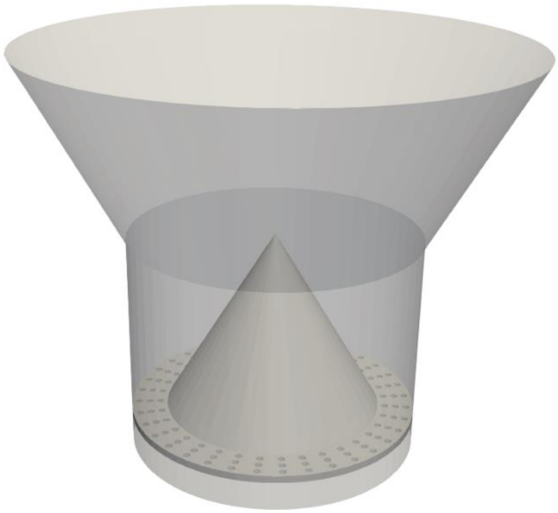

Figure 6-1 Proposed reactor geometry for follow up studies. Including a distributor plate with a central cone and a wider section right above the top of the cone.

Whichever design of dehydrogenation reactor that will ultimately lead to an intensified dehydrogenation process, the development of this reactor will required three separate blocks of process development for the research to be complete. The first block of the process intensification development usually consists of visualisation experiments which have been proposed as one of the next steps to analyse the particle bed entrainment during dehydrogenation. This will feed the second block which is the use of accurate CFD simulations that capture the results of the laboratory experiments, based on a reactive CFD solver. These CFD models then provide the basis for the proposed parametric optimization of the reactor geometry. The optimized geometry should then be further evaluated via process simulation software such as Aspen Plus. This software allows to estimate the process conditions and yield a techno-economic assessment. Completing this final step in the intensified reactor design, will ultimately bring the reactor up to TRL 5, i.e. being validated in an industrial relevant environment. [262]

Appendix I – Video of the LGSFB

Link to the video: https://youtu.be/X9Qnug7ixHY

QR code:

Appendix II – Mathematical Derivation of the catalytic source term

The curve fit of the n – root function using the lsqcurvefit tool in MATLAB yielded equation AIII.1.

$$Y_{H_2} = 1.9734e^{-5} \cdot \sqrt[1.3554]{\tau_{mod}} \qquad (AIII.1)$$

By combining the definition for the Y_{H_2} and equation $AIII.1$, the mass flux of H$_2$ flowing out of the reactor in function of the τ_{mod} could be expressed as equation$AIII.2$:

$$\dot{m}_{H_2} = \frac{1.9734e^{-5} \cdot 9 \cdot MW_{H_2}}{MW_{DBT_{H_{18}}}} \cdot \dot{m}_{H_{18}DBT} \cdot \sqrt[1.3554]{\tau_{mod}} \qquad (AIII.2)$$

This could be further modified to:

$$\dot{m}_{H_2} = \frac{1.9734e^{-5} \cdot 9 \cdot MW_{H_2}}{MW_{DBT_{H_{18}}}} \cdot \rho_{H_{18}DBT} \cdot \dot{V}_{H_{18}DBT} \cdot \sqrt[1.3554]{\tau_{mod}} \qquad (AIII.3)$$

Using the definition of the modified τ_{mod}, which is the ratio of the catalyst mass to the liquid flowrate, the catalyst mass appears in the equation:

$$\dot{m}_{H_2} = \frac{1.9734e^{-5} \cdot 9 \cdot MW_{H_2}}{MW_{DBT_{H_{18}}}} \cdot \rho_{H_{18}DBT} \cdot \dot{V}_{H_{18}DBT} \cdot \sqrt[1.3554]{\frac{m_{cat}}{\dot{V}_{H_{18}DBT}}} \qquad (AIII.4)$$

Rewriting equation $AIII.4$ to the change n-root function to power functions gives:

$$\dot{m}_{H_2} = \frac{1.9734e^{-5} \cdot 9 \cdot MW_{H_2}}{MW_{DBT_{H_{18}}}} \cdot \rho_{H_{18}DBT} \cdot m_{cat}^{0.7378} \cdot \dot{V}_{H_{18}DBT}^{0.2622} \qquad (AIII.5)$$

Equation $AIII.5$ holds for the entire computational domain; however, the source term will be applied to each cell individually and this should be reflected in the calculation of the H$_2$ release rate. Similarly, the mass of catalyst should also be evaluated for each cell individually. The volumetric flowrate within one cell, $\dot{V}_{H_{18}DBT_{cell}}$, is defined as:

$$\dot{V}_{H_{18}DBT_{cell}} = \alpha_{H_{18}DBT} \cdot \frac{V_{cell}}{V_{total}} \dot{V}_{total} \qquad (AIII.6)$$

Equation $AIII.6$ multiplies the volumetric flowrate of the total domain with the ratio of the cell volume on the total volume of the mesh and the volume fraction of liquid within the cell. Summing over all the cells in the computational domain will this yield the total volumetric flowrate, thus relating the volumetric flowrate of the total domain to the volumetric flowrate of a singular cell.

The mass of catalyst within the cell can be found by equation $AIII.7$:

$$m_{cat} = \alpha_{cat} \cdot \rho_{cat} \cdot V_{cell} \qquad (AIII.7)$$

With the value of ρ_{cat} being the particle density of the material. The expression $\alpha_{cat} \cdot \rho_{cat}$ can be seen as the bulk density of the particle phase inside the cell of the mesh.

Looking at Figure 5-2B, which shows the curve fit of the data from Bulgarin et al. [82] , it is clear that this approximation of the H_2 release rate is not yet complete. At high modified residence times, so cells containing a lot of catalyst mass compared at a very low volumetric flowrate, the extrapolation of equation $AIII.1$ exceeds a Y_{H_2} of 1, which is due to the curve fitting nature of the expression. That is why I imposed a secondary condition on the H_2 release rate for modified residence times which are equal to or above $2.5 \cdot 10^6$, this limitation is derived from the definition of a Y_{H_2} equal to 1.

$$if\ \tau_{mod} \geq 2.5e^6 \rightarrow \dot{m}_{H_2} = 9 \cdot \frac{MW_{H_2}}{MW_{H_{18}DBT}} \cdot \rho_{H_{18}DBT} \cdot \dot{V}_{H_{18}DBT} \qquad (AIII.8)$$

Appendix III Source code of the Catalytic Source Term

CatalyticMassSource.H

```
/*---------------------------------------------------------------------------*\
  =========                 |
  \\      /  F ield         | OpenFOAM: The Open Source CFD Toolbox
   \\    /   O peration     | Website:  https://openfoam.org
    \\  /    A nd           | Copyright (C) 2021-2023 OpenFOAM Foundation
     \\/     M anipulation  |
-------------------------------------------------------------------------------
License
    This file is part of OpenFOAM.
    OpenFOAM is free software: you can redistribute it and/or modify it
    under the terms of the GNU General Public License as published by
    the Free Software Foundation, either version 3 of the License, or
    (at your option) any later version.
    OpenFOAM is distributed in the hope that it will be useful, but WITHOUT
    ANY WARRANTY; without even the implied warranty of MERCHANTABILITY or
    FITNESS FOR A PARTICULAR PURPOSE.  See the GNU General Public License
    for more details.
    You should have received a copy of the GNU General Public License
    along with OpenFOAM.  If not, see <http://www.gnu.org/licenses/>.
Class
    Foam::fv::catalyticLOHCMassSource
Description
    This fvModel applies a mass source to the continuity equation and to all
    field equations.
    If the mass flow rate is positive then user-supplied fixed property values
    are introduced to the field equations. If the mass flow rate is negative
    then properties are removed at their current value.
Usage
    Example usage:
    \verbatim
    catalyticLOHCMassSource
    {
        type            catalyticLOHCMassSource;
        selectionMode          all;
        catalystPhase      alpha.particles;
        catalystDensity    rho.particles;
        liquidPhase        alpha.liquid
        liquidDensity      alpha.rho;

      parameter1          1.65 ;
      parameter2          2.8 ;

        volumetricFlowRate
        {
             type   scale;
             scale  squarePulse;
             start 0.5;
             duration 100;
             value  $DBT_InletFlowRateValue;
        }
        fieldValues
        {
            U.gas               (10 0 0);
            T.gas               300;
            k.gas               0.375;
            epsilon.gas         14.855;
        }
    }
    \endverbatim
    If the mass flow rate is positive then values should be provided for all
    solved for fields. Warnings will be issued if values are not provided for
    fields for which transport equations are solved. Warnings will also be
    issued if values are provided for fields which are not solved for.
SourceFiles
    catalyticLOHCMassSource.C
\*---------------------------------------------------------------------------*/
#ifndef catalyticLOHCMassSource_H
#define catalyticLOHCMassSource_H
#include "fvModel.H"
#include "fvCellSet.H"
#include "HashPtrTable.H"
#include "unknownTypeFunction1.H"
// * * * * * * * * * * * * * * * * * * * * * * * * * * * * * * * * * * * * * //
namespace Foam
{
namespace fv
{
/*---------------------------------------------------------------------------*\
                        Class catalyticLOHCMassSourceBase Declaration
\*---------------------------------------------------------------------------*/
class catalyticLOHCMassSourceBase
:
    public fvModel
{
private:
    // Private Data
        //- Name of the phase
        word phaseName_;
        //- Name of the density field
        word rhoName_;
        //- Name of the energy field
        word heName_;
        //- Name of the temperature field
        word TName_;
        //- The set of cells the fvConstraint applies to
        fvCellSet set_;
        //- Field values
        HashPtrTable<unknownTypeFunction1> fieldValues_;

             //- Name of the catalyst phase
        word catalystName_;

        //- Name of the catalyst density field
        word catalystRhoName_;

             //- Name of the liquid phase
        word liquidName_;

             //- Name of the catalyst density field
        word liquidRhoName_;

             //- parameter for the low tau
             scalar parameter1_;
             //- parameter for the high tau
             scalar parameter2_;
    // Private Member Functions
        //- Non-virtual read
        void readCoeffs();
        //- Return the mass flow rate
        virtual scalar volumetricFlowRate() const = 0;
        // Sources
            //- Add a source term to an equation
            template<class Type>
            void addGeneralSupType
            (
                fvMatrix<Type>& eqn,
                const word& fieldName
            ) const;
            //- Add a source term to an equation
            template<class Type>
            void addSupType(fvMatrix<Type>& eqn, const word& fieldName) const;
            //- Add a source term to a scalar equation
            void addSupType(fvMatrix<scalar>& eqn, const word& fieldName) const;
            //- Add a source term to a compressible equation
            template<class Type>
            void addSupType
            (
                const volScalarField& rho,
                fvMatrix<Type>& eqn,
                const word& fieldName
            ) const;
            //- Add a source term to a phase equation
            template<class Type>
            void addSupType
            (
                const volScalarField& alpha,
                const volScalarField& rho,
                fvMatrix<Type>& eqn,
                const word& fieldName
            ) const;
protected:
    // Protected Member Functions
        //- Read the set
        void readSet();
        //- Read the field values
        void readFieldValues();
public:
    //- Runtime type information
    TypeName("catalyticLOHCMassSourceBase");
    // Constructors
        //- Construct from explicit source name and mesh
        catalyticLOHCMassSourceBase
        (
            const word& name,
            const word& modelType,
            const fvMesh& mesh,
            const dictionary& dict
        );
        //- Disallow default bitwise copy construction
        catalyticLOHCMassSourceBase(const catalyticLOHCMassSourceBase&) = delete;
    // Member Functions
        // Checks
            //- Return true if the fvModel adds a source term to the given
            //  field's transport equation
            virtual bool addsSupToField(const word& fieldName) const;
            //- Return the list of fields for which the fvModel adds source term
            //  to the transport equation
            virtual wordList addSupFields() const;
        // Sources
            //- Add a source term to an equation
            FOR_ALL_FIELD_TYPES(DEFINE_FV_MODEL_ADD_SUP);
            //- Add a source term to a compressible equation
            FOR_ALL_FIELD_TYPES(DEFINE_FV_MODEL_ADD_RHO_SUP);
            //- Add a source term to a phase equation
            FOR_ALL_FIELD_TYPES(DEFINE_FV_MODEL_ADD_ALPHA_RHO_SUP);
        // Mesh changes
            //- Update for mesh motion
            virtual bool movePoints();
            //- Update topology using the given map
            virtual void topoChange(const polyTopoChangeMap&);
            //- Update from another mesh using the given map
            virtual void mapMesh(const polyMeshMap&);
            //- Redistribute or update using the given distribution map
            virtual void distribute(const polyDistributionMap&);
        // IO
            //- Read source dictionary
            virtual bool read(const dictionary& dict);
    // Member Operators
        //- Disallow default bitwise assignment
        void operator=(const catalyticLOHCMassSourceBase&) = delete;
};
/*---------------------------------------------------------------------------*\
                          Class catalyticLOHCMassSource Declaration
\*---------------------------------------------------------------------------*/
class catalyticLOHCMassSource
:
    public catalyticLOHCMassSourceBase
{
private:
    // Private Data
        //- Mass flow rate
        autoPtr<Function1<scalar>> volumetricFlowRate_;
    // Private Member Functions
        //- Non-virtual read
        void readCoeffs();
        //- Return the mass flow rate
        virtual scalar volumetricFlowRate() const;
public:
    //- Runtime type information
    TypeName("catalyticLOHCMassSource");
    // Constructors
        //- Construct from explicit source name and mesh
        catalyticLOHCMassSource
        (
            const word& name,
            const word& modelType,
            const fvMesh& mesh,
            const dictionary& dict
        );
    // Member Functions
        // IO
            //- Read source dictionary
            virtual bool read(const dictionary& dict);
};
// * * * * * * * * * * * * * * * * * * * * * * * * * * * * * * * * * * * * * //
} // End namespace fv
} // End namespace Foam
// * * * * * * * * * * * * * * * * * * * * * * * * * * * * * * * * * * * * *
* * //
#endif
//
**********************************************************************
** //
```

CatalyticMassSource.H

```
/*---------------------------------------------------------------------------*\
  =========                 |
  \\      /  F ield         | OpenFOAM: The Open Source CFD Toolbox
   \\    /   O peration     | Website:  https://openfoam.org
    \\  /    A nd           | Copyright (C) 2021-2023 OpenFOAM Foundation
     \\/     M anipulation  |
-------------------------------------------------------------------------------
License
    This file is part of OpenFOAM.
    OpenFOAM is free software: you can redistribute it and/or modify it
    under the terms of the GNU General Public License as published by
    the Free Software Foundation, either version 3 of the License, or
    (at your option) any later version.
    OpenFOAM is distributed in the hope that it will be useful, but WITHOUT
    ANY WARRANTY; without even the implied warranty of MERCHANTABILITY or
    FITNESS FOR A PARTICULAR PURPOSE.  See the GNU General Public License
    for more details.
    You should have received a copy of the GNU General Public License
    along with OpenFOAM.  If not, see <http://www.gnu.org/licenses/>.
\*---------------------------------------------------------------------------*/
#include "catalyticLOHCMassSource.H"
#include "fvMatrices.H"
#include "basicThermo.H"
#include "addToRunTimeSelectionTable.H"
// * * * * * * * * * * * * * Static Member Functions * * * * * * * * * * * * //
namespace Foam
{
namespace fv
{
    defineTypeNameAndDebug(catalyticLOHCMassSourceBase, 0);
    defineTypeNameAndDebug(catalyticLOHCMassSource, 0);
    addToRunTimeSelectionTable(fvModel, catalyticLOHCMassSource, dictionary);
}
}
// * * * * * * * * * * * * * Private Member Functions  * * * * * * * * * * * //
void Foam::fv::catalyticLOHCMassSourceBase::readCoeffs()
{
phaseName_ = coeffs().lookupOrDefault<word>("phase", word::null);
catalystName_=coeffs().lookupOrDefault<word>("catalystPhase","alpha.particles");
catalystRhoName_=coeffs().lookupOrDefault<word>("catalystDensity","rho.particles");
liquidName_ = coeffs().lookupOrDefault<word>("liquidPhase", "alpha.liquid");
liquidRhoName_ = coeffs().lookupOrDefault<word>("liquidDensity", "rho.liquid");
parameter1_ = coeffs().lookup<scalar>("parameter1");
parameter2_ = coeffs().lookup<scalar>("parameter2");
    rhoName_ =
        coeffs().lookupOrDefault<word>
        (
            "rho",
            IOobject::groupName("rho", phaseName_)
        );
    if
    (
        mesh().foundObject<basicThermo>
        (
            IOobject::groupName(physicalProperties::typeName, phaseName_)
        )
    )
    {
        const basicThermo& thermo =
            mesh().lookupObject<basicThermo>
            (
                IOobject::groupName(physicalProperties::typeName, phaseName_)
            );
        heName_ = thermo.he().name();
        TName_ = thermo.T().name();
    }
}
template<class Type>
void Foam::fv::catalyticLOHCMassSourceBase::addGeneralSupType
(
    fvMatrix<Type>& eqn,
    const word& fieldName
) const
{
    const labelUList cells = set_.cells();
    const scalar volumetricFlowRate = this->volumetricFlowRate();
    if (volumetricFlowRate > 0)
    {
        const Type value =
            fieldValues_[fieldName]->value<Type>(mesh().time().userTimeValue());
        forAll(cells, i)
        {
            eqn.source()[cells[i]] -=
                mesh().V()[cells[i]]/set_.V()*volumetricFlowRate*value;
        }
    }
    else
    {
        forAll(cells, i)
        {
            eqn.diag()[cells[i]] +=
                mesh().V()[cells[i]]/set_.V()*volumetricFlowRate;
        }
    }
}
template<class Type>
void Foam::fv::catalyticLOHCMassSourceBase::addSupType
(
    fvMatrix<Type>& eqn,
    const word& fieldName
) const
{
    addGeneralSupType(eqn, fieldName);
}
void Foam::fv::catalyticLOHCMassSourceBase::addSupType
(
    fvMatrix<scalar>& eqn,
    const word& fieldName
) const
{
    const labelUList cells = set_.cells();
if (fieldName == rhoName_)
{
const scalar volumetricFlowRate = this->volumetricFlowRate();
const volScalarField& alphaP =mesh().lookupObject<volScalarField>(catalystName_);
const volScalarField& rhoP = mesh().lookupObject<volScalarField>(catalystRhoName_);
const volScalarField& alphaL = mesh().lookupObject<volScalarField>(liquidName_);
const volScalarField& rhoL = mesh().lookupObject<volScalarField>(liquidRhoName_);

forAll(cells, i)
{
   if (alphaP[cells[i]] > 0.1) // only valid in cells containing particles
   {
       // if tau < smaller than 2.5e6 --> max H2 from extraction
if
( alphaP[cells[i]]*rhoP[cells[i]]*set_.V()*
  max(volumetricFlowRate*alphaL[cells[i]],small) < 2.5e6
)
{

eqn.source()[cells[i]] -=
parameter1_*1.22486e-6 * rhoL[cells[i]]*
pow(mesh().V()[cells[i]]/set_.V()*volumetricFlowRate*alphaL[cells[i]],0.2622)*
pow(alphaP[cells[i]]*rhoP[cells[i]]*mesh().V()[cells[i]],0.7377);
}
else // if tau exceeds the set value, the H2 release rate maxes at a yield of 1
{

       eqn.source()[cells[i]] -=

       parameter2_*0.062068 * rhoL[cells[i]] *
       mesh().V()[cells[i]]/set_.V()*volumetricFlowRate*alphaL[cells[i]];
                           }
}
}
    }
    else if (fieldName == heName_ && fieldValues_.found(TName_))
    {
        const scalar volumetricFlowRate = this->volumetricFlowRate();
        if (volumetricFlowRate > 0)
        {
            if (fieldValues_.found(heName_))
            {
                WarningInFunction
                    << "Source " << name() << " defined for both field "
                    << heName_ << " and " << TName_
                    << ". Only one of these should be present." << endl;
            }
            const basicThermo& thermo =
                mesh().lookupObject<basicThermo>
                (
                    IOobject::groupName
                    (
                        physicalProperties::typeName,
                        phaseName_
                    )
                );
            const scalar T =
                fieldValues_[TName_]->value<scalar>
                (
                    mesh().time().userTimeValue()
                );
            const scalarField hs
            (
                thermo.hs(scalarField(cells.size(), T), cells)
            );
            forAll(cells, i)
            {
                eqn.source()[cells[i]] -=
                    mesh().V()[cells[i]]/set_.V()*volumetricFlowRate*hs[i];
            }
        }
        else
        {
            forAll(cells, i)
            {
                eqn.diag()[cells[i]] +=
                    mesh().V()[cells[i]]/set_.V()*volumetricFlowRate;
            }
        }
    }
    else
    {
        addGeneralSupType(eqn, fieldName);
    }
}
template<class Type>
void Foam::fv::catalyticLOHCMassSourceBase::addSupType
(
    const volScalarField& rho,
    fvMatrix<Type>& eqn,
    const word& fieldName
) const
{
    addSupType(eqn, fieldName);
}
template<class Type>
void Foam::fv::catalyticLOHCMassSourceBase::addSupType
(
    const volScalarField& alpha,
    const volScalarField& rho,
    fvMatrix<Type>& eqn,
    const word& fieldName
) const
```

```
{
    addSupType(eqn, fieldName);
}
void Foam::fv::catalyticLOHCMassSource::readCoeffs()
{
    readSet();
    readFieldValues();
    volumetricFlowRate_.reset
    (
        Function1<scalar>::New("volumetricFlowRate", coeffs()).ptr()
    );
}
Foam::scalar Foam::fv::catalyticLOHCMassSource::volumetricFlowRate() const
{
    return volumetricFlowRate_->value(mesh().time().userTimeValue());
}
// * * * * * * * * * * * * Protected Member Functions  * * * * * * * * * * * //
void Foam::fv::catalyticLOHCMassSourceBase::readSet()
{
    set_.read(coeffs());
}
void Foam::fv::catalyticLOHCMassSourceBase::readFieldValues()
{
    fieldValues_.clear();
    const dictionary& fieldCoeffs = coeffs().subDict("fieldValues");
    forAllConstIter(dictionary, fieldCoeffs, iter)
    {
        fieldValues_.set
        (
            iter().keyword(),
            new unknownTypeFunction1(iter().keyword(), fieldCoeffs)
        );
    }
}
// * * * * * * * * * * * * * * * * Constructors  * * * * * * * * * * * * * * //
Foam::fv::catalyticLOHCMassSourceBase::catalyticLOHCMassSourceBase
(
    const word& name,
    const word& modelType,
    const fvMesh& mesh,
    const dictionary& dict
)
:
    fvModel(name, modelType, mesh, dict),
    phaseName_(),
    rhoName_(),
    heName_(),
    TName_(),
    set_(fvCellSet(mesh)),
    fieldValues_()
{
    readCoeffs();
}
Foam::fv::catalyticLOHCMassSource::catalyticLOHCMassSource
(
    const word& name,
    const word& modelType,
    const fvMesh& mesh,
    const dictionary& dict
)
:
    catalyticLOHCMassSourceBase(name, modelType, mesh, dict),
    volumetricFlowRate_()
{
    readCoeffs();
}
// * * * * * * * * * * * * * * * Member Functions  * * * * * * * * * * * * * //
```

```
bool  Foam::fv::catalyticLOHCMassSourceBase::addsSupToField(const  word&  fieldName)
const
{
    const bool isThisPhase = IOobject::group(fieldName) == phaseName_;
    if
    (
        isThisPhase
     && volumetricFlowRate() > 0
     && !(fieldName == rhoName_)
     && !(fieldName == heName_ && fieldValues_.found(TName_))
     && !fieldValues_.found(fieldName)
    )
    {
        WarningInFunction
            << "No value supplied for field " << fieldName << " in "
            << type() << " fvModel " << name() << endl;
        return false;
    }
    return isThisPhase;
}
Foam::wordList Foam::fv::catalyticLOHCMassSourceBase::addSupFields() const
{
    wordList fieldNames = fieldValues_.toc();
    if (fieldValues_.found(TName_))
    {
        fieldNames[findIndex(fieldNames, TName_)] = heName_;
    }
    return fieldNames;
}
FOR_ALL_FIELD_TYPES(IMPLEMENT_FV_MODEL_ADD_SUP, fv::catalyticLOHCMassSourceBase);
FOR_ALL_FIELD_TYPES(IMPLEMENT_FV_MODEL_ADD_RHO_SUP,
fv::catalyticLOHCMassSourceBase);
FOR_ALL_FIELD_TYPES(IMPLEMENT_FV_MODEL_ADD_ALPHA_RHO_SUP,
fv::catalyticLOHCMassSourceBase);
bool Foam::fv::catalyticLOHCMassSourceBase::movePoints()
{
    set_.movePoints();
    return true;
}
void Foam::fv::catalyticLOHCMassSourceBase::topoChange(const polyTopoChangeMap& map)
{
    set_.topoChange(map);
}
void Foam::fv::catalyticLOHCMassSourceBase::mapMesh(const polyMeshMap& map)
{
    set_.mapMesh(map);
}
void  Foam::fv::catalyticLOHCMassSourceBase::distribute(const  polyDistributionMap&
map)
{
    set_.distribute(map);
}
bool Foam::fv::catalyticLOHCMassSourceBase::read(const dictionary& dict)
{
    if (fvModel::read(dict))
    {
        readCoeffs();
        return true;
    }
    else
    {
        return false;
    }
}
bool Foam::fv::catalyticLOHCMassSource::read(const dictionary& dict)
{
    if (catalyticLOHCMassSourceBase::read(dict))
    {
        readCoeffs();
        return true;
    }
    else
    {
        return false;
    }
}
// *************************************************************************** //
```

Appendix IV Thermophysical properties of $H_{18}DBT$

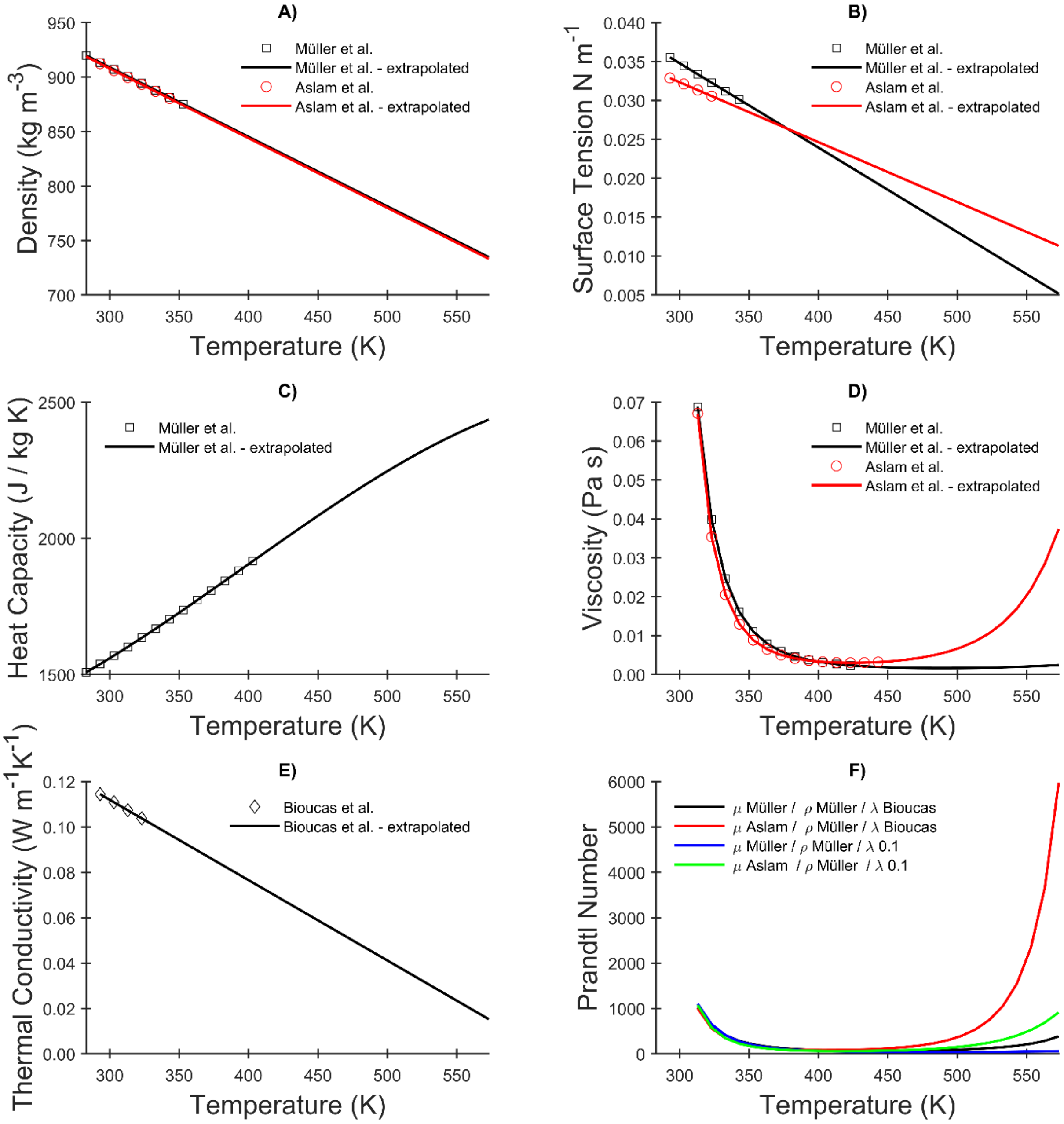

Appendix IV – Plots showing the extrapolated thermophysical properties of $H_{18}DBT$ A) the density, B) Surface Tension, C) Heat Capacity, D) Viscosity, E) Thermal Conductivity, F) Prandtl Number

Appendix V – Curriculum Vitae

PERSONAL INFORMATION

Name	Laurens Van Hoecke
Date of Birth	May 2nd, 1995
Place of Birth	Antwerpen, Wilrijk
Nationality	Belgian
e-mail private	laurensvanhoecke@hotmail.com

EDUCATION

2013 - 2016	Bachelor in Bioscience Engineering (UAntwerp)
2016 - 2018	Master in Bioscience Engineering: Catalytic Technology (KULeuven)
2018 - 2024	PhD in Bioscience Engineering (UAntwerp)

PUBLICATIONS

- Stanislaw P Zankowski, **Laurens Van Hoecke**, Felix Mattelaer, Marc De Raedt, Olivier Richard, Christophe Detavernier, Philippe M Vereecken, *Redox Layer Deposition of Thin Films of* MnO_2 *on Nanostructured Substrates from Aqueous Solutions*, Chemistry of Materials, 2019, 31, 13,4805-4816.
- **Laurens Van Hoecke**, Ludovic Laffineur, Roy Campe, Patrice Perreault, Sammy W. Verbruggen, Siliva Lenaerts, *Challenges in the use of hydrogen for maritime applications, Energy and Environmental Science, 2021, 14, 815-843*
- **Laurens Van Hoecke**, Dieter Boeye, Arturo Gonzalez-Quiroga, Gregory S. Patience, Patrice Perreault, *Experimental methods in chemical engineering: Computational fluid dynamics/finite volume method – CFD/FVM, Can. J. Chem. Eng.* 2023, 101(2), 545
- Patrice Perreault, **Laurens Van Hoecke**, Hesam Pourfallah, Nithin B. Kummamuru, Christian-Renato Boruntea, Patrick Preuster, *Critical challenges towards the*

commercial rollouts of a LOHC-based H2 economy, Current Opinion in Green and Sustainable Chemistry, 2023, 41, 100836

- **Laurens Van Hoecke**, Nithin B. Kummamuru, Hesam Pourfallah, Sammy W. Verbruggen, Patrice Perreault, *Intensified swirling reactor for the dehydrogenation of LOHC, International Journal of Hydrogen Energy, 2024, 51,D, 611-623*

SUBMITTED PUBLICATIONS

- **Laurens Van Hoecke**, Nithin B. Kummamuru, Hesam Pourfallah, Sammy W. Verbruggen, Patrice Perreault, *A Comparison of Multiphase Eulerian – Eulerian Drag model Combinations To Simulations Liquid – Gas – Solid Fluidized Beds,* Submitted to Chemical Engineering Science (9/02/2024)

CONFERENCE CONTRIBUTIONS

Oral Presentations

- Laurens van Hoecke, Sammy W. Verbruggen, Silvia Lenaerts, *Chemical Hydrogen Storage as a Fuel in the Shipping Industry,* 24th National Symposium of Applied Biological Sciences, Ghent, Belgium (04/02/2019)
- Laurens van Hoecke, Patrice Perreault, Sammy W. Verbruggen, Silvia Lenaerts, *The Use of Renewable Hydrogen for Maritime Applications,* 25th National Symposium of Applied Biological Sciences, Ghent, Belgium (31/01/2020)
- Laurens Van Hoecke, Nithin B. Kummamuru, Sammy W. Verbruggen, Patrice Perreault, *CFD – Study for Improved Dehydrogenation of LOHC,* H2&FC PhD and Researcher’s Day, Linkebeek, Belgium (25/05/2022)
- Laurens Van Hoecke, Nithin B. Kummamuru, Sammy W. Verbruggen, Patrice Perreault, *CFD-Assisted Hydrodynamic Characterization Of A Centrifugal Liquid Organic Hydrogen Carrier Dehydrogenation Unit*, 23rd World Hydrogen Energy Conference, Istanbul, Turkey (26/07/2022 – 30/07/2022)
- Laurens Van Hoecke, Nithin B. Kummamuru, Hesam Pourfallah, Sammy W. Verbruggen, Patrice Perreault, *CFD – Study for Enhanced Degassing of a*

Dehydrogenation Reactor for Liquid Organic Hydrogen Carriers, CRF – Chemsys, Blankenberge, Belgium (12/10/2022 – 14/10/2022)

Poster Presentations

- Laurens van Hoecke, Sammy W. Verbruggen, Silvia Lenaerts, *The Use of Hydrogen as a clean fuel in the shipping industry,* 20th Netherlands Catalysis and Chemistry Conference (NCCC), Noordwijkerhout – the Netherlands (04/03/2019 – 06/03/2019)
- Laurens van Hoecke, Sammy W. Verbruggen, Silvia Lenaerts, *Challenges in Hydrogen Storage for Maritime Applications,* 21st Netherlands Catalysis and Chemistry Conference (NCCC), Noordwijkerhout – the Netherlands (02/03/2020 – 02/03/2020)
- Laurens Van Hoecke, Hesam Pourfallah, Patrice Perreault, *CFD Study into Enhanced Degassing During Dehydrogenation of Liquid Organic Hydrogen Carriers*, Hydrogen Research Event, Antwerp, Belgium (04/05/2022)
- Laurens Van Hoecke, Hesam Pourfallah, Patrice Perreault, *CFD Study into Enhanced Degassing During Dehydrogenation of Liquid Organic Hydrogen Carriers*, 26th National Symposium of Applied Biological Sciences, Antwerp, Belgium (08/07/2022)

SUPERVISION OF BACHELOR PROJECTS

- Isabelle Morowa, Margot de Meyer, UAntwerp (2019 – 2020)
  De Generatie van Zeezout Aerosolen in de Sea Box
- Dieter Boeye, UAntwerp (2020 – 2021)
  Centrifugal Reactor Design
- Anouar Hlaloum, UAntwerp (2022 – 2023)
  Shape optimization of hydrogen storage unit:
  Influence of solid particles on fluidization behaviour
- Bilal El Mossaoui, UAntwerp (2022 – 2023)
  Shape Optimization of Hydrogen Storage Reactor Unit

SUPERVISION OF MASTER THESES

- Dieter Boeye, UAntwerp (2021 – 2022)

  Concepts for CFD simulations of LOHCs with OpenFOAM
- Bart Van Boxmeer, UAntwerp (2022 – 2023)

  Form optimization of a swirling fluidization reactor
- Mahmoud Shakleya, UAntwerp (2022 – 2023)

  Optimizing the design of a fluidized bed reactor for the dehydrogenation of $H_{18}DBT$

Bibliography

1. IEA, *The Future of Hydrogen, Seizing toaday's opportunities*. 2019.
2. Turner, J.A., *Sustainable Hydrogen Production.* Science, 2004. **305**(5686): p. 972-974.
3. Ji, M. and J. Wang, *Review and comparison of various hydrogen production methods based on costs and life cycle impact assessment indicators.* International Journal of Hydrogen Energy, 2021. **46**(78): p. 38612-38635.
4. Enerdata, *Global Energy Trends*. 2023, Enerdata: Grenoble. p. 68.
5. Finsterle, W., et al., *The total solar irradiance during the recent solar minimum period measured by SOHO/VIRGO.* Scientific Reports, 2021. **11**(1): p. 7835.
6. Overland, I., J. Juraev, and R. Vakulchuk, *Are renewable energy sources more evenly distributed than fossil fuels?* Renewable Energy, 2022. **200**: p. 379-386.
7. Lin, R.-H., Y.-Y. Zhao, and B.-D. Wu, *Toward a hydrogen society: Hydrogen and smart grid integration.* International Journal of Hydrogen Energy, 2020. **45**(39): p. 20164-20175.
8. Stępień, Z. *A Comprehensive Overview of Hydrogen-Fueled Internal Combustion Engines: Achievements and Future Challenges*. Energies, 2021. **14**, DOI: 10.3390/en14206504.
9. Service, R.F., *The Hydrogen Backlash.* Science, 2004. **305**(5686): p. 958-961.
10. Zhang, F., et al., *The survey of key technologies in hydrogen energy storage.* International Journal of Hydrogen Energy, 2016. **41**(33): p. 14535-14552.
11. Murray, L.J., M. Dinca, and J.R. Long, *Hydrogen storage in metal-organic frameworks.* Chem Soc Rev, 2009. **38**(5): p. 1294-314.
12. Darkrim, F.L., P. Malbrunot, and G.P. Tartaglia, *Review of hydrogen storage by adsorption in carbon nanotubes.* International Journal of Hydrogen Energy, 2002. **27**(2): p. 193-202.
13. Züttel, A., et al., *Hydrogen storage in carbon nanostructures.* International Journal of Hydrogen Energy, 2002. **27**(2): p. 203-212.
14. Zhu, Q.-L. and Q. Xu, *Liquid organic and inorganic chemical hydrides for high-capacity hydrogen storage.* Energy & Environmental Science, 2015. **8**(2): p. 478-512.
15. Aakko-Saksa, P.T., et al., *Liquid organic hydrogen carriers for transportation and storing of renewable energy – Review and discussion.* Journal of Power Sources, 2018. **396**: p. 803-823.
16. Makowski, P., et al., *Organic materials for hydrogen storage applications: from physisorption on organic solids to chemisorption in organic molecules.* Energy & Environmental Science, 2009. **2**(5): p. 480-490.
17. Yadav, M. and Q. Xu, *Liquid-phase chemical hydrogen storage materials.* Energy & Environmental Science, 2012. **5**(12): p. 9698-9725.
18. Schlapbach, L. and A. Züttel, *Hydrogen-storage materials for mobile applications.* Nature, 2001. **414**(6861): p. 353-358.
19. Rollinson, A.N., et al., *Urea as a hydrogen carrier: a perspective on its potential for safe, sustainable and long-term energy supply.* Energy & Environmental Science, 2011. **4**(4): p. 1216-1224.
20. Kar, S., et al., *Advances in catalytic homogeneous hydrogenation of carbon dioxide to methanol.* Journal of CO2 Utilization, 2018. **23**: p. 212-218.
21. Olah, G.A., G.K.S. Prakash, and A. Goeppert, *Anthropogenic Chemical Carbon Cycle for a Sustainable Future.* Journal of the American Chemical Society, 2011. **133**(33): p. 12881-12898.
22. Saeidi, S., N.A.S. Amin, and M.R. Rahimpour, *Hydrogenation of CO2 to value-added products—A review and potential future developments.* Journal of CO2 Utilization, 2014. **5**: p. 66-81.
23. Van Hoecke, L., et al., *Challenges in the use of hydrogen for maritime applications.* Energy & Environmental Science, 2021. **14**(2): p. 815-843.
24. Davison, N. and M.R. Edwards, *Effects of fire on small commercial gas cylinders.* Engineering Failure Analysis, 2008. **15**(8): p. 1000-1008.
25. Tupper, M., et al., *High pressure carbon composite pressure vessel*. 2015: United States of America. p. 11.
26. Rafiee, R. and M.A. Torabi, *Stochastic prediction of burst pressure in composite pressure vessels.* Composite Structures, 2018. **185**: p. 573-583.
27. Barthelemy, H., M. Weber, and F. Barbier, *Hydrogen storage: Recent improvements and industrial perspectives.* International Journal of Hydrogen Energy, 2017. **42**(11): p. 7254-7262.
28. Rivard, E., M. Trudeau, and K. Zaghib *Hydrogen Storage for Mobility: A Review*. Materials, 2019. **12**, DOI: 10.3390/ma12121973.
29. Yamashita, A., et al., *Development of High-Pressure Hydrogen Storage System for the Toyota "Mirai"*. 2015, SAE International.
30. Timmerhaus, K.D. and T.M. Flynn, *Properties of Cryogenic Fluids*, in *Cryogenic Process Engineering*, K.D. Timmerhaus and T.M. Flynn, Editors. 1989, Springer US: Boston, MA. p. 13-38.
31. Friedlander, A., R. Zubrin, and T.L. Hardy, *Benefits of slush hydrogen for space missions*. 1991.

32. Biggs, R.E., *Space shuttle main engine the first ten years.* History of liquid rocket engine development in the United States, 1992: p. 1955-1980.
33. Partridge, J.K., *Fractional consumption of liquid hydrogen and liquid oxygen during the space shuttle program.* AIP Conference Proceedings, 2012. **1434**(1): p. 1765-1770.
34. Notardonato, W.U., et al., *Zero boil-off methods for large-scale liquid hydrogen tanks using integrated refrigeration and storage.* IOP Conference Series: Materials Science and Engineering, 2017. **278**(1): p. 012012.
35. Aasadnia, M. and M. Mehrpooya, *Large-scale liquid hydrogen production methods and approaches: A review.* Applied Energy, 2018. **212**: p. 57-83.
36. Krasae-in, S., J.H. Stang, and P. Neksa, *Development of large-scale hydrogen liquefaction processes from 1898 to 2009.* International Journal of Hydrogen Energy, 2010. **35**(10): p. 4524-4533.
37. Stolzenburg, K., et al. *Efficient Liquefaction of Hydrogen: Results of the IDEALHY project*. in *Energy Symposium*. 2013. Stralsund, Germany.
38. Sherif, S.A., N. Zeytinoglu, and T.N. Veziroğlu, *Liquid hydrogen: Potential, problems, and a proposed research program.* International Journal of Hydrogen Energy, 1997. **22**(7): p. 683-688.
39. Russel, D.A. and G.G. Williams, *History of Chemical Fertilizer Development.* Soil Science Society of America Journal, 1977. **41**(2): p. 260-265.
40. Singh, V., I. Dincer, and M.A. Rosen, *Chapter 4.2 - Life Cycle Assessment of Ammonia Production Methods*, in *Exergetic, Energetic and Environmental Dimensions*, I. Dincer, C.O. Colpan, and O. Kizilkan, Editors. 2018, Academic Press. p. 935-959.
41. Foster, S.L., et al., *Catalysts for nitrogen reduction to ammonia.* Nature Catalysis, 2018. **1**(7): p. 490-500.
42. Mounaïm-Rousselle, C., et al., *Ammonia as Fuel for Transportation to Mitigate Zero Carbon Impact*, in *Engines and Fuels for Future Transport*, G. Kalghatgi, et al., Editors. 2022, Springer Singapore: Singapore. p. 257-279.
43. Frigo, S. and R. Gentili, *Analysis of the behaviour of a 4-stroke Si engine fuelled with ammonia and hydrogen.* International Journal of Hydrogen Energy, 2013. **38**(3): p. 1607-1615.
44. Kobayashi, H., et al., *Science and technology of ammonia combustion.* Proceedings of the Combustion Institute, 2019. **37**(1): p. 109-133.
45. Asif, M., et al., *Recent advances in green hydrogen production, storage and commercial-scale use via catalytic ammonia cracking.* Chemical Engineering Journal, 2023. **473**: p. 145381.
46. Ashcroft, J. and H. Goddin, *Centralised and Localised Hydrogen Generation by Ammonia Decomposition : A technical review of the ammonia cracking process.* 2022. **66**(4): p. 375-385.
47. Isorna Llerena, F., et al., *Effects of Ammonia Impurities on the Hydrogen Flow in High and Low Temperature Polymer Electrolyte Fuel Cells.* Fuel Cells, 2019. **19**(6): p. 651-662.
48. Behrens, M., *Chemical hydrogen storage by methanol: Challenges for the catalytic methanol synthesis from CO2.* Recyclable Catalysis, 2015. **2**(1).
49. Dalena, F., et al., *Chapter 1 - Methanol Production and Applications: An Overview*, in *Methanol*, A. Basile and F. Dalena, Editors. 2018, Elsevier. p. 3-28.
50. Bowker, M., *Methanol synthesis from CO2 hydrogenation.* ChemCatChem, 2019. **11**(17): p. 4238-4246.
51. Stanger, R., et al., *Oxyfuel combustion for CO2 capture in power plants.* International Journal of Greenhouse Gas Control, 2015. **40**: p. 55-125.
52. Enthaler, S., J. von Langermann, and T. Schmidt, *Carbon dioxide and formic acid—the couple for environmental-friendly hydrogen storage?* Energy & Environmental Science, 2010. **3**(9): p. 1207-1217.
53. Chen, Y., et al., *Sustainable production of formic acid and acetic acid from biomass.* Molecular Catalysis, 2023. **545**: p. 113199.
54. Kosider, A., et al., *Enhancing the feasibility of Pd/C-catalyzed formic acid decomposition for hydrogen generation – catalyst pretreatment, deactivation, and regeneration.* Catalysis Science & Technology, 2021. **11**(12): p. 4259-4271.
55. Modisha, P.M., et al., *The Prospect of Hydrogen Storage Using Liquid Organic Hydrogen Carriers.* Energy & Fuels, 2019. **33**(4): p. 2778-2796.
56. Preuster, P., C. Papp, and P. Wasserscheid, *Liquid Organic Hydrogen Carriers (LOHCs): Toward a Hydrogen-free Hydrogen Economy.* Accounts of Chemical Research, 2017. **50**(1): p. 74-85.
57. Cho, J.-Y., et al. *Recent Advances in Homogeneous/Heterogeneous Catalytic Hydrogenation and Dehydrogenation for Potential Liquid Organic Hydrogen Carrier (LOHC) Systems*. Catalysts, 2021. **11**, DOI: 10.3390/catal11121497.
58. Müller, K., J. Völkl, and W. Arlt, *Thermodynamic Evaluation of Potential Organic Hydrogen Carriers.* Energy Technology, 2013. **1**(1): p. 20-24.
59. Huynh, N.-D., S.H. Hur, and S.G. Kang, *Tuning the dehydrogenation performance of dibenzyl toluene as liquid organic hydrogen carriers.* International Journal of Hydrogen Energy, 2021. **46**(70): p. 34788-34796.
60. Perreault, P., et al., *Critical challenges towards the commercial rollouts of a LOHC-based H2 economy.* Current Opinion in Green and Sustainable Chemistry, 2023: p. 100836.
61. Preuster, P., A. Alekseev, and P. Wasserscheid, *Hydrogen Storage Technologies for Future Energy Systems.* Annual Review of Chemical and Biomolecular Engineering, 2017. **8**(1): p. 445-471.
62. Sultan, O. and H. Shaw, *Study of automotive storage of hydrogen using recyclable liquid chemical carriers.* NASA STI/Recon Technical Report N, 1975. **76**: p. 33642.
63. Markiewicz, M., et al., *Hazard assessment of quinaldine-, alkylcarbazole-, benzene- and toluene-based liquid organic hydrogen carrier (LOHCs) systems.* Energy & Environmental Science, 2019. **12**(1): p. 366-383.

64. Niermann, M., et al., *Liquid organic hydrogen carriers (LOHCs) – techno-economic analysis of LOHCs in a defined process chain.* Energy & Environmental Science, 2019. **12**(1): p. 290-307.
65. Lindfors, L.P., T. Salmi, and S. Smeds, *Kinetics of toluene hydrogenation on Ni/Al2O3 catalyst.* Chemical engineering science, 1993. **48**(22): p. 3813-3828.
66. Morawa Eblagon, K., et al., *Study of Catalytic Sites on Ruthenium For Hydrogenation of N-ethylcarbazole: Implications of Hydrogen Storage via Reversible Catalytic Hydrogenation.* The Journal of Physical Chemistry C, 2010. **114**(21): p. 9720-9730.
67. Oh, J., et al., *2-(N-Methylbenzyl)pyridine: A Potential Liquid Organic Hydrogen Carrier with Fast H2 Release and Stable Activity in Consecutive Cycles.* ChemSusChem, 2018. **11**(4): p. 661-665.
68. Teichmann, D., W. Arlt, and P. Wasserscheid, *Liquid Organic Hydrogen Carriers as an efficient vector for the transport and storage of renewable energy.* International Journal of Hydrogen Energy, 2012. **37**(23): p. 18118-18132.
69. Brückner, N., et al., *Evaluation of Industrially Applied Heat-Transfer Fluids as Liquid Organic Hydrogen Carrier Systems.* ChemSusChem, 2014. **7**(1): p. 229-235.
70. Kim, T.W., et al., *Tuning the isomer composition is a key to overcome the performance limits of commercial benzyltoluene as liquid organic hydrogen carrier.* Journal of Energy Storage, 2023. **60**: p. 106676.
71. Ji, X., et al. *Analysis of Dibenzyltoluene Mixtures: From Fast Analysis to In-Depth Characterization of the Compounds*. Molecules, 2023. **28**, DOI: 10.3390/molecules28093751.
72. Aziz, M. *Liquid Hydrogen: A Review on Liquefaction, Storage, Transportation, and Safety*. Energies, 2021. **14**, DOI: 10.3390/en14185917.
73. Liu, Y., et al., *Spread of hydrogen vapor cloud during continuous liquid hydrogen spills.* Cryogenics, 2019. **103**: p. 102975.
74. Markiewicz, M., et al., *Environmental and health impact assessment of Liquid Organic Hydrogen Carrier (LOHC) systems – challenges and preliminary results.* Energy & Environmental Science, 2015. **8**(3): p. 1035-1045.
75. Modisha, P. and D. Bessarabov, *Stress tolerance assessment of dibenzyltoluene-based liquid organic hydrogen carriers.* Sustainable Energy & Fuels, 2020. **4**(9): p. 4662-4670.
76. Yoro, K.O. and M.O. Daramola, *Chapter 1 - CO2 emission sources, greenhouse gases, and the global warming effect*, in *Advances in Carbon Capture*, M.R. Rahimpour, M. Farsi, and M.A. Makarem, Editors. 2020, Woodhead Publishing. p. 3-28.
77. Burton, N.A., et al., *Increasing the efficiency of hydrogen production from solar powered water electrolysis.* Renewable and Sustainable Energy Reviews, 2021. **135**: p. 110255.
78. Moon, C.-S., *Estimations of the lethal and exposure doses for representative methanol symptoms in humans.* Ann Occup Environ Med, 2017. **29**(1).
79. Chen, Q., et al., *Flash point and fire hazard analysis of three organic fuels and their aqueous solutions at low pressures.* Fire and Materials, 2018. **42**(7): p. 805-815.
80. Nowatzki, J., *Anhydrous Ammonia: Managing the Risks.* 2008.
81. National-Research-Council-Committee-on-Acute-Exposure-Guideline-Levels, *Ammonia acute exposure guideline levels*, in *Acute Exposure Guideline Levels for Selected Airborne Chemicals: Volume 6*. 2008, National Academies Press (US).
82. Bulgarin, A., et al., *Purity of hydrogen released from the Liquid Organic Hydrogen Carrier compound perhydro dibenzyltoluene by catalytic dehydrogenation.* International Journal of Hydrogen Energy, 2020. **45**(1): p. 712-720.
83. Willer, M., et al., *Continuous dehydrogenation of perhydro benzyltoluene and perhydro dibenzyltoluene in a packed bed vertical tubular reactor – The role of LOHC evaporation.* International Journal of Hydrogen Energy, 2024. **57**: p. 1513-1523.
84. Ali, A., et al., *Hydrogenation of dibenzyltoluene and the catalytic performance of Pt/Al2O3 with various Pt loadings for hydrogen production from perhydro-dibenzyltoluene.* International Journal of Energy Research, 2022. **46**(5): p. 6672-6688.
85. Jorschick, H., et al., *Hydrogen storage using a hot pressure swing reactor.* Energy & Environmental Science, 2017. **10**(7): p. 1652-1659.
86. Jorschick, H., et al., *Charging a Liquid Organic Hydrogen Carrier with Wet Hydrogen from Electrolysis.* ACS Sustainable Chemistry & Engineering, 2019. **7**(4): p. 4186-4194.
87. Jorschick, H., et al., *Charging a Liquid Organic Hydrogen Carrier System with H2/CO2 Gas Mixtures.* ChemCatChem, 2018. **10**(19): p. 4329-4337.
88. Solymosi, T., et al., *Catalytically activated stainless steel plates for the dehydrogenation of perhydro dibenzyltoluene.* International Journal of Hydrogen Energy, 2021. **46**(70): p. 34797-34806.
89. Liu, H.U., et al., *Centrifugal separation type dehydrogenation reactor and system based on heat pipe heat exchange*. 2022, UNIV XI AN JIAOTONG: CN.
90. Ali, A., A.K. Rohini, and H.J. Lee, *Dehydrogenation of perhydro-dibenzyltoluene for hydrogen production in a microchannel reactor.* International Journal of Hydrogen Energy, 2022. **47**(48): p. 20905-20914.
91. Wunsch, A., M. Mohr, and P. Pfeifer *Intensified LOHC-Dehydrogenation Using Multi-Stage Microstructures and Pd-Based Membranes*. Membranes, 2018. **8**, DOI: 10.3390/membranes8040112.
92. Geißelbrecht, M., et al., *Highly efficient, low-temperature hydrogen release from perhydro-benzyltoluene using reactive distillation.* Energy & Environmental Science, 2020. **13**(9): p. 3119-3128.

93. Rüde, T., et al., *Performance of Continuous Hydrogen Production from Perhydro Benzyltoluene by Catalytic Distillation and Heat Integration Concepts with a Fuel Cell.* Energy Technology, 2023. **11**(3): p. 2201366.
94. Rathke, J., et al., *Reactor apparatus for dehydrogenating a carrier medium*. 2019, HYDROGENIOUS TECHNOLOGIES GMBH: US.
95. Peters, R., et al., *A solid oxide fuel cell operating on liquid organic hydrogen carrier-based hydrogen – A kinetic model of the hydrogen release unit and system performance.* International Journal of Hydrogen Energy, 2019. **44**(26): p. 13794-13806.
96. Weiss, A., et al., *DEVICE AND METHOD FOR THE CATALYTIC RELEASE OF A GAS FROM A CARRIER MATERIAL*. 2022, HYDROGENIOUS LOHC TECH GMBH: WO.
97. Kadar, J., et al., *Boosting power density of hydrogen release from LOHC systems by an inverted fixed-bed reactor design.* International Journal of Hydrogen Energy, 2024. **59**: p. 1376-1387.
98. Heublein, N., M. Stelzner, and T. Sattelmayer, *Hydrogen storage using liquid organic carriers: Equilibrium simulation and dehydrogenation reactor design.* International Journal of Hydrogen Energy, 2020. **45**(46): p. 24902-24916.
99. Solymosi, T., et al., *Nucleation as a rate-determining step in catalytic gas generation reactions from liquid phase systems.* Science Advances, 2022. **8**(46): p. eade3262.
100. Fan, L.-S., *Chapter 11 - Miscellaneous Systems*, in *Gas–Liquid–Solid Fluidization Engineering*, L.-S. Fan, Editor. 1989, Butterworth-Heinemann: Boston. p. 683-731.
101. Oloruntoba, A., Y. Zhang, and C.S. Hsu *State-of-the-Art Review of Fluid Catalytic Cracking (FCC) Catalyst Regeneration Intensification Technologies*. Energies, 2022. **15**, DOI: 10.3390/en15062061.
102. Mishra, S. and R.K. Upadhyay, *Review on biomass gasification: Gasifiers, gasifying mediums, and operational parameters.* Materials Science for Energy Technologies, 2021. **4**: p. 329-340.
103. Fernandes, F.A.N. and E.M.M. Sousa, *Fischer-Tropsch synthesis product grade optimization in a fluidized bed reactor.* AIChE Journal, 2006. **52**(8): p. 2844-2850.
104. Alizadeh, M., et al., *Modeling of fluidized bed reactor of ethylene polymerization.* Chemical Engineering Journal, 2004. **97**(1): p. 27-35.
105. Ho, Y.K., et al., *Control of industrial gas phase propylene polymerization in fluidized bed reactors.* Journal of Process Control, 2012. **22**(6): p. 947-958.
106. Fakeeha, A.H., M.A. Soliman, and A.A. Ibrahim, *Modeling of a circulating fluidized bed for ammoxidation of propane to acrylonitrile.* Chemical Engineering and Processing: Process Intensification, 2000. **39**(2): p. 161-170.
107. Trivedi, U., A. Bassi, and J.-X. Zhu, *Continuous enzymatic polymerization of phenol in a liquid–solid circulating fluidized bed.* Powder Technology, 2006. **169**(2): p. 61-70.
108. Mukherjee, A.K., B.K. Mishra, and K. Ran Vijay, *Application of liquid/solid fluidization technique in beneficiation of fines.* International Journal of Mineral Processing, 2009. **92**(1): p. 67-73.
109. Aldaco, R., A. Garea, and A. Irabien, *Modeling of particle growth: Application to water treatment in a fluidized bed reactor.* Chemical Engineering Journal, 2007. **134**(1): p. 66-71.
110. Ferreira, V.O., et al., *Prediction of the bed expansion of a liquid fluidized bed bioreactor applied to wastewater treatment and biogas production.* Energy Conversion and Management, 2023. **290**: p. 117224.
111. Muroyama, K. and L.-S. Fan, *Fundamentals of gas-liquid-solid fluidization.* AIChE Journal, 1985. **31**(1): p. 1-34.
112. Konovnin, A.A., et al., *Deep Processing of Heavy Resids Based on TAIF-NK JSC Heavy Residue Conversion Complex.* Chemistry and Technology of Fuels and Oils, 2023. **59**(1): p. 1-6.
113. Tian, B., et al., *Process study and CO2 emission reduction analysis of coal liquefaction residue fluidized bed pyrolysis.* Frontiers in Energy Research, 2022. **10**.
114. Wang, J., et al., *Review of (gas)-liquid-solid circulating fluidized beds as biochemical and environmental reactors.* Chemical Engineering Journal, 2020. **386**: p. 121951.
115. Jia, D.E., *Heat and Mass Transfer*, in *Essentials of Fluidization Technology*. 2020. p. 291-331.
116. Mokhtari, M., J. Shabanian, and J. Chaouki, *Effects of solid particles on bubble breakup and coalescence in slurry bubble columns.* Chemical Engineering Science, 2022. **264**: p. 118148.
117. Majumder, S.K., *8 - Mass Transfer Characteristics*, in *Hydrodynamics and Transport Processes of Inverse Bubbly Flow*, S.K. Majumder, Editor. 2016, Elsevier: Amsterdam. p. 307-381.
118. Fan, L.-S., *Chapter 2 - Hydrodynamics of Cocurrent Upward Fluidized Bed Systems (Modes E-I-a-1 and E-I-b; Figure 1.3)*, in *Gas–Liquid–Solid Fluidization Engineering*, L.-S. Fan, Editor. 1989, Butterworth-Heinemann: Boston. p. 33-161.
119. Levenspiel, O., *Chemical Reaction Engineering.* Industrial & Engineering Chemistry Research, 1999. **38**(11): p. 4140-4143.
120. Pjontek, D., A. Donaldson, and A. Macchi, *Three-Phase (Gas–Liquid–Solid) Fluidization*, in *Essentials of Fluidization Technology*. 2020. p. 553-589.
121. Zhang, J.P., et al., *Flow regime identification in gas-liquid flow and three-phase fluidized beds.* Chemical Engineering Science, 1997. **52**(21): p. 3979-3992.
122. Li, X., et al., *Simulation study on the phase holdup characteristics of the gas–liquid-solid mini-fluidized beds with bubbling flow.* Chemical Engineering Journal, 2022. **427**: p. 131488.
123. Neogi, A., H.K. Mohanta, and P.C. Sande, *Study of fluidized bed freeboard for effect of Geldart A particles shape using particle image velocimetry (PIV).* Powder Technology, 2024. **433**: p. 119235.

124. Song, G.H., et al., *Hydrodynamics of three-phase fluidized bed containing cylindrical hydrotreating catalysts.* The Canadian Journal of Chemical Engineering, 1989. **67**(2): p. 265-275.
125. Wen, C.-Y.Y., Y.H., *Mechanics of fluidization.* Chemical Engineering Progress Symposium Series, 1966. **62**.
126. Fan, L.-S., A. Matsuura, and S.-H. Chern, *Hydrodynamic characteristics of a gas-liquid-solid fluidized bed containing a binary mixture of particles.* AIChE Journal, 1985. **31**(11): p. 1801-1810.
127. Akita, K. and F. Yoshida, *Gas Holdup and Volumetric Mass Transfer Coefficient in Bubble Columns. Effects of Liquid Properties.* Industrial & Engineering Chemistry Process Design and Development, 1973. **12**(1): p. 76-80.
128. Hazare, S.R., et al., *Correlating Interfacial Area and Volumetric Mass Transfer Coefficient in Bubble Column with the Help of Machine Learning Methods.* Industrial & Engineering Chemistry Research, 2023. **62**(5): p. 2104-2123.
129. Kitagawa, A., K. Uchida, and Y. Hagiwara, *Effects of bubble size on heat transfer enhancement by sub-millimeter bubbles for laminar natural convection along a vertical plate.* International Journal of Heat and Fluid Flow, 2009. **30**(4): p. 778-788.
130. Matsuura, A. and L.-S. Fan, *Distribution of bubble properties in a gas-liquid-solid fluidized bed.* AIChE Journal, 1984. **30**(6): p. 894-903.
131. Patience, G.S., *Experimental methods in chemical engineering: Preface.* The Canadian Journal of Chemical Engineering, 2018. **96**(11): p. 2312-2316.
132. Robertson, E., et al., *Validation of OpenFOAM numerical methods and turbulence models for incompressible bluff body flows.* Computers \& Fluids, 2015. **123**: p. 122-145.
133. Sadino-Riquelme, C., et al., *Computational fluid dynamic (CFD) modelling in anaerobic digestion: General application and recent advances.* Critical Reviews in Environmental Science and Technology, 2018. **48**(1): p. 39-76.
134. Versteeg, H.K. and W. Malalasekera, *An Introduction to Computational Fluid Dynamics: The Finite Volume Method*. 2007: Pearson Education Limited.
135. Weller, H.G., et al., *A tensorial approach to computational continuum mechanics using object-oriented techniques.* Computers in Physics, 1998. **12**(6).
136. Roache, P.J., *Perspective: A Method for Uniform Reporting of Grid Refinement Studies.* Journal of Fluids Engineering, 1994. **116**(3): p. 405-413.
137. Fox, R.O., *Computational Models for Turbulent Reacting Flows*. Cambridge Series in Chemical Engineering. 2003, Cambridge: Cambridge University Press.
138. Moukalled, F., L. Mangani, and M. Darwish, *The Finite Volume Method in Computational Fluid Dynamics : An Advanced Introduction with OpenFOAM® and Matlab*. Fluid Mechanics and Its Applications, ed. A. Thess. Vol. 113. 2016: Springer. 791.
139. Edwards, M.G. and C.F. Rogers, *Finite volume discretization with imposed flux continuity for the general tensor pressure equation.* Computational Geosciences, 1998. **2**(4): p. 259-290.
140. Eymard, R., T. Gallouët, and R. Herbin, *Finite volume methods*, in *Handbook of Numerical Analysis*. 2000, Elsevier. p. 713-1018.
141. Holzmann, T., *Mathematics, Numerics, Derivations and OpenFOAM*. Vol. Release 7.0. 2019: Holmzann CFD.
142. Murthy, J.Y., *Numerical Methods in Heat, Mass and Momentum Transfer*, in *School of Mechanical Engineering*. 2002, Perdue University. p. 196.
143. Saqr, K.M., *Practical Introduction to CFD, K.M. Saqr, 2nd Edition.pdf*. 2017. p. 50.
144. Ferziger, J.H.P., M., *Computational Methods for Fluid Dynamics*. 3 ed. 2002: Springer Berlin, Heidelberg. 423.
145. Demirdžić, I., *On the Discretization of the Diffusion Term in Finite-Volume Continuum Mechanics.* Numerical Heat Transfer, Part B: Fundamentals, 2015. **68**(1): p. 1-10.
146. Wimshurst, A., *Fluid Mechanics 101 Coarses*. Fluid Mechanics 101 Coarses, ed. A. Wimshurst. Vol. 2021. 2021: Wimshurst, Aiden.
147. ANSYS, *ANSYS Fluent - CFD software | ANSYS*. 2016.
148. Software, S.D.I., *Simcenter STAR-CCM+ User Guide v. 2021.1*. 2021.
149. Patankar, S.V. and D.B. Spalding, *A calculation procedure for heat, mass and momentum transfer in three-dimensional parabolic flows.* International Journal of Heat and Mass Transfer, 1972. **15**(10): p. 1787-1806.
150. Issa, R.I., *Solution of the implicitly discretised fluid flow equations by operator-splitting.* Journal of Computational Physics, 1986. **62**(1): p. 40-65.
151. Courant, R., K. Friedrichs, and H. Lewy, *On the Partial Difference Equations of Mathematical Physics.* IBM Journal of Research and Development, 1967. **11**(2): p. 215-234.
152. Patience, G.S. and J. Chaouki, *Gas phase hydrodynamics in the riser of a circulating fluidized bed.* Chemical Engineering Science, 1993. **48**(18): p. 3195-3205.
153. Tu, J., G.-H. Yeoh, and C. Liu, *Practical Guidelines for CFD Simulation and Analysis*, in *Computational Fluid Dynamics*. 2018. p. 255-290.
154. Fogler, H.S., *Elements of chemical reaction engineering*. 2006.
155. Vandewalle, L.A., G.B. Marin, and K.M. Van Geem, *catchyFOAM: Euler–Euler CFD Simulations of Fluidized Bed Reactors with Microkinetic Modeling of Gas-Phase and Catalytic Surface Chemistry.* Energy \& Fuels, 2020. **35**(3): p. 2545-2561.
156. Lilley, G., *Turbulence Modelling for CFD DC Wilcox DCW Industries, 5354 Palm Drive, La Canada, CA 91011, USA. 1993. 460pp+ software diskette. Illustrated. $75.* The Aeronautical Journal, 1994. **98**(980): p. 405-405.
157. Yusuf, S.N.A., et al., *A Short Review on RANS Turbulence Models.* CFD Letters, 2020. **12**(11): p. 83-96.

158. Menter, F.R., *Two-equation eddy-viscosity turbulence models for engineering applications.* AIAA Journal, 1994. **32**(8): p. 1598-1605.
159. Menter, F.R., M. Kuntz, and R. Langtry, *Ten years of industrial experience with the SST turbulence model.* Turbulence, heat and mass transfer, 2003. **4**(1): p. 625-632.
160. OpenFOAM-Foundation. *blockMesh.C File Reference*. 2020 [cited 2021 12-10]; Available from: https://cpp.openfoam.org/v8/blockMesh_8C.html.
161. OpenFOAM-Foundation. *snappyHexMesh.C File Reference*. 2020 [cited 2021 12-10]; Available from: https://cpp.openfoam.org/v8/snappyHexMesh_8C.html.
162. Ribes, A. and A. Bruneton. *Visualizing results in the SALOME platform for large numerical simulations: An integration of ParaView*. in *2014 IEEE 4th Symposium on Large Data Analysis and Visualization (LDAV)*. 2014.
163. Knupp, P., *Remarks on Mesh Quality*, in *45th AIAA Aerospace Sciences Meeting and Exhibit*. 2007, American Institute of Aeronautics and Astronautics: Reno. p. 10.
164. Gutierrez Marcantoni, L., J. Tamagno, and S. Elaskar, *RANS Simulation of Turbulent Diffusive Combustion Using openFoam.* Journal of Applied Fluid Mechanics., 2016. **9**.
165. Allen, D.T., *The engineering of chemical reactions. By Lanny D. Schmidt, Oxford University Press, New York, 1998 536 pp., $75.00.* AIChE Journal, 1999. **45**(8): p. 1836-1836.
166. OpenFOAM-Foundation. *mapFields.C File Reference*. 2020 [cited 2021 12-10]; Available from: https://cpp.openfoam.org/v8/classFoam_1_1emptyFvPatch.html#details.
167. Slater, J.W. *Examining Spatial (Grid) Convergence*. 2021 10-02-2021 [cited 2021 12-10]; Available from: https://www.grc.nasa.gov/WWW/wind/valid/tutorial/spatconv.html
168. Vandewalle, L.A., et al., *Process Intensification in a Gas–Solid Vortex Unit: Computational Fluid Dynamics Model Based Analysis and Design.* Industrial & Engineering Chemistry Research, 2019. **58**(28): p. 12751-12765.
169. Inthavong, K., et al., *Examining mesh independence for flow dynamics in the human nasal cavity.* Comput Biol Med, 2018. **102**: p. 40-50.
170. Misiulia, D., et al., *High-efficiency industrial cyclone separator: A CFD study.* Powder Technology, 2020. **364**: p. 943-953.
171. Wang, S., et al., *Impact of operating parameters on biomass gasification in a fluidized bed reactor: An Eulerian-Lagrangian approach.* Powder Technology, 2018. **333**: p. 304-316.
172. Stankiewicz, A.I. and J.A. Moulijn, *Process intensification: transforming chemical engineering.* Chemical engineering progress, 2000. **96**(1): p. 22-34.
173. Kuzmin, A.O., *Confined multiphase swirled flows in chemical engineering.* Reviews in Chemical Engineering, 2021. **37**(1): p. 31-68.
174. Geburtig, D., et al., *Chemical utilization of hydrogen from fluctuating energy sources – Catalytic transfer hydrogenation from charged Liquid Organic Hydrogen Carrier systems.* International Journal of Hydrogen Energy, 2016. **41**(2): p. 1010-1017.
175. Wulf, C. and P. Zapp, *Assessment of system variations for hydrogen transport by liquid organic hydrogen carriers.* International Journal of Hydrogen Energy, 2018. **43**(26): p. 11884-11895.
176. Müller, K., et al., *Liquid Organic Hydrogen Carriers: Thermophysical and Thermochemical Studies of Benzyl- and Dibenzyl-toluene Derivatives.* Industrial & Engineering Chemistry Research, 2015. **54**(32): p. 7967-7976.
177. van der Meer, E.H., R.B. Thorpe, and J.F. Davidson, *Dimensionless groups for practicable similarity of circulating fluidised beds.* Chemical Engineering Science, 1999. **54**(22): p. 5369-5376.
178. Knowlton, T.M., S.B.R. Karri, and A. Issangya, *Scale-up of fluidized-bed hydrodynamics.* Powder Technology, 2005. **150**(2): p. 72-77.
179. Kunii, D. and O. Levenspiel, *CHAPTER 3 - Fluidization and Mapping of Regimes*, in *Fluidization Engineering (Second Edition)*, D. Kunii and O. Levenspiel, Editors. 1991, Butterworth-Heinemann: Boston. p. 61-94.
180. Aslam, R., et al., *Thermophysical Studies of Dibenzyltoluene and Its Partially and Fully Hydrogenated Derivatives.* Journal of Chemical & Engineering Data, 2018. **63**(12): p. 4580-4587.
181. Hu, X., et al., *CFD simulations of stirred-tank reactors for gas-liquid and gas-liquid-solid systems using OpenFOAM®.* 2021. **19**(2): p. 193-207.
182. Ishii, M. and N. Zuber, *Drag coefficient and relative velocity in bubbly, droplet or particulate flows.* AIChE Journal, 1979. **25**(5): p. 843-855.
183. Asad, A., C. Kratzsch, and R. Schwarze, *Influence of drag closures and inlet conditions on bubble dynamics and flow behavior inside a bubble column.* Engineering Applications of Computational Fluid Mechanics, 2017. **11**(1): p. 127-141.
184. Li, C., et al., *A Study of Drag Force in Isothermal Bubbly Flow.* The Journal of Computational Multiphase Flows, 2009. **1**(4): p. 295-309.
185. OpenFOAM-Foundation. *IshiiZuber Class Reference*. C++ Source Code Guide 2020 01-09-2022]; Available from: https://cpp.openfoam.org/v8/classFoam_1_1dragModels_1_1IshiiZuber.html#details.
186. Ergun, S. *Fluid flow through packed columns*. 1952.
187. Tabib, M.V. and P. Schwarz, *Quantifying sub-grid scale (SGS) turbulent dispersion force and its effect using one-equation SGS large eddy simulation (LES) model in a gas–liquid and a liquid–liquid system.* Chemical Engineering Science, 2011. **66**(14): p. 3071-3086.

188. Van Cauwenberge, D.J., et al., *CFD-based design of 3D pyrolysis reactors: RANS vs. LES.* Chemical Engineering Journal, 2015. **282**: p. 66-76.
189. Bestion, D., *The difficult challenge of a two-phase CFD modelling for all flow regimes.* Nuclear Engineering and Design, 2014. **279**: p. 116-125.
190. Larsen, B.E., D.R. Fuhrman, and J. Roenby, *Performance of interFoam on the simulation of progressive waves.* Coastal Engineering Journal, 2019. **61**(3): p. 380-400.
191. Park, S., M. Naseem, and S. Lee, *Experimental Assessment of Perhydro-Dibenzyltoluene Dehydrogenation Reaction Kinetics in a Continuous Flow System for Stable Hydrogen Supply.* Materials, 2021. **14**(24).
192. Otálvaro-Marín, H.L. and F. Machuca-Martínez, *Sizing of reactors by charts of Damköhler's number for solutions of dimensionless design equations.* Heliyon, 2020. **6**(11): p. e05386.
193. Grimstad, A.-A., et al., *Degassing Rate of Drilling Fluid Base Oils as Exposed to Depressurisation and Drill String Rotation*, in *SPE/IADC Drilling Conference and Exhibition*. 2017. p. D032S025R002.
194. Blissett, R., et al., *Valorisation of rice husks using a TORBED® combustion process.* Fuel Processing Technology, 2017. **159**: p. 247-255.
195. Liu, L., et al., *Analysis of Hydrocyclone Geometry via Rapid Optimization Based on Computational Fluid Dynamics.* Chemical Engineering & Technology, 2021. **44**(9): p. 1693-1707.
196. Heinrich, M. and R. Schwarze, *3D-coupling of Volume-of-Fluid and Lagrangian particle tracking for spray atomization simulation in OpenFOAM.* SoftwareX, 2020. **11**: p. 100483.
197. Tomiyama, A., et al., *Drag Coefficients of Single Bubbles under Normal and Micro Gravity Conditions.* JSME International Journal Series B, 1998. **41**(2): p. 472-479.
198. Laín, S., et al., *Modelling hydrodynamics and turbulence in a bubble column using the Euler–Lagrange procedure.* International Journal of Multiphase Flow, 2002. **28**(8): p. 1381-1407.
199. Li, P., et al., *Drag models for simulating gas–solid flow in the turbulent fluidization of FCC particles.* Particuology, 2009. **7**(4): p. 269-277.
200. Gidaspow, D., *Hydrodynamics of Fiuidizatlon and Heat Transfer: Supercomputer Modeling.* Applied Mechanics Reviews, 1986. **39**(1): p. 1-23.
201. Zhang, D.Z. and W.B. VanderHeyden, *The effects of mesoscale structures on the macroscopic momentum equations for two-phase flows.* International Journal of Multiphase Flow, 2002. **28**(5): p. 805-822.
202. Méndez, C.G., N. Nigro, and A. Cardona, *Drag and non-drag force influences in numerical simulations of metallurgical ladles.* Journal of Materials Processing Technology, 2005. **160**(3): p. 296-305.
203. Suh, J.-W., et al., *Development of numerical Eulerian-Eulerian models for simulating multiphase pumps.* Journal of Petroleum Science and Engineering, 2018. **162**: p. 588-601.
204. Yu, Y., et al., *Numerical simulation of gas-liquid-solid three-phase flow with the construction of theoretical continuous elements.* Chemical Engineering Science, 2020. **220**: p. 115633.
205. Li, W. and W. Zhong, *CFD simulation of hydrodynamics of gas–liquid–solid three-phase bubble column.* Powder Technology, 2015. **286**: p. 766-788.
206. Hamidipour, M., J. Chen, and F. Larachi, *CFD study on hydrodynamics in three-phase fluidized beds—Application of turbulence models and experimental validation.* Chemical Engineering Science, 2012. **78**: p. 167-180.
207. Panneerselvam, R., S. Savithri, and G.D. Surender, *CFD simulation of hydrodynamics of gas–liquid–solid fluidised bed reactor.* Chemical Engineering Science, 2009. **64**(6): p. 1119-1135.
208. Wang, F., et al., *Measurement of phase holdups in liquid–liquid–solid three-phase stirred tanks and CFD simulation.* Chemical Engineering Science, 2006. **61**(22): p. 7535-7550.
209. Liu, Y., S. Guo, and J. Zhu, *Euler multiphase-CFD simulation on a bubble-driven gas–liquid–solid fluidized bed.* The Canadian Journal of Chemical Engineering, 2023. **101**(7): p. 4255-4269.
210. Neogi, A., H.K. Mohanta, and P.C. Sande, *Particle image velocimetry investigations on multiphase flow in fluidized beds: A review.* Flow Measurement and Instrumentation, 2023. **89**: p. 102309.
211. Tebianian, S., et al., *Investigation of particle velocity in FCC gas-fluidized beds based on different measurement techniques.* Chemical Engineering Science, 2015. **127**: p. 310-322.
212. Hernández-Jiménez, F., et al., *Comparison between two-fluid model simulations and particle image analysis & velocimetry (PIV) results for a two-dimensional gas–solid fluidized bed.* Chemical Engineering Science, 2011. **66**(17): p. 3753-3772.
213. Sánchez-Delgado, S., et al., *Estimation and experimental validation of the circulation time in a 2D gas–solid fluidized beds.* Powder Technology, 2013. **235**: p. 669-676.
214. Sánchez-Delgado, S., et al., *Dense-phase velocity fluctuation in a 2-D fluidized bed.* Powder Technology, 2010. **200**(1): p. 37-45.
215. Asegehegn, T.W., M. Schreiber, and H.J. Krautz, *Investigation of bubble behavior in fluidized beds with and without immersed horizontal tubes using a digital image analysis technique.* Powder Technology, 2011. **210**(3): p. 248-260.
216. Ghatage, S.V., et al., *Stability analysis in solid–liquid fluidized beds: Experimental and computational.* Chemical Engineering Journal, 2014. **256**: p. 169-186.
217. Van Hoecke, L., et al., *Intensified swirling reactor for the dehydrogenation of LOHC.* International Journal of Hydrogen Energy, 2024. **51**: p. 611-623.
218. Schneider, C.A., W.S. Rasband, and K.W. Eliceiri, *NIH Image to ImageJ: 25 years of image analysis.* Nature Methods, 2012. **9**(7): p. 671-675.

219. Ershov, D., et al., *TrackMate 7: integrating state-of-the-art segmentation algorithms into tracking pipelines.* Nature Methods, 2022. **19**(7): p. 829-832.
220. Thielicke, W. and R. Sonntag, *Particle Image Velocimetry for MATLAB: Accuracy and enhanced algorithms in PIVlab.* Journal of Open Research Software, 2021.
221. Peltonen, P., et al., *The ghost fluid method for OpenFOAM: A comparative study in marine context.* Ocean Engineering, 2020. **216**: p. 108007.
222. Wardle, K.E. and H.G. Weller, *Hybrid Multiphase CFD Solver for Coupled Dispersed/Segregated Flows in Liquid-Liquid Extraction.* International Journal of Chemical Engineering, 2013. **2013**: p. 128936.
223. Gidaspow, D., J. Jung, and R.K. Singh, *Hydrodynamics of fluidization using kinetic theory: an emerging paradigm: 2002 Flour-Daniel lecture.* Powder Technology, 2004. **148**(2): p. 123-141.
224. Cornelissen, J.T., et al., *CFD modelling of a liquid–solid fluidized bed.* Chemical Engineering Science, 2007. **62**(22): p. 6334-6348.
225. Yuan, Z., et al., *Simulation study on the flow behavior of wet particles in the power-law liquid-solid fluidized bed.* Powder Technology, 2023. **415**: p. 118117.
226. Cloete, S., et al., *The effect of frictional pressure, geometry and wall friction on the modelling of a pseudo-2D bubbling fluidised bed reactor.* Powder Technology, 2015. **283**: p. 85-102.
227. Černe, G., S. Petelin, and I. Tiselj, *Coupling of the Interface Tracking and the Two-Fluid Models for the Simulation of Incompressible Two-Phase Flow.* Journal of Computational Physics, 2001. **171**(2): p. 776-804.
228. Syamlal, M. and T. O'Brien, *The Derivation of a Drag Coefficient Formula from Velocity-Voidage Correlations.* 1994.
229. Guha, D., et al., *Evaluation of large Eddy simulation and Euler-Euler CFD models for solids flow dynamics in a stirred tank reactor.* AIChE Journal, 2008. **54**(3): p. 766-778.
230. Zhou, X., et al., *CFD-PBM simulations on hydrodynamics and gas-liquid mass transfer in a gas-liquid-solid circulating fluidized bed.* Powder Technology, 2020. **362**: p. 57-74.
231. Hayes, R.E., et al., *CFD modelling of the automotive catalytic converter.* Catalysis Today, 2012. **188**(1): p. 94-105.
232. Porter, S., et al., *Hybrid flow modelling approach applied to automotive catalysts.* Applied Mathematical Modelling, 2016. **40**(19): p. 8435-8445.
233. Park, H.M., *A multiscale modeling of fixed bed catalytic reactors.* International Journal of Heat and Mass Transfer, 2018. **116**: p. 520-531.
234. Pourali, M., et al., *Ammonia decomposition in a porous catalytic reactor to enable hydrogen storage: Numerical simulation, machine learning, and response surface methodology.* Journal of Energy Storage, 2022. **55**: p. 105804.
235. Bian, Z., et al., *A CFD study on H2-permeable membrane reactor for methane CO2 reforming: Effect of catalyst bed volume.* International Journal of Hydrogen Energy, 2021. **46**(77): p. 38336-38350.
236. Greenshields, C. *OpenFOAM 3.0.0 Released*. 2015 [cited 2024 08/02]; Available from: https://openfoam.org/release/3-0-0/.
237. Qiu, Y., et al., *Computational fluid dynamics modeling of biomass catalytic fast pyrolysis in bubbling fluidized reactor: Effects of catalyst parameters on process performance.* AIChE Journal, 2022. **68**(6): p. e17637.
238. Maestri, M. and A. Cuoci, *Coupling CFD with detailed microkinetic modeling in heterogeneous catalysis.* Chemical Engineering Science, 2013. **96**: p. 106-117.
239. Micale, D., et al., *Coupling Euler-Euler and Microkinetic Modeling for the Simulation of Fluidized Bed Reactors: an Application to the Oxidative Coupling of Methane.* Ind Eng Chem Res, 2021. **60**(18): p. 6687-6697.
240. Salciccioli, M., et al., *A review of multiscale modeling of metal-catalyzed reactions: Mechanism development for complexity and emergent behavior.* Chemical Engineering Science, 2011. **66**(19): p. 4319-4355.
241. Solymosi, T., et al., *Nucleation as a rate-determining step in catalytic gas generation reactions from liquid phase systems.* Science Advances, 2022. **8**(46).
242. Choi, C., C. Lee, and I.S. Kim, *Modeling of flow uniformity by installing inlet distributor within the inflow part of a pressurized module using computational fluid dynamics.* Environmental Engineering Research, 2020. **25**(6): p. 969-976.
243. Gonzalez-Quiroga, A., et al., *Design and cold flow testing of a Gas-Solid Vortex Reactor demonstration unit for biomass fast pyrolysis.* Chemical Engineering Journal, 2017. **329**: p. 198-210.
244. Wang, H., et al., *A review of process intensification applied to solids handling.* Chemical Engineering and Processing: Process Intensification, 2017. **118**: p. 78-107.
245. Mohideen, M.F., et al., *Heat transfer in a swirling fluidized bed with geldart type-D particles.* Korean Journal of Chemical Engineering, 2012. **29**(7): p. 862-867.
246. Dodson, C.E. and V.I. Lakshmanan, *An innovative gas-solid torbed reactor for the recycling industries.* JOM, 1998. **50**(7): p. 29-31.
247. Sreenivasan, B. and V.R. Raghavan, *Hydrodynamics of a swirling fluidised bed.* Chemical Engineering and Processing: Process Intensification, 2002. **41**(2): p. 99-106.
248. OpenFOAM-Foundation. *massSource Class Reference*. OpenFoam 11 C++ Source Code Guide 2023 [cited 2024 21/02].
249. Pflüger, A., *Untersuchungen zur Reinheit von Wasserstoff aus der katalytischen Dehydrierung des flüssigen organischen Wasserstoffträgers Perhydro-Dibenzyltoluol*, in *Technische Fakultät*. 2022, Friedrich-Alexander-Universität Erlangen-Nürnberg: Nürnberg. p. 175.

250. de Broqueville, A. and J. De Wilde, *Numerical investigation of gas-solid heat transfer in rotating fluidized beds in a static geometry.* Chemical Engineering Science, 2009. **64**(6): p. 1232-1248.
251. Chen, X., et al., *Hydrogen Production Based on Liquid Organic Hydrogen Carriers through Sulfur Doped Platinum Catalysts Supported on TiO2.* ACS Sustainable Chemistry & Engineering, 2021. **9**(19): p. 6561-6573.
252. Berger Bioucas, F.E., et al., *Thermal Conductivity of Hydrocarbon Liquid Organic Hydrogen Carrier Systems: Measurement and Prediction.* Journal of Chemical & Engineering Data, 2020. **65**: p. 5003-5017.
253. Naz, M.Y., S.A. Sulaiman, and M.A. Bou-Rabee, *Particle tracking velocimetry investigations on density dependent velocity vector profiles of a swirling fluidized bed.* Drying Technology, 2017. **35**(2): p. 193-202.
254. Fan, L.S. and K. Muroyama, *Chapter 3 - Mass Transfer, Mixing and Heat Transfer of Cocurrent Upward Fluidized Bed Systems (Mode E-I-a-1; Figure 1.3)*, in *Gas–Liquid–Solid Fluidization Engineering*, L.-S. Fan, Editor. 1989, Butterworth-Heinemann: Boston. p. 163-249.
255. Epstein, N. and B.P. LeClair, *Liquid fluidization of binary particle mixtures—II. Bed inversion.* Chemical Engineering Science, 1985. **40**(8): p. 1517-1526.
256. Escudié, R., et al., *Layer inversion phenomenon in binary-solid liquid-fluidized beds: Prediction of the inversion velocity.* Chemical Engineering Science, 2006. **61**(20): p. 6667-6690.
257. Di Felice, R. and A. Di Renzo, *Liquid Fluidization*, in *Essentials of Fluidization Technology*. 2020. p. 33-53.
258. Kunii, D. and O. Levenspiel, *Fluidization engineering*. 1991: Butterworth-Heinemann.
259. Pantzali, M.N., et al., *Radial pressure profiles in a cold-flow gas-solid vortex reactor.* AIChE Journal, 2015. **61**(12): p. 4114-4125.
260. De Wilde, J., *Gas–solid fluidized beds in vortex chambers.* Chemical Engineering and Processing: Process Intensification, 2014. **85**: p. 256-290.
261. Lin, A. and G. Bagnato, *Revolutionising energy storage: The Latest Breakthrough in liquid organic hydrogen carriers.* International Journal of Hydrogen Energy, 2024. **63**: p. 315-329.
262. Ouyang, Y., G.J. Heynderickx, and K.M. Van Geem, *Development of intensified reactors: A process intensification methodology perspective.* Chemical Engineering and Processing-Process Intensification, 2022. **181**: p. 109164.